

Electrical
Engineering

Jonas Kornprobst

Surface Source Representations for the Accurate and Stable Solution of Electromagnetic Integral Equations

Surface Source Representations for the Accurate and Stable Solution of Electromagnetic Integral Equations

Jonas Kornprobst

Vollständiger Abdruck der von der TUM School of Computation, Information and Technology der Technischen Universität München zur Erlangung des akademischen Grades eines Doktors der Ingenieurwissenschaften genehmigten Dissertation.

Vorsitz:

apl. Prof. Dr.-Ing. habil. Helmut Gräß

Prüfer*innen der Dissertation:

1. Prof. Dr. Thomas F. Eibert
2. Prof. Dr. Francesca Vipiana

Die Dissertation wurde am 13.06.2022 bei der Technischen Universität München eingereicht und durch die TUM School of Computation, Information and Technology am 08.11.2022 angenommen.

The German National Library has registered this publication in the German National Bibliography. Detailed bibliographic data are available on the Internet at <https://portal.dnb.de>.

Imprint

1. Edition

Copyright © 2023 TUM.University Press

Copyright © 2023 Jonas Kornprobst (ORCID-ID: 0000-0001-8099-0232)

All rights reserved

Layout design and typesetting: Jonas Kornprobst

Cover design: Caroline Ennemoser

Cover illustration: Jonas Kornprobst

TUM.University Press

Technical University of Munich

Arcisstrasse 21

80333 Munich

DOI: 10.14459/2023md1658129

ISBN printed edition: 978-3-95884-081-2

www.tum.de

Abstract

Computational electromagnetics and in particular boundary integral equations are an important tool for the analysis of electromagnetic scattering and radiation scenarios, be it for simulation purposes or for the processing of measured data. By leveraging the algorithms presented in this dissertation, solutions to surface-source problems may be retrieved with less computational effort, with increased reliability, and/or with increased accuracy.

The first part of the thesis focuses on the simulation of radiation and scattering scenarios involving perfectly conducting objects with boundary integral equations, especially tackling the high-frequency accuracy issues of the magnetic field integral equation with a low-order discretization. Several approaches to deal with those inaccuracies are proposed, including a combined-source integral equation and a weak-form discretization scheme for the identity operator appearing inside the magnetic field integral equation. These approaches are discussed with respect to their benefits regarding the solution accuracy, both for the lowest-order Rao-Wilton-Glisson basis functions as well as for a set of hierarchical higher-order functions.

The second topic of this dissertation are surface-source reconstruction methods for near-field antenna measurements and related near-field to far-field transformations. Three distinct problems are treated. First, different choices for equivalent surface sources for the antenna-under-test representation are compared with respect to the ill-posedness of certain choices, the conditioning differences of the system matrices, the achievable accuracy of the reconstructed fields, and the respective diagnostics capabilities. Second, two echo suppression techniques are presented which help to cope with the presence of undesired scattering objects in the vicinity of an antenna under test. This is either done by incorporating knowledge about the scatterer material, shape, and location or by software time-gating based on broadband measurements. Third, the special case of phaseless near-field measurements is considered—lacking a global phase information for the individual measurement samples. Two approaches are discussed, which are both based on specialized receiver hardware which is able to capture coherent subsets of the near-field data, either for multi-frequency measurements or for multi-probe setups. In the former case, the phase retrieval process is based on a non-linear optimization just as for most classical phase retrieval algorithms. The latter approach introduces a linearization of the problem which greatly improves the reliability of the phase retrieval process, bringing it close to standard antenna measurements with full phase information.

Kurzfassung

Numerische Feldberechnung und insbesondere Randintegralgleichungen sind ein wichtiges Werkzeug für die Analyse elektromagnetischer Streu- und Strahlungsszenarien, sei es für Simulationszwecke oder die Verarbeitung von Messdaten. Durch den Einsatz der in dieser Dissertation vorgestellten Algorithmen können Lösungen für Oberflächenquellen-Probleme mit geringerem Rechenaufwand, mit höherer Zuverlässigkeit und/oder mit höherer Genauigkeit gefunden werden.

Der erste Teil der Arbeit befasst sich mit der Simulation von Strahlungs- und Streuszenarien mit Randintegralgleichungen, insbesondere mit den Problemen der Genauigkeit der Magnetfeldintegralgleichung bei hohen Frequenzen und mit einer Diskretisierung niedriger Ordnung. Es werden mehrere Ansätze zur Behandlung dieser Ungenauigkeiten vorgeschlagen, darunter eine Integralgleichung mit kombinierten elektrischen und magnetischen Oberflächenstromquellen und ein Ansatz, der den in der Magnetfeldintegralgleichung auftretenden Identitätsoperator in schwacher Form diskretisiert. Diese Ansätze werden im Hinblick auf ihre Vorteile hinsichtlich der Lösungsgenauigkeit sowohl für die Rao-Wilton-Glisson-Basisfunktionen niedrigster Ordnung als auch für eine Reihe hierarchischer Funktionen höherer Ordnung diskutiert.

Das zweite Thema dieser Dissertation sind Oberflächenquellen-Rekonstruktionsmethoden für Nahfeld-Antennenmessungen und damit verbundene Nahfeld-Fernfeld-Transformationen. Es werden drei verschiedene Probleme behandelt. Erstens werden verschiedene Möglichkeiten zur Darstellung der zu testenden Antenne mit äquivalenten Oberflächenquellen im Hinblick auf die Unzulänglichkeiten bestimmter Varianten untersucht. Außerdem werden die Konditionierungsunterschiede der Systemmatrizen, die erreichbare Genauigkeit der rekonstruierten Felder und die jeweiligen Diagnosemöglichkeiten verglichen. Zweitens werden zwei Verfahren zur Echounterdrückung vorgestellt, die helfen, unerwünschte Streuobjekten in der Nähe einer zu testenden Antenne zu berücksichtigen und die Rekonstruktion entsprechend zu korrigieren. Dies geschieht entweder durch die Einbeziehung von Kenntnissen über das Material, die Form und den Ort des Streuobjekts oder durch Software-Time-Gating auf der Grundlage von Breitbandmessungen. Drittens wird der Sonderfall der phasenlosen Nahfeldmessungen betrachtet, bei denen keine globale Phaseninformation für die einzelnen Messproben vorliegt. Es werden zwei Ansätze diskutiert, die beide auf spezieller Empfängerhardware basieren, die in der Lage ist, kohärente Teilmengen der Nahfelddaten zu erfassen. Dies geschieht

entweder durch simultane Messungen bei mehreren Frequenzen oder durch den Einsatz einer Anordnung mehrerer Sonden. Im ersten Fall basiert der Phasenrückgewinnungsprozess auf einer nichtlinearen Optimierung, wie bei den meisten klassischen Phasenrekonstruktionsalgorithmen. Der letztere Ansatz führt eine Linearisierung des Problems ein, die die Zuverlässigkeit der Phasenrückgewinnung erheblich verbessert und den Algorithmus mit Phasenrekonstruktion in die Nähe von klassischen Antennenmessungen mit vollständiger Phaseninformation bringt.

Contents

1	Motivation & Background	1
2	Electromagnetic Theory & Boundary Integral Equations	5
2.1	Maxwell's Equations in Time-Harmonic Notation	5
2.2	The Radiation of a Current Distribution	7
2.3	Continuity and Boundary Conditions	9
2.4	The Surface Equivalence Theorem: Huygens' Principle	10
2.4.1	A Prerequisite: The Uniqueness Theorem	11
2.4.2	Huygens' Principle	12
2.5	Boundary Integral Equations	13
2.5.1	Quantities of Interest: Near Field, Far Field, Radiation Pat- terns, and Radar Cross-Section	15
2.5.2	Scattering and Radiation Problems	17
	<i>The Electric Field Integral Equation 18 · The Magnetic Field Integral Equation 19 · The Problem of Interior Resonances 19 · Avoiding Inter- ior Resonances: The Combined Field Integral Equation 22 · Avoiding Interior Resonances: The Combined Source Integral Equation 23 · The Interpretation of Combined-Source Fields 24</i>	
2.5.3	Source Reconstruction for Antenna Measurements and Fur- ther Inverse Problems	26
3	Surface Integral Equations and Their Discretization	31
3.1	Discretization of the Electric Field Integral Equation	31
3.1.1	A Walkthrough for the Method of Moments	31
3.1.2	Choosing a Suitable Set of Basis and Testing Functions	34
	<i>An Intuitive Approach 34 · A Theoretical Approach 35</i>	
3.1.3	Intermission: Basis and Testing Functions on a Triangular Mesh	37
	<i>The Rao-Wilton-Glisson Functions 37 · Hierarchical Higher-Order Vector Functions on a Triangular Mesh 39</i>	
3.1.4	The Classical EFIE Discretization	40
3.2	Discretization of the Magnetic Field Integral Equation	41
3.2.1	Choosing a Suitable Set of Basis and Testing Functions	42

3.2.2	The Discretization of the MFIE, Associated Problems, and Solution Approaches	43
	<i>Div-Conforming Basis and Testing Functions for the MFIE 43 · The Problems of the MFIE and Their Reasons 43 · Solution Approaches to the MFIE Accuracy Issues 44</i>	
3.3	The Combined Field Integral Equation	48
4	Accurate Discretization Strategies for the Operator of the PEC MFIE	49
4.1	A Combined Source Integral Equation with a Weak-Form Relation of Electric and Magnetic Currents	50
4.1.1	Brief Revision of Discretization Approaches	51
4.1.2	Pure Rao-Wilton-Glisson Discretization of the Combined Source Integral Equation	54
4.1.3	Comparison of the CSIE Variants	56
4.1.4	Intermission: On the RWG Gram Matrix Inversion	58
4.2	Accurate Identity Operator Discretization: A Basis Transformation Scheme	61
4.2.1	Discretization Approach	61
4.2.2	Field Synthesis and the Construction of Non-Radiating Currents	64
4.2.3	Numerical Results for Field Synthesis	65
4.3	Improved Magnetic Field Integral Equation with Weak-Form Identity Operator Discretization	69
4.3.1	The Discretization Schemes	69
4.3.2	Comparison of the Weak-Form Discretization Approaches	70
4.4	Numerical Investigations of the Single-Field Low-Order Schemes	73
4.4.1	Convergence to the Correct Solution—Mesh Refinement & Choosing the WF-MFIE Weighting Factor	73
	<i>A Cube 73 · A Sphere 79 · Summary 82</i>	
4.4.2	Low-Frequency Behavior	82
4.4.3	Scattering Results for Electrically Small Objects with Accuracy Issues	85
	<i>A Sharp Wedge 85 · A Pyramid 88</i>	
4.5	Numerical Investigations of the CF/CS Schemes	88
4.5.1	More Scattering and Radiation Results	89
	<i>Stealth Object Flamme 89 · Airbus Airplane 94 · An Electrically Large Sphere 96</i>	
4.5.2	Stability at Interior Resonances	97
	<i>Looking at the First Two Resonance Frequencies of a Sphere 97 · Frequency Sweep for Flamme 101 · An Electrically Larger, Overmoded Sphere 101</i>	

4.5.3	Summary	105
4.6	The Trade-Off between Accuracy and Conditioning	106
4.6.1	Electrically Smaller Sphere	107
4.6.2	Stealth Object Flamme	108
4.6.3	Electrically Larger Sphere	109
4.6.4	Airbus Airplane	110
4.6.5	Summary	111
4.7	Higher-Order Rao-Wilton-Glisson Discretization Schemes	111
4.7.1	Higher-Order Combined-Source Integral Equation	112
4.7.2	Higher-Order Weak-Form Scheme for the Magnetic Field Integral Equation	112
	<i>Revisiting the Low-Order Case</i> 112 · <i>The Higher-Order Case</i> 113	
4.7.3	Analyzing the Weighting Factor for Both Proposed HO WF-MFIEs	114
	<i>A 0.5λ Cube</i> 114 · <i>A 1λ Cube</i> 117 · <i>A 0.5λ Sphere</i> 119 · <i>Tackling Geometrical Singularities</i> 120	
4.7.4	Numerical Investigations of the HO Schemes	124
	<i>Mesh Refinement Analysis</i> 124 · <i>Stability at Interior Resonances</i> 126 · <i>Electrically Larger Scattering Scenario</i> 127 · <i>Summary</i> 129	
5	Surface-Source Reconstruction for Antenna Measurements	131
5.1	Linear Equivalent Source Reconstruction	131
5.1.1	General Discretization Strategy	132
5.1.2	Description of the Forward Operator	133
5.1.3	The Normal Equations	136
5.2	Zero-Field Enforcement	138
5.2.1	Combined Source Approximation	139
5.2.2	Love-Current Retrieval via Post-Processing	139
5.2.3	Love-Current Mapping via Calderón Projection	140
5.2.4	Love-Current or Zero-Field Side Constraint	141
5.2.5	Scaling of the Zero-Field Side Conditions	142
	<i>Side Condition Scaling for the NRE</i> 144	
5.3	Source Reconstruction and FF Transformation Results	149
5.3.1	Results with Synthetic Near Field Data	150
	<i>Transformation Results for the Small Synthetic OEWG</i> 150 · <i>A More Realistic Antenna Model</i> 155 · <i>A Large Reflector Antenna</i> 160	
5.3.2	Results for Measurement Data	162
	<i>Source Reconstruction for a Reflector Antenna</i> 162 · <i>NF Measure- ments of a DRH400 AUT</i> 165 · <i>UAV-Based Diagnostics</i> 168 · <i>Post- Processing Based Love-Current Calculation</i> 172	
5.3.3	Summary	173

CONTENTS

5.4	Echo Suppression	174
5.4.1	Echo Source Localization with a MOM Side Constraint . . <i>Theoretical Description 176 · Transformation Results 178</i>	175
5.4.2	Time-Gating for Equivalent Sources & Mutual Coupling .	186
5.5	Phase Retrieval for Source Reconstruction Problems	190
5.5.1	Multi-Frequency Phase Retrieval and the Problem of Local Minima <i>Observation Model and Phase Reconstruction Algorithm 191 · Trans- formation Results for Measurement Data 192</i>	191
5.5.2	Linear Phase Retrieval for Partially Coherent Observations <i>A Linear Phase Retrieval Algorithm 197 · Numerical Results 199</i>	195
6	Contributions & Conclusion <i>Simulation of PEC Scattering and Radiation Scenarios 205 · Source Reconstruction for Antenna Measurements 206</i>	205
	Glossary	209
	Notation	209
	Physical Quantities and Mathematical Symbols	209
	Abbreviations	212
	Bibliography	217
	Publications of the Author	255

Acknowledgment

First and foremost, I would like to express my sincere gratitude to my thesis advisor, Prof. Dr. Thomas Eibert, for his unwavering support and guidance, and for the freedom he granted me in my work—the broad scope of this work is the best proof of this. His mentorship has been an invaluable source of inspiration throughout my doctoral studies. Moreover, I would like to thank Prof. Dr. Vipiana for serving on my thesis committee and Prof. Dr. Helmut Gräß for chairing the committee.

I am greatly indebted to Dr. Alexander Paulus and Dr. Josef Knapp, for their contributions to insightful discussions and for an overall extremely fruitful and congenial collaboration. It was also always a pleasure to work with Raimund Mauermayer—sometimes on a semi-official side project—, whom I want to thank, among many other things, for his advice on particulars of the solver code. I owe a debt of gratitude to my master thesis advisor Dr. Kun Wang for paving my way to the Chair and providing me with invaluable insights and guidance. During a seminar and my stay at the Chair, I had the privilege of meeting and learning from Prof. Dr. Simon Adrian and Dr. Michael Gruber. Their excellent introduction to scientific writing and presentation techniques has been an indispensable resource, and without their seminar, this thesis would certainly look much less appealing.

Furthermore, I would like to acknowledge the vigorous support with practical tasks provided by Thomas Mittereder, which allowed me to focus on my research without getting bogged down in practical details. I am also grateful to Dr. Uwe Siart for his support in administrative tasks and helpful Latex tips, which have saved me countless hours of frustration in both respects. Finally, I would like to thank all other colleagues and fellow doctoral candidates—Arslan Azhar, Prof. Dr. Matthias Ehrnsperger, Christoph Eisner, Fabian Faul, Dr. Gerhard Hamberger, Bernd Hofmann, Dr. Safiullah Khan, Dr. Christian Koenen, Thomas Mittermaier, Dr. Clemens Moroder, Björn Möhring, Dr. Ole Neitz, Daniel Ostrzyharczik, Philipp Schmidbauer, Mehmet Taygur, and Jonas Weindl—for making the stay at the Chair as enjoyable as it was, for making conferences fun and memorable in various ways, and for enriching my time with numerous sporting and cultural activities.

Munich, spring 2023

Jonas Kornprobst

Motivation & Background

“Well, I mean, *yes* idealism, *yes* the dignity of pure research, *yes* the pursuit of truth in all its forms, but there comes a point I’m afraid where you begin to suspect that if there’s any *real* truth, it’s that the entire multi-dimensional infinity of the Universe is almost certainly being run by a bunch of maniacs. And if it comes to a choice between spending yet another ten million years finding that out, and on the other hand just taking the money and running, then I for one could do with the exercise.”

— Douglas Adams, *The Hitchhiker’s Guide to the Galaxy*

EVERYONE’S EVERYDAY LIFE is decisively influenced by modern ways of mobile communication and the related emerging opportunities [Chowdhury et al. 2020; W. Jiang et al. 2021; De Alwis et al. 2021; Tataria et al. 2021]. Other wireless applications such as navigation [Gozick et al. 2011; Betz 2013; Ayyalaso-mayajula et al. 2020], near-field communications [Fischer 2009; Want 2011] and (remote) sensing (e.g., radar and imaging) [Nikolova 2011; Zink et al. 2014; Bilik et al. 2016; Woodhouse 2017; Modiri et al. 2017; García-Fernández et al. 2018b; Freethy et al. 2018; Zheng et al. 2020; Edemsky et al. 2021] are also gaining in importance in countless daily-life situations and other civil and military settings—among other reasons due to providing convenience, enabling an increasing degree of automation, and enabling innovative technologies. There are at least two sides to these advances, whenever new frequency bands, size constraints, or beamforming and multi-user requirements come into play: the involved signal and data processing [Massa et al. 2015; Kornprobst et al. 2016; Molisch et al. 2017; Kornprobst et al. 2017a; X. Yang et al. 2017; M. Wang et al. 2019] and the physical layer for power/signal transmission via antennas [K. Wang et al. 2016; Hamberger et al. 2016; Kornprobst et al. 2017b; Y. Li et al. 2017; Kornprobst et al. 2018a, 2018b; Nayeri et al. 2018; Mahmood et al. 2020; Singh et al. 2020; Kornprobst et al. 2021b]. There are many other areas in which similar electromagnetic effects play a role, including microwave heating, spectroscopy, electric motors, alternating-current power grids, (high-speed) wired data connections, and optical systems.

The basis of all these applications is found in electromagnetism—one of the four known fundamental interactions—, which describes, among others, electromagnetic radiation. Our understanding of these electromagnetic phenomena is based on Maxwell’s [1865] equations and special relativity [Einstein 1905].

This thesis can be subsumed into the field of computational electromagnetics (CEM), which aims to model the interaction of electromagnetic fields with the environment [Harrington 1968; Peterson et al. 1997; Chew et al. 2001; Jin 2011; Rylander et al. 2012; Sumithra and Thiripurasundari 2017]. Two topics concerning such interactions are covered. The first one is the simulation of radiation and scattering scenarios with the goal of imitating and predicting real-world behavior based upon our understanding of real-world physics and the derived models. The second topic is source reconstruction: The goal is to build and adapt models based on real-world observations in order to match simulations with constructed devices or to obtain insights about electromagnetic properties of unknown objects.

Only very few problems in CEM can be solved with (closed-form) analytical solutions. Hence, numerical simulation models are indispensable. The growth in available computing power has enabled a massive increase in the practical use cases of such methods since the 2nd half of the 20th century. Today's use of analytical methods is mostly limited to the verification of the solutions obtained with numerical methods in canonical scenarios [Shafieipour et al. 2017; Manohar and Rahmat-Samii 2017; Erricolo 2017; Gürel 2017] and to the exploration of asymptotic and approximate methods [Senior and Volakis 1995; Bouche et al. 1997; Adana et al. 2011; Balanis 2012]—but measured and numerical benchmark solutions are equally important [Marchand et al. 2017; Massey and Yilmaz 2017; Massey et al. 2018; Massey 2018].

There are many ways to classify numerical methods in CEM. Aspects for comparison include the accuracy, the speed and computation effort, and the applicability and limitations. Regarding the last point, this thesis is mostly concerned with time-harmonic scenarios, which work with the steady state at a single frequency [Harrington 1961]. Without any claim to be all-encompassing, there are differential equation, integral equation, and asymptotic solvers. Differential equation solvers, such as the finite element method (FEM), work with local variations of the electromagnetic quantities and are well-suited for objects with arbitrary material compositions and geometries. However, they may suffer from accuracy issues for electrically large scenarios due to numerical dispersion [J.-Y. Wu and R. Lee 1997; J.-F. Lee et al. 1997; Deraemaeker et al. 1999; Lou and Jin 2006; Kabir et al. 2013]. Integral equation solvers yield accurate results independent of the problem size but have a harder time accounting for granular changes of material properties since they typically work with the boundary surfaces of volumetric objects. Furthermore, these formulations require fully populated matrices for describing the interactions between all discretization elements. Hence, it is not directly obvious whether the reduction to the surface decreases the computational complexity or the full population of the system matrices causes an increased complexity as compared to differential equation solvers. With the use of fast methods exhibiting quasi-linear complexity—for instance, employing a multi-level fast multipole method

(MLFMM) accelerated matrix-vector product (MVP)—, integral equation methods gain a certain advantage in terms of computational complexity while maintaining a controlled accuracy. The third and final relevant method are asymptotic solvers, which approximate the electromagnetic behavior for electrically large objects. Of course, the accuracy may be compromised but these methods make the simulation of very large scenarios feasible in the first place. Hybridization between the three types of methods enables us to leverage the respective advantages and still simulate the electrically largest scenarios possible [Chew et al. 2001; Ma et al. 2012; B.-Y. Wu and Sheng 2013; Z.-L. Liu et al. 2014; Karagounis et al. 2015].

The scope of this thesis lies on integral equation methods. Given an accelerated MLFMM solver and two application scenarios [simulation of perfect electric conductor (PEC) objects and source reconstruction], we focus on the solver accuracy, the well-posedness of the problem and uniqueness of the solution, and the well-conditioning of the system matrix, which is directly related to the iterative solver convergence speed.

The thesis is structured as follows. Chapter 2 introduces the relevant time-harmonic electromagnetic theory upon which the remainder of the thesis is mostly based—apart from one minor excursus to the time domain. The method of moments (MOM) as a general discretization approach and its application to several integral equations (IEs) for the treatment of PEC objects are discussed in Chapter 3. One of these IEs, the magnetic field integral equation (MFIE), exhibits serious drawbacks in its classical discretization which are tackled from various angles in Chapter 4. The subsequent Chapter 5 examines several aspects of source-reconstruction problems: the impact of choosing the (surface-source) reconstruction model, modeling and suppressing the impact of adverse environmental measurement conditions via echo suppression techniques, and source reconstruction with imperfect information, where the phase information of complex observations is (at least partially) unavailable. Chapter 6 summarizes all contributions presented in this thesis.

Electromagnetic Theory & Boundary Integral Equations

Seen from outside, and even more so from within, the process of scientific research is disorderly and confusing. It is tempting to deduce that scientists themselves are disorderly and confused. In a way, they are – that’s what research involves. If you knew what you were doing it wouldn’t be research.

– Terry Pratchett, *Darwin’s Watch*

MAXWELL’S EQUATIONS are the governing equations of the behavior of electromagnetic fields. Their formulation is too general to tackle the specific problems investigated in this thesis. Hence, it is necessary to derive specific problem formulations as treated in the following chapters. For the specific circumstances of this thesis, the notation of electromagnetic quantities is introduced and the relevant theorems are briefly summarized in Section 2.1. To establish a basis for the subsequent chapters, the radiation problem is solved in Section 2.2. The continuity and boundary conditions introduced in Section 2.3 as well as the surface equivalence theorem presented in Section 2.4 are employed as prerequisites for boundary integral equations, which are discussed for radiation, scattering, and source reconstruction in Section 2.5.

2.1 Maxwell’s Equations in Time-Harmonic Notation

The general task addressed in this thesis is to solve electromagnetic problems in three-dimensional space. The underlying space of such a setting is spanned by the three spatial dimensions (described by the position vector $\mathbf{r} \in \mathbb{R}^3$) and the one dimension of time as described by the variable t . Since all scenarios are restricted to the time-harmonic case, the $e^{j\omega t}$ time-dependence is suppressed and the time-derivatives are simplified to the factor $j\omega$, where $\omega = 2\pi f$ represents the angular frequency. The quantities of interest are the three-dimensional, complex-valued electric field vector $\mathbf{e} \in \mathbb{C}^3$, the electric displacement field \mathbf{d} , the magnetic field \mathbf{h} , the magnetic flux density \mathbf{b} , the electric volume current and charge densities \mathbf{j}_v and $\rho_{e,v}$, and the fictitious magnetic ones \mathbf{m}_v and $\rho_{m,v}$. Typically, all these quantities

are evaluated at a position \mathbf{r} in this thesis.

As the foundation for time-harmonic scenarios, we use the famous Maxwell's [1865] equations in differential form [Harrington 1961; Jin 2011; Balanis 2012]

$$\operatorname{div} \mathbf{d} = \varrho_{e,v}, \quad (2.1)$$

$$\operatorname{div} \mathbf{b} = \varrho_{m,v}, \quad (2.2)$$

$$-\operatorname{curl} \mathbf{e} = j\mathbf{k}\mathbf{h} + \mathbf{m}_v, \quad (2.3)$$

$$\operatorname{curl} \mathbf{h} = j\mathbf{k}\mathbf{e} + \mathbf{j}_v, \quad (2.4)$$

where the del-operator ∇ may be employed to express the divergence as $\nabla \bullet = \operatorname{div}$ and the curl as $\nabla \times = \operatorname{curl}$ as derivatives with respect to \mathbf{r} .

Combining (2.1) and (2.4) and analogously (2.2) and (2.3) gives the charge conservation (or current continuity) conditions

$$\operatorname{div} \mathbf{j}_v = -j\omega\eta\varrho_{e,v}, \quad \operatorname{div} \mathbf{m}_v = -j\omega\varrho_{m,v}. \quad (2.5)$$

Material properties are considered in (2.3) and (2.4) by the wavenumber

$$k = \omega \sqrt{\left(\varepsilon + \frac{\kappa_e}{j\omega}\right)\left(\mu + \frac{\kappa_m}{j\omega}\right)}, \quad (2.6)$$

which contains—considering scalar quantities for linear, homogeneous, and isotropic materials only—the permittivity $\varepsilon = \varepsilon_0\varepsilon_r$, the permeability $\mu = \mu_0\mu_r$, as well as the electrical and magnetic conductivities κ_e and κ_m . The wavenumber simplifies to $k = \omega\sqrt{\varepsilon\mu}$ for non-conductive materials and to $k_0 = \omega\sqrt{\varepsilon_0\mu_0}$ in free space—always indicated by a subscript $(\cdot)_0$. This very wavenumber is employed to determine the wavelength $\lambda = 2\pi/\operatorname{Re}\{k\}$ and the speed of light $c = \lambda f$. In more detail, the material properties are linked to the electromagnetic fields by the constitutive relations

$$\mathbf{d} = \varepsilon\mathbf{e}, \quad \mathbf{b} = c^{-1}\mathbf{h}, \quad (2.7)$$

$$\mathbf{j}_v = \eta\kappa_e\mathbf{e}, \quad \mathbf{m}_v = \kappa_m\eta^{-1}\mathbf{h}, \quad (2.8)$$

the latter two of which are also known as Ohm's [1827] law.¹

As the attentive reader has noticed, scaled versions of the classical magnetic field $\mathbf{h} = \eta^{-1}\mathbf{h}$ and the classical electric current density $\mathbf{j}_v = \eta^{-1}\mathbf{j}_v$ are employed in this thesis. This normalization has been chosen in order to avoid conditioning

1. The magnetic current and charge densities are purely fictitious quantities, not real physical phenomena, as is the magnetic conductivity. The currents and charges are employed for the description of equivalent scenarios and help in handling certain scenarios. The magnetic conductivity κ_m is introduced for symmetry reasons—in a time-harmonic description, both conductivities are redundant with respect to the complex permittivity/permeability anyhow.

issues and to condense the notation. The scaling factor is the wave impedance of the background material

$$\eta = \sqrt{\frac{\kappa_m + j\omega\mu}{\kappa_e + j\omega\varepsilon}}, \quad (2.9)$$

which simplifies to $\eta = \sqrt{\mu/\varepsilon}$ for non-conductive materials and to $\eta_0 = \sqrt{\mu_0/\varepsilon_0}$ for free space.

In the international system of units, commonly known as SI units, the speed of light in vacuum

$$c_0 = 299\,792\,458 \text{ m s}^{-1} \quad (2.10)$$

is a universal constant which is defined without uncertainty in the up-to-date 2018 CODATA recommended values [Tiesinga et al. 2020]. The permittivity, the permeability, and the wave-impedance of vacuum are deemed to be measured quantities, i.e., their numerical values are given as

$$\varepsilon_0 = 8.854\,187\,812\,8 \cdot 10^{-12} \text{ A s V}^{-1} \text{ m}^{-1}, \quad (2.11)$$

$$\mu_0 = 1.256\,637\,062\,12 \cdot 10^{-6} \text{ V s A}^{-1} \text{ m}^{-1}, \quad (2.12)$$

$$\eta_0 = 376.730\,313\,668 \, \Omega, \quad (2.13)$$

all subject to a relative standard uncertainty of $1.5 \cdot 10^{-10}$. If the electric current density and the magnetic field are not normalized as indicated above, this uncertainty affects Maxwell's equations. Theoretical analyses are of course not affected.

2.2 The Radiation of a Current Distribution

Maxwell's equations do not immediately reveal how to solve problems in CEM. A potential next step is to calculate the radiation of a constant-current element with infinitesimal length, i.e., the radiation of a so-called Hertzian or Fitzgerald dipole. In order to analyze the different contributions in the radiated fields, the magnetic vector potential \mathbf{a} [Neumann 1845; Weber 1846; Thomson 1851; A. C. T. Wu and C. N. Yang 2006] and the corresponding electric scalar potential ϕ are employed as auxiliary quantities with the Lorenz gauge $\text{div } \mathbf{a} = -jk\phi$ [Lorenz 1867]. The magnetic field is (by definition) calculated as

$$\mathbf{h} = \text{curl } \mathbf{a} \quad (2.14)$$

and the electric field [by leveraging (2.3) and the Lorenz gauge condition] as

$$\mathbf{e} = -jk\mathbf{a} - \text{grad } \phi = -jk\mathbf{a} - jk^{-1} \text{grad div } \mathbf{a} \quad (2.15)$$

from electric sources in the absence of magnetic ones—hence, we have $\text{div } \mathbf{b} = \mathbf{0}$ in this case. The effect of magnetic sources may be considered separately due to linearity and the related superposition principle. This allows to rewrite Maxwell's equations—in particular (2.4)—as the Helmholtz equation

$$\Delta \mathbf{a} + k^2 \mathbf{a} = -\mathbf{j}_v \quad (2.16)$$

with the Laplace operator $\Delta = \text{div } \mathbf{grad}$. In a homogeneous medium of infinite extent, the scalar Green's function

$$g(\mathbf{r}, \mathbf{r}') = G_{j_v}^{\mathbf{a}}(\mathbf{r}, \mathbf{r}') = \frac{e^{-jk|\mathbf{r}-\mathbf{r}'|}}{4\pi|\mathbf{r}-\mathbf{r}'|} \quad (2.17)$$

is obtained for the radiated fields, which fulfills the Sommerfeld [1912, 1949] radiation condition

$$\lim_{\|\mathbf{r}\| \rightarrow \infty} \|\mathbf{r}\| \left(\frac{\partial}{\partial \|\mathbf{r}\|} + jk \right) g(\mathbf{r}, \mathbf{r}') = 0 \quad (2.18)$$

for outgoing waves with an observation coordinate \mathbf{r} and a source coordinate \mathbf{r}' . The same procedure for the electric vector potential \mathbf{f} of magnetic current densities yields the very same Green's function $g(\mathbf{r}, \mathbf{r}')$ due to duality [Balanis 2012].

From now on, surface current densities \mathbf{j} and \mathbf{m} on a surface s are considered instead of volume current densities. The same is done for surface charge densities ϱ_e and ϱ_m . Thus, the dimensionality of the radiation integrals is reduced by one. With this adjustment, the vector potential is calculated as

$$\mathbf{a}(\mathbf{r}) = \iint_s g(\mathbf{r}, \mathbf{r}') \mathbf{j}(\mathbf{r}') d^2 r' . \quad (2.19)$$

For the magnetic field in (2.14), we find the simplification

$$\mathbf{h}(\mathbf{r}) = \mathbf{curl} \iint_s g(\mathbf{r}, \mathbf{r}') \mathbf{j}(\mathbf{r}') d^2 r' = \iint_s \mathbf{grad} g(\mathbf{r}, \mathbf{r}') \times \mathbf{j}(\mathbf{r}') d^2 r' \quad (2.20)$$

utilizing $\mathbf{curl}(g\mathbf{j}) = \mathbf{grad} g \times \mathbf{j} + g \mathbf{curl} \mathbf{j}$ and utilizing the fact that $\mathbf{j}(\mathbf{r}')$ has no \mathbf{r} -dependence [Bladel 2007]. Then, the electric and magnetic fields of an arbitrary surface current distribution on s —with $\mathbf{r}' \in s$ unless stated otherwise—are calculated as

$$\begin{aligned} \mathbf{e}(\mathbf{r}) = & -jk \iint_s g(\mathbf{r}, \mathbf{r}') \mathbf{j}(\mathbf{r}') d^2 r' - jk^{-1} \mathbf{grad} \text{div} \iint_s g(\mathbf{r}, \mathbf{r}') \mathbf{j}(\mathbf{r}') d^2 r' \\ & - \iint_s \mathbf{grad} g(\mathbf{r}, \mathbf{r}') \times \mathbf{m}(\mathbf{r}') d^2 r' , \end{aligned} \quad (2.21)$$

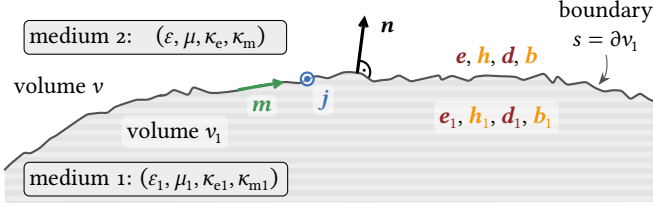


Fig. 2.1: Boundary surface between two media.

$$\begin{aligned}
 \mathbf{h}(\mathbf{r}) = & -jk \iint_s g(\mathbf{r}, \mathbf{r}') \mathbf{m}(\mathbf{r}') d^2r' - jk^{-1} \mathbf{grad} \operatorname{div} \iint_s g(\mathbf{r}, \mathbf{r}') \mathbf{m}(\mathbf{r}') d^2r' \\
 & + \iint_s \mathbf{grad} g(\mathbf{r}, \mathbf{r}') \times \mathbf{j}(\mathbf{r}') d^2r'. \quad (2.22)
 \end{aligned}$$

Even though (2.21) and (2.22) provide the basis for the field calculation from sources in homogeneous media, these equations are not applicable per se for general material distributions. However, Huygen's principle serves as a remedy to create equivalent problems for which homogeneous media of infinite extent may be assumed.

2.3 Continuity and Boundary Conditions

Let us assume a surface s between two volumes with the unit normal \mathbf{n} pointing from a first volume v_1 into a second volume v . The continuity conditions for the electromagnetic fields on s read [Jin 2011]

$$\mathbf{n} \times (\mathbf{e}_1 - \mathbf{e}) = \mathbf{m}, \quad \mathbf{n} \times (\mathbf{h} - \mathbf{h}_1) = \mathbf{j}, \quad (2.23)$$

$$\mathbf{n} \cdot (\mathbf{d} - \mathbf{d}_1) = \varrho_e, \quad \mathbf{n} \cdot (\mathbf{b} - \mathbf{b}_1) = \varrho_m, \quad (2.24)$$

where the surface current densities \mathbf{m} and \mathbf{j} on the interface cause a jump in the electric and magnetic fields, respectively. In Fig. 2.1, this scenario is changed such that s is a boundary between two media. Then, the continuity conditions are still valid as the so-called boundary conditions for the boundary surface s . In this thesis, the focus lies on medium 1 being a perfect conductor with infinite electric conductivity. This changes the boundary conditions on the surface of the PEC object

to

$$\mathbf{n} \times \mathbf{e} = \mathbf{0}, \quad (2.25)$$

$$\mathbf{n} \times \mathbf{h} = \mathbf{j}, \quad (2.26)$$

$$\mathbf{n} \cdot \mathbf{d} = \varrho_e, \quad (2.27)$$

$$\mathbf{n} \cdot \mathbf{b} = 0. \quad (2.28)$$

If medium 1 is not a perfect but a good electrical conductor, the tangential electric field on the interface does not completely vanish. Instead, the tangential electric field is related to the magnetic field via the normalized surface impedance

$$\eta_s = \frac{\eta_1}{\eta} = \frac{1}{\eta} \sqrt{\frac{\kappa_{m1} + j\omega\mu_1}{\kappa_{e1} + j\omega\varepsilon_1}} \approx \frac{1 + j}{\eta} \sqrt{\frac{\omega\mu_1}{2\kappa_{e1}}}. \quad (2.29)$$

This relation is known as the Leontovich impedance boundary condition (IBC) [Leontovich 1948; Senior and Volakis 1995; Balanis 2012]

$$\mathbf{e} \times \mathbf{n} = \eta_s \mathbf{n} \times \mathbf{h} \times \mathbf{n}. \quad (2.30)$$

For thin dielectric coatings with $(\varepsilon_{r,c}, \mu_{r,c})$ and thickness d_c on a PEC medium, the surface impedance

$$\eta_s = j \sqrt{\frac{\mu_{r,c}}{\varepsilon_{r,c}}} \tan(kd_c \sqrt{\mu_{r,c}\varepsilon_{r,c}}) \quad (2.31)$$

may be employed for the IBC in (2.30).

2.4 The Surface Equivalence Theorem: Huygens' Principle

The Huygens' [1690] principle is a method of analysis for wave propagation, where each point on a primary wavefront is assumed to emit secondary spherical waves. In the more mathematical formulation by Love [1901] and Schelkunoff [1936], it provides the basis for boundary integral equations since it allows to introduce equivalent problems with simplified material distributions. These can be solved numerically for arbitrarily shaped objects since their associated Green's functions are well-known.

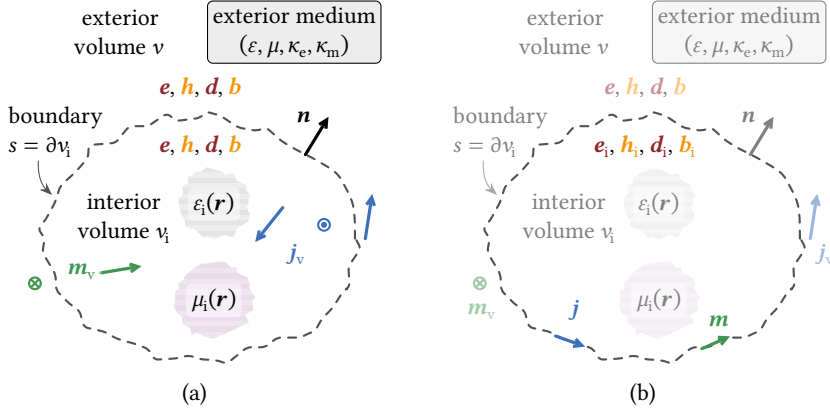


Fig. 2.2: The surface equivalence principle. (a) An arbitrary closed surface s for the demonstration of the uniqueness theorem. (b) An equivalent problem for the exterior fields.

2.4.1 A Prerequisite: The Uniqueness Theorem

Consider a closed surface s enclosing a volume v_i with the outward unit normal \mathbf{n} , see Fig. 2.2(a). Known electromagnetic sources may exist both inside and outside of v_i . The uniqueness theorem provides the insight that the electromagnetic fields inside of v_i are unique if the tangential field components either of $\mathbf{n} \times \mathbf{e}$, of $\mathbf{n} \times \mathbf{h}$, or mutually exclusive parts of both are known on the whole surface s [Rubinowicz 1926; Stratton 1941; Balanis 2012]. While this holds for lossy media in v_i and even if the loss dissipation in v_i approaches zero, this uniqueness theorem breaks down in the lossless case for interior solutions—i.e., the interior fields can be superimposed with so-called interior resonances if only either the electric or the magnetic field components are known.

The uniqueness theorem proves particularly useful whenever exterior solutions (in a volume of infinite extent, i.e., outside of v_i) are of interest. Enforcing outgoing waves at infinite distance—e.g., by imposing the Sommerfeld radiation condition (2.18) for the scalar Green's function or the equivalent condition for vector fields by Müller [1948] and Silver [1949]—is equivalent to imposing a small loss as pointed out by Chew [1995] and the field solution according to (2.21) and (2.22) is unique if the tangential field components either of $\mathbf{n} \times \mathbf{e}$, of $\mathbf{n} \times \mathbf{h}$, or mutually exclusive parts of both are known on the whole surface s —whether the medium is lossy or lossless.

2.4.2 Huygens' Principle

The Huygens principle is an immediate consequence of the uniqueness theorem and the continuity conditions. As discussed, the exterior solution is unique if at least one of the tangential field components $\mathbf{n} \times \mathbf{e}$ or $\mathbf{n} \times \mathbf{h}$ is known everywhere on s for the scenario depicted in Fig. 2.2(a). Figure 2.2(b) depicts an equivalent setup for these unique exterior fields: Equivalent surface current densities

$$\mathbf{m} = (\mathbf{e} - \mathbf{e}_i) \times \mathbf{n}, \quad \forall \mathbf{r} \in s \quad (2.32)$$

$$\mathbf{j} = \mathbf{n} \times (\mathbf{h} - \mathbf{h}_i) \quad \forall \mathbf{r} \in s \quad (2.33)$$

are introduced to replace all interior sources, which leads to the surface equivalence principle or Huygens' principle—in other words, there are infinitely many descriptions of the original scenario in Fig. 2.2(a) depending on the choice of the interior fields \mathbf{e}_i and \mathbf{h}_i . Note that the subscript $(\cdot)_i$ labels the interior fields evaluated on s , and the lack of a subscript denotes the exterior fields evaluated on s in (2.32) and (2.33). While the equivalent electric and magnetic surface current densities are obviously not unique, the uniqueness of exterior fields produced by these currents holds true. The interior fields do not influence the exterior solution at all.

Three special choices of the interior fields are evident, for which not only the exterior fields but also the equivalent currents are unique. Only magnetic currents \mathbf{m} result from choosing $\mathbf{n} \times \mathbf{h} = \mathbf{n} \times \mathbf{h}_i$ and only electric currents \mathbf{j} result from $\mathbf{n} \times \mathbf{e} = \mathbf{n} \times \mathbf{e}_i$. Obviously, these two approaches may suffer from interior resonances if the medium in the volume v_i is lossless. The outstanding third version of the equivalent currents is obtained if the interior fields $\mathbf{e}_i = \mathbf{h}_i = \mathbf{o}$ are deliberately chosen as zero. The resulting equivalent surface current densities

$$\mathbf{m}_L = \mathbf{e} \times \mathbf{n}, \quad (2.34)$$

$$\mathbf{j}_L = \mathbf{n} \times \mathbf{h} \quad (2.35)$$

are known as the Love currents. They are often called *physical* since the equivalent currents are directly related to the unique exterior fields and not superimposed by interior solutions.

Another equivalent current representation worth mentioning is obtained by combining the electric and magnetic currents via [Brakhage and Werner 1965; Bolomey and Tabbara 1973; Mautz and Harrington 1979; Rogers 1985; Morita et al. 1990; Buffa and Hiptmair 2005; Darbas 2006; Steinbach and Windisch 2009; Melenk 2012]

$$\mathbf{m}_{CS} = \mathbf{n} \times \mathbf{j}_{CS}, \quad (2.36)$$

which is typically called a combined source (CS) solution or the Brakhage-Werner

trick.² The interior fields are implicitly defined in this case (as this is obviously required for a unique solution). The CS condition reminds of the IBC (employing equivalent Love currents)

$$\mathbf{m}_L = \mathbf{e} \times \mathbf{n} = \eta_s \mathbf{j}_L \times \mathbf{n} = \eta_s \mathbf{n} \times \mathbf{h} \times \mathbf{n}, \quad (2.37)$$

however, with a change of sign. Also, the equivalent CS currents in (2.36) are no Love currents as opposed to the ones in the IBC. The discussion of the impact of this choice is left for later since part of the context is still missing.

There exist further non-Love equivalent currents which are for instance employed in the single-source surface integral equations [Marx 1982; Glisson 1984; Harrington 1989; Yeung 1999; Menshov and Okhmatovski 2013; Shi and Liang 2015; Patel et al. 2017; Lori et al. 2018]. However, these do not necessarily offer similar benefits as Love-current or CS solutions.

The greatest benefit of the Huygens principle, though, stems from the Love-current representation of the equivalent currents. The zero field inside \mathcal{v}_i allows a deliberate manipulation of the material properties in \mathcal{v}_i without influencing the exterior field solution. In the following, a homogeneous background medium in the exterior volume \mathcal{v} is assumed.³ The material distribution in \mathcal{v}_i may still be arbitrary; however, after introducing equivalent Love currents, the material inside \mathcal{v}_i may be changed to the background material. Then, it is possible to employ the Green's function for a homogeneous medium and the equivalent current representation may even be changed again.

2.5 Boundary Integral Equations

The Huygens' principle can be exploited to calculate equivalent sources from given boundary values for the fields. In a rather general manner, the total electric and magnetic fields

$$\mathbf{e} = \mathbf{e}^{\mathcal{v}} + \mathbf{e}^{\mathcal{s}}, \quad \mathbf{h} = \mathbf{h}^{\mathcal{v}} + \mathbf{h}^{\mathcal{s}} \quad (2.38)$$

are evaluated everywhere in the exterior solution volume \mathcal{v} , i.e., outside of or on the surface \mathcal{s} . The total fields are separated according to two distinct source types: The incident field $\mathbf{e}^{\mathcal{v}}$ originates from sources somewhere in \mathcal{v} and is assumed to be known a priori in most cases—one notable exception are unknown echo sources in antenna

2. The combination of a Hertzian and a Fitzgerald dipole according to (2.36) is known as Huygens radiator and shows a directive radiation characteristic with the main beam in \mathbf{n} -direction and a null in the opposite direction [Schelkunoff and Friis 1952; Luk and B. Wu 2012; Niemi et al. 2012].

3. In this thesis, this is done for the sake of knowing the Green's function according to (2.17). In other cases, for which the Green's function can be evaluated (e.g., layered media or an infinite PEC half space), the equivalence principle also proves to be very useful since homogeneous objects of finite extent may be eliminated.

measurements. The field \mathbf{e}^s is radiated by yet-to-determine equivalent surface sources on s , i.e., this is typically the unknown quantity. This field is expressed by radiation integrals from the equivalent surface sources; hence, (2.38) becomes an IE. After introducing the quantities of interest which are to be calculated with the help of boundary IEs, three cases of how the mentioned fields \mathbf{e}^v and \mathbf{e}^s are composed are discussed in the following.

The constant in these different scenarios is the total field, which is evaluated at the observation coordinate \mathbf{r} on a surface a with unit normal \mathbf{n} . This surface may coincide with s , but it may also be located in v , e.g., (closed) around s in some distance. The former case is referred to as a surface integral equation (SIE), as the boundary integral method (BIM), as the MOM, or as the boundary element method (BEM); while the latter one may pose a source-reconstruction problem. Both can be seen as boundary-IE-based inverse problems since the sources which have generated the observations on a shall be retrieved.

The challenging part is the calculation of the fields \mathbf{e}^s and \mathbf{h}^s from (2.21) and (2.22) on a . When evaluating the fields of sources placed on the Huygens surface s at an observation coordinate \mathbf{r} located on the surface a , we obtain

$$\mathbf{n}(\mathbf{r}) \times \mathbf{e}^s(\mathbf{r}) = \mathcal{T}\{j\}(\mathbf{r}) - \left[\frac{1}{2} \mathcal{I}\{m\}(\mathbf{r}) - \mathcal{K}\{m\}(\mathbf{r}) \right], \quad (2.39)$$

$$\mathbf{n}(\mathbf{r}) \times \mathbf{h}^s(\mathbf{r}) = \mathcal{T}\{m\}(\mathbf{r}) + \left[\frac{1}{2} \mathcal{I}\{j\}(\mathbf{r}) - \mathcal{K}\{j\}(\mathbf{r}) \right] \quad (2.40)$$

employing the dyadic electric field integral operator for electric currents

$$\mathcal{T}\{j\}(\mathbf{r}) := k \mathcal{T}_s\{j\}(\mathbf{r}) + k^{-1} \mathcal{T}_h\{j\}(\mathbf{r}) \quad (2.41)$$

composed of the singular (or vector potential)

$$\mathcal{T}_s\{j\}(\mathbf{r}) := -j \mathbf{n}(\mathbf{r}) \times \iint_s g(\mathbf{r}, \mathbf{r}') j(\mathbf{r}') d^2 r' \quad (2.42)$$

and hypersingular (or scalar potential) operators

$$\mathcal{T}_h\{j\}(\mathbf{r}) := -j \mathbf{n}(\mathbf{r}) \times \left(\mathbf{grad} \operatorname{div} \iint_s g(\mathbf{r}, \mathbf{r}') j(\mathbf{r}') d^2 r' \right) \quad (2.43)$$

as well as the magnetic field operator for electric currents composed of the identity operator

$$\mathcal{I}\{j\}(\mathbf{r}) := j(\mathbf{r}) = \iint_s \delta_s(\mathbf{r}, \mathbf{r}') j(\mathbf{r}') d^2 r' \quad (2.44)$$

with the Dirac surface delta distribution $\delta_s(\mathbf{r}, \mathbf{r}')$ for the surface s and the magnetic

field integral operator

$$\mathcal{K}\{j\}(r) := -n(r) \times \left(\iint_s \text{grad } g(r, r') \times j(r') d^2 r' \right). \quad (2.45)$$

If the surfaces s and a coincide, the \mathcal{K} integral operator has to be evaluated in a Cauchy principal value sense in (2.45) and the \mathcal{I} operator contributes to the evaluated magnetic field. If s and a are apart, only \mathcal{K} is considered.

2.5.1 Quantities of Interest: Near Field, Far Field, Radiation Patterns, and Radar Cross-Section

All considerations so far concerned a valid description of the electromagnetic fields everywhere. This generally applicable description of the fields is in particular employed in the so-called near field (NF) of the currents, whereas approximations may simplify the handling of the involved operators at an electrically large distance. This is the case in many applications, where the distances between the radiating structures and the objects interacting with them are much larger than the wavelength or the objects' dimensions. The so-called far field (FF) approximations are obtained when the fields originate from a region of finite extent and when they are evaluated for the limiting case of infinite distance, i.e., $\|r\| \rightarrow \infty$. Then, the del-operator is replaced by $-jk\mathbf{u}_r$, where \mathbf{u}_r is the unit vector in radial direction, and $\|r - r'\|$ is replaced by $\|r\| - \mathbf{u}_r \cdot r'$ for phase terms and by $\|r\|$ for magnitude terms. In practical scenarios, the limit $\|r\| \rightarrow \infty$ is reached only approximately. A common rule of thumb for antennas large compared to the wavelength is $\|r\| > 2D^2/\lambda$ with D being the diameter of the minimum sphere around all radiating structures [Stutzman and Thiele 2013; Balanis 2016].

For the case of electric sources only and a known magnetic vector potential, we have

$$\mathbf{h}_{\text{FF}} = -jk\mathbf{u}_r \times \mathbf{a}_{\text{FF}}, \quad \mathbf{e}_{\text{FF}} = -jk(\mathbf{a}_{\text{FF}} - \mathbf{u}_r \mathbf{u}_r \cdot \mathbf{a}_{\text{FF}}) = \mathbf{h}_{\text{FF}} \times \mathbf{u}_r \quad (2.46)$$

with the vector potential

$$\mathbf{a}_{\text{FF}}(r) = \frac{e^{-jk\|r\|}}{4\pi\|r\|} \iint_s e^{jk\mathbf{u}_r \cdot r'} j(r') d^2 r', \quad (2.47)$$

which is evaluated according to the radiation integral (2.19) but considering the FF approximation for the scalar Green's functions (2.17). For magnetic currents and the associated vector potential \mathbf{f}_{FF} , we find by duality

$$\mathbf{e}_{\text{FF}} = jk\mathbf{u}_r \times \mathbf{f}_{\text{FF}}, \quad \mathbf{h}_{\text{FF}} = -jk(\mathbf{f}_{\text{FF}} - \mathbf{u}_r \mathbf{u}_r \cdot \mathbf{f}_{\text{FF}}) = \mathbf{u}_r \times \mathbf{e}_{\text{FF}}. \quad (2.48)$$

As seen in (2.47), the fields decay in every direction with $1/\|\mathbf{r}\|$ in a homogeneous medium of infinite extent. For inherently radiating objects, i.e., antennas, interesting properties are the angle-dependent radiation pattern

$$C(\vartheta, \varphi) = \frac{\|\mathbf{e}_{\text{FF}}(\mathbf{r})\|}{\max_{(\vartheta, \varphi)} \|\mathbf{e}_{\text{FF}}(\mathbf{r})\|} \quad \text{for } \|\mathbf{r}\| = \text{const. and } \|\mathbf{r}\| \rightarrow \infty \quad (2.49)$$

and the directivity

$$D(\vartheta, \varphi) = \frac{4\pi C(\vartheta, \varphi)}{\iint C(\vartheta, \varphi)^2 \sin \vartheta d\vartheta d\varphi}, \quad (2.50)$$

which measures the power density radiated in a certain direction (ϑ, φ) as compared to the power density of an ideal isotropic radiator radiating the same total power. Here, the angles ϑ and φ denote the polar and azimuthal angles of the spherical coordinates, i.e., they are part of the position vector \mathbf{r} . The gain

$$G(\vartheta, \varphi) = \zeta D(\vartheta, \varphi) \quad (2.51)$$

is related to the directivity via the efficiency ζ . If dielectric, magnetic, and ohmic loss are considered, we speak of the radiation efficiency, which equals “the ratio of the total power radiated by an antenna to the net power accepted by the antenna” [IEEE Antennas and Propagation Society 2014], and of the (absolute) gain. If mismatch loss is considered in addition, we speak of the total radiation efficiency (the ratio of radiated power and available power) and of the realized gain.

For scattering scenarios, the scattered field of an object is often expressed by means of the bi-static radar cross-section (RCS)

$$\sigma(\vartheta, \varphi) = \lim_{\|\mathbf{r}\| \rightarrow \infty} 4\pi \|\mathbf{r}\|^2 \frac{\|\mathbf{s}^s(\mathbf{r})\|}{\|\mathbf{s}^v(\mathbf{r})\|} = 4\pi \|\mathbf{r}\|^2 \frac{\|\mathbf{s}_{\text{FF}}^s(\mathbf{r})\|}{\|\mathbf{s}_{\text{FF}}^v(\mathbf{r})\|} = 4\pi \|\mathbf{r}\|^2 \frac{\|\mathbf{e}_{\text{FF}}^s(\mathbf{r})\|^2}{\|\mathbf{e}_{\text{FF}}^v(\mathbf{r})\|^2}, \quad (2.52)$$

where the energy flux is represented via the Poynting vector

$$\mathbf{s} = \frac{1}{2\eta} \mathbf{e} \times \mathbf{h}^* \underset{\|\mathbf{r}\| \rightarrow \infty}{\approx} \frac{1}{2\eta} \mathbf{u}_r \|\mathbf{e}_{\text{FF}}\|^2 \quad (2.53)$$

with the complex conjugate $(\cdot)^*$. If the scattered field is evaluated only in a single direction opposite to the incident plane wave incidence \mathbf{k} , we speak of the monostatic RCS. In order to relate the RCS to the electrical size of the scatterer, we employ the normalized RCS

$$\sigma(\vartheta, \varphi) / \lambda^2 = 4\pi \frac{\|\mathbf{r}\|^2}{\lambda^2} \frac{\|\mathbf{e}_{\text{FF}}^s(\mathbf{r})\|^2}{\|\mathbf{e}_{\text{FF}}^v(\mathbf{r})\|^2}. \quad (2.54)$$

The electric field may also be analyzed by its polarization components. A typical

choice in the FF are the components tangential to the radiation direction \mathbf{u}_r : $[\mathbf{e}_{\text{FF}}]_\vartheta$ and $[\mathbf{e}_{\text{FF}}]_\varphi$. The component-wise RCS is defined accordingly as

$$\sigma_\vartheta(\vartheta, \varphi) = 4\pi\|\mathbf{r}\|^2 \frac{\|[\mathbf{e}_{\text{FF}}^s(\mathbf{r})]_\vartheta\|^2}{\|\mathbf{e}_{\text{FF}}^v(\mathbf{r})\|^2}. \quad (2.55)$$

2.5.2 Scattering and Radiation Problems

The difference between radiation and scattering problems lies in the origin of the exterior field \mathbf{e}^v . For radiation problems, the excitation is closely placed in the NF—for instance, a delta gap in the mesh or the excitation of a waveguide mode. We call \mathbf{e}^v or \mathbf{h}^v the excitation and $\mathbf{e} = \mathbf{e}^v + \mathbf{e}^s$ and $\mathbf{h} = \mathbf{h}^v + \mathbf{h}^s$ the radiated fields. With an impinging wave originating from some distance—possibly even infinitely far away—, we speak of a scattering problem. Then, \mathbf{e}^v is referred to as the incident field and \mathbf{e}^s as the scattered field. Both scenarios are treated in the same mathematical way.

The investigations in this thesis are restricted to PEC objects. For scatterers with material distributions, IEs for homogeneous dielectric objects such as the Müller or the Poggio-Miller-Chang-Harrington-Wu-Tsai boundary IEs may be employed [Müller 1969; Poggio and E. K. Miller 1973; T.-K. Wu and Tsai 1977; Y. Chang and Harrington 1977; Mautz and Harrington 1977; Harrington 1989]. Alternatively, hybrid formulations such as the finite-element boundary-integral (FE-BI) method can be used [Marin 1982; Jin and Liepa 1988; Gong and Glisson 1990; Jin et al. 1991; Gedney et al. 1992; Eibert et al. 1999]. For electrically large scenarios, a hybridization of SIEs with asymptotical methods such as the (uniform) geometrical theory of diffraction or physical optics is feasible [Helmers et al. 1999; P. Persson and Josefsson 2001; Alaydrus et al. 2002; Chew et al. 2002; Tzoulis and Eibert 2005]. The particular implementation challenges of SIEs as they are presented in the following are discussed in more detail in Chapter 3.

Figure 2.3(a) shows an electromagnetic wave $(\mathbf{e}^v, \mathbf{h}^v)$, for instance a plane wave

$$\mathbf{e}^v(\mathbf{r}) = e_0 \mathbf{p} e^{-j\mathbf{k}\cdot\mathbf{r}}, \quad \mathbf{h}^v(\mathbf{r}) = \frac{\mathbf{k}}{k} \times \mathbf{e}^v(\mathbf{r}) \quad (2.56)$$

with amplitude e_0 , polarization according to the complex unit vector \mathbf{p} , for instance $\mathbf{p} = \mathbf{u}_x$ for x -polarization, and wave vector \mathbf{k} with $\|\mathbf{k}\| = k$, for instance $\mathbf{k} = k\mathbf{u}_z$ for propagation in $+z$ -direction, impinging on a PEC scattering object. The incident field \mathbf{e}^v causes a scattered field \mathbf{e}^s due to the presence of the scatterer and its boundary condition $\mathbf{n} \times \mathbf{e} = \mathbf{o}$.

The scenario after introducing equivalent Love currents is shown in Fig. 2.3(b). Due to the boundary conditions (2.25) and (2.26), only the electric Love currents are nonzero. Intriguingly, the Love currents match the real physical currents for

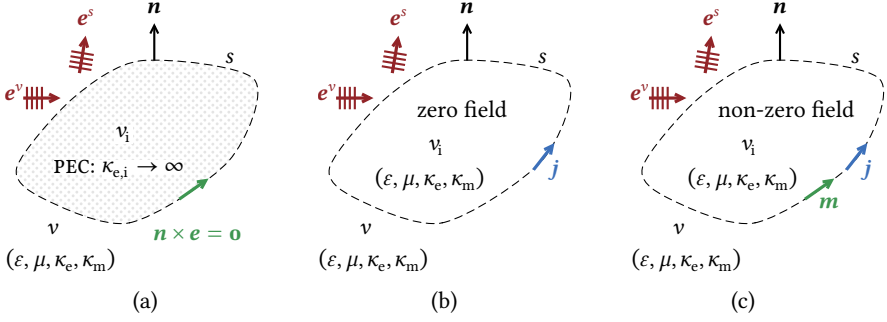


Fig. 2.3: The surface equivalence principle applied for the derivation of boundary IEs for a PEC scattering scenario. (a) A PEC scatterer. (b) Equivalent Love-current problem for the exterior fields. (c) Equivalent non-Love-current problem for the exterior fields.

PEC objects—this does not hold true in general. In this step, the scatterer in v_i was already replaced by the background material, which is possible due to the zero field caused by the equivalent Love currents. This offers the advantage of employing the Green's function of the homogeneous background medium.

Figure 2.3(c) shows a facultative second application of the Huygens principle. After altering the medium inside v_i , the equivalent currents may be chosen as non-Love ones which results in a non-zero interior field. This is exploited in the following for constructing different IEs.

Stratton and Chu [1939] have proposed the first SIEs for electromagnetic diffraction problems. Those IEs work with the tangential and normal field components on s . In this thesis, we employ a formulation which works with the tangential field components only, which was proposed by Maue [1949].

The Electric Field Integral Equation

For the case of PEC objects, the total electric field

$$\mathbf{n} \times \mathbf{e}^v + \mathbf{n} \times \mathbf{e}^s = \mathbf{0} \quad (2.57)$$

is known to vanish on s from (2.25), which leads to the electric field integral equation (EFIE) if the radiation operators of the equivalent currents are employed to express \mathbf{e}^s . We obtain the classical EFIE with Love currents [Maue 1949]

$$\mathbf{e}^v \times \mathbf{n} = \mathcal{T} \mathbf{j}_L \quad (2.58)$$

or a version with generic electric and magnetic currents

$$\mathbf{e}^v \times \mathbf{n} = \mathcal{T}\mathbf{j} - \left[\frac{1}{2}\mathbf{I} - \mathcal{K} \right] \mathbf{m}. \quad (2.59)$$

The Magnetic Field Integral Equation

For PEC boundary conditions, the statement about the magnetic field

$$\mathbf{n} \times \mathbf{h}^v + \mathbf{n} \times \mathbf{h}^s = \mathbf{j}_L \quad (2.60)$$

can only be made if the appearing currents are Love currents since only they pose restrictions on the magnetic field. Furthermore, it is apparent that the MFIE does not work for open objects, viz., objects with zero volume but with a non-zero surface area—if we imagine that the volume v_i becomes infinitesimally thin until both sides of the surface s touch, the superposition of the two boundary conditions $\mathbf{j} = \mathbf{n} \times \mathbf{h}$ from both sides of the surface merge and vanish. The EFIE does not suffer from this restriction. Again, the scattered field \mathbf{h}^s is expressed by a radiation operator, which yields the MFIE [Fock 1946; Maue 1949]

$$\mathbf{h}^v \times \mathbf{n} = \left[\frac{1}{2}\mathbf{I} + \mathcal{K} \right] \mathbf{j}_L. \quad (2.61)$$

The Problem of Interior Resonances

If the background medium is lossless, the interior resonance problem is evidently not avoided for the EFIE and the MFIE with a Love-current solution. Hence, the interior solution is not unique at distinct frequencies; for the MFIE, even the exterior fields do not exhibit a unique solution. The fact that interior resonances—eigen-solutions to an interior problem—may occur for the discussed integral equations has been stated already as early as in 1949 [Maue 1949; Waterman 1965]. Later, this was observed to cause numerical artefacts [Mei and Bladel 1963; Andreasen and Mei 1964; Andreasen 1964] which even lead to a surface-current measurement for a “PEC” scattering setup [Mei and Moberg 1965]; the theoretical explanations for these observed phenomena were pointed out afterwards [Klein and Mittra 1975; Yaghjian 1981; Peterson and Mittra 1987; Peterson 1990]. During these early observations, it became already clear that increasing the computational accuracy helps to circumvent the interior resonance problem to some extent [Andreasen and Mei 1964; Andreasen 1964; Eibert and V. Hansen 1996].

For the EFIE, we imagine a PEC cavity (complementary to the originally considered PEC object). Such an equivalent scenario is depicted in Fig. 2.4(a). There exist non-trivial homogeneous solutions \mathbf{j}_{IR}^{PEC} for the tangential electric field in (2.57),

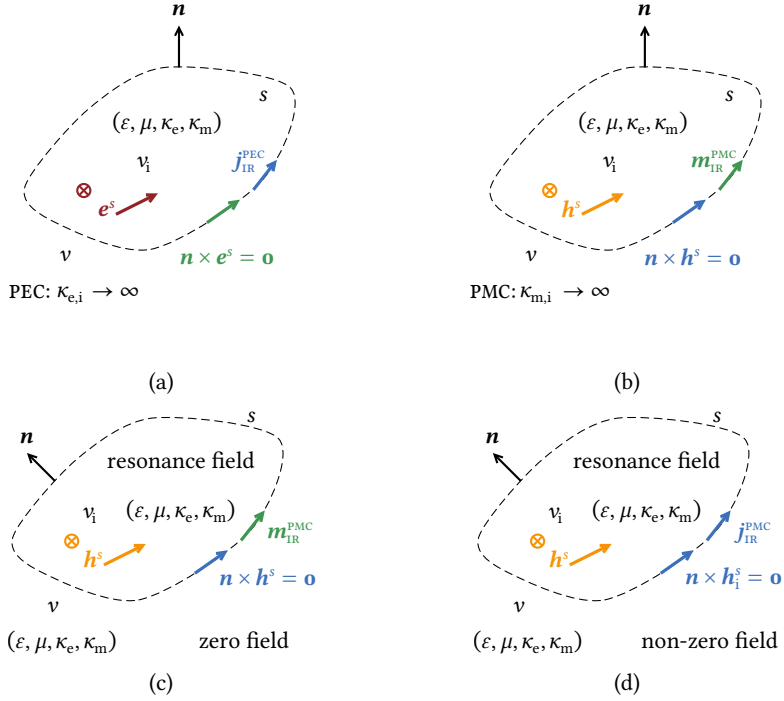


Fig. 2.4: The interior resonance problem of surface IEs. (a) A PEC cavity filled with the background material of the original problem. (b) Likewise, a PMC cavity. (c) The equivalent Love-current scenario for (b). (d) A possible equivalent non-Love-current scenario for (b).

viz. non-trivial solutions to

$$\mathcal{T} \mathbf{j}_{\text{IR}}^{\text{PEC}} = \mathbf{n} \times \mathbf{e}^s = \mathbf{0} \quad (2.62)$$

at discrete interior resonance frequencies according to the cavity modes. The tangential magnetic field on the cavity walls corresponds to the current $\mathbf{j}_{\text{IR}}^{\text{PEC}}$.

A similar effect is observed for the MFIE. However, the origin of the interior resonances for the PEC MFIE is slightly less obvious, since the related perfect magnetic conductor (PMC) cavity as shown in Fig. 2.4(b) supports only magnetic surface current densities $\mathbf{m}_{\text{IR}}^{\text{PMC}}$ on its boundary s (tangential electric fields of the

cavity mode).⁴ The transition to electric currents is achieved via the Huygens' principle.

First, we introduce a problem equivalent to the PMC cavity with magnetic Love currents placed in a homogeneous material of infinite extent in Fig. 2.4(c). Thereafter, we arbitrarily choose specific alternative equivalent currents in Fig. 2.4(d) according to the Huygens principle described by (2.32) and (2.33) such that we find vanishing equivalent magnetic surface current densities

$$\mathbf{o} = (\mathbf{e}^s - \mathbf{e}_i^s) \times \mathbf{n} = \mathbf{e}^s \times \mathbf{n} + \mathbf{m}_{\text{IR}}^{\text{PMC}}, \quad (2.63)$$

and non-zero equivalent electric surface current densities

$$\mathbf{j}_{\text{IR}}^{\text{PMC}} = \mathbf{n} \times (\mathbf{h}^s - \mathbf{h}_i^s) = \mathbf{n} \times \mathbf{h}^s. \quad (2.64)$$

Note that $\mathbf{n} \times \mathbf{h}_i^s = \mathbf{o}$ on s . The exterior fields \mathbf{h}^s and \mathbf{e}^s on s are not directly defined but depend on each other. In the case at hand, we express \mathbf{e}^s in terms of the newly found equivalent electric currents in (2.63) and solve the (PEC scattering) equation⁵

$$\mathcal{T} \mathbf{j}_{\text{IR}}^{\text{PMC}} = \mathbf{m}_{\text{IR}}^{\text{PMC}}. \quad (2.65)$$

This procedure of applying the Huygens principle as in the previous steps has already been passed through earlier in this section, cf. the steps taken in Fig. 2.3. The resulting equivalent electric currents $\mathbf{j}_{\text{IR}}^{\text{PMC}}$ constitute non-Love-current versions of the interior-resonance PMC cavity eigensolutions—i.e., non-trivial solutions to

$$\left[\frac{1}{2} \mathbf{I} + \mathcal{K} \right] \mathbf{j}_{\text{IR}}^{\text{PMC}} = \mathbf{n} \times \mathbf{h}^s = \mathbf{o}. \quad (2.66)$$

Obviously, these equivalent currents $\mathbf{j}_{\text{IR}}^{\text{PMC}}$ contain a radiating component, since a non-Love current representation of an interior solution does exhibit non-zero exterior fields.

The discussed homogeneous solutions to the EFIE and MFIE are parasitic to the original problem and occur in theory at discrete resonance frequencies only. Due to limitations of the discretization, the influence is present at some bandwidth around the discrete frequencies dependent mostly on the computational accuracy. For the EFIE, two numerical issues arise as a consequence. Numerical cancellation errors deteriorate the solution accuracy and the non-trivial null space of the

4. Chew and Song [2007] and Chew et al. [2008] have demonstrated (with an elaborate gedanken experiment) that the “interior resonance” scattering currents $\mathbf{j}_{\text{IR}}^{\text{PMC}}$ constitute an *exterior* PEC scattering solution with a suitably constructed excitation. However, such a solution still emanates from the PMC cavity, whose magnetic currents $\mathbf{m}_{\text{IR}}^{\text{PMC}}$ are the excitation of the mentioned PEC scattering problem. The very same scattering problem has to be solved in the context of our discussion.

5. This equation even reveals the relation of the interior-resonance currents of the EFIE and the MFIE since $\mathbf{m}_{\text{IR}}^{\text{PMC}} \propto \mathbf{j}_{\text{IR}}^{\text{PEC}}$ by duality.

system of equation worsens the conditioning dramatically, resulting in increased solution times for iterative solvers. These two issues appear more emphasized for electrically large scenarios, where the parasitic interior problem becomes strongly overmoded. The MFIE is affected much more than the EFIE. Unfortunately, the exterior fields of the parasitic MFIE solution deteriorate the accuracy much more than the purely interior parasitic EFIE solution. This happens even without any numerical cancellation effects. An increased condition number due to numerical effects is also observed for the MFIE.

Several approaches to tackle the interior resonance problem have been reported, for instance by numerically extracting the vector in the operator nullspace related to the parasitic interior resonance solution, by adding a small loss term to the wavenumber, or by enforcing zero interior fields [Medgyesi-Mitschang and D.-S. Wang 1985; Murphy et al. 1990; Canning 1991; Correia 1993; Martin and Ola 1993; Canning 1995; Leviatan and Baharav 1995; Mohsen et al. 1995; Caorsi et al. 1996; Tsalamengas 2016]. The combined field integral equation (CFIE) is nowadays the prevalent approach to fix the interior resonance problem for PEC scattering scenarios. The combined source integral equation (CSIE) is closely related but has received much less attention. Both are introduced in the following.

Avoiding Interior Resonances: The Combined Field Integral Equation

Fortunately, the non-trivial solutions to the PEC and PMC cavities differ from each other—one being purely interior with $\mathbf{n} \times \mathbf{e}^s = \mathbf{o}$ and the other one being combined interior & exterior with $\mathbf{n} \times \mathbf{h}_1^s = \mathbf{o}$. A combination of the EFIE and MFIE operators—a combined field (CF) solution—is able to eliminate the problem of the non-trivial nullspace caused by interior resonances. The prevalent way to do so is the CFIE [Oshiro et al. 1970; Poggio and E. K. Miller 1973; Mautz and Harrington 1978]

$$[\chi_{\text{CF}} \mathbf{n} \times \mathbf{e}^v + (1 - \chi_{\text{CF}}) \mathbf{h}^v] \times \mathbf{n} = \left[\chi_{\text{CF}} \mathbf{n} \times \mathcal{T} + (1 - \chi_{\text{CF}}) \left(\frac{1}{2} \mathbf{I} + \mathcal{K} \right) \right] \mathbf{j}_L \quad (2.67)$$

with a weighting $0 \leq \chi_{\text{CF}} \leq 1$. We attain a pure MFIE for $\chi_{\text{CF}} = 0$ and a pure EFIE for $\chi_{\text{CF}} = 1$.

In the CFIE, either the magnetic or the electric field receives an additional 90° -rotation. This helps to enforce a unique solution [Mautz and Harrington 1978]. As a starting point, we assume that there exists a non-trivial homogeneous solution $\mathbf{j}_{\text{hom}}^{\text{CFIE}}$ to the CFIE. In this homogeneous equation

$$\left[\chi_{\text{CF}} \mathbf{n} \times \mathcal{T} + (1 - \chi_{\text{CF}}) \left(\frac{1}{2} \mathbf{I} + \mathcal{K} \right) \right] \mathbf{j}_{\text{hom}}^{\text{CFIE}} = \chi_{\text{CF}} \mathbf{n} \times \mathbf{n} \times \mathbf{e}^s + (1 - \chi_{\text{CF}}) \mathbf{n} \times \mathbf{h}^s = \mathbf{o}, \quad (2.68)$$

the scattered fields can be rearranged as the IBC

$$\chi_{\text{CF}} \mathbf{n} \times \mathbf{e}^s \times \mathbf{n} = (1 - \chi_{\text{CF}}) \mathbf{n} \times \mathbf{h}^s. \quad (2.69)$$

If this IBC can be fulfilled by scattered fields or by any fields produced by equivalent electric surface currents on s , a non-trivial homogeneous solution to the CFIE exists—and hence a non-trivial nullspace in the CFIE operator. In order to show that this is indeed impossible, we take a look at the Poynting vector [according to (2.53)]

$$\mathbf{s} = \frac{1}{2\eta} (\mathbf{n} \times \mathbf{e}^s \times \mathbf{n}) \times \mathbf{h}^{s*} = \frac{1 - \chi_{\text{CF}}}{2\eta\chi_{\text{CF}}} (\mathbf{n} \times \mathbf{h}^s) \times \mathbf{h}^{s*} = -\frac{1 - \chi_{\text{CF}}}{2\eta\chi_{\text{CF}}} \mathbf{n} \|\mathbf{h}^s\|_2^2 \quad (2.70)$$

for tangential surface fields on s (which are evaluated by the use of $\mathbf{n} \times \mathbf{e}^s \times \mathbf{n}$ instead of \mathbf{e}^s). Apparently, the power flow has to be real and inwards oriented on every point on the surface for the considered IBC.

However, this is not possible for fields originating from surface sources on s , since such sources exhibit an outwards power flow through s

$$\text{Re} \left\{ \iint_s \mathbf{s} \cdot \mathbf{n} \, d^2r \right\} \geq 0 \quad (2.71)$$

greater equal zero. This contradicts (2.70) and we deduce that $\mathbf{j}_{\text{hom}}^{\text{CFIE}} = \mathbf{0}$.

From these considerations, it becomes clear that the CFIE is equivalent to enforcing a lossy impedance boundary for the homogeneous solution. Since our basic assumption was a lossless background medium—only then, the interior resonance problem occurs at all—, resonances can only be found at complex frequencies [Jin 2011].

Avoiding Interior Resonances: The Combined Source Integral Equation

Instead of combining the electric and magnetic fields, a similar effect can be achieved by employing the generic EFIE (2.59) and imposing the CS condition (2.36), which is a uniqueness constraint formulated for the sources instead of the fields,

$$\mathbf{m}_{\text{CS}} = \frac{1 - \chi_{\text{CS}}}{\chi_{\text{CS}}} \mathbf{n} \times \mathbf{j}_{\text{CS}} \quad (2.72)$$

with the weighting $0 \leq \chi_{\text{CS}} \leq 1$. This leads to the CSIE [Brakhage and Werner 1965; Bolomey and Tabbara 1973; Mautz and Harrington 1979; Rogers 1985; Morita et al. 1990]

$$\mathbf{e}^v \times \mathbf{n} = \mathcal{T} \mathbf{j}_{\text{CS}} + \frac{\chi_{\text{CS}} - 1}{\chi_{\text{CS}}} \left[\frac{1}{2} \mathbf{I} - \mathcal{K} \right] \mathbf{n} \times \mathbf{j}_{\text{CS}}. \quad (2.73)$$

As for the CFIE, the weighting factor χ_{CS} is designed in a way that with 1, we have a pure \mathcal{T} operator, with 0 a pure MFIE operator, and with 0.5 an equal weighting of both. With the same choice for $\chi_{CS} = \chi_{CF}$, the CSIE is the adjoint formulation of the CFIE [Mautz and Harrington 1979; Harrington 1989]. With a similar reasoning as presented above for the CFIE, Mautz and Harrington [1979] have shown that a non-trivial homogeneous solution to the CSIE would exhibit a Poynting vector pointing inwards everywhere on s , which is a contradiction to the behavior of surface currents on s in a lossless medium. In particular, the equivalent CS currents enforce a wave propagation into the direction of \mathbf{n} , i.e., into the solution domain, and the propagation of scattered fields through the scatterer is suppressed to some extent.

The Interpretation of Combined-Source Fields

The CS currents are obviously different from Love currents, which are the prevalent choice for solving PEC scattering IEs. At most frequencies, it is sufficient to look at the EFIE or MFIE solutions in order to see the differences of Love and CS currents. Only at interior resonance frequencies, the particular property of an interior zero field, which is related to a Love current solution, is enforced just by the CFIE and not the EFIE or MFIE alone. The influence of interior resonances is eliminated since the outward-oriented Poynting vector of sources on the surface s enforces that there is no non-trivial homogeneous solution to the CSIE and the CFIE (the latter with Love currents). As mentioned above, the decisive property of Love currents (zero interior fields) can be conveniently examined at frequencies where no interior resonances are observed. The same holds for the radiation properties of CS currents.

Here, we look at plane-wave scattering (incidence direction $\mathbf{k} = k\mathbf{u}_z$ and polarization $\mathbf{p} = \mathbf{u}_x$) at a PEC sphere with a diameter of 1 m.⁶ The simulation frequency is 200 MHz, meaning that the sphere is simulated below the first interior resonance. Figure 2.5 depicts the total and scattered electric NFs produced by the Love current and CS solutions. The exterior fields—both total and scattered—in both cases are visually indistinguishable and even theoretically identical. For the Love current solution, we observe a zero total field as well as $\|\mathbf{e}^s\| = e_0$ inside the scatterer, just as expected. The CS solution shows a quite strong total field inside the scatterer with field values fluctuating around e_0 , i.e., similar to the field of the incident wave. Looking at solely the scattered field \mathbf{e}^s reveals why. The combination of approximately orthogonal electric and magnetic currents—known as the so-called Huygens radiator for just two dipole current elements—exhibits an outward-oriented radiation characteristic with suppressed radiation into the interior region. Hence, the

6. The sphere is discretized with 999 Rao-Wilton-Glisson (RWG) unknowns. The details on how the currents are calculated are discussed in Chapter 3 for the EFIE and in Chapter 4 for the CSIE.

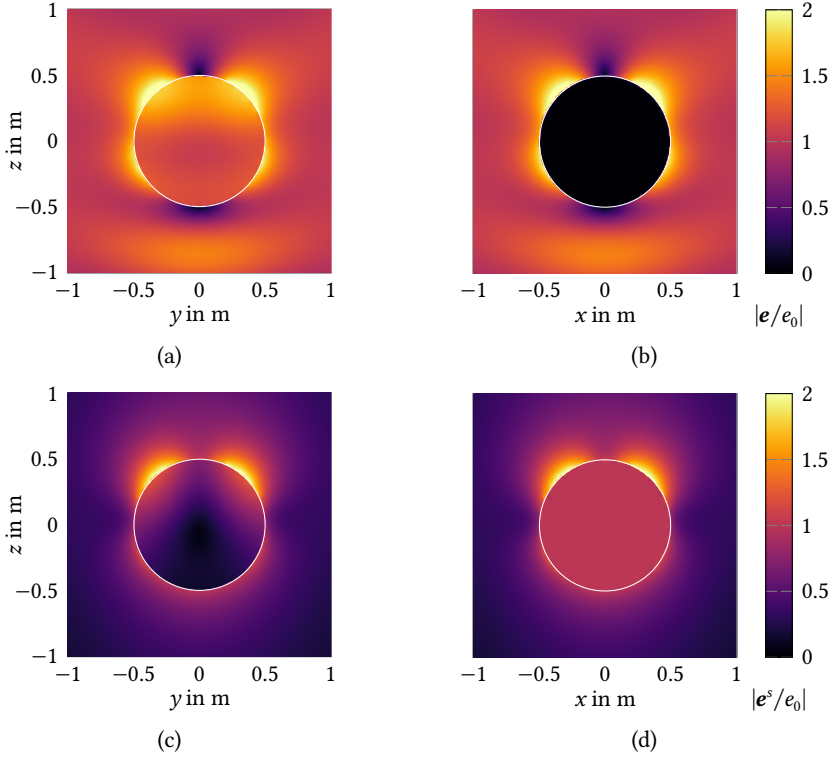


Fig. 2.5: The impact of choosing Love or CS currents on the magnitude of the electric NF. (a) Total electric field \mathbf{e} of the CSIE solution. (b) Total field \mathbf{e} of the EFIE/Love current solution. (c) Scattered field \mathbf{e}^s of the CSIE solution. (d) Scattered field \mathbf{e}^s of the EFIE solution.

scattered field (lacking the incident field component \mathbf{e}^v) shows a close to vanishing field inside the scatterer. As this concerns the interior fields only, there are of course no relevant effects on the exterior solution.

Whenever there is no field from exterior sources to consider—for instance for most source reconstruction problems—the CS and Love current solutions are fairly similar. Whenever there is a non-vanishing field \mathbf{e}^v , Love-current solutions suppress the total field \mathbf{e} inside v_1 while CS solutions suppress some of the scattered field \mathbf{e}^s inside v_1 .

2.5.3 Source Reconstruction for Antenna Measurements and Further Inverse Problems

Source reconstruction is based on a different underlying assumption than radiation or scattering problems: The boundary values are determined by observation samples collected with a field probe, not by physical boundary conditions of the material of an object under consideration. The field samples of \mathbf{e}^s or \mathbf{h}^s are taken on the observation surface a in the NF or FF, which is enclosing the Huygens surface s —which, in turn, encloses the object under test—at some reasonable distance.

Typically, all radiation originates from within v_1 . This may be achieved in practice by going into a controlled environment such as an anechoic chamber [Parini et al. 2020].⁷ In order to reduce the required size of such chambers—and, on a related note, their cost—, antenna measurements are often conducted in the NF, even though most of the time only the antenna under test (AUT) FF properties are of interest in order to characterize an AUT or to make sure that an AUT meets its specifications. So-called near-field far-field transformation (NFFFT) algorithms are then required to calculate the properties of interest in a post-processing step [Tice and Richmond 1955; Ludwig 1971; Johnson et al. 1973; Yaghjian 1986]. These algorithms may even provide additional benefits. Source reconstruction algorithms with a suitable reconstruction basis filter and average random errors. Since such a reconstruction basis only provides a limited number of degrees of freedom (DOFs) for the radiated fields, some parts of systematic errors can also be taken care of. With more measurement samples than required by the Nyquist sampling limit, more robustness against measurement noise and other errors is attained for NFFFT algorithms.

Equivalent surface-current models are one of the reconstruction bases which give the possibility to incorporate geometrical information about the AUT into the NFFFT. By this, they may provide diagnostic and spatial filtering capabilities [Petre and Sarkar 1992; Sarkar and Taaghoul 1999; Alvarez et al. 2007; Araque Quijano and Vecchi 2010a; Jørgensen et al. 2010; Foged et al. 2014; Parini et al. 2020; Eibert et al. 2016; Kornprobst et al. 2019b; Kornprobst et al. 2021a]. Such an equivalent current model for an NF antenna measurement setup is schematically illustrated in Fig. 2.6, with the equivalent surface currents placed on the Huygens surface s . The first step—introducing an equivalent scenario just as in Fig. 2.3(b) and eliminating any (unknown) AUT material—has already been carried out. Hence, the equivalent surface sources on the Huygens’ surface s radiate in free space—or any other surrounding medium with an evaluable radiation operator. The surface s fully and tightly encloses the AUT (whose material composition and exact geometric location

7. One notable exception occurs if there are non-ideal environmental influences beyond the control of the measurement engineer. Then, echo suppression and source localization techniques are a must to ensure high-quality measurement results.

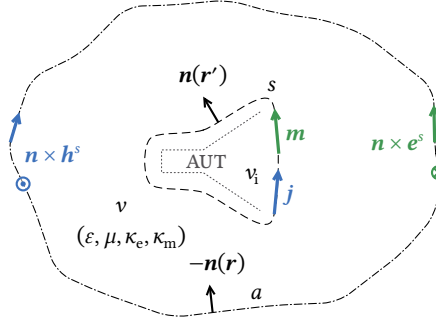


Fig. 2.6: An equivalent scenario for an antenna measurement setup. The AUT is replaced by the background material and enclosed by the Huggens surface s . Observations are taken from the tangential fields on a at some distance to the AUT.

may remain unknown). Ideally, the observation surface a shall be placed around v_i , spatially separated at some distance, and closed. If a is not closed, the valid angular range of the reconstruction is limited and truncation errors may reduce the reconstruction accuracy, in particular at the borders of a . Furthermore, the field sampling has to be sufficiently dense to capture all DOFs in the fields coming from s (and maybe even undesired influences in addition). For a convex surface s , an approximate value for the required number of measurements is given by a half-wavelength sampling on s projected on a . With continuous field observations at $\mathbf{r} \in a$ and equivalent surface sources at $\mathbf{r}' \in s$, the boundary integral equation for the measured tangential electric $\mathbf{e}^s(\mathbf{r})$ on a reads

$$\mathbf{n}(\mathbf{r}) \times \mathbf{e}^s(\mathbf{r}) = \mathcal{T}\{j(\mathbf{r}')\}(\mathbf{r}) - \left[\frac{1}{2} \mathcal{L}\{m(\mathbf{r}')\}(\mathbf{r}) - \mathcal{K}\{m(\mathbf{r}')\}(\mathbf{r}) \right]. \quad (2.74)$$

A similar equation holds true for the magnetic field by duality, see (2.40).

This equivalent source representation with electric and magnetic surface current densities, proposed by Alvarez et al. [2007], is not unique as we know from the equivalence theorems [Huygens 1690; Love 1901; Schelkunoff 1936; Martini et al. 2008]. Thus, the inverse problem is ill-posed [Kiliç and Eibert 2015; T. B. Hansen et al. 2019]. Unique solutions can be attained if we choose purely electric or magnetic surface current densities [Petre and Sarkar 1992, 1994; Sarkar and Taaghhol 1999; Eibert and Schmidt 2009; Eibert et al. 2010; Araque Quijano and Vecchi 2010b, 2010a; Eibert et al. 2011] or combinations of electric and magnetic surface current densities such as Love currents [Araque Quijano and Vecchi 2009; Jørgensen et al. 2010; Araque Quijano and Vecchi 2010b, 2010a; Jørgensen et al. 2011b; Jørgensen et al. 2012a; Foged et al. 2014; Kiliç and Eibert 2015; Korn-

probst et al. 2019b; Kornprobst et al. 2019e; Kornprobst et al. 2019f; Kornprobst et al. 2021a] or CSs [Eibert and Vojvodic 2016; Eibert et al. 2016; Eibert and T. B. Hansen 2017; Kornprobst et al. 2019b; Kornprobst et al. 2021a]. Worth mentioning is also the work by K. Persson and Gustafsson [2005], K. Persson et al. [2010], and K. Persson et al. [2014], where the focus was on radome applications and where the body-of-revolution symmetry was utilized in order to decompose the inverse equivalent current problem by the corresponding eigenmodes.

Many variants of and extensions to this problem are worth researching—possibly inspired by real-world measurement challenges with innovative measurement setups [Faul et al. 2018; Faul et al. 2019; Mauermayer et al. 2019; Kornprobst et al. 2020]. The handling of electrically large measurement scenarios has to be done in a computationally efficient manner [J. E. Hansen 1988; Bucci et al. 1991; Coifman et al. 1993; Chew et al. 2001; K. Zhao et al. 2005; Eibert 2005; Alvarez et al. 2008; Schmidt and Eibert 2009; Lopez et al. 2009; Eibert and Schmidt 2009; Qureshi et al. 2013; Foged et al. 2014; Y. Wang et al. 2018; Varela et al. 2020]. Reducing the required number of measurement samples, which are closely related to the DOFs in the radiated fields, is one way to reduce measurement times to the practicable minimum [Bucci and Gennarelli 1988; D’Agostino et al. 2009; Cornelius et al. 2016; Hofmann et al. 2019; Bangun et al. 2020]. Probe correction takes care of the behavior of the probe antenna if its behavior is different from an idealized Hertzian or Fitzgerald dipole [Larsen 1977; Schmidt et al. 2008; Eibert et al. 2015]. In the presumably most extreme case, a correction of the non-ideal fields of compact ranges and plane-wave generators may be investigated [Johnson et al. 1969; Bucci et al. 2013; Gemmer and Heberling 2019; Scattone et al. 2021]. Echo suppression with additional radiation sources *outside* of v_1 has already been mentioned [Foged et al. 2013b; Yinusa 2015; Paulus et al. 2019; Knapp et al. 2019a; Knapp et al. 2019b; Kornprobst et al. 2019d; Knapp et al. 2020]; a variation of sources outside of v_1 is considered when the surrounding medium is not free space but for instance a half-space [Mauermayer and Eibert 2018; Eibert and Mauermayer 2018a, 2018b; Saccardi et al. 2019]. A variety of closely related problems is found in phaseless antenna measurements, where only the field magnitude $\|e^s(\mathbf{r})\|$ is measured [Yaccarino and Rahmat-Samii 1999; Pierri et al. 1999; Paulus et al. 2017b; Paulus et al. 2020; Kornprobst et al. 2021d; Knapp et al. 2021; Paulus et al. 2021]. This possibly leads to a much harder-to-solve non-linear and non-convex source reconstruction problem.

Antenna measurements are the only measurement task with an associated inverse problem discussed in this thesis, but by far not the only one in electromagnetics. The most notable other case is inverse scattering [Y. Wang and Chew 1989; Bucci and Isernia 1997; Kılıç and Eibert 2015; Colton and Kress 2019], where the mono- or bi-static scattering behavior of an object under test is measured and reconstructed by suitable algorithms. Microwave imaging may be seen as an inverse scattering task, where the goal is to retrieve an object’s spatially varying

electromagnetic behavior or material composition [Schnattinger 2014; Neitz 2015]. These scenarios can be tackled by reconstructing scattering currents, idealized scattering centers or material distributions. The first one is closely related to source reconstruction for antenna measurements.

Surface Integral Equations and Their Discretization

I have always believed that scientific research is another domain where a form of optimism is essential to success: I have yet to meet a successful scientist who lacks the ability to exaggerate the importance of what he or she is doing, and I believe that someone who lacks a delusional sense of significance will wilt in the face of repeated experiences of multiple small failures and rare successes, the fate of most researchers.

– Daniel Kahneman, *Thinking, Fast and Slow*

BOUNDARY INTEGRAL EQUATIONS can be employed for the simulation of radiation and scattering problems. The continuous description of these problems has been introduced in the preceding chapter and is here transformed into numerically solvable, discretized problems according to the MOM. This is done for the EFIE in Section 3.1 and the MFIE in Section 3.2, whose advantages and drawbacks, as well as state-of-the-art solution approaches to the respective problems, are discussed in these sections. The CFIE discretization is discussed in Section 3.3.

3.1 Discretization of the Electric Field Integral Equation

3.1.1 A Walkthrough for the Method of Moments

The MOM is a numerical technique to transform a linear operator equation (often with an integral operator as part of a boundary IE) into a linear system of equations [Harrington 1968; Morita et al. 1990; Peterson et al. 1997; Jin 2011; Gibson 2014]. It follows the method of weighted residuals (potentially a variational approach): With a given linear operator, and a choice of basis (or ansatz/expansion/trial) and weighting (or testing) functions, a minimization of the residual presumably yields the best possible approximation to the true solution within a given basis. For instance, the FEM may be seen as a subset of the MOM with a differential operator instead of an integral operator.

The flexibility of the MOM allows a vast number of choices for the basis and testing functions. Whereas some fundamental properties such as div-conformity seem evident for the expansion functions of current densities, such considerations

turn out to be more cumbersome for the testing functions. Well-known approaches for the choice of the testing functions include Dirac delta testing with Hertzian dipoles for three-dimensional fields (point matching or collocation method), just the same as the basis functions (Galerkin testing), or any other than the basis functions (Petrov-Galerkin method). Among all these options, the MOM does not reveal—for given operators and/or basis functions—how a testing function should look like or which testing function is superior to others. This issue can be tackled by operator theory in a mathematically rigorous manner.

The initial step of the MOM is to expand the surface current densities with N basis functions \mathbf{v}_n as

$$\mathbf{j} = \sum_{n=1}^N [j]_n \mathbf{v}_n, \quad \mathbf{m} = \sum_{n=1}^N [\mathbf{v}]_n \mathbf{v}_n, \quad (3.1)$$

where each basis function receives an unknown coefficient $[j]_n$ or $[\mathbf{v}]_n$ leading to the column vectors $\mathbf{i} \in \mathbb{C}^N$ and $\mathbf{v} \in \mathbb{C}^N$. The basis functions for electric and magnetic current unknowns do not have to be same; here, this is only an exemplary choice which is discussed in more detail when specific basis functions are introduced.

There are two major possibilities for the expansion functions: entire-domain vs. sub-domain functions. While the former are defined on the complete surface s of the scatterer, the latter are functions with compact support, for the n th expansion function on a subdomain $s_n \subset s$. This is for instance achieved by meshing the object under consideration and defining sub-domain functions only on one or several, possibly adjacent, mesh cells. Hence, sub-domain functions offer more versatility for the modeling of arbitrary geometries and are nowadays the conventional choice.

Unlike the basis functions, the discretization of the operators depends on the field quantities of interest. This step, i.e., choosing a suitable set of weighting functions, is to be discussed for each equation separately. The procedure of MOM itself is discussed in detail for the EFIE first.

Evaluating the EFIE (2.58) for the discretized electric surface current densities according to (3.1) leads to

$$\sum_{n=1}^N [j]_n \mathcal{T} \mathbf{v}_n = \mathbf{e}^v \times \mathbf{n}. \quad (3.2)$$

The field description also has to be transformed into single numerical values instead of the continuous description. This is done with a set of weighting functions on a surface a . Except for exotic approaches such as the method of auxiliary sources [Popovidi-Zaridze et al. 1978; Bogdanov et al. 1999; Kaklamani and Anastassiou 2002; J. Lee and Nam 2005], the source surface s and the observation surface

a typically coincide when scattering objects are treated.¹ As a sub-domain function, the m th weighting function \mathbf{w}_m (of overall M functions) exhibits a compact support on $a_m \subset a$. We attain the inner-product-like interaction integral

$$\langle \mathbf{w}_m, \mathbf{e}^v \times \mathbf{n} \rangle = \iint_a \mathbf{w}_m(\mathbf{r}) \cdot (\mathbf{e}^v(\mathbf{r}) \times \mathbf{n}(\mathbf{r})) \, d^2r \quad \text{for } m \in \{1, 2, \dots, M\}. \quad (3.3)$$

This leads, when employed for (3.2), to the linear system of equations

$$\sum_{n=1}^N [i]_n \langle \mathbf{w}_m, \mathcal{T} \mathbf{v}_n \rangle = \langle \mathbf{w}_m, \mathbf{e}^v \times \mathbf{n} \rangle \quad \text{for } m \in \{1, 2, \dots, M\}. \quad (3.4)$$

In a compact notation, the equation may be written in matrix form as

$$\mathbf{T}_{\mathbf{w}, \mathbf{v}} \mathbf{i} = \mathbf{e}_{\mathbf{w}}, \quad (3.5)$$

where the subscripts \mathbf{v} and \mathbf{w} denote the choice of a set of basis and weighting functions, respectively. The unknown coefficients are collected in the vector \mathbf{i} . The system matrix—here $\mathbf{T}_{\mathbf{w}, \mathbf{v}} \in \mathbb{C}^{M \times N}$ —has entries given as

$$[\mathbf{T}_{\mathbf{w}, \mathbf{v}}]_{mn} = \langle \mathbf{w}_m, \mathcal{T} \mathbf{v}_n \rangle \quad \text{for } m \in \{1, 2, \dots, M\}, n \in \{1, 2, \dots, N\} \quad (3.6)$$

and the entries of the right-hand-side vector $\mathbf{e}_{\mathbf{w}} \in \mathbb{C}^M$ of the equation system are given as

$$[\mathbf{e}_{\mathbf{w}}]_m = \langle \mathbf{w}_m, \mathbf{e}^v \times \mathbf{n} \rangle \quad \text{for } m \in \{1, 2, \dots, M\}. \quad (3.7)$$

The matrix entries are numerically evaluated leveraging a singularity cancellation technique [Duffy 1982; R. Graglia 1987; Khayat and Wilton 2005; Ismatullah and Eibert 2008; L. Li et al. 2014a]. The most common choice is $M = N$ for the system matrix to be quadratic and, in the best case, non-singular. For SIEs, this is the only case to be considered in the remainder of this chapter.

The whole discretization procedure from (3.1) to (3.7) is called MOM; however, as indicated above, the question of picking suitable basis or testing functions remains unanswered and has to be deduced from the properties of the discretized operators.

1. This choice is usual and reasonable in the case of scattering or radiating problems as shown in Fig. 2.3. For antenna measurements, see Fig. 2.6, the separation of source and observation surfaces is much more common. The formalism with the observation surface a holds in any case, though.

3.1.2 Choosing a Suitable Set of Basis and Testing Functions

An Intuitive Approach

Taking the same basis \mathbf{v} for \mathbf{j} and \mathbf{m} —as suggested in (3.1)—is not necessary but reasonable to some extent. In order to fulfill the physics-based current continuity conditions (2.5), divergence-conforming expansion functions are equally appropriate for both equivalent current types. Approaches with a non-div-conforming basis for the current densities—or, more specifically, containing curl-conforming parts—may lead to spurious solutions [Rao et al. 1982; Yuan 1990; Schroeder and Wolff 1994; B.-N. Jiang et al. 1996].² Furthermore, it may not be possible to evaluate hypersingular integrals which lead to diverging field values [Maue 1949].³

Thus, the choice of \mathbf{v} is rather clear in favor of a div-conforming set of basis functions based on the properties of current densities. The questions of how this is reflected in the equations and of how to choose the appropriate testing functions remain. For quite some time, the answer to these two issues has been evident—at least for the EFIE operator due to its contained hypersingular contribution: The integral $\|\mathbf{r} - \mathbf{r}'\|^{-3}$ appearing in \mathcal{T}_h simply cannot be evaluated for a self-coupling term, i.e., for $s_n \cap a_n \neq \emptyset$. Hence, the numerical evaluation of (2.43) has to be discussed in more detail. The first step is to take one del-operator into the integral—converting it into a surface derivative—and apply it to the current densities—and no longer to the Green's function—as⁴

$$\mathcal{T}_h\{\mathbf{v}_n\}(\mathbf{r}) = -\mathbf{j}(\mathbf{r}) \times \mathbf{grad} \iint_{s_n} g(\mathbf{r}, \mathbf{r}') \operatorname{div}'_s \mathbf{v}_n(\mathbf{r}') d^2r'. \quad (3.8)$$

It is obvious that div-conforming basis functions present an advantage in the evaluation of this integral. The second step is the interaction integral with the testing function, which is reformulated by the application of a surface Gauss theorem to [Bladel 2007]

$$\langle \mathbf{w}_m, \mathcal{T}_h \mathbf{v}_n \rangle = -\mathbf{j} \iint_{a_m} \mathbf{w}_m(\mathbf{r}) \cdot \left(\mathbf{n}(\mathbf{r}) \times \mathbf{grad} \iint_{s_n} g(\mathbf{r}, \mathbf{r}') \operatorname{div}'_s \mathbf{v}_n(\mathbf{r}') d^2r' \right) d^2r$$

2. This holds true for SIEs. For the FEM, a curl-conforming basis is required for the fields.

3. This is the case for the \mathcal{T} operator, viz., the electric field of electric currents and the magnetic field of magnetic currents. Even if we consider non-div-conforming basis functions for the classical MFIE, in which only the magnetic field of electric currents is evaluated, the electric field cannot be evaluated in the post-processing. This has been for instance studied by Rao and Wilton [1990] for curl-conforming expansion functions of magnetic currents.

4. We employ $\operatorname{div}_s(g\mathbf{v}) = g \operatorname{div}_s \mathbf{v} + \mathbf{grad}_s g \cdot \mathbf{v}$ with $\operatorname{div}_s \mathbf{v} = \mathbf{0}$ since $\mathbf{v}(\mathbf{r}')$ has no \mathbf{r} -dependence; then, $\mathbf{grad}_s g = -\mathbf{grad}'_s g$ with a derivative after \mathbf{r}' ; finally, a surface Gauss theorem helps to move the derivative to the surface current densities [Bladel 2007].

$$\begin{aligned}
 &= -j \iint_{a_m} \operatorname{div}_a (\mathbf{n}(\mathbf{r}) \times \mathbf{w}_m(\mathbf{r})) \iint_{s_n} g(\mathbf{r}, \mathbf{r}') \operatorname{div}'_s \mathbf{v}_n(\mathbf{r}') d^2r' d^2r \\
 &\quad -j \oint_{\partial a_m} \mathbf{u}_{t,m}(\mathbf{r}) \cdot \mathbf{w}_m(\mathbf{r}) \iint_{s_n} g(\mathbf{r}, \mathbf{r}') \operatorname{div}'_s \mathbf{v}_n(\mathbf{r}') d^2r' d\mathbf{r}. \quad (3.9)
 \end{aligned}$$

Here, we have assumed that the m th weighting function exhibits compact support on a_m , and that this support has a unit tangential vector $\mathbf{u}_{t,m}$ on ∂a_m , positively-oriented according to the outward unit normal \mathbf{n} .⁵

With the choice of curl-conforming testing functions, the line integral in (3.9) vanishes. Additionally, $\mathbf{n} \times \mathbf{w}$ is then div-conforming which simplifies the evaluation of the surface integral. Just from looking at this interaction integral, we have arrived at choosing div-conforming basis and curl-conforming testing functions for the EFIE. Note that the tangential electric field inside the EFIE was written as the rotated version $\mathbf{n} \times \mathbf{e}$ to reach this conclusion.

However, div- and curl-conformity is not the only decisive feature. A well-conditioned system matrix is also desirable. An indicator can be how dominant the diagonal entries of the matrix are, which happens only for a significant overlap between the basis function domain s_n and the weighting function domain a_n of the n th functions. Furthermore, the respective functions $\mathcal{T}\mathbf{v}_n$ and \mathbf{w}_n should point approximately into the same direction for every $\mathbf{r} \in s_n \cap a_n$ —in other words, the angle between $\mathcal{T}\mathbf{v}_n$ and \mathbf{w}_n should be as small as possible. This ensures a large value of the dot product inside the interaction integral $\langle \mathbf{w}_n, \mathcal{T}\mathbf{v}_n \rangle$ of the self-coupling terms. Due to the mapping properties of the \mathcal{T} operator, this desired behavior can be achieved by $\mathbf{w} = \mathbf{n} \times \mathbf{v}$ —viz., $\mathcal{T}\mathbf{v}_n$ is approximately co-linear with $\mathbf{n} \times \mathbf{v}_n$ on s_n —, which has the very welcome bonus effect that the weighting functions are curl-conforming for a div-conforming basis.

A Theoretical Approach

The question of the correct choice of a set of testing functions for a given basis and operator can be answered mathematically much more rigorously with the help of operator theory [Cessenat 1996]. For the further discussion, the concept of Sobolev spaces is briefly introduced, which are—without rigorously introducing all necessary definitions in this context—complete normed vector spaces of integrable functions whose weak-sense derivatives up to a certain order are integrable up to a certain order. For the case of electromagnetic fields on a smooth surface s , we consider Hilbert spaces with square-integrable weak-sense derivatives up to a order of $1/2$ [Cessenat 1996; Nédélec 2001]. Square-integrability makes sense from

5. Another way to define $\mathbf{u}_{t,m}$ is via the outward unit normal \mathbf{n} on a and the outward unit normal $\mathbf{u}_{n,m}$ on ∂a_m lying in the tangent plane to a_m as $\mathbf{u}_{t,m} = \mathbf{n} \times \mathbf{u}_{n,m}$. For a sketch, see Fig. 3.1(a) on p. 38.

a physical point of view as it implies finite solution energy.

In the case of a one-dimensional generalized complex-valued function $f(\mathbf{r})$ dependent on a three-dimensional position vector $\mathbf{r} \in \mathbb{R}^3$ but with the restriction that $\mathbf{r} \in s$, we have the Sobolev space

$$H^{-1/2}(s) = \{f \in \mathcal{S}'(s) : \|f\|_{H^{-1/2}(s)} < \infty\} \quad (3.10)$$

with the space \mathcal{S}' of tempered distributions and the associated norm

$$\|f\|_{H^{-1/2}(s)}^2 = \iint_s |f(\mathbf{r})|^2 d^2r + \iint_s \iint_s \frac{|f(\mathbf{r}) - f(\mathbf{r}')|^2}{\|\mathbf{r} - \mathbf{r}'\|} d^2r' d^2r. \quad (3.11)$$

The first integral ensures finite energy in the function itself and the latter ensures the same yet in presence of a $\|\mathbf{r} - \mathbf{r}'\|^{-1}$ singularity, which is somewhat comparable to the presence of the Green's function $g(\mathbf{r}, \mathbf{r}')$ inside an integral.

We deduce the three-dimensional case for tangential vector fields $\mathbf{v} \in \mathbb{C}^3$ as

$$\mathbf{H}_t^{-1/2}(s) = \{\mathbf{v} \in (H^{-1/2}(s))^3, \mathbf{n} \cdot \mathbf{v} = 0\}. \quad (3.12)$$

The particular two sub-spaces of $\mathbf{H}_t^{-1/2}(s)$, which we are interested in, are

$$H^{-1/2}(\text{div}_s, s) = \{\mathbf{v} \in \mathbf{H}_t^{-1/2}(s), \text{div}_s \mathbf{v} \in H^{-1/2}(s)\} \text{ and} \quad (3.13)$$

$$H^{-1/2}(\text{curl}_s, s) = \{\mathbf{v} \in \mathbf{H}_t^{-1/2}(s), \text{curl}_s \mathbf{v} \in H^{-1/2}(s)\}, \quad (3.14)$$

which may be seen as a more formal definition of the widely used terms *div-conforming* and *curl-conforming*. The surfacic divergence is defined as

$$\text{div}_s \mathbf{v} := \text{div} \mathbf{v} \quad (3.15)$$

since $\mathbf{v} \in \mathbf{H}_t^{-1/2}(s)$ with $\mathbf{n} \cdot \mathbf{v} = 0$ and the surfacic curl as

$$\text{curl}_s \mathbf{v} := \mathbf{curl} \mathbf{v} \cdot \mathbf{n} = \text{div}_s(\mathbf{v} \times \mathbf{n}). \quad (3.16)$$

Their respective norms are defined according to (3.11) as

$$\|\mathbf{v}\|_{H^{-1/2}(\text{div}_s, s)}^2 = \|\mathbf{v}\|_{\mathbf{H}_t^{-1/2}(s)}^2 + \|\text{div}_s \mathbf{v}\|_{H^{-1/2}(s)}^2, \quad (3.17)$$

$$\|\mathbf{v}\|_{H^{-1/2}(\text{curl}_s, s)}^2 = \|\mathbf{v}\|_{\mathbf{H}_t^{-1/2}(s)}^2 + \|\text{curl}_s \mathbf{v}\|_{H^{-1/2}(s)}^2. \quad (3.18)$$

The spaces $H^{-1/2}(\text{div}_s, s)$ and $H^{-1/2}(\text{curl}_s, s)$ are dual to each other [Cessenat 1996; Nédélec 2001]. As seen from (3.16), any div-conforming function is converted to a

curl-conforming one by a $\mathbf{n} \times 90^\circ$ -rotation on a surface, and vice versa.

Forging a bridge back to the topic of the EFIE discretization, we choose basis functions in $\mathbf{H}^{-1/2}(\text{div}_s, s)$ due to current continuity. The EFIE operator \mathcal{T} as defined in this thesis constitutes a mapping from $\mathbf{H}^{-1/2}(\text{div}_s, s)$ to $\mathbf{H}^{-1/2}(\text{div}_s, s)$. The MOM as described above does not suggest any particular type of testing functions. However, its proper application requires that the testing is performed in the dual space of the range of the operator under consideration [Cessenat 1996; Q. Chen and Wilton 1990; Q. Chen 1990; Nédélec 2001; Tong et al. 2009; Buffa and Christiansen 2007; Ylä-Oijala et al. 2010; Cools et al. 2011; Yan et al. 2011a; Ylä-Oijala et al. 2012b; Yan and Jin 2013; Ylä-Oijala et al. 2013b; Ylä-Oijala et al. 2014; Adrian 2018]. It follows for the EFIE that the field evaluation should be performed in the dual space of $\mathbf{H}^{-1/2}(\text{div}_s, s)$, which is $\mathbf{H}^{-1/2}(\text{curl}_s, s)$. This was already the result of the simplistic reasoning above.

However, testing in the dual space is not sufficient. What was mentioned before as the goal of a well-conditioned system matrix is—put mathematically—known as the Ladyzhenskaya–Babuška–Brezzi condition or inf-sup condition. This comprises not only well-posedness but also existence and uniqueness of the solution, both for the analytical/continuous problem (ensured by the uniqueness theorem except for interior resonances) and for the discretized problem (ensured by a proper choice of basis and testing functions). Furthermore, it is a requirement that the discretized solution converges to the analytical solution when the mesh is refined, i.e., when the discretization density increases. For the classical RWG-discretized EFIE, these conditions are fulfilled.

3.1.3 Intermission: Basis and Testing Functions on a Triangular Mesh

The Rao-Wilton-Glisson Functions

The introduction of div-conforming functions by Rao et al. [1982]—also known from the works of Raviart and Thomas [1977] or Nédélec [1980] as the basis of lowest polynomial order—defined on adjacent pairs of facets on a triangular mesh was a breakthrough for SIEs since spurious solutions were avoided for the first time. As compared to other meshes, triangular mesh cells provide a great deal of flexibility for the geometric modeling. An n th RWG function is assigned to all pairs of (adjacent) triangles, which share an n th interior edge of the mesh. These two triangles are denoted as s_n^+ and s_n^- with $s_n = s_n^+ \cup s_n^-$; their respective area is A_n^\pm . A

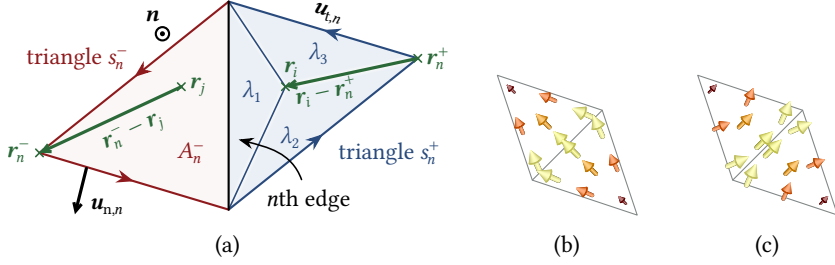


Fig. 3.1: Illustrations of the RWG functions on a single pair of adjacent triangles. (a) Depiction of the relevant vectors and quantities. (b) A single $\boldsymbol{\beta}$ function. (c) A single $\boldsymbol{\alpha}$ function.

single function may be defined as

$$\boldsymbol{\beta}_n = \begin{cases} \frac{\mathbf{r} - \mathbf{r}_n^+}{2A_n^+} & \text{for } \mathbf{r} \in s_n^+, \\ \frac{\mathbf{r}_n^- - \mathbf{r}}{2A_n^-} & \text{for } \mathbf{r} \in s_n^-, \\ \mathbf{0} & \text{for } \mathbf{r} \in s \setminus s_n, \end{cases} \quad (3.19)$$

see Fig. 3.1, where \mathbf{r}_i and \mathbf{r}_j are two possible realizations of \mathbf{r} . In contrast to [Rao et al. 1982], the functions are not scaled with the length of the interior edge. The RWG functions are div-conforming—they live in $H^{-1/2}(\text{div}_s, s)$ —since the normal vector component is continuous everywhere, in particular across the shared edge. Consequently, their rotated counterparts $\boldsymbol{\alpha} = \boldsymbol{\beta} \times \mathbf{n}$ are curl-conforming.

The definition in (3.19) is tedious to deal with for numerical integration schemes. Typically, quadrature is performed in a triangle-specific barycentric coordinate system with the coordinates

$$1 = \lambda_1 + \lambda_2 + \lambda_3, \quad (3.20)$$

$$\mathbf{r} = \mathbf{r}_{\text{node1}}\lambda_1 + \mathbf{r}_{\text{node2}}\lambda_2 + \mathbf{r}_{\text{node3}}\lambda_3. \quad (3.21)$$

The barycentric coordinates λ_k depend on the coordinate \mathbf{r} . With the total area of the triangle $\|(\mathbf{r}_{\text{node1}} - \mathbf{r}_{\text{node3}}) \times (\mathbf{r}_{\text{node2}} - \mathbf{r}_{\text{node3}})\|/2$, each barycentric coordinate corresponds to the normalized area of the respective subtriangle, see Fig. 3.1, according to

$$\lambda_1 = \frac{\|(\mathbf{r}_{\text{node2}} - \mathbf{r}) \times (\mathbf{r}_{\text{node3}} - \mathbf{r})\|}{\|(\mathbf{r}_{\text{node1}} - \mathbf{r}_{\text{node3}}) \times (\mathbf{r}_{\text{node2}} - \mathbf{r}_{\text{node3}})\|}. \quad (3.22)$$

This allows one to rewrite the RWG function definition as, here given for $\boldsymbol{\beta}_n$ inside

the triangle s_n^+ as depicted in Fig. 3.1(a),

$$\boldsymbol{\beta}_n = \mathbf{n} \times (\lambda_2 \mathbf{grad} \lambda_3 - \lambda_3 \mathbf{grad} \lambda_2) \quad \text{for } \mathbf{r} \in s_n^+, \quad (3.23)$$

where the edge vectors $\mathbf{n} \times \mathbf{grad} \lambda_3$ and $\mathbf{grad} \lambda_2 \times \mathbf{n}$ are constant on s_n^+ . Considering all functions on one triangle at the same time, the quadrature of only three scalar linear functions is sufficient. For $\text{div} \boldsymbol{\beta}_n = \pm 1/A$, $\mathbf{r} \in s_n^+$, the constant function has to be integrated in addition. Overall, only a $1/\|\mathbf{r} - \mathbf{r}'\|$ singularity inside $g(\mathbf{r}, \mathbf{r}')$ has to be evaluated for the EFIE.

The RWG functions are a polynomial basis of order $p = 0.5$. Along the direction of current flow, they exhibit a piecewise-linear rooftop-alike dependence, and, along the lateral direction, a constant one. For a smooth modeling of typically sinusoidal current distributions, a rather dense discretization with a triangle edge length h of about $\lambda/10$ is commonly employed. To avoid this dense discretization and allow approximately for the naively expected, coarser discretization density with an sampling of approximately $\lambda/2$ unknowns per surface dimension (and an even larger h), higher-order (HO) functions may be employed.

Hierarchical Higher-Order Vector Functions on a Triangular Mesh

There are two ways to define HO functions: either interpolatory or hierarchical [Peterson 2006]. In the hierarchical case, the functions are designed to be (nearly) orthogonal and low-order (LO) functions form a subset of the HO ones. The HO basis considered in this thesis has been proposed in [Ismatullah and Eibert 2009a, 2009b; Ismatullah 2010; L. Li et al. 2014b; L. Li 2016]. It is a 90° rotated version $\boldsymbol{\beta} = \mathbf{n} \times \boldsymbol{\alpha}$ of the basis presented in [Sun et al. 2001; Y. Zhu and Cangellaris 2006], which is done to make the curl-conforming FEM basis div-conforming.

The functions are defined via a polynomial description with barycentric (or simplex) coordinates $\lambda_1 + \lambda_2 + \lambda_3 = 1$, see Fig. 3.1(a). Then, the three half RWG functions in one triangle (e.g., in s_n^+) may be defined as

$$\mathbf{v} = \mathbf{n} \times (\lambda_i \mathbf{grad} \lambda_j - \lambda_j \mathbf{grad} \lambda_i) \quad \text{for } i \in \{1, 2\}, j \in \{2, 3\}, \text{ and } i \neq j. \quad (3.24)$$

A sign for each triangle with respect to the global surface orientation has to be considered, if the function is an edge-element and has to be continuous across triangle boundaries. The vectors $\mathbf{n} \times \mathbf{grad} \lambda_j$ describe the edge vectors of the triangles. The RWG functions represent the first-order div-conforming space (edge-related). They exhibit linear variation only in one direction, hence we speak of a polynomial order of $p = 0.5$. The first polynomial order ansatz functions ($p = 1$) are completed by the functions

$$\mathbf{v} = \mathbf{n} \times (\lambda_i \mathbf{grad} \lambda_j + \lambda_j \mathbf{grad} \lambda_i) \quad \text{for } i \in \{1, 2\}, j \in \{2, 3\}, \text{ and } i \neq j \quad (3.25)$$

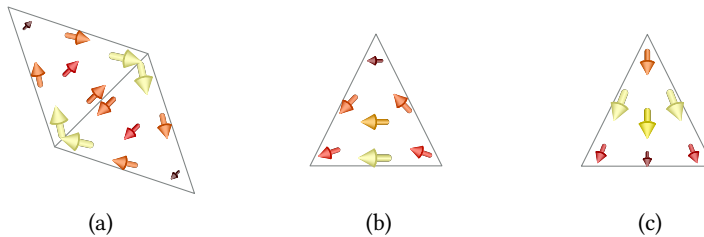


Fig. 3.2: Div-conforming hierarchical HO basis functions. (a) Exemplary $p = 1.0$ function on two adjacent facets. (b) First $p = 1.5$ function on a single facet. (c) Second $p = 1.5$ function on a single facet.

in the first-order rotational subspace (again edge-oriented). In a similar way, polynomial functions of the simplex coordinates may be defined up to arbitrary polynomial orders. The $p = 1.5$ expansion functions are obtained by including the (face-associated) second-order div-conforming subspace, the $p = 2$ subspace by the (both face- and edge-associated) second-order rotational subspace. The highest order considered in this work is $p = 2.5$ including the third-order div-conforming subspace with face-associated functions.

The HO basis is finally built by putting together the half edge-associated functions and collecting them and the face-associated functions in a set of functions β . Up to order $p = 1.5$, the HO basis functions are shown in Fig. 3.2.

3.1.4 The Classical EFIE Discretization

Following the preceding argumentation with $\mathbf{v} = \beta$ and $\mathbf{w} = \alpha$, a conforming discretization of the EFIE with RWG functions (or the hierarchical HO functions) reads

$$\mathbf{T}_{\alpha, \beta} \mathbf{i} = \mathbf{e}_{\alpha}. \quad (3.26)$$

This classical discretization of the EFIE (with an RWG basis) yields very accurate results. However, its system matrix $\mathbf{T}_{\alpha, \beta}$ suffers from ill-conditioning due to several reasons—apart from the interior resonance problem. Looking at the electric field radiated by an electric current—given by (2.15)—, there are two distinct contributions from the vector and scalar potential. These can also be identified in the first line of (2.21), where the singular integral for electric surface current densities \mathbf{j} scales with k , and the hyper-singular integral for j scales with $1/k$. This is the cause of the so-called low-frequency (LF) breakdown, which leads to conditioning issues for electrically small problems and to numerical accuracy issues at extremely LFs. Well-studied approaches for solving the LF problem are loop-star/tree decompositions and Calderón preconditioning [Wilton and Glisson 1981; Mautz and Harrington

1984; J.-S. Zhao and Chew 2000; J.-F. Lee et al. 2003; Eibert 2004; Andriulli et al. 2008; Stephanson and J.-F. Lee 2009; Yan et al. 2009; Andriulli 2012; Andriulli et al. 2013; Adrian et al. 2017, 2019]. A further issue causing conditioning problems is the dense-discretization breakdown. This happens due to the spatial derivatives in the hypersingular operator \mathcal{T}_h , which leads to the condition number of the EFIE increasing with decreasing mesh size according to h^{-2} , i.e., quadratically inversely proportional to the average triangle edge length h . This can be solved for instance by quasi-Helmholtz decompositions or Calderón preconditioning [Contopanagos et al. 2002; Adams 2004; Darbas 2006; R.-S. Chen et al. 2009; Andriulli et al. 2010; Andriulli and Vecchi 2012; Adrian et al. 2014]. Dély et al. [2019] have identified and tackled another issue: the ill-conditioning when the frequency increases along with the discretization density, i.e., a high-frequency (HF) breakdown unrelated to interior resonances. Apart from numerical issues in extreme cases, all these EFIE breakdowns concern the condition number of the system matrix and not the accuracy, which typically remains excellent. Hence, the EFIE solution serves as an accurate reference at the frequency ranges and discretization densities considered in this thesis, in particular when an h - or p -refined solution is considered.

3.2 Discretization of the Magnetic Field Integral Equation

Following the procedure, which was introduced for the discretization of the EFIE, for the MFIE (2.61), the linear system of equations

$$\left[\frac{1}{2} \mathbf{G}_{\mathbf{w}, \mathbf{v}} + \mathbf{K}_{\mathbf{w}, \mathbf{v}} \right] \mathbf{i} = \mathbf{h}_{\mathbf{w}} \quad (3.27)$$

is obtained, where we have the discretized identity operator in the form of a so-called Gram matrix with the entries

$$[\mathbf{G}_{\mathbf{w}, \mathbf{v}}]_{mn} = \langle \mathbf{w}_m, \mathbf{v}_n \rangle \quad \text{for } m \in \{1, 2, \dots, N\}, n \in \{1, 2, \dots, N\}, \quad (3.28)$$

the discretized MFIE integral operator as a matrix with the entries

$$[\mathbf{K}_{\mathbf{w}, \mathbf{v}}]_{mn} = \langle \mathbf{w}_m, \mathbf{K} \mathbf{v}_n \rangle \quad \text{for } m \in \{1, 2, \dots, N\}, n \in \{1, 2, \dots, N\}. \quad (3.29)$$

as well as the right-hand-side vector with its entries given as

$$[\mathbf{h}_{\mathbf{w}}]_m = \langle \mathbf{w}_m, \mathbf{h}^{\mathbf{v}} \times \mathbf{n} \rangle \quad \text{for } m \in \{1, 2, \dots, N\}. \quad (3.30)$$



Fig. 3.3: Tangential field (real part) evaluation on a surface placed $\lambda/20$ over an RWG basis (length $\lambda/6$, width $\lambda/12$) for an electric surface current density. (a) Electric field over a planar function. (b) Magnetic field over a planar function.

3.2.1 Choosing a Suitable Set of Basis and Testing Functions

At first sight, the \mathcal{K} integral operator including a $1/\|\mathbf{r} - \mathbf{r}'\|^2$ singularity seems to be the challenging part for the discretization—more than the identity operator. However, a look on the interaction integral

$$\langle \mathbf{w}_m, \mathcal{K} \mathbf{v}_n \rangle = - \iint_{a_m} \mathbf{w}_m(\mathbf{r}) \cdot \left(\mathbf{n}(\mathbf{r}) \times \iint_{s_n} \mathbf{grad} g(\mathbf{r}, \mathbf{r}') \times \mathbf{v}_n(\mathbf{r}') d^2 r' \right) d^2 r \quad (3.31)$$

reveals that the self-coupling integral vanishes for planar surfaces,⁶ since the singularity has already been extracted from the integral leading to its evaluation in a Cauchy principal-value sense. Hence, there is no self-interaction integral for planar surfaces—the identity operator \mathcal{I} takes care of the self-interaction. For smooth non-planar (e.g., curvilinear) surfaces or at edges, the integral has some small contribution, but accurate quadrature and singularity treatment techniques help to avoid any numerical issues.

Shifting the derivative operator from the Green's function to the testing functions is in principle possible for certain basis functions, but neither necessary nor recommended for the integral in (3.31).⁷ The second part of the “intuitive” approach to the choice of the testing functions for the EFIE was to determine an appropriate direction of the testing functions to attain a diagonally dominant system matrix. The same considerations can be done for the MFIE. In order to clarify the differences between the MFIE and the EFIE, a visualization of the fields of one RWG basis function is given in Fig. 3.3, where the tangential fields on a planar surface placed with $\lambda/20$ distance over a planar RWG electric surface current density are shown.

6. The vector $\mathbf{grad} g(\mathbf{r}, \mathbf{r}') \times \mathbf{j}(\mathbf{r}')$ is co-linear with the unit normal $\mathbf{n}(\mathbf{r}')$ and $\mathbf{n}(\mathbf{r}') = \mathbf{n}(\mathbf{r})$ if the surfaces s_n at \mathbf{r}' and a_m at \mathbf{r} are in the same plane. Then, we have $\mathbf{n} \times \mathbf{n} = \mathbf{0}$.

7. It is possible to shift the derivative to the basis functions, which requires a curl-conforming basis. This is nonsense due to charge conservation, though.

It is observed that the tangential electric field $\text{Re}\{(\mathcal{T}\mathbf{j}) \times \mathbf{n}\}$ and the tangential magnetic field $\text{Re}\{(-\mathcal{K}\mathbf{j}) \times \mathbf{n}\}$ over the source triangles (i.e., the self-coupling fields) are approximately orthogonal. This suggests that the testing functions for the EFIE and MFIE—both for PEC objects with purely electric currents—should be approximately orthogonal in order to achieve well-conditioned system matrices.

This fact has been one of the major issues of SIEs. The MFIE operator—just as the EFIE one—constitutes a mapping from $\mathbf{H}^{-1/2}(\text{div}_s, s)$ to $\mathbf{H}^{-1/2}(\text{div}_s, s)$. Hence, operator theory suggests weighting functions in $\mathbf{H}^{-1/2}(\text{curl}_s, s)$. Together with the goal of obtaining a diagonally-dominant matrix, this cannot be achieved with RWG functions. This conflict can be resolved though when working with the dual mesh.

3.2.2 The Discretization of the MFIE, Associated Problems, and Solution Approaches

Div-Conforming Basis and Testing Functions for the MFIE

Historically, when discretizing the MFIE, the goal was to obtain a well-conditioned system of equations. This is very simply achieved by choosing the same set of functions as basis and testing functions, i.e., $\mathbf{v} = \mathbf{w} = \boldsymbol{\beta}$, which leads to the linear system of equations

$$\left[\frac{1}{2} \mathbf{G}_{\boldsymbol{\beta}, \boldsymbol{\beta}} + \mathbf{K}_{\boldsymbol{\beta}, \boldsymbol{\beta}} \right] \mathbf{i} = \mathbf{h}_{\boldsymbol{\beta}}. \quad (3.32)$$

This choice causes several problems, some of which appear with particular emphasis when an RWG basis is employed.

The Problems of the MFIE and Their Reasons

The classically discretized MFIE behaves completely different than the EFIE: While the condition number is always stable and rather small (except for interior resonances of course), the solution accuracy is severely deteriorated in many scenarios; the classical MFIE is generally seen as inaccurate. This has several underlying reasons, based on the discretization of both the \mathcal{I} and \mathcal{K} operators. The accuracy of the classical MFIE is usually lower than the accuracy of the EFIE for the same discretization density. However, if a lowest-order (zeroth order, to be more precise) mesh with planar cells is taken to model a smooth surface (e.g., most prominently a sphere), the negative influence on the accuracy of the imperfect modeling of the geometry is approximately on the same level than the inherent inaccuracy of the classical MFIE. Then, the inaccuracy of the MFIE is hidden—at least to a large extent—by the inaccuracy caused by the meshed geometry representation. For sharp-edged objects, the inaccuracy of the MFIE is more pronounced and also easier to observe since it is so prevalent that it can easily deteriorate the solution quality

by one order of magnitude.

This happens equally for electrically small and large scenarios as long as the simulation frequency is not chosen too small. Unfortunately, for large problems, the CFIE (including the MFIE) is widely employed to ensure a well-conditioned system of equations at and around interior resonance frequencies. Hence, the MFIE inaccuracy issues may affect any HF scattering or radiation scenario concerning closed objects. The reason of this problem is not solely the wrong testing space of the classical MFIE but it has been quite clearly identified that the discretization of the identity operator is the root cause of HF problems [Gürel and Ergül 2009; Ergül and Gürel 2009; Yan et al. 2011a]. Put simply, the identity operator (2.44) exhibits a Dirac delta distribution integral kernel, which negates the positive influence of the variational integral equation solution to the scattering problem.

The second problem is a rather serious LF breakdown. The classical RWG-tested MFIE shows a stable and good conditioning behavior at LFs. However, Y. Zhang et al. [2003] reported that the real part of the divergence of the retrieved current distributions has erroneously a constant limit. This issue contaminates the current solution already at mildly LFs. Looking at the FF of these currents, the problem seems to be less severe since the inaccuracies occur at frequencies one or two decades lower, cf. the numerical studies in Subsection 4.4.2. Bogaert et al. [2011b] and Bogaert et al. [2014] have identified the lack of dual-space testing in the classical MFIE as the reason that the divergence of the current, i.e., the charge distribution, is not modeled properly.

Solution Approaches to the MFIE Accuracy Issues

For the LF breakdown of the MFIE, it is clear that testing in $\mathbf{H}^{-1/2}(\text{curl}_s, s)$ instead of $\mathbf{H}^{-1/2}(\text{div}_s, s)$ does not suffice to cure the problem. Dual-space testing with functions defined on the dual mesh—with functions as proposed by Q. Chen and Wilton [1990] and Q. Chen [1990], Buffa and Christiansen [2007], or Bogaert et al. [2013]—is strictly necessary. Each basis functions (Buffa-Christiansen (BC) or razor-blade) on the dual mesh is associated with an edge of the primal (triangular) mesh but exhibits an approximately orthogonal current flow with respect to the original RWG function. Those functions are associated with the nodes of the dual mesh since the definitions of faces/edges and nodes of the dual mesh are interchanged as compared to the primal one. For LF scenarios, loop/tree or loop/star decompositions are of particular interest—which are approximately related to the scalar and vector potential contributions in the fields, and where the loop functions exhibit zero charge and divergence. Early approaches to fix the EFIE LF breakdown were based on them, as was the original discovery of the MFIE LF breakdown by Y. Zhang et al. [2003]. With the dual basis, there is also a duality between loops and stars [Stephanson and J.-F. Lee 2009]. That is, each RWG loop function is associated

with a dual basis star function and vice versa. This explains the working principle of the Calderón multiplicative preconditioner and also why the dual basis is required for the testing of the LF MFIE. There are additional issues such as the behavior for global loops for the MFIE at LFs [Bogaert et al. 2011a] but we will not go into the details of this since it is not in the scope of this work.

The HF inaccuracies of the MFIE have gotten much more attention and are also the main focus of the discretization schemes proposed in Chapter 4. In general, testing in the dual space with the dual basis is also a solution to the accuracy issues [Cools et al. 2011; Yan et al. 2011b; Yan et al. 2013; Ylä-Oijala et al. 2013b; Ylä-Oijala et al. 2014]. However, the inaccuracy has been also investigated from different perspectives which are discussed in the following. Rius et al. [2001] and Ergül and Gürel [2004b] were among the first to report that the classical RWG-MFIE exhibits a poor accuracy with RWG functions (which is nowadays assumed to be a known fact), especially for scatterers with electrically small features and sharp edges. The inaccuracies persist for electrically large problems though. The discretization of the highly-singular identity operator, which may be seen as Dirac delta integration kernel as in (2.44), has been identified to be one root cause of the inaccuracies at HFs by Davis and Warnick [2004, 2005], Warnick and Peterson [2007], Ergül and Gürel [2009], Gürel and Ergül [2009], Yan et al. [2011b], and Kornprobst and Eibert [2018a, 2018c, 2018e].

Rao and Wilton [1990], Peterson [2002], Ubeda and Rius [2005b], Ergül and Gürel [2006], and Peterson [2008] have studied curl-conforming bases, such as $n \times$ RWG functions, for the electric currents in the MFIE operator—possibly with the goal of improving the discretization accuracy. This is feasible since the MFIE integral operator \mathcal{K} by itself does not really require a div-conforming basis [Peterson 2002]. However, only with a div-conforming basis, the non-solenoidal part of the current can be modeled correctly. This also makes sense from the view of physically div-conforming surface current densities [Gürel et al. 1999]. Subsequently, it prevents the use of the CFIE (which is required for electrically large problems) and also leads to issues in the more general dielectric case, where the electric fields must also be computed from these functions with the need to appropriately handle the additionally introduced hyper-singular line charges [Rao and Wilton 1990]. The same problem arises when a monopolar RWG basis is considered [Ubeda and Rius 2005a, 2006; L. Zhang et al. 2010], where no additional constraint is considered as it is done for instance in discontinuous Galerkin approaches [Peng et al. 2013], which then yield the same solution as the classical RWG-MFIE and only show conditioning and implementation but no accuracy differences. In addition to introducing the issue of non-physical line charges—and maybe even introducing spurious solutions—, these approaches do not provide MFIE discretizations with satisfying accuracy.

Karaosmanoğlu and Ergül [2016, 2017] have numerically optimized the quadra-

ture weights for the evaluation of the MFIE matrix entries in order to arrive at accurate but problem-specific integration rules. Then, an erroneous integration compensates the MFIE inaccuracy. The underlying issues of the MFIE are not resolved and this method is not transferable to previously unknown scattering scenarios.

Some approaches for an improved MFIE discretization focus on edges in the geometry [Rius et al. 2001; Ergül and Gürel 2004b; Pan et al. 2014; Huang et al. 2016]. This is certainly a particular topic of interest but does by far not cover the whole spectrum of HF inaccuracies of the RWG-MFIE which also appear for smooth objects. Furthermore, the “solid-angle correction” seems to be based on a misconception of the “half” Dirac delta integrations resulting in the $\mathbf{I}/2$ part of the MFIE operator [Maue 1949; Eibert and V. Hansen 1997; Ergül and Gürel 2004b; Michalski and Kucharski 2014]. For a correct modelling of edges, a consideration of singular basis functions—allowing an infinite current flow along the edges but not perpendicular to them—seems to be the more expedient way [Meixner 1949; Maue 1949; Meixner 1972; Bladel 1991; Brown and Wilton 1999; R. D. Graglia and Lombardi 2008].

Another approach to solve the MFIE inaccuracy is to employ an HO expansion for the current distribution. Ergül and Gürel [2004a, 2007] and Ylä-Oijala et al. [2005] have demonstrated that an improved MFIE-operator accuracy is achievable with the full first-order functions proposed by Trintinalia and Ling [2000] (also called linear-linear basis functions), which was extended to HO expansion functions in [Ylä-Oijala et al. 2008]. Alternatively, Ismatullah and Eibert [2009a] have shown the same for a rotated Nédélec basis [Nédélec 1980; Wandzura 1992; R. D. Graglia et al. 1997]; Pan et al. [2014] have employed a Coiflet basis; and Gil and Conde-Pumpido [2020] have incorporated a solenoidal/non-solenoidal decomposition in addition to HO functions which improves the modeling of the problematic star/tree current solution inside the MFIE. The question remains, though, whether the improved accuracy is observed since HO functions are more accurate in general due to their increased number of provided DOFs for the modelling of the current flow or whether the MFIE issues really disappear. This aspect is studied in Section 4.7. The reasonable expectation is that the inaccuracies persist at a lower level without extra measures—similar to choosing a finer discretization density with RWG functions only.

Basis (or testing) functions approximately orthogonal to RWG functions, proposed by Jakobus and Landstorfer [1993] for the magnetic currents in dielectric scattering, have been analyzed by Gürel et al. [1999] but only for the EFIE. These are not defined on a dual mesh and they thus do not allow to construct divergence-free loops. Moreover, the Gram matrix condition number of the interaction between RWG and Jakobus-Landstorfer functions is significantly larger than for the RWG Gram matrix due to the design of the functions, which is reflected in the condi-

tioning of such an MFIE. A similar approach is found in [Mackenzie et al. 2009], where a basis approximately orthogonal to RWG functions has been proposed. This basis is neither div- nor curl-conforming and hence not generally suitable for the expansion of surface current densities.

In summary, all these approaches do not really solve the MFIE inaccuracy problem at HFs in a satisfying manner. In the literature, only mixed discretizations with BC-alike (testing) functions have been reported to offer solutions to the MFIE problems with a satisfactory accuracy [Q. Chen and Wilton 1990; Q. Chen 1990; Buffa and Christiansen 2007; Tong et al. 2009; Cools et al. 2009; Cools et al. 2010; Cools et al. 2011; Yan et al. 2011a, 2011b; Yan et al. 2013]. When we employ the rotated BC functions $\tilde{\boldsymbol{\alpha}} = \tilde{\boldsymbol{\beta}} \times \mathbf{n}$ defined on the barycentric refinement of the primal triangular mesh, we obtain the BC-MFIE

$$\left[\frac{1}{2} \mathbf{G}_{\tilde{\boldsymbol{\alpha}}, \tilde{\boldsymbol{\beta}}} + \mathbf{K}_{\tilde{\boldsymbol{\alpha}}, \tilde{\boldsymbol{\beta}}} \right] \mathbf{j} = \mathbf{h}_{\tilde{\boldsymbol{\alpha}}}. \quad (3.33)$$

In this thesis, the Julia package boundary element analysis and simulation toolkit (BEAST) by Cools et al. [2021] is employed for all numerical results related to BC functions. This mixed discretization constitutes a kind of reference for an accurate MFIE implementation. The same holds true for the mixed discretization of the CSIE and the EFIE with IBC which involves the electric field radiation operator of magnetic surface currents [Ylä-Oijala et al. 2010; W. D. Li et al. 2012; Ylä-Oijala et al. 2012a; Ylä-Oijala et al. 2013a; Yan and Jin 2013] since both are closely related to the operator of the PEC MFIE. Discretization schemes with a dual basis and dual mesh are of course not limited to triangular meshes. For instance, Smith and Peterson [2005] have investigated a dual basis for the CFIE discretized on quadrilateral meshes; R. Chang and Lomakin [2013] extended the use of the Calderón multiplicative preconditioner for mixed triangular/quadrilateral meshes.

Conveniently, both the accuracy issues at HFs and the LF breakdown are solved with such a mixed discretization of the MFIE operator. However, this is computationally costly since the full system matrix grows by a factor of 36 if the matrix is set up for the refined mesh. Even when accelerated by fast methods, an increase by a factor of 6 may remain. This is of course implementation-specific and may be less severe if the factor only comes into play during the setup of the system matrix, but a common way is to set up the RWG-matrix for the barycentric refinement of the mesh and define RWG- and BC-functions on a coarser level by mapping matrices [Andriulli et al. 2008]. It is still desirable to avoid this computational overhead if possible and to work with standard RWGs—given that the mentioned issues of the MFIE are resolved.

3.3 The Combined Field Integral Equation

As discussed in Subsection 2.5.2, the CFIE is the prevalent way to cope with the problem of interior resonances, which worsens the conditioning of the EFIE and the MFIE and introduces parasitic exterior solutions for the MFIE. Having the RWG discretizations of both IEs in mind, the classical CFIE is attained by the weighted superposition of the EFIE (3.26) and the MFIE (3.32). This can be seen as taking RWG functions for both the basis and the testing functions in the continuous description (2.67) of the CFIE (with the weighting factor $0 < \chi_{\text{CF}} < 1$), leading to

$$\left[\chi_{\text{CF}} \mathbf{T}_{\alpha,\beta} + (1 - \chi_{\text{CF}}) \left(\frac{1}{2} \mathbf{G}_{\beta,\beta} + \mathbf{K}_{\beta,\beta} \right) \right] \mathbf{i} = \mathbf{C}_{\chi} \mathbf{i} = \chi_{\text{CF}} \mathbf{e}_{\alpha} + (1 - \chi_{\text{CF}}) \mathbf{h}_{\beta}. \quad (3.34)$$

The CFIE inherits all properties (positive and negative) of the EFIE and the MFIE to some extent, but the weighting χ_{CF} may adjust how strong the CFIE suffers from a respective problem. For instance, it is common to choose χ_{CF} close to one to avoid the negative influence of the MFIE on the accuracy. This already helps to reduce the condition number of the overall system matrix \mathbf{C}_{χ} since this choice counteracts the influence of interior resonances on the EFIE. Hence, the iterative solver convergence is negatively affected by choosing a large value for χ but to a lower degree than for the plain EFIE. This is of course no satisfactory solution and covers, by far, not all the issues of the EFIE and the MFIE at both LFs and HF. Tackling all the issues of both IEs simultaneously (for scattering scenarios involving dielectric and PEC bodies) is actively researched [Adrian et al. 2016; Guzman et al. 2017; Adrian 2018; Chhim et al. 2018; G.-Y. Zhu et al. 2019; Merlini 2019; Chhim et al. 2020; Merlini et al. 2020; Hofmann et al. 2021; Adrian et al. 2021].

Some of these issues, especially the inaccuracy stemming from the RWG-MFIE, can be resolved by replacing the MFIE by the BC-MFIE. This yields the BC-CFIE

$$\left[\chi_{\text{BC-CF}} \mathbf{T}_{\alpha,\beta} + (1 - \chi_{\text{BC-CF}}) \mathbf{G}_{\beta,\beta} \mathbf{G}_{\tilde{\alpha},\beta}^{-1} \left(\frac{1}{2} \mathbf{G}_{\tilde{\alpha},\beta} + \mathbf{K}_{\tilde{\alpha},\beta} \right) \right] \mathbf{i} \\ = \chi_{\text{BC-CF}} \mathbf{e}_{\alpha} + (1 - \chi) \mathbf{G}_{\beta,\beta} \mathbf{G}_{\tilde{\alpha},\beta}^{-1} \mathbf{h}_{\tilde{\alpha}}. \quad (3.35)$$

Note that a mapping from rotated BC testing functions to standard RWG functions is necessary [Beghein et al. 2012]. With sophisticated preconditioning techniques, this may change. Each IE has to be discretized appropriately on their own, and the two discretized systems of equations have to be combined in a suitable way. For instance when the Calderón multiplicative preconditioner is employed for the EFIE, which maps the RWG basis onto BC testing functions for the EFIE, the BC-MFIE remains untouched [Cools et al. 2010].

Accurate Discretization Strategies for the Operator of the PEC MFIE

We have a habit in writing articles published in scientific journals to make the work as finished as possible, to cover all the tracks, to not worry about the blind alleys or to describe how you had the wrong idea first, and so on. So there isn't any place to publish, in a dignified manner, what you actually did in order to get to do the work.

— Richard Feynman, *Nobel Lecture*

AN ACCURATE DISCRETIZATION for the operator of the PEC MFIE is an unsolved challenge when the computationally costly barycentric refinement of the mesh shall be avoided. Two approaches to tackle this issue are discussed in this chapter. First, several discretization strategies with an RWG-only basis are compared to mixed-discretization approaches for the MFIE operator. Second, HO expansions are analyzed with regard to the discretization accuracy of the MFIE operator. As a first step toward an accurate discretization of the PEC MFIE operator, a CSIE based on a mixed RWG/BC discretization and an RWG-only CSIE discretization scheme are presented in Section 4.1. The work related to the RWG-based CSIE in this section and related subsequent numerical investigations are based on [Kornprobst and Eibert 2017c, 2017a, 2017b, 2018a, 2018c, 2018f]. Section 4.2 introduces an accurate weak-form (WF) LO discretization scheme for the RWG-discretized identity operator; the results therewithin are partially based on [Kornprobst and Eibert 2018e]. In Section 4.3, we incorporate the WF identity operator discretization into the RWG-MFIE. This section and subsequent results are based on [Kornprobst and Eibert 2018d, 2018f, 2018e, 2019; Kornprobst et al. 2019a]. Section 4.4 presents scattering results for the IEs a LO RWG basis, demonstrating that the proposed discretization of the magnetic-currents radiation operator inside the CSIE and the WF-MFIE show a superior accuracy (in particular for structures with sharp edges) as compared to the classical MFIE—on a level close to the BC-tested MFIE and the standard EFIE. Section 4.5 focuses on electrically larger scattering and radiation scenarios suffering from interior resonances, where we find that the CSIE and the WF-CFIE exhibit an iterative solver convergence faster than the EFIE (for the CSIE) or comparable to the standard CFIE (for the WF CFIE) as well as a greatly improved accuracy. The interior resonance problem is also well under control. In

Section 4.6, the tradeoff between accuracy and conditioning when choosing the CF/CS combination factor is investigated for several scenarios. The work is extended to hierarchical HO expansion functions for both the CSIE and the WF-MFIE in Subsection 4.7.2. The results therewithin are based in part upon [Kornprobst et al. 2021c; Kornprobst and Eibert 2018b, 2019, 2022].

4.1 A Combined Source Integral Equation with a Weak-Form Relation of Electric and Magnetic Currents

The analytical description of the CSIE has already been introduced in Subsection 2.5.2 on p. 17. For a better understanding, we briefly repeat the most important aspects here and conflate the CSIE with the discretization procedure discussed in Subsection 3.1.1 on p. 31. The CSIE [see (2.73)]

$$\mathbf{e}^v \times \mathbf{n} = \mathcal{T} \mathbf{j}_{CS} + \frac{\chi_{CS} - 1}{\chi_{CS}} \left[\frac{1}{2} \mathcal{I} - \mathcal{K} \right] \mathbf{n} \times \mathbf{j}_{CS}. \quad (4.1)$$

combines the MFIE and EFIE operators, which implies that the CSIE should be interior-resonance free just as the CFIE.

Even though the discretization and the resulting systems of equations are fairly similar, the CSIE has not attracted much attention. While many (more or less sound) discretization schemes have been proposed for the MFIE which are applicable to the CFIE—Subsection 3.2.2 was particularly focused on triangular meshes with RWG basis functions—, one has to search in detail to find any literature at all concerning the CSIE. Treating dielectric scattering with a mixed-discretization CSIE has been proposed by Ylä-Oijala et al. [2012a] and Ylä-Oijala et al. [2013a], but no related literature exists about the PEC CSIE. For the method of auxiliary sources (i.e., working with displaced sources instead of continuous sources on s), the CSIE has been investigated by J. Lee and Nam [2005]. A pure RWG discretization has been reported by Glisson [1992] and Ismatullah and Eibert [2009b] for the similar IBC .

The task of discretizing the CSIE features the same challenge as the CFIE: The alignment of vectorial sources and vectorial fields—i.e., the alignment of basis and testing functions in three-dimensional space, in particular for self-coupling terms—is to some extent required for a well-conditioned system matrix. However, it is not trivially achievable for the combination of the \mathcal{T} and $[\mathcal{I}/2 - \mathcal{K}]$ operators in particular when BC functions shall be avoided. In the case of the CSIE, the necessary $\mathbf{n} \times$ rotation is applied to the current unknowns instead of the evaluated fields.

Since the standard RWG-tested EFIE is accurate, we want to retain this quality. This determines the basis functions for the electric surface current densities to be

RWG functions in $\mathbf{H}^{-1/2}(\text{div}_s, s)$

$$\mathbf{j}_{\text{CS}} = \sum_{n=1}^N [i_{\text{CS}}]_n \boldsymbol{\beta}_n \quad (4.2)$$

and the testing functions for the \mathcal{T} operator to be rotated RWGs $\boldsymbol{\alpha}$ in the dual space $\mathbf{H}^{-1/2}(\text{curl}_s, s)$ of the operator. Just as for the standard EFIE with Love currents, we obtain the matrix $\mathcal{T}_{\boldsymbol{\alpha}, \boldsymbol{\beta}}$. The testing functions for the radiation operator $[\mathcal{L}/2 - \mathcal{K}]$ of the magnetic currents are then set to be rotated RWGs.

4.1.1 Brief Revision of Discretization Approaches

The more challenging part is to choose suitable basis functions for the magnetic surface current densities. Both considered operators (the ones of the PEC EFIE and the MFIE) constitute mappings from $\mathbf{H}^{-1/2}(\text{div}_s, s)$ to $\mathbf{H}^{-1/2}(\text{div}_s, s)$. The \mathcal{T} operator has been tested in its dual space accordingly. For the MFIE, dual-space testing might be achievable with a div-conforming RWG or BC basis. However, the discretization of the MFIE operator is not the only demanding task. The CS condition

$$\mathbf{m}_{\text{CS}} = \frac{1 - \chi_{\text{CS}}}{\chi_{\text{CS}}} \mathbf{n} \times \mathbf{j}_{\text{CS}}, \quad (4.3)$$

see (2.72), has to be looked at simultaneously. Choosing div-conforming RWG basis functions for the expansion of \mathbf{j}_{CS} poses restrictions on the discretization of the MFIE operator and simultaneously on the discretization of the magnetic surface current densities. In the literature, several ways to discretize the magnetic surface currents have been reported for comparable scenarios in the combination with RWGs for \mathbf{j} . These are reviewed in the following.

We call (4.3) a *strong-form* condition, since a fixed relation between the two current types is enforced point-wise everywhere on s . Implementing such a strong-form rotation of div-conforming expansion function leads to a curl-conforming basis, which originates quite naturally from (4.3), when the \mathbf{n} -rotation yields $\boldsymbol{\alpha}$ functions for \mathbf{m}_{CS} according to

$$\mathbf{m}_{\text{CS}} = \sum_{n=1}^N [\mathbf{v}_{\text{CS}}]_n \boldsymbol{\alpha}_n = \frac{\chi_{\text{CS}} - 1}{\chi_{\text{CS}}} \sum_{n=1}^N [i_{\text{CS}}]_n \boldsymbol{\beta}_n \times \mathbf{n} = \frac{1 - \chi_{\text{CS}}}{\chi_{\text{CS}}} \mathbf{n} \times \mathbf{j}_{\text{CS}} \quad (4.4)$$

or just for the n th basis function coefficient

$$[\mathbf{v}_{\text{CS}}]_n = \frac{\chi_{\text{CS}} - 1}{\chi_{\text{CS}}} [i_{\text{CS}}]_n \quad \text{for } n \in \{1, 2, \dots, N\}. \quad (4.5)$$

The whole system of equations then reads

$$\left[\mathbf{T}_{\alpha,\beta} + \frac{1 - \chi_{\text{CS}}}{\chi_{\text{CS}}} \left(\frac{1}{2} \mathbf{G}_{\alpha,\alpha} - \mathbf{K}_{\alpha,\alpha} \right) \right] \mathbf{i} = \mathbf{e}_{\alpha}. \quad (4.6)$$

Since $\mathbf{G}_{\beta,\beta} = \mathbf{G}_{\alpha,\alpha}$, the magnetic-currents part of this CSIE is well-conditioned. However, this part of the equation may suffer from the same inaccuracy problems as the standard RWG-MFIE.

While such a discretization has never been published for scattering scenarios to the author's knowledge,¹ Rao and Wilton [1990] have employed curl-conforming rotated RWGs for the expansion of the magnetic currents for dielectric scattering; and Glisson [1992] has done the same for an IBC, which is closely related to the CS condition. As already discussed in Subsection 3.2.2, this leads to problems regarding the integration of hypersingular line charges prohibiting the evaluation of the magnetic field on s —which is required for the dielectric scattering scenario as discussed by Rao and Wilton [1990]. The solution in their work is to distribute the line charge over some adjacent area as “charge patches.” Such tricks do not seem appropriate for a discretization procedure which should converge to the true solution—and also not for the div-conforming nature of surface current densities.

The alternative is found in a *weak-form* (WF) rotation of the basis functions. Just as for the IEs themselves, a variational approach is followed and leads, in some sense, to the desired best approximation of the orthogonal current flow within a given basis. In [Ylä-Oijala et al. 2012a; Ylä-Oijala et al. 2013a], the only reported discretization of a CSIE for dielectric objects on a triangular mesh (a mixed RWG/BC basis for the electric/magnetic currents) is found. A similar approach has been reported for the expansion of the magnetic currents with div-conforming BC functions inside the closely related IBC [Ylä-Oijala et al. 2010; W. D. Li et al. 2012; Yan and Jin 2013; Dély et al. 2017]. In this thesis, the CSIE for PEC scattering is analyzed, which has not been reported so far.

Both currents are modeled by their respective basis functions as

$$\mathbf{j}_{\text{CS}} = \sum_{n=1}^N [i_{\text{CS}}]_n \boldsymbol{\beta}_n, \quad \mathbf{m}_{\text{CS}} = \sum_{n=1}^N [v_{\text{CS}}]_n \tilde{\boldsymbol{\beta}}_n, \quad (4.7)$$

with the RWG basis $\boldsymbol{\beta}$ for the electric currents and the BC basis $\tilde{\boldsymbol{\beta}}$ for the magnetic

1. Eibert et al. [2016] have reported such a CS implementation for inverse source problems, where the very NF evaluation of reconstructed sources is not as decisive as the more distant NF or the FF.

currents, and (4.3) is tested appropriately by rotated RWGs as

$$\sum_{n=1}^N [v_{\text{CS}}]_n \langle \boldsymbol{\alpha}_m, \tilde{\boldsymbol{\beta}}_n \rangle = \frac{1 - \chi_{\text{CS}}}{\chi_{\text{CS}}} \sum_{n=1}^N [i_{\text{CS}}]_n \langle \boldsymbol{\alpha}_m, \mathbf{n} \times \boldsymbol{\beta}_n \rangle \quad \text{for } m \in \{1, 2, \dots, M\}. \quad (4.8)$$

Written as a matrix equation, we have

$$\mathbf{G}_{\boldsymbol{\alpha}, \tilde{\boldsymbol{\beta}}} \mathbf{v} = \frac{\chi_{\text{CS}} - 1}{\chi_{\text{CS}}} \mathbf{G}_{\boldsymbol{\alpha}, \boldsymbol{\alpha}} \mathbf{i} = \frac{\chi_{\text{CS}} - 1}{\chi_{\text{CS}}} \mathbf{G}_{\boldsymbol{\beta}, \boldsymbol{\beta}} \mathbf{i}. \quad (4.9)$$

The well-conditioned mixed Gram matrix $\mathbf{G}_{\boldsymbol{\alpha}, \tilde{\boldsymbol{\beta}}}$ has to be inverted to attain the magnetic current coefficients from the electric current ones. Then, the CS relation is enforced globally in a variational sense. Overall, the system of equations

$$\left[\mathbf{T}_{\boldsymbol{\alpha}, \boldsymbol{\beta}} + \frac{1 - \chi_{\text{CS}}}{\chi_{\text{CS}}} \left(\frac{1}{2} \mathbf{G}_{\boldsymbol{\alpha}, \tilde{\boldsymbol{\beta}}} - \mathbf{K}_{\boldsymbol{\alpha}, \tilde{\boldsymbol{\beta}}} \right) \mathbf{G}_{\boldsymbol{\alpha}, \tilde{\boldsymbol{\beta}}}^{-1} \mathbf{G}_{\boldsymbol{\alpha}, \boldsymbol{\alpha}} \right] \mathbf{i} = \mathbf{e}_{\boldsymbol{\alpha}} \quad (4.10)$$

is obtained. For the implementation, the Julia package BEAST by Cools et al. [2021] is employed. Interestingly, the RWG Gram matrix $\mathbf{G}_{\boldsymbol{\alpha}, \boldsymbol{\alpha}} = \mathbf{G}_{\boldsymbol{\beta}, \boldsymbol{\beta}}$ appears in the discretization of the identity, when the electric current unknowns in (4.10) are considered. Since the magnetic currents are expanded with a BC basis, this equation is referenced as BC-CSIE in the following. For the case of $\chi_{\text{CS}} = 0$, considering only the \mathbf{I} and \mathbf{K} operators, we have

$$\left(\frac{1}{2} \mathbf{G}_{\boldsymbol{\alpha}, \tilde{\boldsymbol{\beta}}} - \mathbf{K}_{\boldsymbol{\alpha}, \tilde{\boldsymbol{\beta}}} \right) \mathbf{v} = \mathbf{e}_{\boldsymbol{\alpha}}. \quad (4.11)$$

This EFIE with only magnetic currents (expanded by BC functions) is referred to as M-EFIE. It is similar to the BC-MFIE with interchanged basis and testing functions.

Admittedly, the discretization of the \mathbf{I} and \mathbf{K} operators is appropriate. This subsequently results in a well-conditioned and well-tested system matrix; however, the resulting surface current densities are not really smooth, at least visually, cf. Figs. 7 and 8 in [Dély et al. 2017]. Furthermore, this approach suffers from the increased computational effort of BC functions and cannot simply be extended to HO schemes.

4.1.2 Pure Rao-Wilton-Glisson Discretization of the Combined Source Integral Equation

In order to avoid the computationally costly BC functions, we work with RWG basis functions only for the discretization of both electric and magnetic surface current densities. The work of Ismatullah and Eibert [2009b] even precedes the WF discretization approaches with IBCs mentioned earlier. Similar approaches for IBC SIEs with an RWG basis have been reported by Stupfel [2015] and Ylä-Oijala et al. [2018]. Just as for the mixed basis case, these formulations implement the (IBC instead of CS) side constraint (SC) in a WF. Both types of equivalent surface current densities are expanded with RWG basis functions according to (3.1) as

$$\mathbf{j}_{\text{CS}} = \sum_{n=1}^N [i_{\text{CS}}]_n \boldsymbol{\beta}_n, \quad \mathbf{m}_{\text{CS}} = \sum_{n=1}^N [v_{\text{CS}}]_n \boldsymbol{\beta}_n. \quad (4.12)$$

Bearing in mind the issues of a curl-conforming basis for (magnetic) currents, we do not employ div-conforming functions directly for the discretization of the CS condition (4.3) but the WF relation is obtained by inserting the basis function expansion into (4.3). We test the equation

$$\sum_{n=1}^N [v]_n \boldsymbol{\beta}_n = \frac{1 - \chi_{\text{CS}}}{\chi_{\text{CS}}} \sum_{n=1}^N [i]_n \mathbf{n} \times \boldsymbol{\beta}_n. \quad (4.13)$$

with RWG functions

$$\sum_{n=1}^N [v]_n \langle \boldsymbol{\beta}_m, \boldsymbol{\beta}_n \rangle = \frac{1 - \chi_{\text{CS}}}{\chi_{\text{CS}}} \sum_{n=1}^N [i]_n \langle \boldsymbol{\beta}_m, \mathbf{n} \times \boldsymbol{\beta}_n \rangle \quad \text{for } m \in \{1, 2, \dots, N\}, \quad (4.14)$$

which yields a WF relation between the magnetic and electric current unknowns via the RWG Gram matrices as

$$\mathbf{G}_{\boldsymbol{\beta}, \boldsymbol{\beta}} \mathbf{v} = \frac{\chi_{\text{CS}} - 1}{\chi_{\text{CS}}} \mathbf{G}_{\boldsymbol{\alpha}, \boldsymbol{\beta}} \mathbf{i}, \quad (4.15)$$

where $\mathbf{G}_{\boldsymbol{\alpha}, \boldsymbol{\beta}} = -\mathbf{G}_{\boldsymbol{\beta}, \boldsymbol{\alpha}}$ was used. This WF CS condition finds a global approximation of a 90° rotation for the magnetic current vector within the RWG basis. Considering only one exemplary element of the electric current vector—setting one specific element in the unknowns vector to one and all others to zero—all magnetic current coefficients may be non-zero. The resulting current distribution of such a WF rotation of a single electric current function is depicted in Fig. 4.1. It is observed that the orthogonal current flow is modeled well inside the original pair of triangles. In addition, the current is distributed over neighboring triangles.

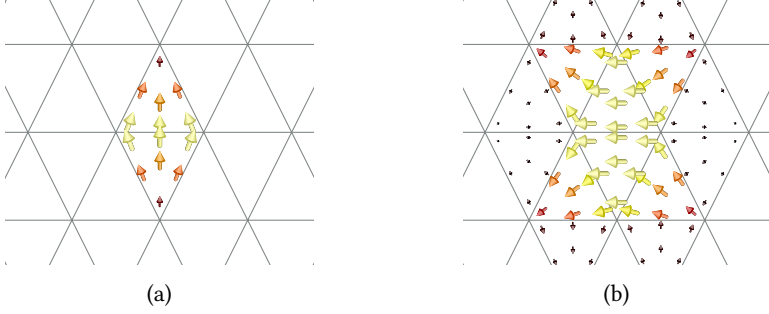


Fig. 4.1: Illustration of the WF rotation. (a) Original electric current RWG basis i with only one entry. (b) Superposition of magnetic current RWG basis functions for a WF rotation $\mathbf{G}_{\beta,\beta}^{-1} \mathbf{G}_{\alpha,\beta} i$ © 2018 IEEE [Kornprobst and Eibert 2018e].

With this WF CS condition, the EFIE (2.73) is discretized as the linear system of equations

$$\mathbf{T}_{\alpha,\beta} i + \left[\frac{1}{2} \mathbf{G}_{\alpha,\beta} - \mathbf{K}_{\alpha,\beta} \right] \mathbf{v} = \mathbf{e}_{\alpha}. \quad (4.16)$$

Augmenting the EFIE with the CS condition as a SC yields [Kornprobst and Eibert 2018a]

$$\begin{bmatrix} \mathbf{T}_{\alpha,\beta} & \left(\frac{1}{2} \mathbf{G}_{\alpha,\beta} - \mathbf{K}_{\alpha,\beta} \right) \\ (\chi_{\text{CS}} - 1) \mathbf{G}_{\alpha,\beta} & \chi_{\text{CS}} \mathbf{G}_{\beta,\beta} \end{bmatrix} \begin{bmatrix} i \\ \mathbf{v} \end{bmatrix} = \begin{bmatrix} \mathbf{e}_{\alpha} \\ \mathbf{0} \end{bmatrix}. \quad (4.17)$$

Here, the additional CS equations are solved as a part of the overall system of equations. This leads to a sub-optimal conditioning of the overall system matrix since it is difficult to optimally scale the CS SC [Kornprobst and Eibert 2018c]. A better way is to explicitly invert the well-conditioned RWG Gram matrix to get rid of the magnetic current unknowns, which leads to [Kornprobst and Eibert 2018c]

$$\left[\mathbf{T}_{\alpha,\beta} + \frac{1 - \chi_{\text{CS}}}{\chi_{\text{CS}}} \left(\frac{1}{2} \mathbf{G}_{\alpha,\beta} - \mathbf{K}_{\alpha,\beta} \right) \mathbf{G}_{\beta,\beta}^{-1} \mathbf{G}_{\alpha,\beta} \right] i = \mathbf{e}_{\alpha}. \quad (4.18)$$

If we compare this WF CSIE with the strong-form approach pursued in (4.6), it is noticeable that the discretization of the MFIE operator is significantly different. In the strong-form approach, the identity operator is discretized to an RWG Gram matrix $\mathbf{G}_{\beta,\beta}$, which is well-conditioned but is known to cause the inaccuracies of the RWG-MFIE. In the WF approach, the RWG- $n \times$ RWG Gram matrix $\mathbf{G}_{\alpha,\beta}$ appears instead, which is not ideal either. This matrix is degenerate with $\dim \ker \mathbf{G}_{\alpha,\beta} \approx N/3$, and it exhibits zeros on the main diagonal. The complete discretization of the \mathbf{I} operator consisting of the matrix multiplication $\mathbf{G}_{\alpha,\beta} \mathbf{G}_{\beta,\beta}^{-1} \mathbf{G}_{\alpha,\beta}$ is typically

diagonally dominant though. Due to the non-trivial null space of the Gram matrix $\mathbf{G}_{\alpha,\beta}$, the CSIE relies on the EFIE operator part of the system matrix and weightings χ close to 0 are not feasible.

The WF discretization of the CS condition, see Fig. 4.1 for a visualization, helps to cope with the strong singularity of the identity operator, which was identified as one of the root causes of the MFIE problems in literature [Davis and Warnick 2004; Ergül and Gürel 2009; Yan et al. 2011b]. In conjunction with the correct dual-space testing of the electric field, this proposed CSIE provides an accuracy similar to the standard EFIE: to be exact, an accurate discretization but with an improved conditioning and without the interior resonance problem.

4.1.3 Comparison of the CSIE Variants

For detailed numerical results, we refer to Section 4.4 and Section 4.5. Here, we briefly analyze the differences of the “CS with SC” version (4.17) and the version with “explicit inversion of the CS condition” (4.18); both for a weighting $\chi_{CS} = 0.5$. We consider scattering from a PEC sphere with 1 m diameter at the frequencies 200 MHz—below any resonance—and 371.8 MHz—hitting the second interior resonance. The frequency-normalized radii kr of the sphere are 2.096 and 3.896. The mesh of the sphere exhibits $N = 999$ RWG functions and an average triangle edge length $h = 0.104$ m, i.e., 0.07λ and 0.129λ . The singular value (SV) spectra of the CSIE system matrices are compared to the standard MFIE, EFIE, and CFIE in Fig. 4.2 at both considered frequencies. At both frequencies, we observe some well-known facts. The EFIE has a clear separation of larger and smaller SVs, which is more pronounced at lower frequencies, while the MFIE does not experience such an effect and the CFIE is mildly affected by the EFIE. At the interior resonance frequency in Fig. 4.2(b), the last SV of the MFIE and EFIE drop to almost zero—their respective condition numbers are 167.8 and 1692.4. The CFIE maintains an excellent condition number of 4.6. Both CSIE versions do not offer a condition number as low as the CFIE, but the SV distribution is more favorable than for the EFIE (i.e., mostly larger SVs) and the drop at the last SV is effectively avoided with condition numbers 27.3 for the CSIE with explicit inversion of the CS constraint and 29.0 for the CSIE with the SC. Apart from the slightly better condition number, the CSIE with the explicit inversion of the CS condition exhibits only half the number of unknowns and a potentially beneficial distribution of the SVs (possibly also a beneficial distribution of the eigenvalues in the complex plane). When solving the equation with an iterative solver such as the generalized minimum residual method (GMRES) [Saad and Schultz 1986], this CSIE hence converges even faster than indicated by the only slightly lower condition number [Kornprobst and Eibert 2018c]. Figure 4.3 shows the iterative solver convergence to a stopping threshold of 10^{-5} for a plane wave scattered by the afore-mentioned 1-m diameter sphere. The CSIE with explicit

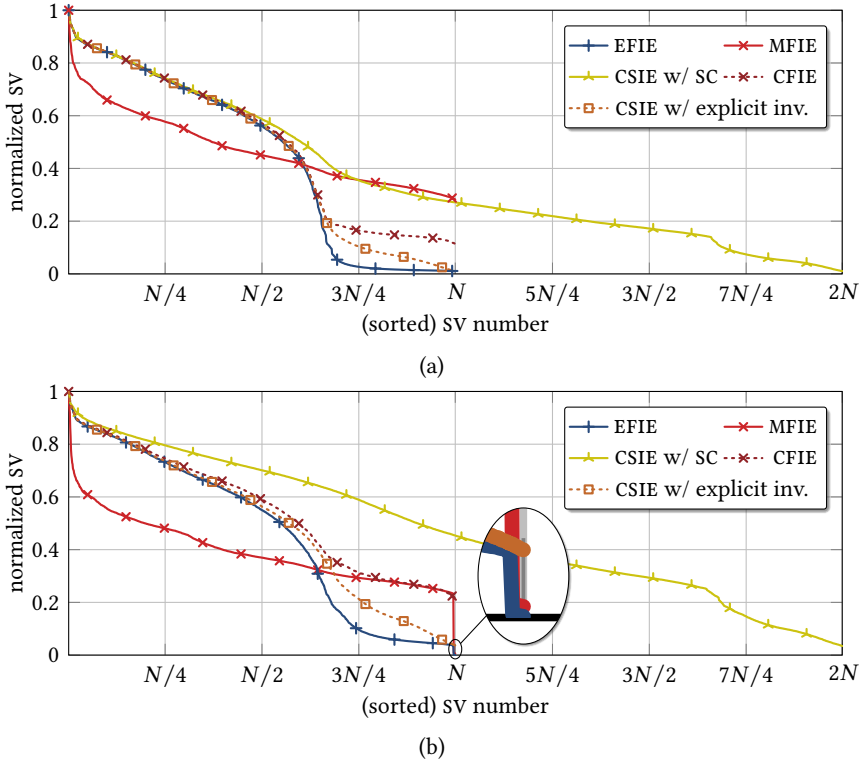


Fig. 4.2: The SV spectra of scattering system matrices of a PEC sphere. (a) $kr = 2.096$. (b) $kr = 3.896$.

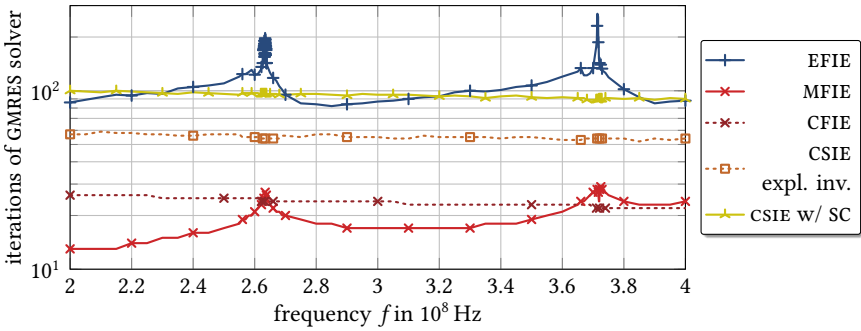


Fig. 4.3: Iterative solver convergence of the CSIE versions over frequency for the 1-m diameter PEC sphere.

inversion of the CS condition converges within about 55 iterations while the CSIE with SC takes between 100 and 90. The CSIE solutions are indistinguishable and the accuracy of both versions is comparable to the EFIE. Due to its advantages, we only consider the CSIE (4.18) with explicit inversion of the CS condition hereafter.

4.1.4 Intermission: On the RWG Gram Matrix Inversion

What was skipped in the above discussion is *how* the Gram matrix is explicitly inverted. For each matrix multiplication with $\mathbf{G}_{\beta,\beta}^{-1}$, a nested conjugate gradient method (CG) solver [Hestenes and Stiefel 1952] with a termination threshold of 10^{-7} was used, which is two orders of magnitude lower than the IE solver threshold for the results presented in Fig. 4.3. This intermediate solution is calculated extremely fast since the RWG Gram matrix is sparse with only $5N$ entries and rather well-conditioned. Kornprobst et al. [2019a] have compared the straight-forward iterative inversion by the CG to a diagonally-preconditioned CG solution and to one with an approximate inverse (AI) preconditioner.

The diagonally preconditioned Gram matrix

$$\mathbf{G}_{\beta,\beta}^{\text{diag}} = \text{diag}(\mathbf{G}_{\beta,\beta})^{-1} \mathbf{G}_{\beta,\beta}. \quad (4.19)$$

is evaluated very efficiently. All off-diagonal matrix entries are already divided by the respective diagonal entry when stored. Hence, no divisions are necessary during the solution and only N multiplications with the diagonal entries are required after the iterative solution—while these N multiplications are even saved during the iterative solution since the preconditioned matrix has ones on its main diagonal.

The AI is based on the “monopolar” RWG representation, i.e., splitting all RWG interactions in half by considering single triangles only. This introduces an intermediate step when calculating the Gram matrix. The Gram matrix block-diagonal is set up triangle-wise as

$$\tilde{\mathbf{G}}_{\beta,\beta} = \begin{bmatrix} \mathbf{G}_1 & \cdots & \mathbf{0} & \cdots & \cdots \\ \vdots & \ddots & \mathbf{0} & \cdots & \cdots \\ \mathbf{0} & \mathbf{0} & \mathbf{G}_i & \mathbf{0} & \cdots \\ \vdots & \vdots & \mathbf{0} & \ddots & \cdots \\ \vdots & \vdots & \vdots & \vdots & \ddots \end{bmatrix}, \quad (4.20)$$

where \mathbf{G}_i is the 3×3 monopolar RWG interaction matrix on the i th triangle. The standard RWG Gram matrix is calculated as

$$\mathbf{G}_{\beta,\beta} = \mathbf{M}^T \tilde{\mathbf{G}}_{\beta,\beta} \mathbf{M}, \quad (4.21)$$

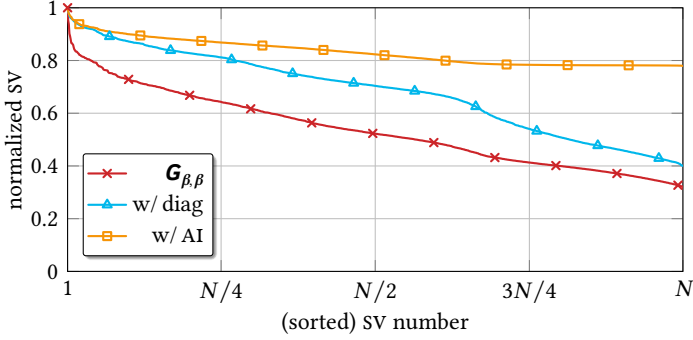


Fig. 4.4: Spectrum of the (potentially preconditioned) RWG Gram matrix for the 1-m diameter sphere with $N = 999$.

where $\mathbf{M} \in \mathbb{R}^{2N \times N}$ is a mapping matrix, which contains a single entry with magnitude one, value ± 1 , in each of the N rows. The pseudo-inverse of \mathbf{M} is easily calculated as $\mathbf{M}^+ = 1/2 \mathbf{M}^T$. The inverse of the block matrix $\tilde{\mathbf{G}}_{\beta,\beta}$ is obtained by inverting all sub-matrices \mathbf{G}_i on the main diagonal, which is feasible in closed form. Unfortunately, the matrix inversion theorem $(\mathbf{A}\mathbf{B})^{-1} = \mathbf{B}^{-1}\mathbf{A}^{-1}$ only holds true for full-rank matrices—and \mathbf{M} is tall and thus singular. Hence, the multiplication of the pseudo-inverses according to

$$\mathbf{G}_{\beta,\beta}^{\text{AI}} = \frac{1}{4} \mathbf{M}^T \tilde{\mathbf{G}}_{\beta,\beta}^{-1} \mathbf{M}, \quad (4.22)$$

can only serve as an AI. This AI has the same number of entries $5N$ as the RWG Gram matrix. Using it as a preconditioner doubles the computational cost per MVP.

The inversion of a Gram matrix is frequency-independent. Hence, we can look at the preconditioners for some objects in a general manner. First, the spectrum of the three system matrices ($\mathbf{G}_{\beta,\beta}$ and the two preconditioned variants) is shown in Fig. 4.4 for the previously considered sphere with $N = 999$. Clearly, the diagonal preconditioner works well; and the AI works even better.

How does this translate into praxis? Is the additional effort worth it? The iterative solver performance for two scenarios is analyzed in Tab. 4.1 regarding the efficiency of the preconditioners. The analysis is based on condition numbers, number of iterations to convergence for a CG solver with residual r_{th} (given is an average number for hundreds of random right-hand sides), and the norm of the residual error vector, i.e., $\|r\|_2 = \|\mathbf{x}^{\text{CG}} - \boldsymbol{\xi}\|_2$, with the CG solution \mathbf{x}^{CG} and the real solution $\boldsymbol{\xi}$. The considered scenarios are the previously mentioned sphere and a sharp wedge with an opening angle of 3° , whose Gram matrix shows a larger condition number.

Tab. 4.1: Analysis of the CG iterative solver behavior for inverting (preconditioned) RWG Gram matrices for different meshes.

(a) The 999 unknowns sphere.

Matrix $\mathbf{A} =$	$\text{cond}(\mathbf{A})$	its. $r_{\text{th}} = 10^{-12}$	avg. $\ \mathbf{r}\ _2$
$\mathbf{G}_{\beta,\beta}$	3.13	12	$1.8 \cdot 10^{-11}$
$\mathbf{G}_{\beta,\beta}^{\text{diag}}$	2.5	10	$4.7 \cdot 10^{-11}$
$\mathbf{G}_{\beta,\beta}^{\text{AI}} \mathbf{G}_{\beta,\beta}$	1.28	6	$2.5 \cdot 10^{-12}$

(b) A sharp wedge with 1284 unknowns.

Matrix $\mathbf{A} =$	$\text{cond}(\mathbf{A})$	its. $r_{\text{th}} = 10^{-10}$	avg. $\ \mathbf{r}\ _2$
$\mathbf{G}_{\beta,\beta}$	68.4	33	$5.7 \cdot 10^{-9}$
$\mathbf{G}_{\beta,\beta}^{\text{diag}}$	31.5	27	$5.8 \cdot 10^{-8}$
$\mathbf{G}_{\beta,\beta}^{\text{AI}} \mathbf{G}_{\beta,\beta}$	50.9	16	$1.4 \cdot 10^{-9}$

The accuracies of the three preconditioners are similar. To be on the safe side, it is advised to choose the CG termination threshold below the iterative solver threshold of the whole system, e.g., by two orders of magnitude. Otherwise, the insufficient accuracy of the repeatedly calculated CS solutions may introduce noise and prevent the main iterative solver to converge. The effect of the diagonal preconditioner is minor but consistent. Hence, it is worth being employed since it does not increase the computational effort. The AI is cutting the required number of iterations approximately in half. However, this is offset by doubling the computational effort per preconditioned MVP. As a result, it is not worth the extra effort.

Güler et al. [2018] have found that the inversion of a sparse Gram matrix with a direct solver—by lower-upper or Cholesky decompositions—suffers from a complexity larger than $\mathcal{O}(N \log N)$; making it unattractive to precompute the inverse. On a related note, it is known that inverses of sparse matrices can unfortunately lose the sparsity property, which has for instance been studied by Wiedenmann [2015] with regard to optimized direct solvers for sparse matrices (employed for preconditioners based on a lower-upper factorization of a thinned-out system matrix). Overall, direct solvers for the Gram matrix inverse computation seem to increase the effort disproportionately. Hence, the Gram matrix inverse is calculated with a diagonally preconditioned iterative CG solver when needed in this work.

4.2 Accurate Identity Operator Discretization: A Basis Transformation Scheme

The CSIE integrates the EFIE and MFIE operators into one single IE. In the following, we focus on the MFIE alone and discuss how the insights gained from the pure RWG CSIE can be transferred to the MFIE. The inaccuracy of the RWG-discretized MFIE operator can be seen as separated in the discretization of the \mathbf{I} and \mathbf{K} operators. The correct handling of both is crucially important at low frequencies. At HFs, it is well-known that the dual-space testing of these operators is not the most decisive factor but how the high spectral content of the \mathbf{I} is taken care of. The accurate WF CSIE gives the motivation to develop a similar discretization scheme for the standard MFIE. The starting point is evidently the identity operator.

4.2.1 Discretization Approach

From an IE operator point of view, the strong form CS condition as well as the identity operator, are highly singular operators. This becomes obvious by writing the identity operator with a Dirac delta integral kernel as done in (2.44). The high spectral content of these operators requires careful discretization to obtain an isotropically averaging low-pass effect [Davis and Warnick 2004; Ergül and Gürel 2009; Yan et al. 2011b].

The adaptation of the WF CS condition inside the discretization of the standard MFIE appears to be possible only indirectly since it approximates a 90° vector rotation instead of an identity. We introduce the two fictitious electric surface current distributions $\hat{\mathbf{j}}$ and $\tilde{\mathbf{j}}$ and perform the 90°-rotation twice as

$$\hat{\mathbf{j}} = \mathbf{n} \times \tilde{\mathbf{j}} = \mathbf{n} \times (\mathbf{j} \times \mathbf{n}) = \mathbf{j} \quad \text{with } \tilde{\mathbf{j}} = \mathbf{j} \times \mathbf{n}. \quad (4.23)$$

Overall, $\hat{\mathbf{j}}$ reproduces the original \mathbf{j} and $\tilde{\mathbf{j}}$ is a 90°-rotated intermediate version of the current—very similar to the CS rotation.

It is possible to discretize both of these strong-form rotations just as the WF CS condition, yielding the two linear systems of equations [see (4.12)–(4.15)]

$$\mathbf{G}_{\beta,\beta} \hat{\mathbf{i}} = -\mathbf{G}_{\alpha,\beta} \tilde{\mathbf{i}}, \quad (4.24)$$

$$\mathbf{G}_{\beta,\beta} \tilde{\mathbf{i}} = \mathbf{G}_{\alpha,\beta} \mathbf{i}. \quad (4.25)$$

Combining both of these systems is summarized in one single matrix \mathbf{R} , leading to

$$\hat{\mathbf{i}} = \mathbf{R} \mathbf{i} = -\mathbf{G}_{\beta,\beta}^{-1} \mathbf{G}_{\alpha,\beta} \mathbf{G}_{\beta,\beta}^{-1} \mathbf{G}_{\alpha,\beta} \mathbf{i}. \quad (4.26)$$

Effectively, this means to perform two subsequent WF vector rotations by 90° and

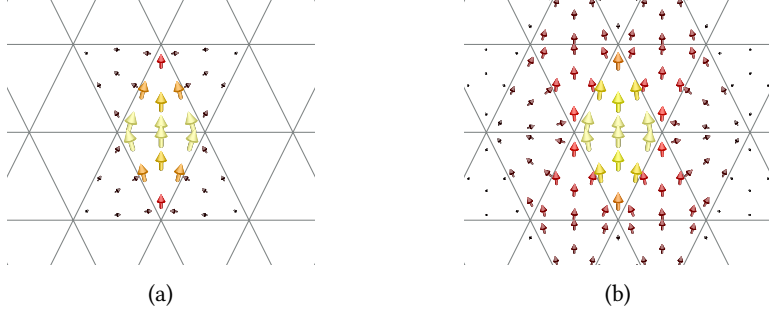


Fig. 4.5: Illustration of the WF discretization scheme for the identity operator © 2018 IEEE [Kornprobst and Eibert 2018e]. (a) One column of the classically discretized Gram matrix $\mathbf{G}_{\beta,\beta}$. (b) One column of the newly introduced Gram matrix including a WF basis transformation $\mathbf{G}_{\beta,\beta}\mathbf{R}$.

an inversion in sign, i.e., multiplication by -1 . As discussed for the CSIE, the matrix $\mathbf{G}_{\alpha,\beta}$ is singular and the matrix \mathbf{R} inherits this non-trivial null space. Hence, such an approach to approximate the identity operator has to fail. It may not be employed solely as a WF identity operator discretization which tries to cope with the high spectral content. In order to fix this issue, we augment the WF representation by the identity matrix $\mathbf{I} \in \mathbb{R}^{N \times N}$. This leads to the WF basis transformation

$$\hat{i} = \mathbf{W}_\gamma i = [\gamma \mathbf{I} + (1 - \gamma) \mathbf{R}] i. \quad (4.27)$$

Beginning with the RWG current coefficients in i , the WF identity scheme is applied to these coefficients (with a weighting $\gamma < 1$). The resulting current coefficients in \hat{i} approximate the ones in i since the identity operator is discretized in a WF. We can multiply the WF basis transformation matrix \mathbf{W}_γ with any operator. For instance, we rewrite the discretized identity operator $\mathbf{G}_{\beta,\beta}$ as the matrix

$$\mathbf{G}_{\beta,\beta} \mathbf{W}_\gamma = \gamma \mathbf{G}_{\beta,\beta} + (\gamma - 1) \mathbf{G}_{\alpha,\beta} \mathbf{G}_{\beta,\beta}^{-1} \mathbf{G}_{\alpha,\beta}. \quad (4.28)$$

When discussing the WF-MFIE, it will become clear that this is the preferable way of how to implement the basis transformation (4.27). For a better understanding of the WF scheme, we visualize one column of $\mathbf{G}_{\beta,\beta}$ in Fig. 4.5(a), where interactions only with adjacent triangles are observed. The vector-valued field associated with one column of $\mathbf{G}_{\beta,\beta} \mathbf{R}$ is shown in Fig. 4.5(b), where the identity is approximated globally by all RWG functions. This may be seen as a kind of regularization to the standard identity operator—similar to changing the Dirac delta integration kernel or similar to employing more spread-out BC functions. Just as for the CSIE, we

have to make sure that the weighting γ is not too small in order to avoid issues induced by the non-trivial $\ker \mathbf{G}_{\alpha,\beta}$.

Instead of relying on the heuristically found addition of an identity matrix, another approach to solve the null space problem of $\mathbf{G}_{\alpha,\beta}$ is to take care of the kernel and co-kernel of $\mathbf{G}_{\alpha,\beta}$ individually. The projection matrix into the image of the $n \times \text{RWG-RWG}$ Gram matrix $\text{im } \mathbf{G}_{\alpha,\beta} = \text{im } \mathbf{G}_{\alpha,\beta}^{\text{H}}$

$$\mathbf{P}_{\alpha,\beta} = \mathbf{G}_{\alpha,\beta}^+ \mathbf{G}_{\alpha,\beta} = \mathbf{G}_{\alpha,\beta} \mathbf{G}_{\alpha,\beta}^+, \quad (4.29)$$

with a generalized inverse $(\cdot)^+$ (for instance the Moore-Penrose pseudo-inverse), is able to isolate the influence of the null space. Then, the contributions in the null space and the image can be treated separately.

We can identify a term in (4.28), which is subtracted from the original Gram matrix, with the same $(\gamma - 1)$ prefactor as the part suffering from the $\mathbf{G}_{\alpha,\beta}$ null space by rewriting it as

$$\mathbf{G}_{\beta,\beta} \mathbf{W}_\gamma = \mathbf{G}_{\beta,\beta} + (\gamma - 1) \mathbf{G}_{\beta,\beta} + (\gamma - 1) \mathbf{G}_{\alpha,\beta} \mathbf{G}_{\beta,\beta}^{-1} \mathbf{G}_{\alpha,\beta} \quad (4.30)$$

and project the image and the inverse image of this subtracted term $(\gamma - 1) \mathbf{G}_{\beta,\beta}$ into $\text{im } \mathbf{G}_{\alpha,\beta}$, leading to

$$\begin{aligned} \mathbf{G}_{\beta,\beta} \mathbf{W}_\gamma^{\text{proj}} &= \mathbf{G}_{\beta,\beta} + (\gamma - 1) \mathbf{P}_{\alpha,\beta} \mathbf{G}_{\beta,\beta} \mathbf{P}_{\alpha,\beta} + (\gamma - 1) \mathbf{G}_{\alpha,\beta} \mathbf{G}_{\beta,\beta}^{-1} \mathbf{G}_{\alpha,\beta} \\ &= \mathbf{G}_{\beta,\beta} + (\gamma - 1) \mathbf{P}_{\alpha,\beta} (\mathbf{G}_{\beta,\beta} + \mathbf{G}_{\alpha,\beta} \mathbf{G}_{\beta,\beta}^{-1} \mathbf{G}_{\alpha,\beta}) \mathbf{P}_{\alpha,\beta}. \end{aligned} \quad (4.31)$$

This has the effect that the correction term trailing $\mathbf{G}_{\beta,\beta}$ only influences the result in the co-image of $\mathbf{G}_{\alpha,\beta}$ if the input vector has contributions in $\text{im } \mathbf{G}_{\alpha,\beta}$, since $\mathbf{G}_{\alpha,\beta} = \mathbf{P}_{\alpha,\beta} \mathbf{G}_{\alpha,\beta} = \mathbf{G}_{\alpha,\beta} \mathbf{P}_{\alpha,\beta}$.

Using solely the matrix $\mathbf{G}_{\alpha,\beta}$ for the discretization of the \mathbf{I} operator does not work since it is singular. Introducing the weighting scheme helps to cope with this issue. There remains an uncertainty for the plain \mathbf{I} -addition method in (4.27) or (4.28) whether it suffers from the singular matrix $\mathbf{G}_{\alpha,\beta}$ in the presence of $\mathbf{G}_{\beta,\beta}$. If this is the case, the projection-based method (4.31) still should provide reliable results. The effect is expected to be more emphasized for $\gamma \rightarrow 0$, where the non-trivial $\ker \mathbf{G}_{\alpha,\beta}$ becomes dominant. However, the computational effort is increased by the additionally required pseudoinverse calculation inside the projection matrix.

4.2.2 Field Synthesis and the Construction of Non-Radiating Currents

Typically, the \mathcal{I} and \mathcal{K} operators appear together in SIEs such as the MFIE. In order to analyze each on its own, a separation of the two operators is of interest. For the identity operator \mathcal{I} , this isolated analysis may be achieved when a suitable formulation for the construction of non-radiating currents is considered [Ergül and Gürel 2009; Yan et al. 2011a]. Here, we assume an incident plane wave in free space and a meshed sphere in free space without any boundary condition or scattering behavior. Hence, the field of the surface sources on s

$$\mathbf{e}^s(\mathbf{r}) = \mathbf{h}^s(\mathbf{r}) = \mathbf{0}, \quad \mathbf{r} \in \nu, \quad (4.32)$$

in the exterior volume ν vanishes. In the interior of s , in the volume ν_i , the surface current densities \mathbf{j} and \mathbf{m} on s synthesize the incident field according to

$$\mathbf{e}^s(\mathbf{r}) = \mathbf{e}^\nu(\mathbf{r}) = \mathbf{e}(\mathbf{r}), \quad \mathbf{r} \in \nu_i, \quad (4.33)$$

$$\mathbf{h}^s(\mathbf{r}) = \mathbf{h}^\nu(\mathbf{r}) = \mathbf{h}(\mathbf{r}), \quad \mathbf{r} \in \nu_i. \quad (4.34)$$

Assuming Love currents according to (2.34) and (2.35), this leads to the set of equations [Ergül and Gürel 2009; Yan et al. 2011a]

$$\begin{bmatrix} \mathcal{I} & 0 \\ 0 & \mathcal{I} \end{bmatrix} \begin{bmatrix} \mathbf{m} \\ \mathbf{j} \end{bmatrix} = \begin{bmatrix} \mathbf{e}^\nu \times \mathbf{n} \\ \mathbf{n} \times \mathbf{h}^\nu \end{bmatrix}, \quad (4.35)$$

which are studied with four different discretizations. First, it is expanded and tested by RWGs as

$$\begin{bmatrix} \mathbf{G}_{\beta,\beta} & \mathbf{0} \\ \mathbf{0} & \mathbf{G}_{\beta,\beta} \end{bmatrix} \begin{bmatrix} \mathbf{v} \\ \mathbf{i} \end{bmatrix} = \begin{bmatrix} \mathbf{e}_\beta \\ -\mathbf{h}_\beta \end{bmatrix} \quad (4.36)$$

This is similar to the discretization of the identity operator in the standard RWG-MFIE. It is also possible to implement the proposed WF identity operator discretization with RWGs, which leads to the system of equations

$$\begin{bmatrix} \mathbf{G}_{\beta,\beta} \mathbf{W}_\gamma & \mathbf{0} \\ \mathbf{0} & \mathbf{G}_{\beta,\beta} \mathbf{W}_\gamma \end{bmatrix} \begin{bmatrix} \mathbf{v} \\ \mathbf{i} \end{bmatrix} = \begin{bmatrix} \mathbf{e}_\beta \\ -\mathbf{h}_\beta \end{bmatrix}. \quad (4.37)$$

Another way is to test the identity with BC functions [Yan et al. 2011a]

$$\begin{bmatrix} \mathbf{G}_{\tilde{\alpha},\beta} & \mathbf{0} \\ \mathbf{0} & \mathbf{G}_{\tilde{\alpha},\beta} \end{bmatrix} \begin{bmatrix} \mathbf{v} \\ \mathbf{i} \end{bmatrix} = \begin{bmatrix} \mathbf{e}_{\tilde{\alpha}} \\ -\mathbf{h}_{\tilde{\alpha}} \end{bmatrix}. \quad (4.38)$$

The same non-radiating surface current densities are described if the incident surface fields are represented by radiation integrals. Then, the identity operator may be eliminated completely, which yields the equation

$$\begin{bmatrix} \mathcal{T} & \mathcal{K} \\ -\mathcal{K} & \mathcal{T} \end{bmatrix} \begin{bmatrix} \mathbf{j} \\ \mathbf{m} \end{bmatrix} = \frac{1}{2} \begin{bmatrix} \mathbf{n} \times \mathbf{e}^v \\ \mathbf{n} \times \mathbf{h}^v \end{bmatrix}. \quad (4.39)$$

These integral operators are discretized with EFIE-alike testing, i.e., rotated RWG testing functions, as [Ergül and Gürel 2009]

$$\begin{bmatrix} \mathcal{T}_{\alpha,\beta} & \mathcal{K}_{\alpha,\beta} \\ -\mathcal{K}_{\alpha,\beta} & \mathcal{T}_{\alpha,\beta} \end{bmatrix} \begin{bmatrix} \mathbf{i} \\ \mathbf{v} \end{bmatrix} = -\frac{1}{2} \begin{bmatrix} \mathbf{e}_\alpha \\ \mathbf{h}_\alpha \end{bmatrix}. \quad (4.40)$$

It is possible to leave the identity as a part of the operator, i.e., accompanying \mathcal{K} with \mathcal{I} . This yields the interior Calderón projector, which inherently has a non-trivial null space. This would foil the objective of separating the influence of integral operators and the identity and of studying the influence of the identity operator separately.

4.2.3 Numerical Results for Field Synthesis

For a numerical analysis, we consider a sphere with 1λ diameter with 1239 RWG electric and magnetic current unknowns each; the average triangle edge length h is about $\lambda/10$. The incident (to synthesize) plane wave exhibits a wave vector $\mathbf{k} = \mathbf{u}_z$, i.e., the unit vector in z -direction, an amplitude $e_0 = 1$ V/m and $\mathbf{p} = \mathbf{u}_x$ polarization. The synthesized electric FF is evaluated for $\|\mathbf{r}\| = 1\lambda$ and, as an error measure, the arithmetically averaged normalized field

$$\epsilon^{\text{FF}} = \text{avg}_{\|\mathbf{r}\|=\lambda} \|\mathbf{e}_{\text{FF}}^s(\mathbf{r})/e_0\| \quad (4.41)$$

is calculated in 1° -steps in the $\vartheta = 90^\circ$ -, $\varphi = 0^\circ$ -, and $\varphi = 90^\circ$ -cuts. This FF should be close to zero, since the equivalent currents are constructed in a way that they are non-radiating—or, more aptly named, Love current sources for interior plane-wave field synthesis.

Hence, the synthesized interior field is of equal importance. It should match the incident plane wave whose fields are recreated by the surface currents on the Huygens surface. For the analysis of the electric field $\mathbf{e}(\mathbf{r})$ with $\mathbf{r} \in \nu_i$, a regular Cartesian grid with a step size $\lambda/25$ in all three directions is chosen for the evaluation. Only field samples for $\|\mathbf{r}\| \leq 0.45\lambda$ are considered in order to avoid the negative influence of the evanescent fields near the reconstruction surface s . The deviation of the synthesized field \mathbf{e}^s with respect to the incident field \mathbf{e}^v is averaged

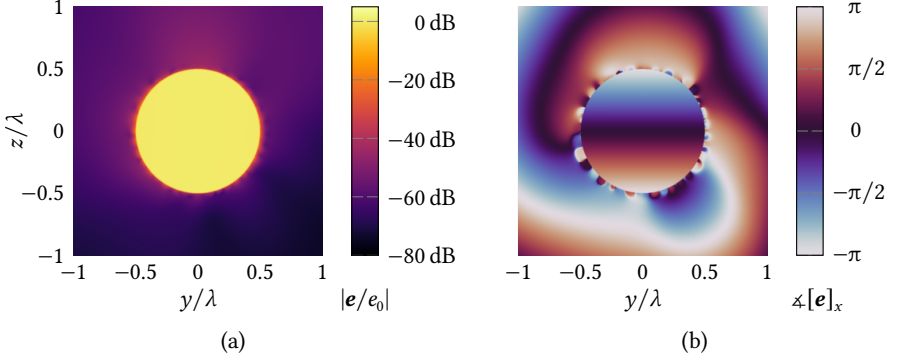


Fig. 4.6: Synthesized plane-wave field with magnitude $e_0 = 1$ V/m inside a sphere with 1λ diameter with the discretized RWG identity operator (4.36). (a) Magnitude of the synthesized electric field \mathbf{e} . (b) Phase of the $[\mathbf{e}]_x$ component of the synthesized electric field.

over all those samples and is given as the interior NF error

$$\epsilon^{\text{NF},i} = \text{avg}_{\|\mathbf{r}\| \in \mathcal{V}_i} (\mathbf{e}(\mathbf{r}) - \mathbf{e}^{\text{V}}(\mathbf{r})) / e_0. \quad (4.42)$$

Before going into the details about the numerical results, the synthesized plane-wave field is shown in Fig. 4.6. Inside the sphere, we see a constant magnitude and the phase distribution of a plane wave in propagation direction; outside, the field values are very low and the phase varies arbitrarily.

The interesting part about the WF discretization scheme for the identity operator is the choice of γ . Hence, the two quantities of interest—the achieved zero-field level in the FF and the field synthesis quality—are shown for different values of γ in Fig. 4.7. We observe that the influence on the supposed zero FF is marginal; that is why Fig. 4.7(a) with a focused ordinate range comprises the FFs of the RWG and WF-RWG discretized \mathcal{I} operator only. The two other discretizations show field values tens of decibels lower. At the same time, the accuracy of the synthesized field is improved by over 10 dB in the best case as seen in Fig. 4.7(b), coming much closer to the BC-tested-identity and integral-operator formulations. For $\gamma \rightarrow 0$, the solution diverges due to the negative influence of the non-trivial $\ker \mathbf{G}_{\alpha,\beta}$ for the WF-RWG formulation. The projection-based WF does not have this diverging behavior. Nevertheless, the error increases in a similar fashion for small weights but is bounded. Except for very small weights ($\gamma < 0.2$), the accuracy with the projection is slightly worse than for the WF scheme without. For both versions, the improvement is best with $\gamma \approx 0.6$.

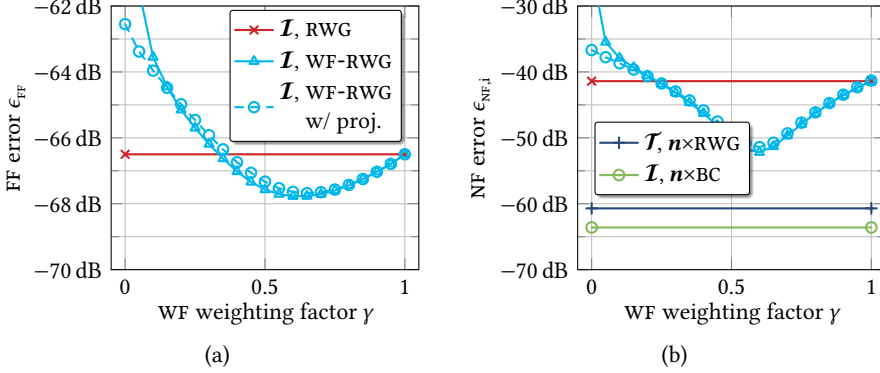


Fig. 4.7: Analysis of the WF weighting factor γ for a 1λ diameter sphere. (a) Averaged FF magnitude of the non-radiating currents. (b) Error of the synthesized electric NF $\text{avg} \|(\mathbf{e}^s - \mathbf{e}^v)/\mathbf{e}_0\|$.

Next, we consider a cube with 1λ edge length and $h \approx \lambda/10$, which features 2232 RWG unknowns for both surface current types. This scenario is a bit different since the incident wave is aligned with the object such that the incident tangential field vanishes on four faces (out of six in total). Unlike the scattering case, the identity operator does not show a worsened behavior for edged objects since no singular current distribution on the edges is to be expected. The analyses are carried out in the same way as before and the results are very similar to the case of the sphere. The interior NF is evaluated only at a distance of larger than 0.05λ to the mesh in Fig. 4.8(a). Again, the best value for γ is observed to be at (slightly above) 0.6.

An additional test case is a sphere with 3.6λ diameter with 14 466 RWG unknowns for each current and again with $h \approx \lambda/10$. The accuracy of the synthesized NF versus the WF weighting factor is analyzed in Fig. 4.8(b). The distance of interior field samples to the mesh is again kept greater than 0.05λ ; however, the sampling density is only $\lambda/10$ in the three Cartesian directions.

The field synthesis accuracy improvements are similar to the first scenario in both other cases. The same holds for the FF, which is not shown in detail. The accuracy numbers for all considered scenarios and all formulations—the WF case with $\gamma = 0.6$ —are given in Tab. 4.2.

We conclude that the projection-based approach has no significant benefit—possibly even a slight disadvantage—for weightings which yield an improved accuracy. At very small values $\gamma < 0.2$, a diverging error is prevented. These values of the weighting factor are, however, not of interest due to the observed large error levels. Overall, the increased computational effort of computing a projection and the involved pseudoinverse instead of only inverting the well-conditioned matrix

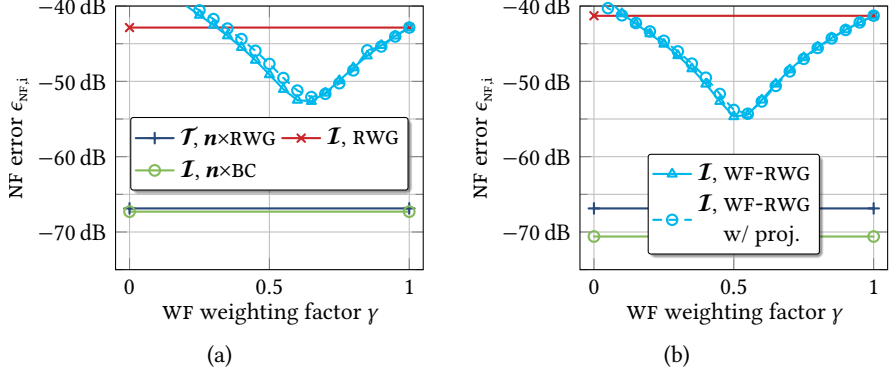


Fig. 4.8: Analysis of the WF weighting factor γ regarding the error of the synthesized electric NF. (a) A cube with 1λ edge length. (b) A sphere with 3.6λ diameter.

Tab. 4.2: Quality of the exterior zero field and interior synthesized plane wave for three scenarios. Both WF discretization schemes with $\gamma = 0.6$.

main diagonal	testing function	\mathcal{I}			\mathcal{T}	
		RWG	WF-RWG	WF proj.	$n \times BC$	$n \times RWG$
1λ sphere	ϵ^{FF}	-66.5 dB	-67.8 dB	-67.6 dB	-95.4 dB	-85.2 dB
	$\epsilon^{NF,i}$	-41.4 dB	-52.2 dB	-52.2 dB	-63.6 dB	-60.7 dB
1λ cube	ϵ^{FF}	-61.8 dB	-64.2 dB	-62.3 dB	-82.3 dB	-82.7 dB
	$\epsilon^{NF,i}$	-42.9 dB	-52.5 dB	-52.2 dB	-67.3 dB	-66.9 dB
3.6λ sphere	ϵ^{FF}	-52.3 dB	-52.9 dB	-52.8 dB	-87.5 dB	-70.4 dB
	$\epsilon^{NF,i}$	-41.3 dB	-52.5 dB	-52.7 dB	-70.6 dB	-66.4 dB

$\mathbf{G}_{\beta,\beta}$ does not seem to be worth the effort. The sparse Gram matrix can easily be inverted iteratively within a few iterations—for instance with the diagonally preconditioned conjugate gradient method [Hestenes and Stiefel 1952; Güler et al. 2018; Kornprobst et al. 2019a]. Hence, only the simpler approach without the projection is employed for the following investigations.

It has to be noted though that neither the standard RWG identity operator discretization nor the improved WF RWG discretization come close to the accuracy of the identity operator tested with the dual BC-function or the field synthesis with radiation operators, which both operate at tens of decibels smaller errors.

4.3 Improved Magnetic Field Integral Equation with Weak-Form Identity Operator Discretization

We have demonstrated in the previous section that a WF basis transformation scheme helps to reduce the discretization error of the identity operator when handled solely with RWG functions since the high spectral content is taken care of. In this section, this insight is incorporated into the MFIE.

4.3.1 The Discretization Schemes

Inspired by the RWG discretization of the CSIE, there are several possibilities of how to integrate the WF basis transformation scheme as proposed in (4.27) into the MFIE. One may follow a similar strategy as for the magnetic current unknowns resulting from the WF CS condition: The matrix \mathbf{W}_γ is employed for the total electric current unknowns, i.e., to the MFIE matrix as a whole. If multiplied from the right just before the electric currents, this leads to

$$\left[\frac{1}{2} \mathbf{G}_{\beta,\beta} + \mathbf{K}_{\beta,\beta} \right] \mathbf{W}_\gamma i = h_\beta. \quad (4.43)$$

This equation is referred to as WF-basis MFIE.

It is also possible to implement a WF-RWG testing scheme. Then, the matrix \mathbf{W}_γ is multiplied from the left as

$$\mathbf{G}_{\beta,\beta} \mathbf{W}_\gamma \mathbf{G}_{\beta,\beta}^{-1} \left[\frac{1}{2} \mathbf{G}_{\beta,\beta} + \mathbf{K}_{\beta,\beta} \right] i = h_\beta. \quad (4.44)$$

This equation is referred to as WF-testing MFIE in the following. In these two cases, the WF scheme is applied to the discretized \mathbf{I} and \mathbf{K} operators. It is not to expect that the WF scheme cures the MFIE LF breakdown since a proper dual-space testing in a sense of curl-conforming testing functions and in a dual-mesh sense would be needed to do so. In particular for HF scenarios, improvements may be observed where the accuracy issues of the MFIE arise mostly from the \mathbf{I} operator.

It is also possible to introduce the basis transformation (4.27) solely for the discretized identity operator of the classical MFIE (3.32)—i.e., the RWG Gram matrix. This matches more the strategy pursued in Section 4.2 than the magnetic-current part of CSIE discretization in Section 4.1. Employing the WF basis transformation to the Gram matrix only as

$$\left[\frac{1}{2} \mathbf{G}_{\beta,\beta} \mathbf{W}_\gamma + \mathbf{K}_{\beta,\beta} \right] i = \left[\frac{\gamma}{4} \mathbf{G}_{\beta,\beta} + \frac{\gamma-1}{4} \mathbf{G}_{\alpha,\beta} \mathbf{G}_{\beta,\beta}^{-1} \mathbf{G}_{\alpha,\beta} + \mathbf{K}_{\beta,\beta} \right] i = h_\beta \quad (4.45)$$

is called WF identity MFIE in the following. If the matrix \mathbf{W}_γ is introduced for



Fig. 4.9: Two models for the analysis of the the WF basis transformation scheme in the RWG-tested MFIE © 2018 IEEE [Kornprobst and Eibert 2018e]. (a) A sphere. (b) A Pyramid.

the testing functions of the Gram matrix only, this results in the same system of equations.

It remains to find the best version among the three proposed variations for the WF-MFIE discretization. Additionally, the weighting factor γ has to be chosen. In order to evaluate the accuracy of the MFIE, several scattering scenarios are investigated.

4.3.2 Comparison of the Weak-Form Discretization Approaches

The two PEC scatterers as depicted in Fig. 4.9 are considered: a small sphere and a small sharp-edged pyramid, where the accuracy issues of the RWG-MFIE appear in a pronounced manner. The sphere has a diameter of 0.67λ (below its first resonance) and is meshed with $h \approx \lambda/14$, leading to 999 RWG unknowns. The scattered field is caused by a linearly-polarized plane wave. We consider two different reference solutions: a Mie series expansion and an EFIE solution with 1.5th order expansion functions on a refined mesh, whose surfaces exactly matches the coarsely discretized sphere. The relative FF RCS error of the \mathbf{u}_ψ -polarized electric field, with $\psi \in \{\varphi, \vartheta\}$,

$$\epsilon_{\psi}^{\text{FF}}(\vartheta, \varphi) = \frac{\|[\mathbf{e}_{\text{FF}}^{\text{s}}(\mathbf{r})]_{\psi} - [\mathbf{e}_{\text{FF,ref}}^{\text{s}}(\mathbf{r})]_{\psi}\|}{\max_{\vartheta, \varphi} \|[\mathbf{e}_{\text{FF,ref}}^{\text{s}}(\mathbf{r})]_{\vartheta}, [\mathbf{e}_{\text{FF,ref}}^{\text{s}}(\mathbf{r})]_{\varphi}\|} \quad \text{for } \|\mathbf{r}\| = \text{const. and } \psi \in \{\vartheta, \varphi\} \quad (4.46)$$

is then calculated in the $\vartheta = 90^\circ$, $\varphi = 0^\circ$, and $\varphi = 90^\circ$ cuts. In Fig. 4.10(a), the average and maximum RCS errors are analyzed for the different proposed MFIEs and a varying weighting factor γ with respect to a Mie series reference solution. All three WF-MFIE solutions diverge at $\gamma \rightarrow 0$. The WF identity MFIE performs better by a few decibels. Its error levels come close to the ones of the EFIE and BC-MFIE (around -38 dB peak error and -47 dB mean error), which is a good deal

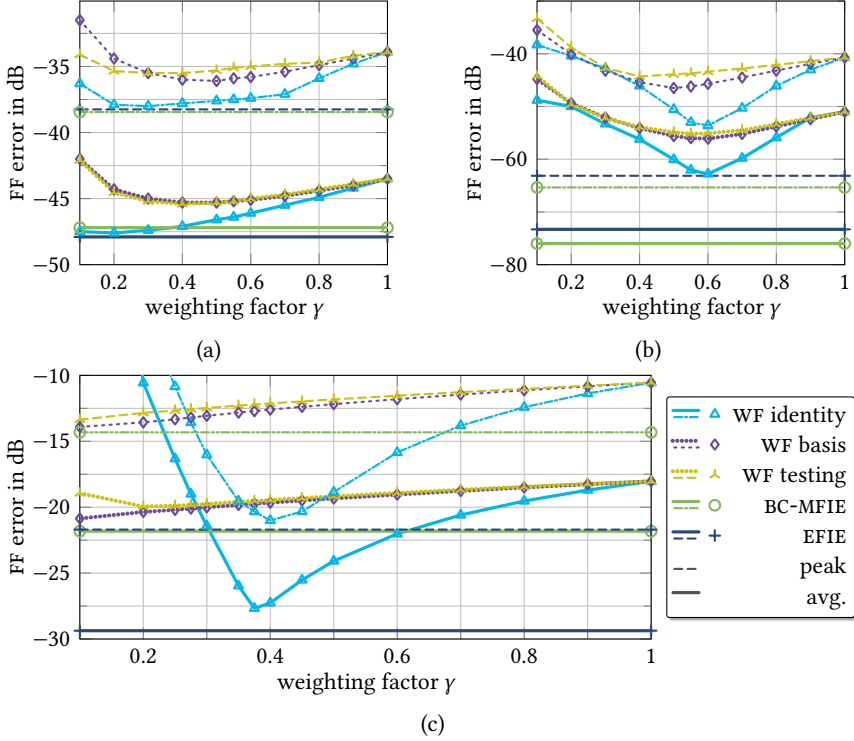


Fig. 4.10: Analysis of the influence of the weighting factor γ on the three WF-MFIE discretization schemes for two scattering scenarios. (a) Relative FF RCS error for the sphere with respect to a Mie series expansion. (b) Error for the sphere with respect to a HO EFIE solution on a refined mesh. (c) Error for the pyramid with respect to an EFIE solution on a refined mesh.

better than the RWG-MFIE, whose error can be read off at $\gamma = 1$ (-34 dB peak and -43 dB mean error). In Fig. 4.10(b), the HO EFIE solution on a refined mesh is taken as the reference instead of the Mie series expansion. This is a more meaningful “true” solution since the enforced boundary conditions of the considered scatterers match exactly. Hence, all SIEs consistently achieve a lower error. In particular, the increased accuracies of the EFIE and the BC-MFIE are remarkable (-64 dB peak and -75 dB mean error). The WF schemes cannot keep up with these accuracy levels and the classical MFIE falls even further behind. The accuracy improvement is the most for the WF identity variant. Specifically, it is more than 10 dB at $\gamma \approx 0.6$ as compared to the RWG-MFIE (-41 dB peak and -51 dB mean error). Furthermore,

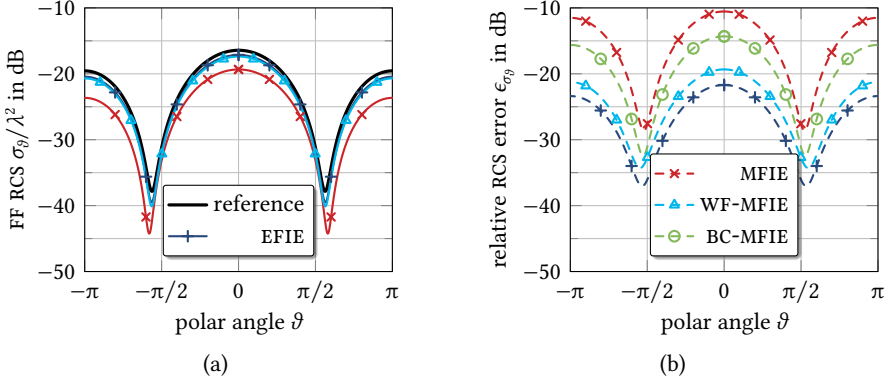


Fig. 4.11: Scattering from the small pyramid. The WF-MFIE is the variant with an WF identity, $\gamma = 0.5$. (a) Co-polar RCS in the $\varphi = 0^\circ$ cut. (b) Relative error in the same cut.

we observe that the Mie series expansion is not the best choice for the reference solution since the surface discretization error covers most of the SIE discretization error—excluding the RWG-MFIE which fares worst.

The second considered scattering scenario is a pyramid exhibiting a basis of $0.19\lambda \times 0.19\lambda$ and a height of 0.135λ . It is discretized with an average edge length $h \approx \lambda/10$ leading to 36 RWG unknowns. The incident field is a plane wave with \mathbf{u}_x polarization and $\mathbf{k} = -k\mathbf{u}_z$. The FF RCS error is calculated in the $\vartheta = 90^\circ$, $\varphi = 0^\circ$, and $\varphi = 90^\circ$ cuts with reference to an EFIE solution on a refined mesh with 576 unknowns. Figure 4.10(c) shows the peak and average RCS errors for the EFIE (-22 dB and -29 dB), the BC-MFIE (-14 dB and -22 dB), and the RWG-MFIE at $\gamma = 1$ (-11 dB and -18 dB). The application of the WF scheme to the basis or testing functions achieves an accuracy improvement which reaches almost BC-MFIE levels; the WF identity scheme achieves a larger improvement—coming close to the EFIE accuracy at $\gamma \approx 0.4$. Again, all three WF-MFIE solutions diverge at $\gamma \rightarrow 0$. The RCS and the related relative errors are shown in Fig. 4.11 for the co-polarized field component in the $\varphi = 0^\circ$ cut. The bi-static RCS of the EFIE, the BC-MFIE, and the WF-MFIE are visually indistinguishable on the chosen scale. The error in Fig. 4.11(b) shows the differences though. Small scatterers with sharp edges such as the treated pyramid are eye-catching illustrations of the inaccuracy of the classical MFIE. Figure 4.11(a) strikingly shows how much the MFIE solution is off.

In both scenarios, only employing the WF scheme for the identity operator discretization achieves a better accuracy and is therefore chosen for further investigations. The WF discretization of the \mathcal{K} operator is neither fully meaningful nor does it give an improvement in performance as significant as the WF representa-

tion of solely the \mathcal{I} operator. The question remains how to optimally choose the weighting factor γ . This is analyzed in detail in the following section. The two scenarios discussed so far are just a brief start. Nevertheless, it already became apparent that $0.4 \leq \gamma \leq 0.6$ might be a range of reasonable values.

4.4 Numerical Investigations of the Single-Field Low-Order Schemes

We investigate the discussed SIEs for PEC scattering scenarios with a single (dominant) integral operator for either the electric or the magnetic field. These include the classical EFIE and MFIE as well as the BC-tested MFIE, the CSIE with dominant magnetic currents, and the WF-MFIE. In a first step, the optimal weighting factor for the RWG WF-MFIE is searched for. This is done for several mesh refinement scenarios spanning fine and coarse meshes as well as objects of differing electrical size. Then, the LF behavior of the proposed SIEs is studied. We investigate several sharp-edged objects with accuracy issues and evaluate the NF and FF accuracies thereafter.

4.4.1 Convergence to the Correct Solution—Mesh Refinement & Choosing the WF-MFIE Weighting Factor

It is important for any discretization that the solution converges to the correct solution when the mesh is refined. For the MFIE, there are two cases of interest: objects with (sharp) edges and objects with smooth surfaces. The latter exhibit a drawback in the accuracy analysis, which was observed already in Subsection 4.3.2. While objects with smooth surfaces are not that problematic from the electromagnetics point of view, they are not representable with a linear (order $p = 1$) triangular mesh. Hence, the object's surface discretization error is expected to dominate even though the employed RWGs exhibit only 0.5th order. For objects with sharp edges, the mesh is able to conform with the desired surface perfectly but the MFIE accuracy is negatively affected by the geometric singularities. We study both types of scatterers in the following.

A Cube

The first scenario is plane-wave scattering from a PEC cube with 0.5λ edge length. Figure 4.12 shows four of the employed 14 models for the mesh refinement analysis. The average triangle edge length h ranges from 0.28λ for the coarsest mesh to 0.035λ for the finest mesh; the respective number of electric current RWG unknowns N ranges from 72 to 4302. The CSIE also exhibits the same number of unknowns since

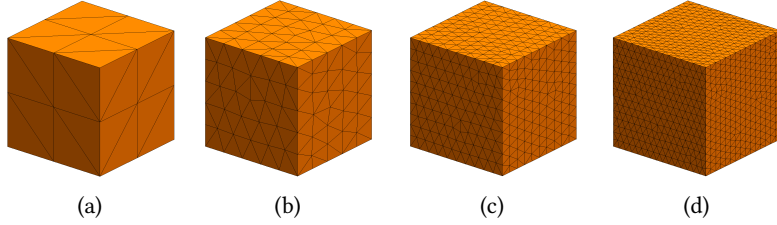


Fig. 4.12: Some of the cuboid models for the mesh refinement analysis © 2018 IEEE [Kornprobst and Eibert 2018e].

the magnetic currents are directly calculated from the electric current unknowns vector. All systems of equations are solved iteratively by the GMRES with a residual stopping criterion of 10^{-4} . The nested CG solvers for the Gram matrix inversion are stopped at 10^{-8} . An 2.5th order EFIE solution on the finest mesh is taken as the reference, which is calculated with a GMRES termination threshold of 10^{-6} .

First, we consider $\gamma = 0.5$ for the WF-MFIE. The bi-static RCS in the $\varphi = 0^\circ$ cut for an impinging plane wave with $\mathbf{p} = \mathbf{u}_x$ and $\mathbf{k} = -k\mathbf{u}_z$ is shown in Fig. 4.13 for one of the considered meshes with $h \approx \lambda/10$ ($N = 504$). The reference solution is not shown since the co-polarization σ_ϑ is visually indistinguishable and the cross-polarization $\sigma_\varphi < -80$ dB lies below the abscissa. The accuracy of the EFIE is best among the considered SIEs; the MFIE fares the worst. The other SIEs—viz. the BC-MFIE, the M-CSIE, and the WF-MFIE—perform in between. Note that we choose a weighting factor $\chi_{\text{CS}} = 1/11$ for the M-CSIE in order to obtain a dominant magnetic-current part—in other words, the surface impedance linking magnetic and electric currents overweighs the magnetic ones by a factor of 10 as compared to the standard CSIE. The WF-MFIE comes off well in the co-polarization but not so in the cross-polarization. Nonetheless, the cross-pol error is too low to matter—still lower than any co-pol error.

Such RCS calculations in the $\varphi = 0^\circ$, $\varphi = 90^\circ$, and $\vartheta = 90^\circ$ cuts provide the basis to compute the arithmetic average of the bi-static RCS FF error ϵ^{FF} according to (4.46) for all considered meshes and SIEs. Figure 4.14 shows the results of this mesh refinement study. Figure 4.14(a) shows the maximum FF error. As for the single mesh, the EFIE performs best, the MFIE worst, and the other SIEs somewhere in between. The same is observed in Fig. 4.14(b) for the averaged FF error. In Fig. 4.14(c), the arithmetically averaged relative error of the current coefficients

$$\epsilon_i = \frac{\text{avg}\|i - i_{\text{EFIE}}\|}{\max\|i_{\text{EFIE}}\|} \quad (4.47)$$

with respect to the EFIE solution on the respective mesh is shown. A consistent

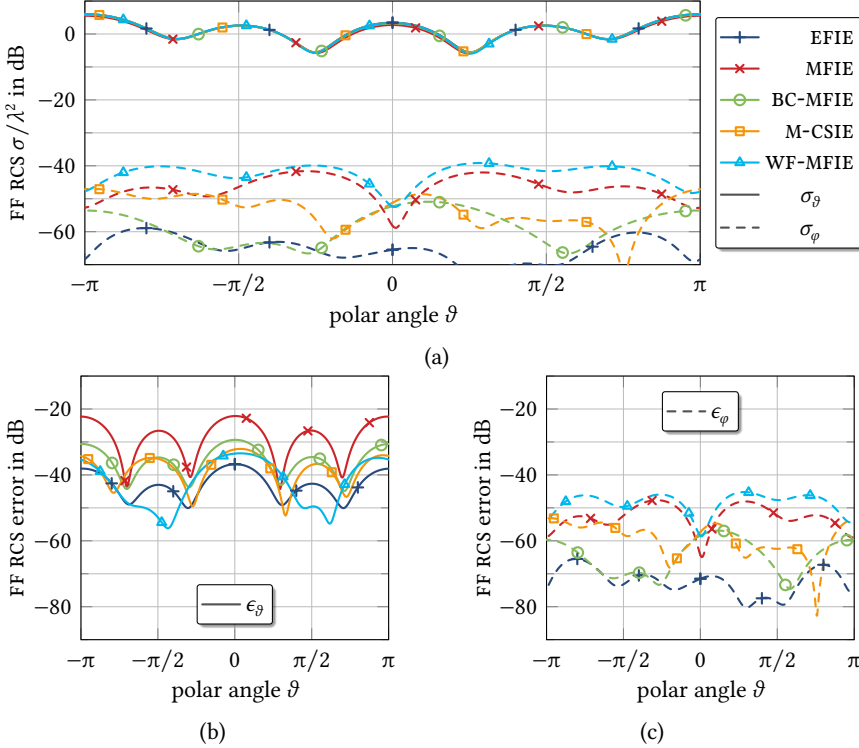


Fig. 4.13: Scattering from a PEC cube for various SIEs in the $\varphi = 0^\circ$ cut. WF-MFIE with $\gamma = 0.5$, M-CSIE with $\chi_{cs} = 1/11$. (a) Both polarizations of the bi-static RCS. (b) Relative RCS error of the co-polarization σ_ϑ . (c) Relative RCS error of the cross-polarization σ_φ .

advantage of the WF-MFIE over the standard MFIE is observed. Figure 4.14(d) provides the number of iterations for convergence with the GMRES solver. This may be seen as an estimate for the condition number of the respective IE formulations. The EFIE shows the typical dense-mesh breakdown, whereas all MFIEs do not suffer from this issue. The MFIE and the WF-MFIE are mostly on par and the BC-MFIE converges within a few iterations less. This advantage has to be taken with a grain of salt, though, as the setup and possibly also the involved MVP is computationally more costly. The M-CSIE starts on a similar level as the EFIE—with 38 iterations instead of below 20 for the MFIEs—but exhibits a lower slope: The EFIE ends up with 161 iterations for the finest mesh; the M-CSIE only takes 59. Hence, the dense-mesh breakdown is indeed avoided in its total severity. This is caused by the (weak) EFIE

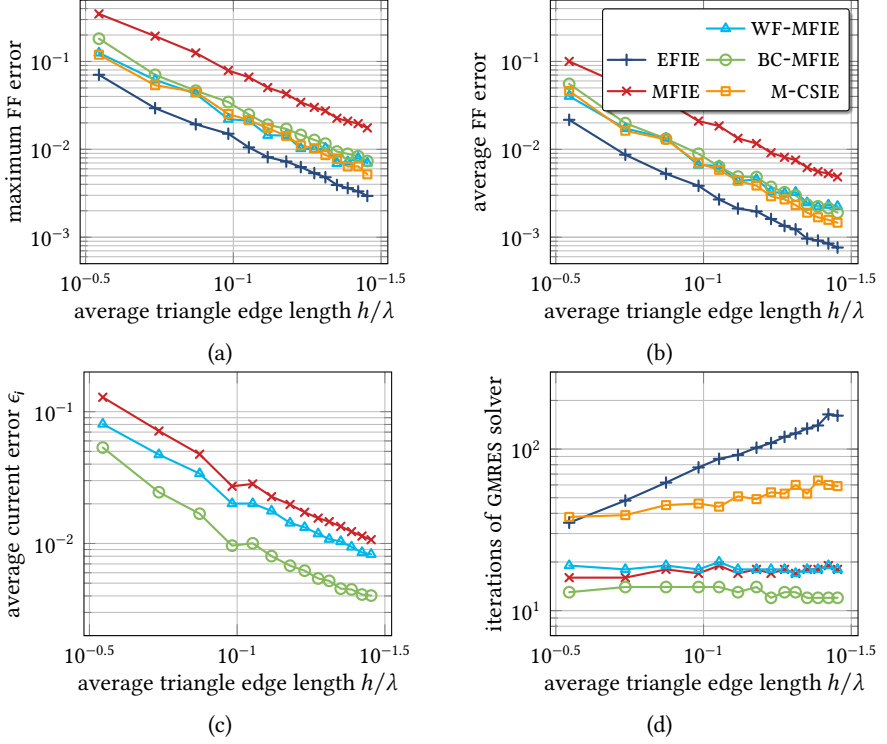


Fig. 4.14: Mesh refinement analysis for a 0.5λ cube, lowest-order RWG basis functions ($p = 0.5$), $\gamma = 0.5$. (a) Maximum relative FF error. (b) Arithmetically averaged relative FF error. (c) Arithmetically averaged relative current-coefficient error. (d) Solver iterations as condition number estimate.

presence in the null space of the Gram matrix $\mathbf{G}_{\alpha,\beta}$.

With this experiment in mind, we carry out an analysis for the WF weighting factor γ . The scenario under consideration is the same mesh refinement for a 0.5λ cube. The models' changing mesh parameter leads to great variations in the achievable error of more than one order of magnitude, see Fig. 4.14(b). First, the arithmetically averaged FF error $\epsilon_{\text{IE}}^{\text{FF},k}$ of the k th mesh is calculated for the angles (ϑ, φ) and for the two polarizations $(\mathbf{u}_\vartheta, \mathbf{u}_\varphi)$, based on (4.46). Then, an appropriate choice to condense all the errors into one number is the geometric mean of the arithmetic averages

$$\tau^{\text{IE}}(\gamma) = \left(\prod_{k=1}^K \epsilon_{\text{IE}}^{\text{FF},k}(\gamma) \right)^{1/K} = \exp \left(\sum_{k=1}^K \ln \epsilon_{\text{IE}}^{\text{FF},k}(\gamma) \right), \quad (4.48)$$

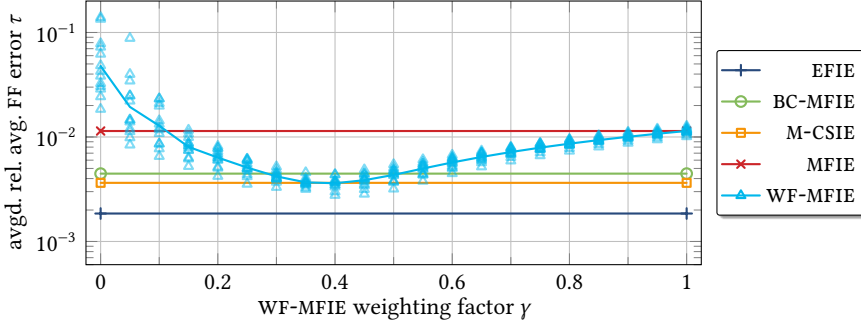


Fig. 4.15: Optimal WF-MFIE weighting factor for scattering from the mesh refinement models of a 0.5λ cube, lowest-order RWG basis functions ($p = 0.5$).

where the order of the error is averaged due to the contained logarithm. Fig. 4.15 compares the error level of the WF-MFIE to the other considered SIEs. Since the error values fluctuate from mesh to mesh and do not follow the ideal convergence trend [Wegler 2011; Dölz et al. 2019; Jin 2011], the variation for each mesh at each value of γ is also contained as a scatter plot. The baseline is given by the EFIE error, and the individual error values are adjusted to the (geometric) mean ratio between EFIE and WF-MFIE error levels. Such a seemingly complicated way to calculate the error relationship is required to cope with error levels approximately between 10^{-1} and 10^{-3} . Given γ and the k th mesh, a scatter-plot marker is shown accordingly in Fig. 4.15 at the error level

$$\tau^{\text{WF-MFIE}}(\gamma, k) = \tau^{\text{EFIE}} \epsilon_{\text{WF-MFIE}}^{\text{FF},k} / \epsilon_{\text{EFIE}}^{\text{FF},k}. \quad (4.49)$$

Above $\gamma \approx 0.3$, the spread between the minimum and maximum deviations of the WF-MFIE to the EFIE is reasonably small. Below $\gamma < 0.1$, the error is worse than for the standard MFIE—the reason being the discussed non-trivial null space in the WF basis transformation. The lowest error levels, close to the ones of the M-CSIE and the BC-MFIE, are found at $0.3 \lesssim \gamma \lesssim 0.5$. It makes sense to choose one of the larger values in this range to avoid the issues of low γ values.

Next, we double the simulation frequency and repeat the same analysis for a 1λ cube. 20 triangular meshes with h ranging from 0.37λ to 0.027λ are considered with N between 162 and 30 240. All the steps of calculating FF RCS errors are performed in the same way. The only difference is the lower iterative solver threshold of 10^{-6} . Figure 4.16 shows the weighting analysis for γ . We see that the WF-MFIE comes close to, but never reaches the M-CSIE and BC-MFIE error levels.

Exemplary results of the FF errors and solver iterations for all individual meshes

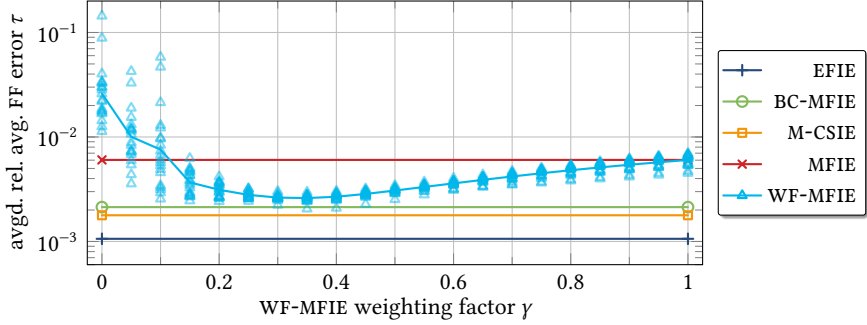


Fig. 4.16: Optimal WF-MFIE weighting factor for scattering from the mesh refinement models of a 1λ cube, lowest-order RWG basis functions ($p = 0.5$).

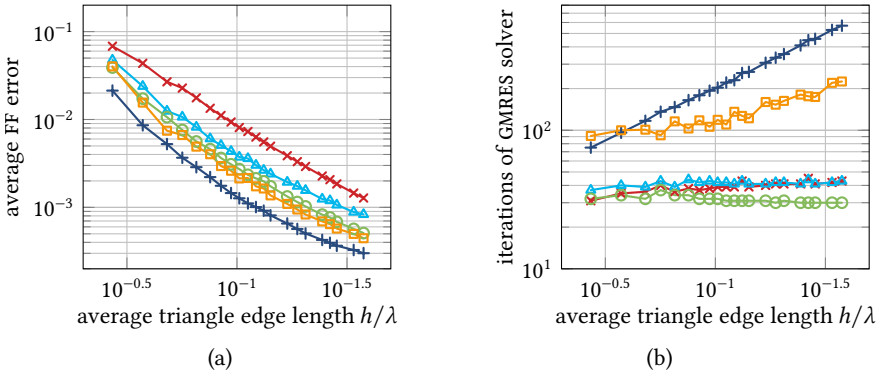


Fig. 4.17: Mesh refinement analysis for a 1λ cube, lowest-order RWG basis functions ($p = 0.5$), $\gamma = 0.5$. For the legend, cf. for instance Fig. 4.16. (a) Arithmetically averaged relative FF error. (b) Iterative solver convergence.

are shown in Fig. 4.17. For these results, γ is chosen as 0.5 again (to maintain consistency among the scattering scenarios). While the WF-MFIE shows a lower error than the plain RWG MFIE, a consistent disadvantage for the WF-MFIE over all other SIEs is observed. Lower values of γ improve the WF-MFIE error in this scenario. Furthermore, the WF-MFIE error levels show a slight stagnation towards finer meshes. The BC-MFIE converges a bit faster with 30 instead of about 40 iterations for the other two MFIEs; but this is again offset by the larger computational effort.

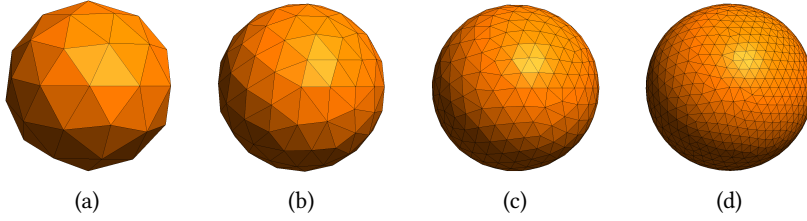


Fig. 4.18: Some of the sphere models for the mesh refinement analysis © 2018 IEEE [Kornprobst and Eibert 2018e].

A Sphere

A similar mesh refinement study as for the cubes is performed for a PEC sphere with a diameter of 0.5λ . The triangle edge length h ranges from 0.14λ to 0.034λ with N from 126 to 2388. Four of the 16 meshes are shown in Fig. 4.18. Again, an M-CSIE with a dominant magnetic current part due to $\chi_{CS} = 1/11$ is considered. For the initial RCS analysis, the WF-MFIE is considered with $\gamma = 0.5$. For all IEs, the GMRES threshold is set to 10^{-4} . The FF RCS errors are evaluated with respect to a Mie series expansion. The same is done for the scattered NF at a radius of 0.6λ , i.e., with a distance of 0.1λ to the sphere. The associated NF error is calculated analogously to (4.46).

Figure 4.19(a) shows the iterative solver convergence. The EFIE suffers from the dense-mesh breakdown; the M-CSIE not really but starts already on the same (high) level as the EFIE. The BC-MFIE converges fastest, the standard MFIE fares slightly worse, and the WF-MFIE again slightly worse—all within only a small number of iterations. This basically confirms the findings for the scattering from the cubes. The more interesting part is the accuracy analysis. For all three considered error measures, see Fig. 4.19(b) and (c), the classical RWG-MFIE performs the worst and all other SIEs show exactly the same error level with an accuracy advantage of about 3 dB over the MFIE. The reason why the same accuracy (and just such a small advantage) is observed for the EFIE, the BC-MFIE, the M-CSIE, and the WF-MFIE lies in the surface discretization of the sphere, which exhibits a non-negligible discretization error of the curved surface with linear edges ($p = 1$) [Wegler 2011]. Furthermore, the discretized spheres are effectively smaller than the ideal sphere considered in the Mie series expansion. This imperfection is clearly visible in Fig. 4.18. The same effect has already been observed in Section 4.3. There, it was mitigated by choosing a HO EFIE solution on a refined mesh as a reference. Here, we follow the same strategy in order to reach a reasonable accuracy judgment since the imperfect geometric modeling has a larger accuracy impact than the use of RWG functions. For each of the considered meshes, a refined version has

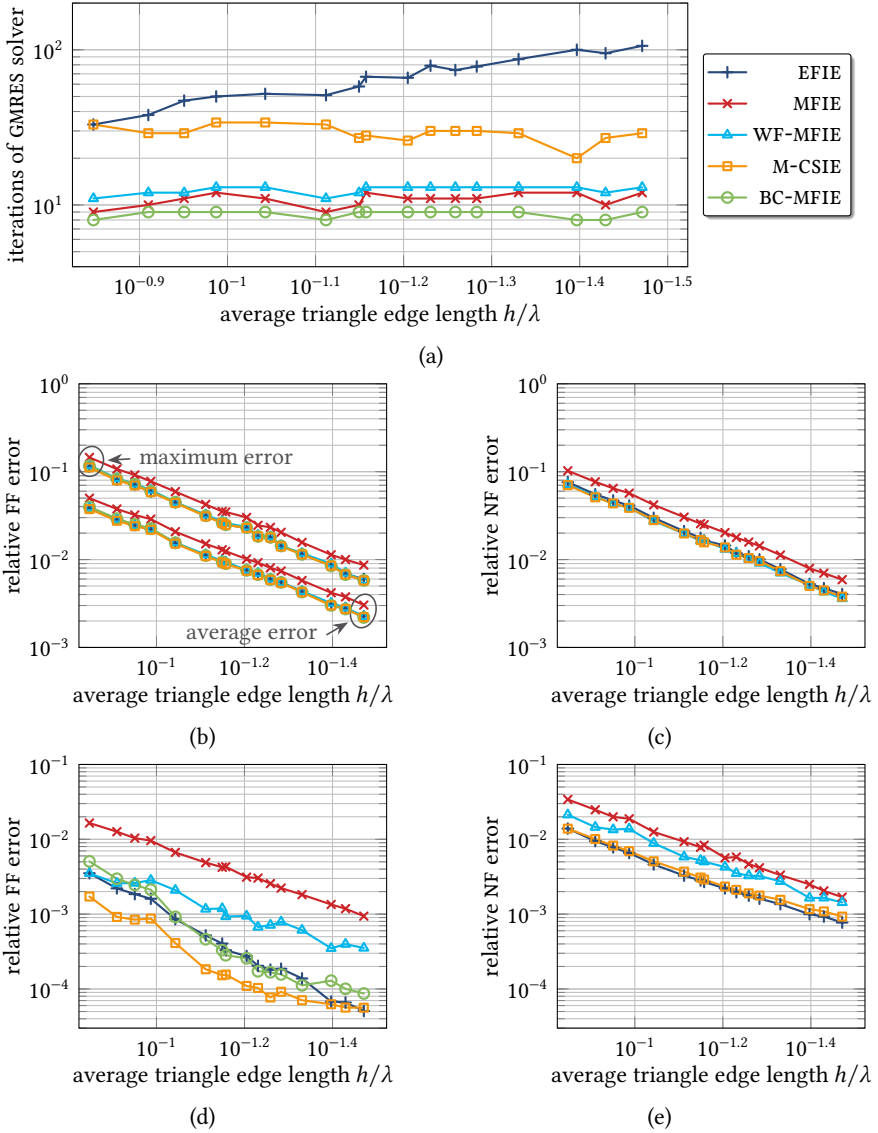


Fig. 4.19: Mesh refinement analysis for a 0.5λ diameter sphere with RWG functions, $\gamma = 0.5$. (a) Solver iterations as condition number estimate. (b) Maximum and mean FF errors w.r.t. a Mie series solution. (c) Mean NF errors w.r.t. a Mie series solution. (d) Mean FF errors w.r.t. a 1.5th order EFIE solution. (e) Mean NF errors w.r.t. a 1.5th order EFIE solution.

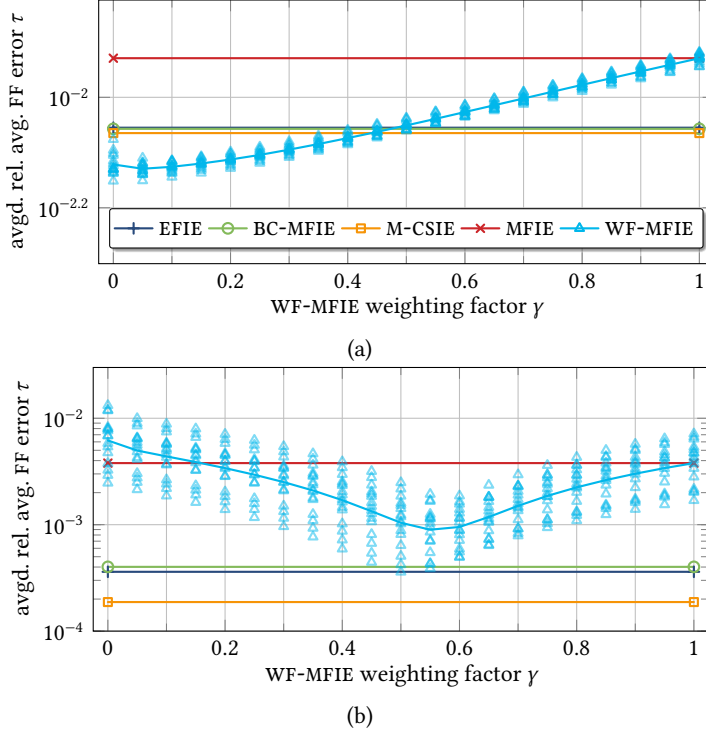


Fig. 4.20: Optimal WF-MFIE weighting factor for scattering from the mesh refinement models of a 0.5λ sphere, lowest-order RWG basis functions ($p = 0.5$). Note the different ordinate scales of the subfigures. (a) Error w.r.t. a Mie series solutions. (b) Error w.r.t. a HO EFIE solution on a refined mesh.

been created—replacing each triangle with 4 smaller ones—and the 1.5th order EFIE solution is employed as a reference solution.

The corresponding results are shown in Fig. 4.19(d) and (e). This leads to generally much lower error levels and differences between the more accurate versions. The most accurate one is the M-CSIE, followed by the EFIE and BC-MFIE which are on a comparable level. For the coarser meshes, the WF-MFIE FF error comes close to the EFIE error but the WF-MFIE performs worse for finer meshes and ends up in between of the EFIE/BC-MFIE and the MFIE. The NF error of the WF-MFIE is between the accurate solutions (EFIE and M-CSIE) and the classical MFIE.

Equipped with this suitable reference solution, we can calculate the WF-MFIE FF error for $0 < \gamma < 1$ in Fig. 4.20(b) [Fig. 4.20(a) with the Mie series reference for

completeness]. The same methodology as for the cubes is followed, i.e., we show the geometric average τ (over the various meshes) of the arithmetically averaged RCS FF errors. At around $0.5 < \gamma < 0.6$, the WF-MFIE performs best, but reaches EFIE/BC-MFIE error levels only halfway. Nevertheless, for the prominent case of $h \approx 0.1\lambda$, the accuracy is similar to the more accurate SIEs.

Summary

Considering the different scenarios—scattering from a pyramid, a cube at two frequencies, and a sphere at two frequencies—, choosing $\gamma = 0.5$ seems a good compromise to cure the inaccuracy problem of the standard RWG-MFIE for some scenarios fully and for others partially. One way to further improve the WF-MFIE is to put more weight on the WF scheme when the objects' edges are sharper and less weight on smooth surface areas, for which we refer to the discussion in Subsection 4.7.3. On such smooth surfaces, a more conservative choice of $\gamma \approx 0.6$ also improves the MFIE accuracy significantly and circumvents the null space problems to an even higher degree of certainty.

4.4.2 Low-Frequency Behavior

We study one LF scattering scenario in order to determine whether the LF breakdown of the standard RWG-MFIE still occurs in the proposed formulation. It is, however, not expected that the problem is solved by the WF-MFIE. For the CSIE, this is not directly clear but the dual-space testing of the electric field may be able to circumvent the wrong discretization of the charge for the MFIE operator.

We consider a PEC sphere with a diameter of 1 m. Its triangular mesh exhibits 126 RWG unknowns. For now, the considered frequency is 5 kHz, leading to a diameter of about $1.67 \cdot 10^{-5}\lambda$. The bi-static RCS for plane-wave scattering with $\mathbf{p} = \mathbf{u}_x$ and $\mathbf{k} = k\mathbf{u}_z$ is given in Fig. 4.21. The reference solution for calculating the error in Fig. 4.21(b) is a 1.5th order EFIE solution on a refined mesh (with 1680 unknowns), which is known to be accurate at such frequencies despite the slower iterative solver convergence. Numerical cancellation errors which cause accuracy deterioration for the EFIE only become an issue at even lower frequencies—at the considered frequency, the accuracy is still excellent. The EFIE offers the most accurate solution with an average FF error of -57.5 dB. We observe that the M-CSIE is still accurate at such a rather LF with an average FF error of -57.3 dB, whereas the accuracy of the two MFIEs is deteriorated (-11.1 dB and -11.2 dB on average).

Performing this kind of analysis for a frequency sweep yields Fig. 4.22. At the lower end of the frequency range (at 20 kHz), the diameter of the sphere is $6.7 \cdot 10^{-5}\lambda$; at the upper end (at 500 MHz), it is 0.67λ . We observe the transition to the HF regime at the highest studied frequencies. The discretization density becomes

4.4 NUMERICAL INVESTIGATIONS OF THE SINGLE-FIELD LO SCHEMES

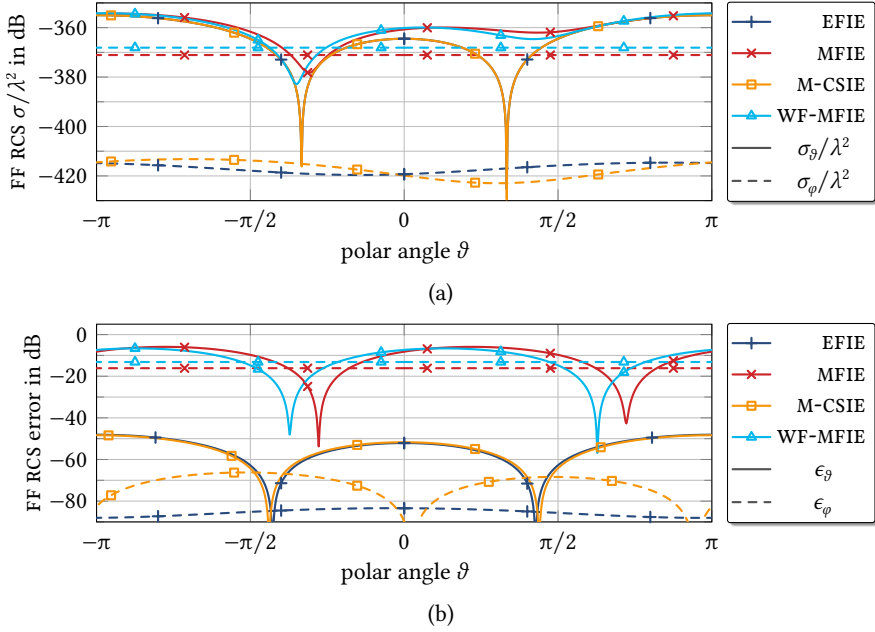


Fig. 4.21: Scattering from a 1-m diameter PEC sphere at $f = 5$ kHz for various SIEs in the $\varphi = 0^\circ$ cut. WF-MFIE with $\gamma = 0.5$, M-CSIE with $\chi_{cs} = 1/11$. (a) The bi-static RCS. (b) Relative error of the bi-static RCS.

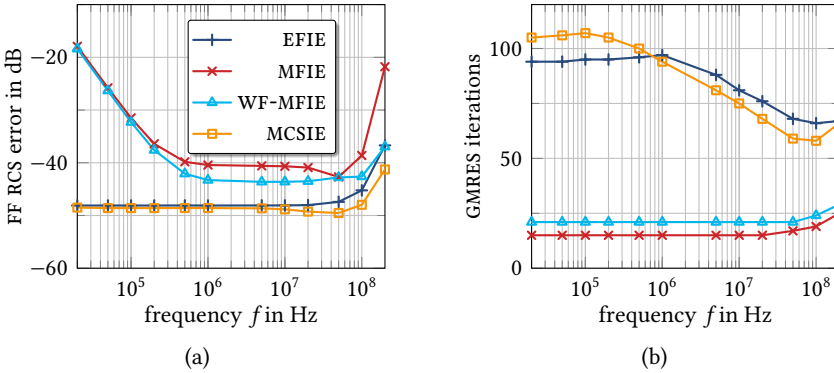


Fig. 4.22: Frequency sweep of the LF sphere. (a) FF RCS error. (b) GMRES iteration count for convergence to a residual of 10^{-10} .

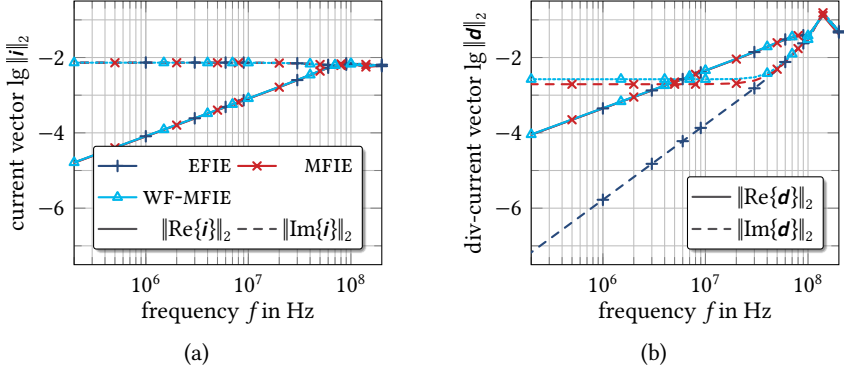


Fig. 4.23: Norm of (a) the retrieved electric surface current density unknowns and of (b) the divergence of the current density at LFs.

already rather coarse with an average edge length h of about 0.3λ . For each IE, a different behavior is observed. The EFIE LF breakdown causes the iteration count to increase with decreasing frequency already at 50 MHz and $h \approx 0.04\lambda$. The M-CSIE shows a similar behavior as the EFIE, with a slightly increased accuracy and a faster iterative solver convergence. Only below 1 MHz, it converges slower than the EFIE while maintaining marginally better accuracy. This threshold coincides with the MFIE's LF breakdown: While the iterative solver convergence is not affected for both the classical RWG-MFIE and the WF-MFIE, the FF error increases significantly below 1 MHz.

What we notice in the FF does not reveal the whole truth about the LF issues of the MFIE, though. The underlying reason is that the real part of the divergence of the current exhibits erroneously a constant limit at LF as reported first by Y. Zhang et al. [2003]. Bogaert et al. [2011b] and Bogaert et al. [2014] have shown that this is caused by the wrong choice of the testing functions. Only dual-space testing can mitigate this issue. Hence, we cannot expect the WF scheme to solve this problem of the MFIE. In Fig. 4.23, we analyze the current and the charge coefficients separately. Figure 4.23(a) shows that $\|i\|_2$ exhibits the same behavior over frequency for all three IEs. The erroneous contribution in the MFIE solution is not visible. The picture changes when we consider the divergence of the current on the i th triangle, which is related to the charge on the i th triangle via the current continuity conditions (2.5),

$$q_{e,i} = \frac{j}{\omega\eta} \sum_{k=1}^3 \text{div}_s j_{k,i} \quad \text{with } j_{k,i} = [i]_{m(k,i)} \beta_{m(k,i)} \quad (4.50)$$



Fig. 4.24: A sharp wedge employed for demonstrating the MFIE's inaccuracy © 2018 IEEE [Kornprobst and Eibert 2018e]. (a) The studied coarse mesh. (b) The refined mesh used for calculating for the EFIE reference solution.

for the three RWG functions on the respective triangle. The function $m(k, i)$ maps the number of the triangle i and the number of the triangle-wise RWG function k on the suitable unknown number $n \in \{1, 2, \dots, N\}$. Note that $\text{div}_s \boldsymbol{\beta}_{m(k,i)}$ is constant ($\pm 1/A_{m(k,i)}^\pm$) on s_i for each RWG function [Rao et al. 1982]. We introduce a div-current vector as a proxy for the triangle-wise surface charge density accordingly

$$[\mathbf{d}]_k = \sum_{i=1}^3 \text{div}_s \mathbf{j}_{k,i} \quad \text{for } k \in \{1, 2, \dots, K\} \quad (4.51)$$

with the total number of triangles K .

In Fig. 4.23(b), the erroneous limit in $\|\text{Re}\{\mathbf{d}_{(\text{WF-MFIE})}\}\|_2$ appears at around 50 MHz and lower. This is more than one decade higher than the highest frequency at which the error in the FF becomes observable, and might be even considered closer to HF than LF scenarios with $h \approx 0.05\lambda$ and a sphere diameter of $\lambda/6$. As the testing space is not changed by the WF scheme, the LF breakdown persists for the WF-MFIE.

4.4.3 Scattering Results for Electrically Small Objects with Accuracy Issues

In the following, we analyze some scattering results for the various IEs in more detail. We focus in particular on the FF and NF accuracy and in the limiting case the surface current densities. All of these measures show severe inaccuracies for sharp-edged scatterers when solved with the classical RWG-MFIE.

A Sharp Wedge

The first scenario is an electrically small wedge discretized with 84 RWG unknowns, see Fig. 4.24. The simulation frequency is chosen such that the average triangle edge length is $\lambda/11$. The base rectangle has dimensions of $0.08\lambda \times 0.27\lambda$, the height

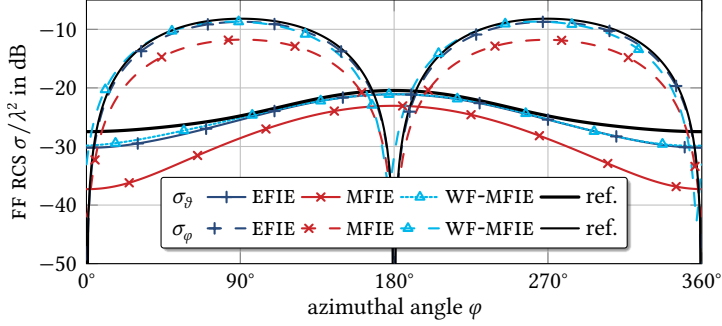


Fig. 4.25: Bi-static RCS from the wedge.

is 0.27λ . Accordingly, the wedge angle is 16.5° . The RWG EFIE solved on a refined mesh with $\lambda/128$ discretization, see Fig. 4.24(b), is employed as reference solution. Figure 4.25 compares the bi-static RCS of the EFIE, the MFIE, and the WF-MFIE to the reference solution for a plane-wave incidence with $\mathbf{p} = \mathbf{u}_x$ and $\mathbf{k} = -k\mathbf{u}_z$. The MFIE shows an absolute error of a couple of decibels. In relative terms, the EFIE and the WF-MFIE exhibit maximum FF errors of about -22 dB. The MFIE fares much worse with a maximum error of -9 dB.

The scattered NF is depicted in Fig. 4.26. Figures 4.26(a) and 4.26(e) show the absolute values of the electric and magnetic fields of the reference solution, respectively. The relative errors ϵ^{NF} of the electric and magnetic NFs are calculated similar as the FF, cf. (4.46), for each polarization \mathbf{u}_ψ as

$$\epsilon_{\psi}^{\text{NF}}(\mathbf{r}) = \frac{\|[\mathbf{e}^s(\mathbf{r})]_{\psi} - [\mathbf{e}_{\text{ref}}^s(\mathbf{r})]_{\psi}\|}{\max_{\mathbf{r}} \|\mathbf{e}_{\text{ref}}^s(\mathbf{r})\|}, \quad (4.52)$$

or, as it is done here, as the overall relative error

$$\epsilon^{\text{NF}}(\mathbf{r}) = \frac{\|\mathbf{e}^s(\mathbf{r}) - \mathbf{e}_{\text{ref}}^s(\mathbf{r})\|}{\max_{\mathbf{r}} \|\mathbf{e}_{\text{ref}}^s(\mathbf{r})\|}. \quad (4.53)$$

It is observed that the WF-MFIE offers improvements for both electric and magnetic NFs, while it cannot achieve EFIE error levels completely. The arithmetically averaged electric NF errors in the considered cut plane read -34.7 dB, -40.8 dB, -44.7 dB for the MFIE, the WF-MFIE, and the EFIE respectively; as well as -17.7 dB, -25.0 dB, and -28.9 dB for the magnetic NF.

A word about the iterative solver convergence: The GMRES solver for MFIE, the WF-MFIE, and the EFIE converges within 26, 31, and 63 iterations to a residual of

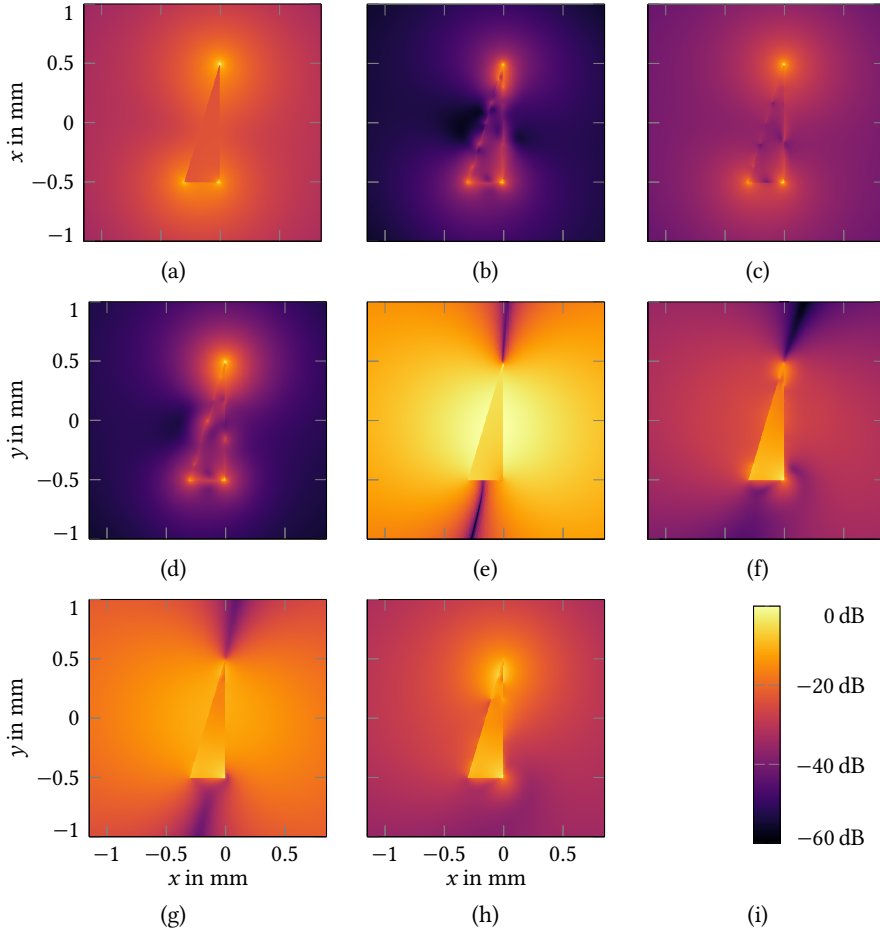


Fig. 4.26: Scattered NF field around and inside a sharp wedge: normalized absolute field values and relative vector error magnitudes of the fields © 2018 IEEE [Kornprobst and Eibert 2018e]. (a) Electric field reference solution. (b) Electric field error of the EFIE. (c) Electric field error of the MFIE. (d) Electric field error of the WF-MFIE. (e) Magnetic field reference solution. (f) Magnetic field error of the EFIE. (g) Magnetic field error of the MFIE. (h) Magnetic field error of the WF-MFIE. (i) Colorbar for all plots.

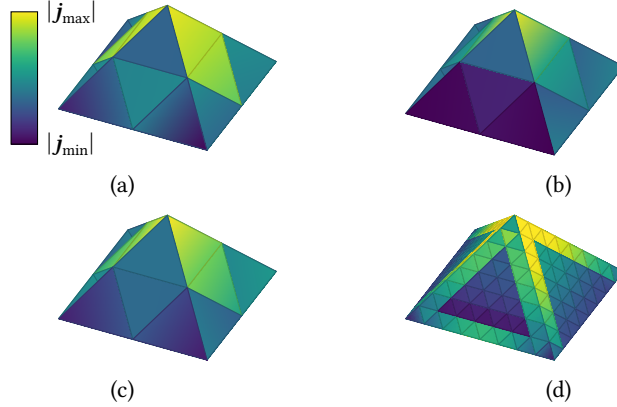


Fig. 4.27: Electric surface current distribution on a small pyramid © 2018 IEEE [Kornprobst and Eibert 2018e]. (a) EFIE. (b) MFIE. (c) WF-MFIE. (d) EFIE reference on a refined mesh.

10^{-6} . The nested diagonally preconditioned CG solver for the inversion of $\mathbf{G}_{\beta,\beta}$ converges within 10 iterations to 10^{-10} . Overall, the computational cost for the weak-form rotation is more or less negligible, even for such a small problem and even though the Gram matrix is not really well-conditioned due to deformed triangles, see Subsection 4.1.4.

A Pyramid

The bi-static RCS of the electrically small pyramid, as already shown in Fig. 4.9(b), is considered in Fig. 4.11. The RWG-MFIE is found to exhibit a much larger error. Here, we look at the accuracy of the surface current densities in Fig. 4.27 for the same scattering scenario as before. The WF-MFIE and EFIE solutions give very similar results, whereas the MFIE solution differs quite a lot. Of course, the EFIE solution on a finer mesh looks quite different. Nevertheless, it is clear that the currents of the EFIE and WF-MFIE solutions are more accurate than the MFIE one.

4.5 Numerical Investigations of the CF/CS Schemes

In this section, extensive studies on the behavior of the proposed LO discretization schemes are carried out for electrically larger objects (spanning at least multiple wavelengths). First, several scattering problems and one radiation scenario are discussed looking at the FF in detail. Then, several scattering scenarios are investi-

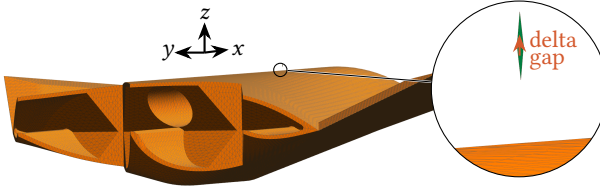


Fig. 4.28: Rear view of the stealth object flamme with a pair of triangles on top © 2018 IEEE [Kornprobst and Eibert 2018e].

gated regarding the stability and accuracy of the interior-resonance free IEs. The studied IEs comprise the CFIE, the BC-CFIE, the BC-CSIE, the CSIE, as well as the WF-CFIE.

4.5.1 More Scattering and Radiation Results

Stealth Object Flamme

Figure 4.28 shows the PEC stealth object Flamme meshed with 52 782 triangles (i.e., 79 173 RWG unknowns) [Gürel et al. 2003; Eibert 2005]. At the simulation frequency of 8 GHz, the size of the (scaled) object is 16λ in x -direction, 6.4λ in y -direction, and 1.6λ in z -direction and $h \approx 0.08\lambda$. For the incident field, we consider a dipole-like excitation placed on top of the scatterer [Kornprobst and Eibert 2018e]. The distance of the excitation to the PEC surface is 0.05λ (in z -direction) and consists of a pair of deformed triangles, each with a height of 0.027λ and a width of 0.005λ , whose gap is excited with a voltage source.

The GMRES stopping criterion is chosen as 10^{-5} for all simulations. The EFIE converges within 1277 iterations, the WF-CFIE within 125, and the CFIE within 126. The MLFMM accuracy parameter is chosen as $D_0 = 5.0$ and the box size is 0.2λ . The reference solution is a CFIE solution on a refined mesh with 287 923 RWG unknowns, computed with $\chi_{\text{CF}} = 0.999$ and a stopping criterion of 10^{-8} .

In Fig. 4.29, the calculated radiation patterns are compared. The maximum errors of the CFIE, the WF-CFIE, and the EFIE are -29.6 dB, -36.6 , and -43.4 dB. The negative influence of the MFIE operator is reduced with the WF scheme but does not disappear completely.

We consider the same object Flamme for scattering from a plane wave with polarization $\mathbf{p} = \mathbf{u}_y$ and wave vector $\mathbf{k} = k\mathbf{u}_x$ at a frequency of 10 GHz. The incident wave is directly illuminating the probably most challenging part of the Flamme—the rear as shown in Fig. 4.28—with lots of sharp edges and cavity-like structures. With the same RWG mesh as before (except for the dipole excitation), the mesh size h is about 0.1λ . For this scattering problem, we consider a 1.5th order

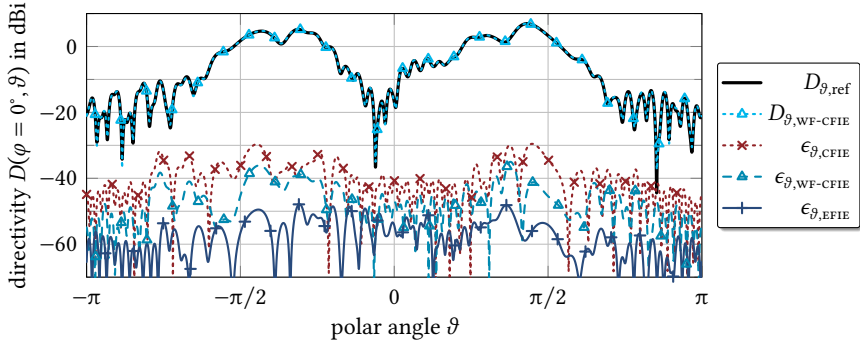


Fig. 4.29: Directivity of the “dipole” placed on top of the Flamme.

CFIE solution on a refined mesh with 1 055 640 unknowns as a reference, computed with $\chi_{\text{CF}} = 0.99$, a stopping criterion of $3 \cdot 10^{-6}$, and an MLFMM box size of 0.125λ . For the reference, an inner-outer preconditioning scheme for the GMRES solver is employed [Saad 1996; Eibert 2007].

Even for the standard MFIE, the iterative solver convergence is quite slow with a convergence within 1238 iterations due to the deformed mesh and the large electrical size. For the WF-MFIE, the number of iterations to convergence increases to 1580. The M-CSIE converges faster with just 549 iterations, while the EFIE struggles much more and takes 4697 iterations to convergence. The CF/CS formulations are able to cope with this to some extent. The CFIE and WF-CFIE converge within 323 and 395 iterations, respectively. The CSIE with equal weighting of MFIE and EFIE operators performs worse with 457 iterations.

The bi-static RCSs of the reference solution and the solution with the largest error—obviously, the standard RWG-MFIE—in the $\vartheta = \pi/2$ cut plane are shown in Fig. 4.30. The RCS error for all considered IEs, separately for the φ - and ϑ -components of the RCS, are shown in Fig. 4.31. The MFIE is particularly inaccurate with a maximum ϵ_φ error of -15.9 dB. This is also visible in the RCS plot itself, quite similar to the previously discussed scattering scenarios for objects with sharp edges—cf. Figs. 4.11 and 4.25. The inaccuracies are observable also at large RCS levels, for instance looking into the shadow region at $\varphi = 0$ or looking at the monostatic RCS at $\varphi = \pi$ which is off by several decibels. Sorted in descending order, we find the average RCS errors for the MFIE, WF-MFIE, CFIE, WF-CFIE, M-CSIE, CSIE, and EFIE as -33.2 dB, -37.0 dB, -44.6 dB, -50.9 dB, -53.3 dB, -61.5 dB, and -65.5 dB, respectively. The WF-CFIE shows an advantage of about 6 dB over the classical CFIE; the CSIE performs another 10 dB better; and the EFIE even another 5 dB. Over the angular range shown in Fig. 4.31, only the CSIE reaches the EFIE error level.

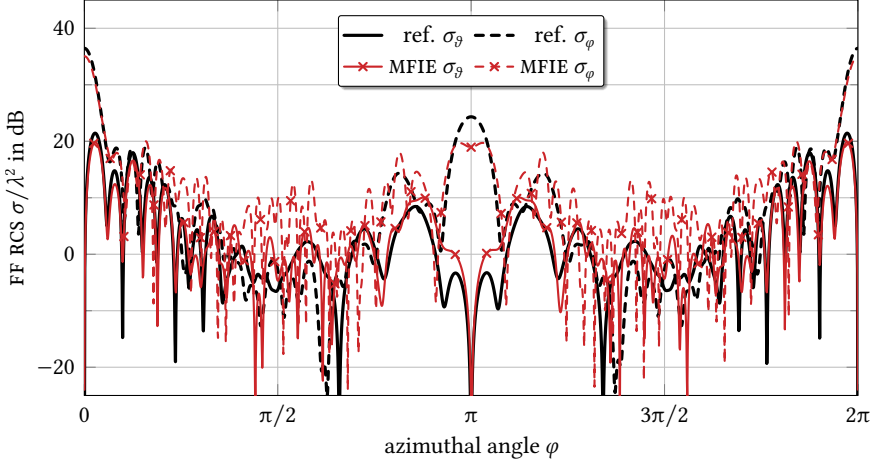


Fig. 4.30: Bi-static RCS for plane-wave scattering from a PEC Flamme at 10 GHz with $\mathbf{k} = k\mathbf{u}_x$, for the HO reference solution and the RWG-MFIE solution, $\vartheta = \pi/2$.

As another scattering scenario involving the stealth object Flamme, we increase the simulation frequency further to 12 GHz, i.e., $h \approx 0.12\lambda$. Furthermore, the incident plane wave exhibits $\mathbf{p} = \mathbf{u}_x$ and $\mathbf{k} = -k\mathbf{u}_z$, which means the wave is impinging from above on a mostly planar surface. This incident field results in a right-hand side that is easier to handle for some IEs. The MFIE converges within 1067 iterations, the WF-MFIE within 1618, the M-CSIE within 481, and the EFIE within 4827. The interior-resonance-free formulations show, as expected, a faster convergence rate with 228 iterations to convergence for the CFIE, 275 for the WF-CFIE, and 311 for the CSIE.

Since the Gram matrix is not really well-conditioned for this scattering scenario—as indicated by the slow iterative solver convergence of the MFIE and by the large the ratio of the longest to the shortest triangle edge length ($0.37\lambda/0.005\lambda \approx 89$)—, we look at the performance of the Gram matrix inversion in more detail. The calculations are run on an AMD Ryzen 9 3950X with 16 cores (32 threads) and a maximum boost clock up to 4.7 GHz. The MLFMM-accelerated MVP may be parallelized with OpenMP (but is limited by the memory-speed for more than 7 threads at a 3.9-fold speed-up); the other parts of the solver—the GMRES and CG methods, or the NF and Gram MVPs—are not worth to parallelize since the memory throughput limits the calculations anyhow, in particular for large problems. For computationally intense tasks such as the setup of the NF interaction matrix, the observed speed-up in wall time is 19.7-fold. For the Gram matrix inversion, we have chosen a challenging threshold of 10^{-12} . For the CSIE, the average time to convergence is 0.0386 s, i.e.,

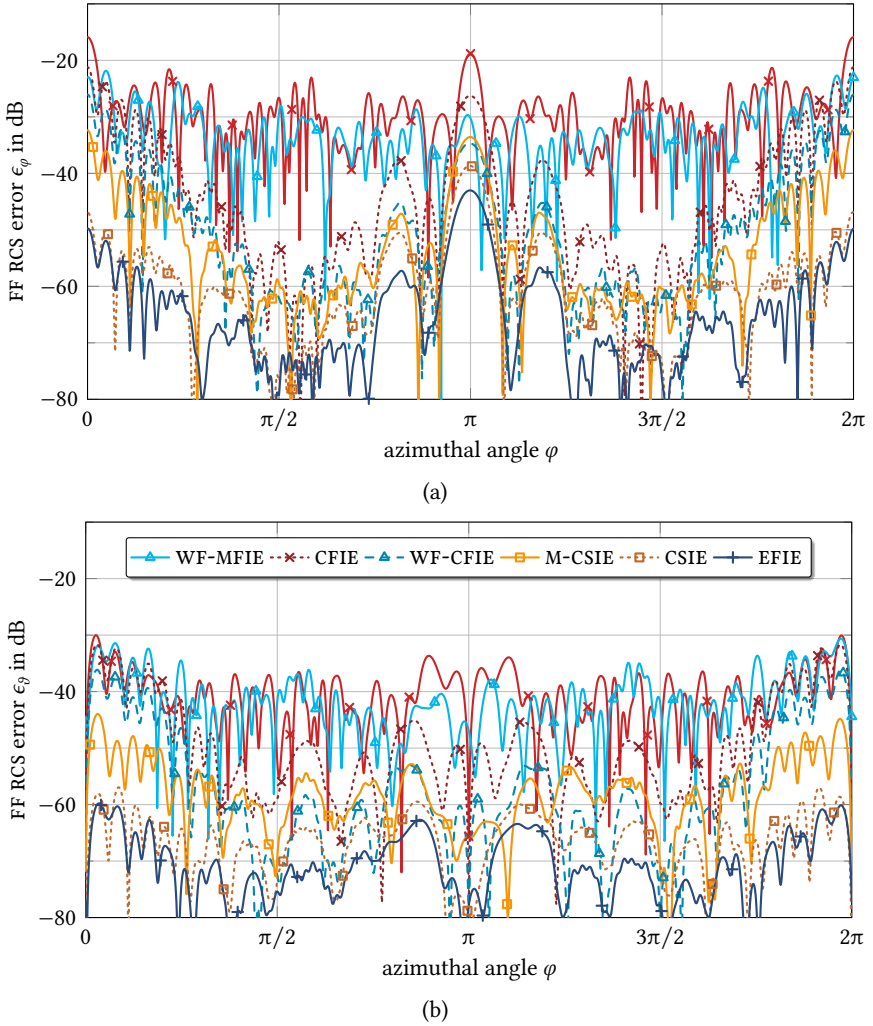


Fig. 4.31: Bi-static RCS error for plane-wave scattering from a PEC Flamme at 10 GHz with $\mathbf{k} = k\mathbf{u}_x$, shown for various IEs, $\vartheta = \pi/2$. (a) Error for the σ_ϕ component. (a) Error for the σ_ϑ component.

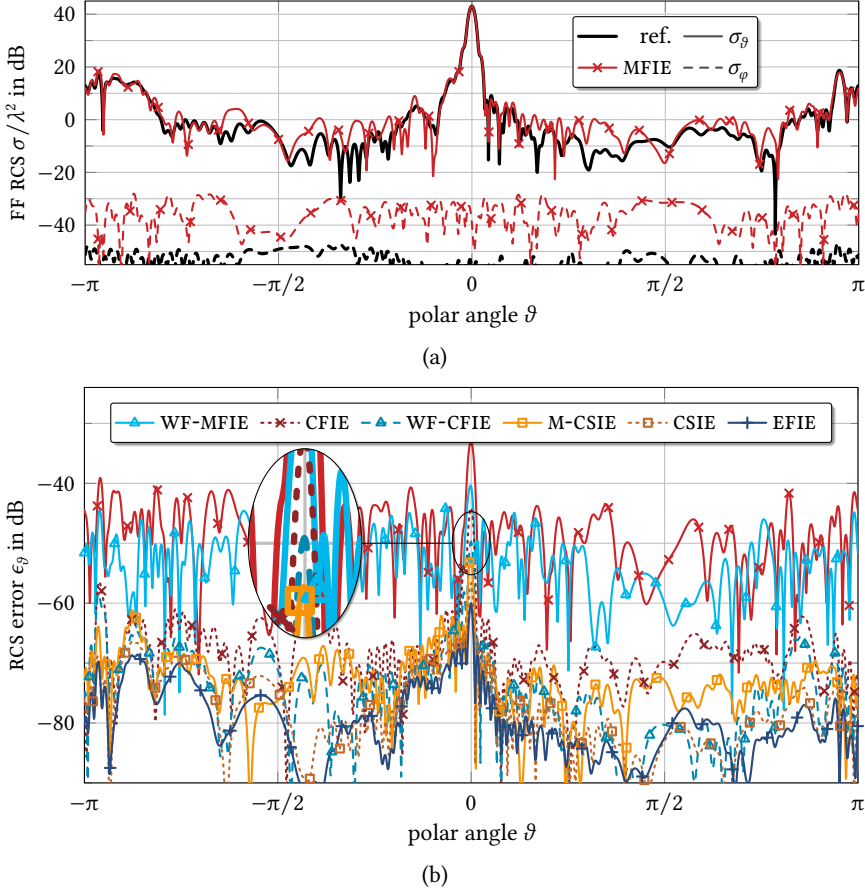


Fig. 4.32: Bi-static RCS and RCS errors for plane-wave scattering from a PEC Flamme at 12 GHz with $\mathbf{k} = -k\mathbf{u}_z$, shown for various IEs, $\varphi = 0$. (a) Bi-static RCS of the reference and the MFIE solutions. (a) Error for the σ_θ component.

63.4 CG iterations with 0.59 ms per MVP. Similarly for the WF-CFIE with different right-hand sides for the Gram matrix inversions, the CG solver converges within 67.8 iterations and 0.0378 s on average, with about the same 0.58 ms per MVP. The CPU time taken by one complete CSIE MVP (including magnetic currents, without exploiting symmetries) is 4.98 s; the time for one WF-CFIE MVP is 2.42 s; both running on a single thread. The time taken by the Gram matrix inversion contributes about 0.78% and 1.6%, which is more or less negligible.

Figure 4.32 shows the RCS in the $\varphi = 0$ cut plane and the error of various IEs for the dominant σ_θ component—the error for the σ_φ component is much lower for

all solutions in this cut. As seen in Fig. 4.32(a), even the most inaccurate solution (obviously the classical MFIE) shows a much better agreement with the reference solution for this incident wave. Clearly, the illumination of the scatterer matters; and here we consider a less challenging scenario. Visually apparent deviations in the RCS magnitude are only seen at about 40 dB below the peak, i.e., below the large mono-static RCS. The error of the dominating σ_{ϑ} -component of the RCS is shown in Fig. 4.32(b). Some differences are observed at the angle $\vartheta = 0$, where all solutions show their largest error. In the other regions, all IEs except for the two MFIEs are doing fairly well. The maximum errors of the MFIE, WF-MFIE, CFIE, WF-CFIE, M-CSIE, CSIE, and EFIE as -33.1 dB, -40.4 dB, -44.1 dB, -49.7 dB, -52.4 dB, -56.6 dB, and -60.0 dB, respectively. The average errors are all much lower, viz. -53.3 dB, -56.4 dB, -70.9 dB, -75.7 dB, -76.5 dB, -81.0 dB, and -83.1 dB. Just as for the first incident wave, the WF-CFIE offers accuracy improvements over the classical CFIE, but the CSIE comes somewhat closer to EFIE accuracy levels.

Airbus Airplane

Another electrically larger scatterer is a PEC airplane Airbus A320 with 756 288 RWG unknowns at 470 MHz ($\lambda \approx 0.64$ m), with a total object length of about 38 m in z -direction, a span of 36 m in x -direction, and a height of 12 m in y -direction [Kornprobst and Eibert 2018e]. The average triangle edge length h is about 0.1λ . The model is simulated for plane wave incidence with $\mathbf{k} = -k\mathbf{u}_z$ and $\mathbf{p} = \mathbf{u}_x$ polarization, hitting the airplane from the front. The MVP is accelerated by the MLFMM with $D_0 = 5$ and a box size of 0.2λ . For the iterative solution with GMRES, an inner-outer preconditioning scheme, with 20 iterations in the first inner loop and 10 iterations in the innermost loop, is employed. Additionally, all system matrices are diagonally preconditioned. In case of the WF-CFIE, the standard CFIE matrix diagonal is employed. In case of the CSIE, the standard EFIE matrix diagonal is employed. The reference solution is calculated on a refined mesh (3 025 152 RWG unknowns) with the CFIE and $\chi_{\text{CF}} = 0.999$.

The CFIE converges within 24 iterations of the outer GMRES solver to a residual of 10^{-5} , the WF-CFIE within 25 iterations, and the CSIE within 30, while the EFIE takes 300 iterations to converge to a residual of just $2 \cdot 10^{-5}$.

The bi-static RCS in the $\varphi = \pi/2$ cut plane is shown in Fig. 4.33. Even the CFIE solution is at least visually indistinguishable from the reference except for some parts of the cross-polarization σ_{ϑ} . The cross-polarization exhibits such a small magnitude that its error is much lower than for the co-polarization, which is why only ϵ_{φ} is shown in Fig. 4.33(b). The CFIE shows a maximum/average relative error of -48.0 dB/ -73.1 dB, while the WF-CFIE is more accurate by about 10 dB with -57.1 dB/ -82.2 dB. The CSIE performs another 10 dB better regarding the maximum error, but only a couple of decibels better regarding the average error

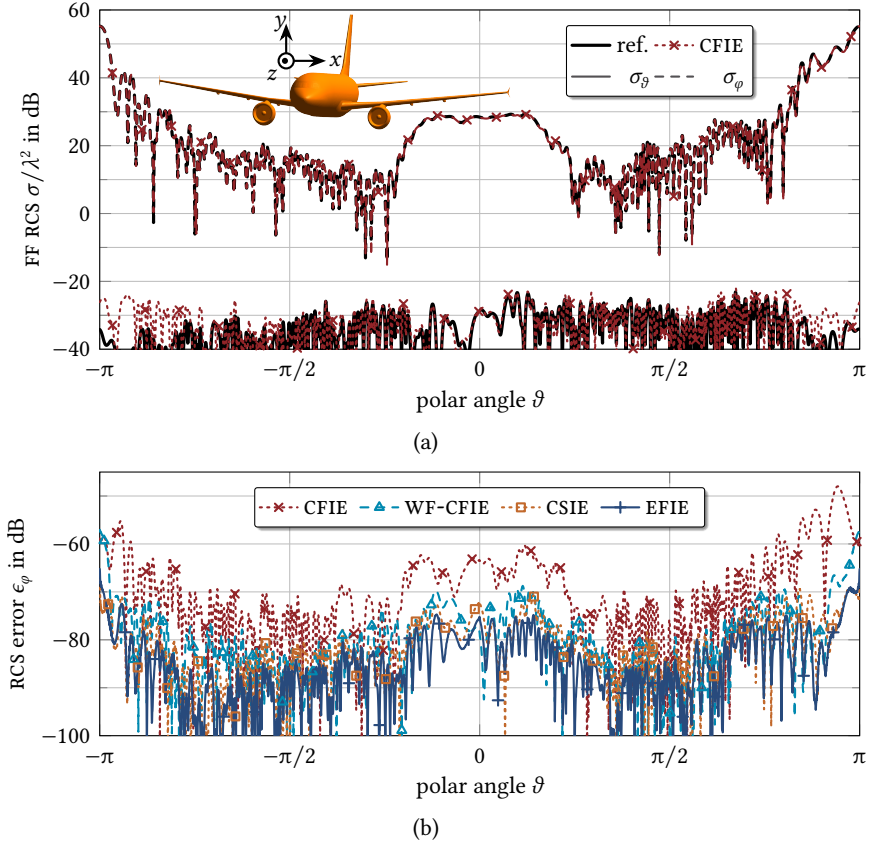


Fig. 4.33: Bi-static RCS and RCS errors for plane-wave scattering from a PEC Airbus airplane at 150 MHz with $\mathbf{k} = -k\mathbf{u}_z$, errors shown for various IEs, $\varphi = \pi/2$. (a) Bi-static RCS of the reference and MFIE solutions. (a) Error for the σ_φ component.

with -67.6 dB/ -86.1 dB. The EFIE has a slightly worse maximum error, but the best average one with -65.2 dB/ -88.7 dB.

For a further analysis of this scattering scenario regarding other choices of the CF/CS weighting factors, including the MFIEs and a CSIE with dominant magnetic currents, we refer to Section 4.6.

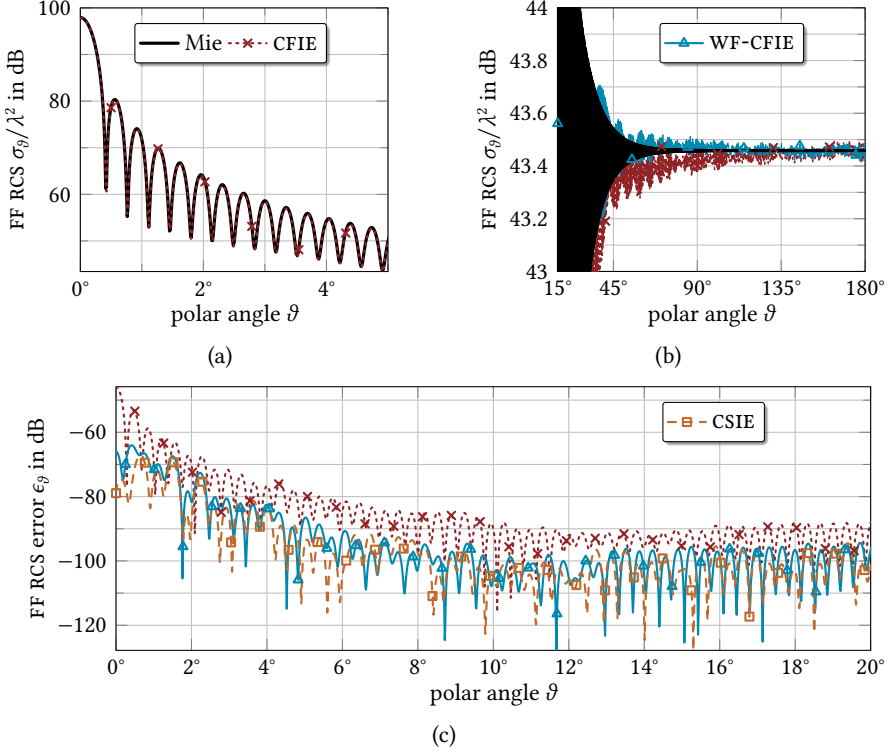


Fig. 4.34: Bi-static RCS and RCS errors for plane-wave scattering from a 168λ sphere with $\mathbf{k} = k\mathbf{u}_z$, errors shown for various IEs, $\varphi = 0$. (a), (b) Bi-static RCS of the Mie series and the (WF)-CFIE solutions. (c) Error for the dominant σ_{ϑ} component.

An Electrically Large Sphere

Last but not least, a PEC sphere with 168λ diameter, 0.1λ mean edge length discretization, and 30 631 608 RWG unknowns is simulated for a plane wave with $\mathbf{p} = \mathbf{u}_x$ polarization and $\mathbf{k} = k\mathbf{u}_z$ incidence. The MVP is accelerated by the MLFMM with a box size on the lowest level of 0.1λ and an accuracy parameter of $D_0 = 5.5$. With an inner-outer preconditioned GMRES solver with a termination threshold of 10^{-4} , all three considered interior-resonance free IEs converge within 4 iterations. The final residual of the CFIE is $1.36 \cdot 10^{-4}$; the WF-CFIE exhibits $1.78 \cdot 10^{-4}$ and the CSIE $3.13 \cdot 10^{-4}$. Though not visible in the small number of iterations, the residuals tell the same story about the conditioning of the system matrices as before.

In Fig. 4.34, the bi-static co-polarized RCS of the three interior-resonance free IEs

is compared to the Mie series reference. Since the RCS shows the largest magnitude in the shadow region (around $\vartheta = 0$), the error levels are dominated by the RCS in this region. The CFIE error is generally larger, which is visible in Fig. 4.34(b) and Fig. 4.34(c). The RCS and RCS errors are only shown in selected angular ranges due to the strong fluctuations and the large dynamic range.

The classical CFIE shows a maximum error of -45.8 dB and an average error of -98.7 dB, while the WF-CFIE shows errors of only -61.5 dB and -104.5 dB. The CSIE performs slightly better with -62.8 dB and -105.4 dB. Note that the average errors of the WF-CFIE and the CSIE are limited by the chosen MLFMM accuracy parameter.

As for the previous considered scenarios, the CSIE shows the best accuracy with the same choice of $\chi = 0.5$, closely trailed by the WF-CFIE but with a somewhat slower iterative solver convergence.

4.5.2 Stability at Interior Resonances

For HF boundary IEs applied to objects spanning more than about 0.5λ , interior resonances may occur and negatively affect the iterative solver convergence and the solution accuracy if no countermeasures are taken. This problem is studied in this subsection for all proposed IEs and the conventional RWG discretizations.

Looking at the First Two Resonance Frequencies of a Sphere

We revisit the scattering scenario discussed in Fig. 4.3: Plane-wave scattering from a 1-m diameter PEC sphere with 999 unknowns, where the MOM systems of equations are solved by the GMRES method to a threshold of 10^{-5} . The considered frequency range goes from 200 MHz to 400 MHz, covering the first two interior resonances of a PEC sphere with free-space background. The average triangle edge length of the mesh ranges from 0.07λ to 0.14λ .

Figure 4.35 shows the obtained error levels, the iterative solver convergence, and the system matrix condition numbers of the RWG-discretized SIEs. Figure 4.35(a) analyses the relative arithmetically averaged FF RCS error with respect to a solution obtained by a Mie series expansion. As noted in previous discussions of scattering results, the issue here is that the models do not match: The Mie series assumes a perfect 1-m diameter sphere and the IEs are calculated on a discretized boundary of an effectively smaller body. One approach is to calculate the Mie series solution for a smaller sphere. An appropriate value here might be a diameter of 0.996 m. However, the two surfaces would still not coincide.

Hence, a 1.5th order EFIE solution on a refined mesh is taken as the reference in Fig. 4.35(b) for the RWG-based discretizations and in Fig. 4.36(a) for the mixed discretization schemes. Error levels drop by about 10 dB for the more accurate IEs; and more distinct differences between the IEs become apparent. In more detail,

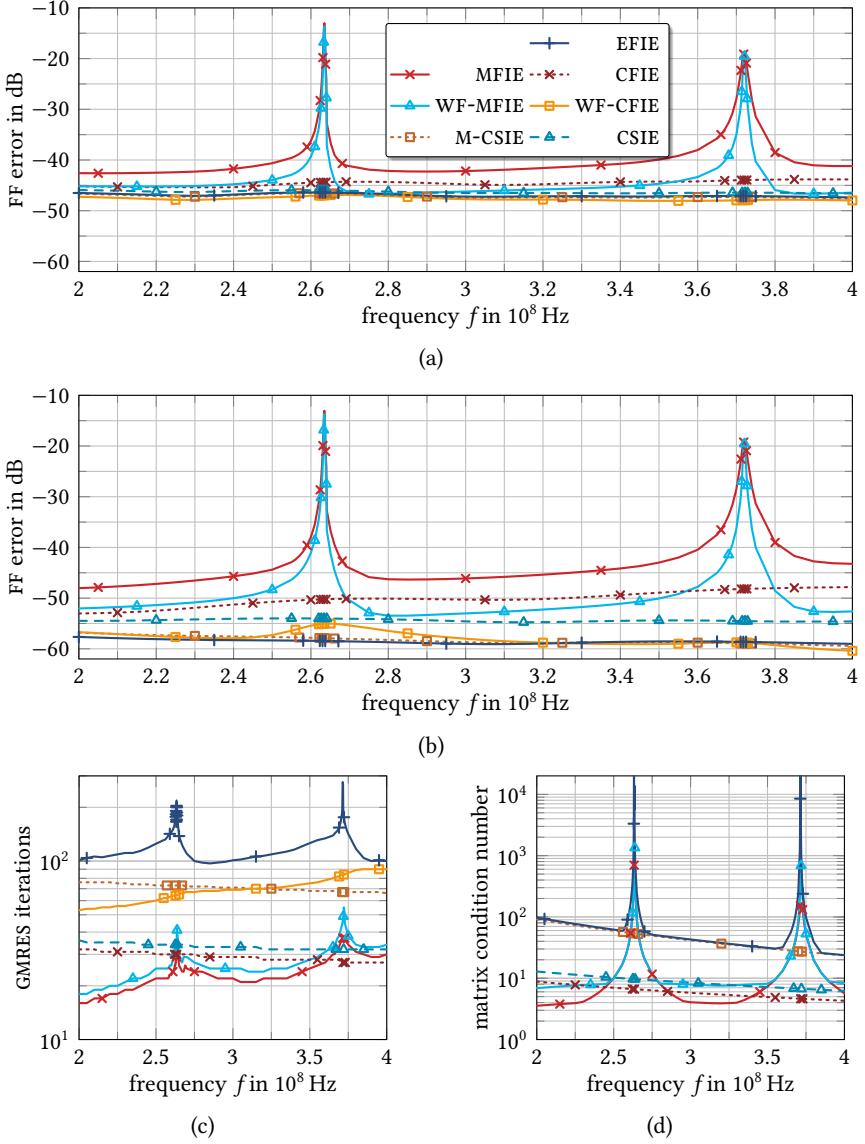


Fig. 4.35: Analysis of the accuracy and conditioning of classical RWG SIEs and WF RWG SIEs around the first two interior resonance frequencies of a PEC sphere. (a) Average FF RCS errors w.r.t. to a Mie series reference. (b) Average FF RCS errors w.r.t. to a HO EFIE reference on a refined mesh. (c) Number of GMRES iterations to 10^{-5} . (d) System matrix condition numbers.

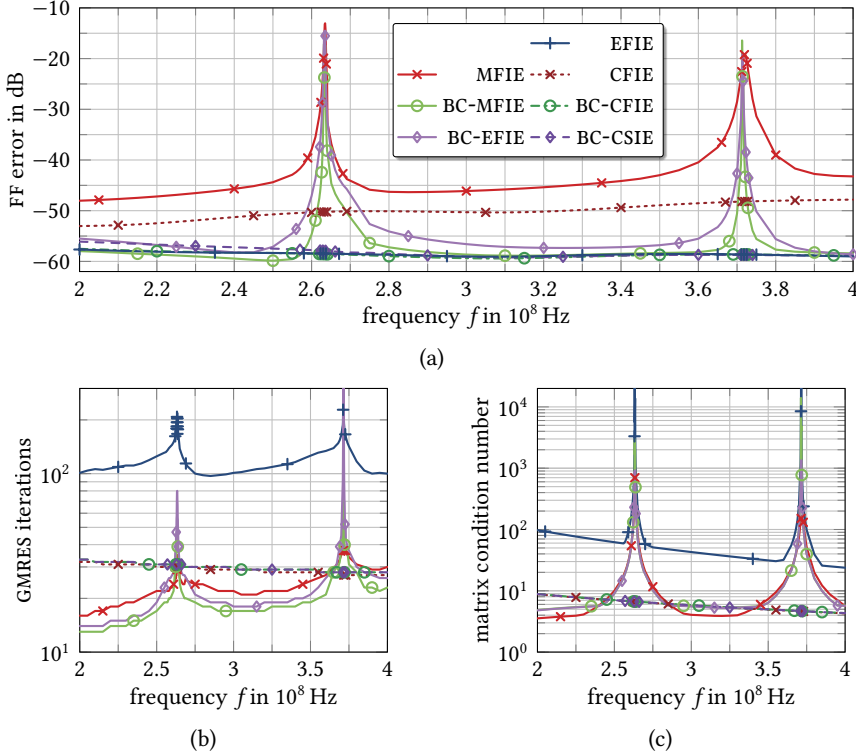


Fig. 4.36: Analysis of the accuracy and conditioning of classical RWG SIEs and mixed-discretization SIEs around the first two interior resonance frequencies of a PEC sphere. (a) Average FF RCS errors w.r.t. to a HO EFIE reference on a refined mesh. (b) Number of GMRES iterations to 10^{-5} . (c) System matrix condition numbers.

the classical MFIE shows the worst accuracy with a “base level” of around -45 dB and severely worsened accuracy around the interior resonance frequency. The effect of the parasitic exterior solution (cf. the discussion of interior resonances in Subsection 2.5.2) is noticeable, leading to errors up to -13 dB at 263.5 MHz.² The WF-MFIE (in Fig. 4.35) and also the BC-MFIE (in Fig. 4.36) show the same worst-case error at the same frequencies albeit with a lower bandwidth—indicating that the parasitic exterior solution is excited in the same manner. The erroneous solution shows a smaller bandwidth though and the WF-MFIE error comes close to EFIE

2. Around the interior resonance frequency, the frequency sampling step is chosen as 0.1 MHz; except for the EFIE, whose accuracy is less sensitive and, hence, the sampling step is reduced to 0.001 MHz in the critical regions.

levels of below -50 dB when the influence of the interior resonances is negligible. Only the RWG M-CSIE and the BC-MFIE as well as the BC-EFIE achieve to reach the EFIE error, though.

This translates to the CFIE error levels. The classical CFIE with $\chi_{CF} = 0.5$ is influenced by the inaccurate MFIE and reaches on average an error of about -50 dB. The WF-CFIE comes closer to the EFIE error levels (e.g., 3 dB worse at 200 MHz). The CSIE ($\chi_{CS} = 0.5$), BC-CFIE ($\chi_{CF} = 0.5$), and BC-CSIE ($\chi_{CS} = 0.5$) are just as accurate as the EFIE with an error of about -58 dB. We observe the same for the M-CSIE ($\chi_{CS} = 1/11$), whose accuracy is only slightly influenced at the first interior resonance and not at all at the second one. Even though the EFIE is affected in its condition number and solver convergence, the interior resonances only have a minor effect on the error. Its error only slightly increases at very distinct frequencies, and this is even suppressed almost completely in the presented results by choosing very accurate quadrature rules and an effective singularity cancellation technique. Seen is a minor influence at the second resonance: At around 371.5 MHz, the error increases by 0.2 dB when simulating in 1 kHz steps. For lower-accuracy settings, the bandwidth of erroneous solutions increases and errors above -50 dB are easily observable.

The effect of interior resonances at the iterative solver convergence and the condition number of the EFIE system matrix is more severe—see Figs. 4.35(c) and 4.35(d), as well as Figs. 4.36(b) and 4.36(c). The EFIE shows the worst performance in this regard, in particular at interior resonances. The WF-MFIE and MFIE are also strongly affected (in particular regarding the condition number). The BC-MFIE and BC-EFIE are affected more, which is most probably due to the different implementation in the BEAST Julia package, for instance a different quadrature. Both even fail to converge at all at 371.5 MHz within 1000 GMRES iterations. While the condition numbers of BC-MFIE and BC-EFIE are lower than the one of the classical MFIE, the reverse is observed for the respective CFIE/CSIE condition numbers. The reason is found in the mappings from RWG to BC functions via the Gram matrices, which are only present in the CF/CS equations. The M-CSIE suffers from no negative effects, but the iterative solver convergence is rather slow. The condition number (not shown) is the exactly same as for the CSIE, since it is dominated by the lowest EFIE SVs. For both of them, the condition number is the same as the EFIE but without the increase around the interior resonance frequencies. However, only the CSIE keeps the increasing number of solver iterations with increasing frequency well under control. A similar effect is observed for both CFIEs, albeit at a much better conditioning. The WF versions of the MFIE and the CFIE performs slightly worse than the standard versions, but the observed behavior is otherwise the same.

Overall, the BC-CFIE, the BC-CSIE, the CSIE, and the WF-CFIE are able to cope with the interior resonance problem in a similar manner as the CFIE such that the non-trivial interior-resonance null space is removed and the problem becomes

well-posed. The increase in iterative solver iterations and condition number is well under control for all four IEs. The BC-CFIE and BC-CSIE stand out since they achieve EFIE accuracy with the lowest increase with regard to the condition number solver iterations. The number of iterations is increased just by one as compared to the classical CFIE, whereas the WF-CFIE takes three to five iterations more and the CSIE is even slower. However, the at least six-fold increased computational effort of the matrix setup and potentially each MVP has to be kept in mind. The CSIE is able to offer the same excellent accuracy albeit at the cost of more than double the iterations to convergence. The WF-CFIE comes quite close to the EFIE error levels at an only minor cost regarding the conditioning.

Frequency Sweep for Flamme

For an electrically larger and geometrically more challenging scattering scenario, we look again at the stealth object Flamme from Subsection 4.5.1. The simulation settings are chosen just as in Subsection 4.5.1 for the scattering from a plane wave with $\mathbf{k} = k\mathbf{u}_x$ at 10 GHz; however, the simulation frequency is swept from 8 GHz to 12 GHz in steps of 50 MHz. The results regarding error levels and iterative solver convergence are shown in Fig. 4.37.

Studying the iterative solver convergence in Fig. 4.37(a) reveals several interesting aspects. The classical MFIE suffers much less from fluctuating convergence levels than the EFIE and the WF-MFIE. It is noteworthy that the WF-MFIE struggles with an increasing number of iterations with increasing frequency similar to the EFIE and M-CSIE. Opposed to this, all three interior-resonance free IEs show a downward trending number of iterations with increasing frequency. This decrease is not monotonous, though; at around 10 GHz, we observe an increased number of iterations for all of these IEs and the M-CSIE.

For both the average error in Fig. 4.37(b) and the maximum error in Fig. 4.37(c), the most interesting observation is made for the WF-MFIE. At 8.3 GHz, the error is quite large—an interior resonance hits the solution much harder for the WF scheme. The WF-CFIE is unaffected by this and shows a stable behavior. In general, the WF-MFIE is more accurate than the MFIE. The WF-CFIE is more accurate than the CFIE, both in the range of 5 dB to 10 dB. The M-CSIE exhibits errors close to the WF-CFIE and the CSIE performs better by about 10 dB—on a similar level as the EFIE. It remains to be investigated which choices of χ_{CF} and χ_{CS} offer the fastest convergence rate at the best, EFIE-alike accuracy.

An Electrically Larger, Overmoded Sphere

For electrically larger scattering scenarios, the interior resonance problem becomes more severe. Effectively, there is an influence of some neighboring interior reso-

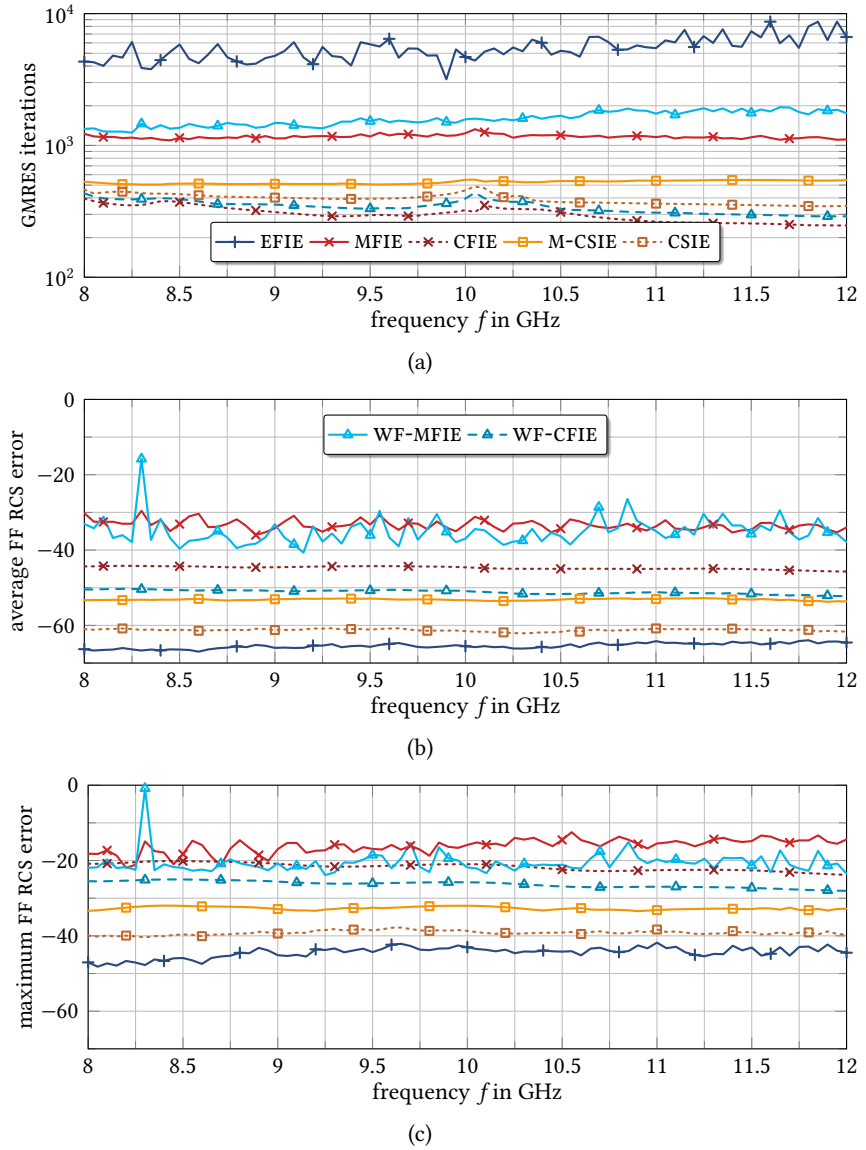


Fig. 4.37: Analysis of the accuracy and iterative solver convergence of various SIEs for the PEC Flamme. (a) Number of GMRES iterations to 10^{-5} . (b) Average relative FF RCS errors w.r.t. to a HO CFIE reference. (c) Maximum relative FF RCS errors w.r.t. to a HO CFIE reference.

nance at every simulation frequency. We consider again a 1-m diameter sphere, which is now meshed much finer leading to 242 238 RWG unknowns for both electric and magnetic surface currents [Kornprobst and Eibert 2017b]. The MVP is accelerated by the MLFMM with an accuracy parameter $D_0 = 5.5$ and a box size of 0.25λ . At a frequency of 4.42 GHz, the mean edge length h of the utilized triangular mesh is approximately $\lambda/10$ and the diameter is about 14.7λ . In order to examine the interior resonance problem, the frequency is swept from 4 GHz to 5 GHz in steps of 5 MHz.

Figure 4.38(a) shows the number of iterations which the GMRES solver takes for convergence to a threshold of 10^{-5} . The EFIE, MFIE, and WF-MFIE show strong fluctuations dependent on the simulation frequency; the M-CSIE also but somewhat reduced with $\chi_{cs} = 1/11$. The EFIE fares by far worst with the number of GMRES iterations almost always above 10^3 . In some cases, this also has minor consequences for the FF error, see Fig. 4.38(b) for the average error, and in particular Fig. 4.38(c) for the maximum error, which is worsened by a couple of decibels at a few frequencies. The MFIE and WF-MFIE converge within a couple of hundred iterations; the WF-MFIE always performs slightly worse. This results in a significantly faster solution time than for the EFIE at any of the considered frequencies. However, the FF error is significantly affected for both of them by the erroneous exterior contribution of the interior resonances, while the WF-MFIE beats the MFIE handily at almost any frequency. The M-CSIE does not suffer as much from interior resonances due to its EFIE part (converging within around 200 iterations), which also has the effect that its accuracy is on almost the same level as the CSIE with $\chi_{cs} = 0.5$.

The three interior-resonance-free formulations show a stable behavior: Their iterative solver convergence is not affected by the choice of the solution frequency. The classical CFIE converges within the lowest number of iterations, between 61 and 63, closely trailed by the WF-CFIE with 68 or 69 iterations to convergence. The CSIE falls a bit behind with 122 to 124 iterations. All of them beat the IEs suffering from interior resonances regarding the pure number of iterations.³

The classical CFIE shows an about 11 dB worse average error and an about 35 dB worse maximum error than the EFIE. The WF-CFIE trails the EFIE by less than 5 dB for the average error and 15 dB for the maximum error. The CSIE fares better than the EFIE regarding the average error by up to two decibels but trails the EFIE by about 5 dB for the maximum error. While a similar behavior (a benefit for the CSIE) has been observed previously—for instance in Fig. 4.19—, it remains to be seen whether this is really the case or whether this is an artifact of employing the not

3. Note that one iteration of the CSIE contains two MVPs for the electric and magnetic current unknowns, respectively. This means doubled computational effort per solver iteration even if the symmetric parts of the matrices are stored efficiently and only the memory of one full matrix is occupied. Hence, the computation time spent for the CSIE and the MFIE/CFIE is similar.

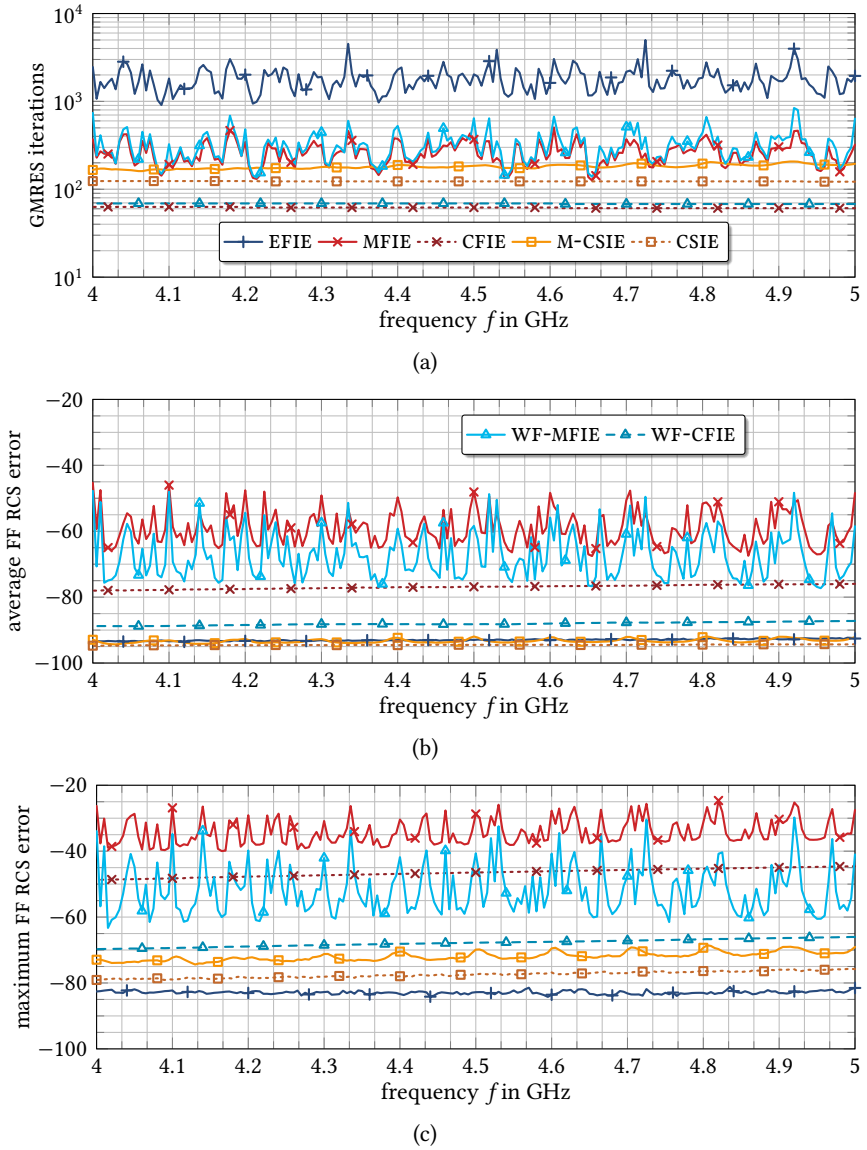


Fig. 4.38: Analysis of the accuracy and iterative solver convergence of various SIEs for a 1-m diameter PEC sphere. (a) Number of GMRES iterations to 10^{-5} . (b) Average relative FF RCS errors w.r.t. to a Mie series reference. (c) Maximum relative FF RCS errors w.r.t. to a Mie series reference.

Tab. 4.3: Error level comparison with Mie and HO references for the 1-m diameter PEC sphere at 5 GHz.

reference solution	Mie series		HO CFIE, $\chi_{CF} = 0.999$	
	ϵ_{avg}^{FF}	ϵ_{max}^{FF}	ϵ_{avg}^{FF}	ϵ_{max}^{FF}
MFIE	-48.4 dB	-27.5 dB	-51.8 dB	-27.1 dB
CFIE	-76.2 dB	-44.8 dB	-78.0 dB	-44.6 dB
WF-MFIE	-58.5 dB	-41.1 dB	-60.9 dB	-41.1 dB
WF-CFIE	-87.0 dB	-66.6 dB	-88.8 dB	-64.0 dB
M-CSIE	-92.9 dB	-71.2 dB	-97.3 dB	-71.9 dB
CSIE	-94.8 dB	-76.1 dB	-100.3 dB	-71.2 dB
EFIE	-92.6 dB	-81.4 dB	-98.2 dB	-79.7 dB

perfectly matching Mie series reference solution.

In order to investigate this, a 1.5th order CFIE solution with $\chi_{CF} = 0.999$ on a refined mesh is taken as another reference solution. The number of unknowns increases to 3 229 840. In addition to diagonal preconditioning, an inner-outer preconditioning scheme was employed with 25 iterations on a second level and 10 iterations on the third, innermost level. The preconditioned GMRES solver converged to 10^{-7} after 226 iterations. This solution was only calculated at a frequency of 5 GHz. Table 4.3 gives an overview over the error levels of the various IEs at that frequency. While most results only differ by a couple of decibels and the observations are the same as for previous scenarios, the EFIE exhibits a lower average FF error than the M-CSIE with the better reference solution (and closes the gap to the CSIE halfway). The average errors of the CSIE and the EFIE are so close to the expected minimum given by the MLFMM accuracy parameter $D_0 = 5.5$ that no real insight is found here except that they are all rather accurate. Overall, we find that the Mie series offers an acceptably accurate reference solution for this electrically larger sphere, where the surface discretization error takes a back seat.

4.5.3 Summary

All CF and CS formulations involving both the EFIE and MFIE operators are shown to be interior-resonance free; they give rise to well-posed systems of equations. This includes the classical RWG CFIE, the RWG WF-CFIE, the RWG CSIE, as well as the BC-CFIE and the BC-CSIE with a mixed discretization. Three formulations are able to achieve an accuracy close to the EFIE for smooth surfaces but suffer a bit from edges in the geometry: the RWG CSIE, the BC-CFIE, and the BC-CSIE. The WF-CFIE falls a bit behind in terms of accuracy.

Regarding the bare number of iterations and in terms of the condition number, only the WF-CFIE, the BC-CFIE, and the BC-CSIE are able to come very close to the classical CFIE; the very accurate RWG CSIE falls a bit behind. Hence, the formulation with mixed RWG/BC functions seem clearly favorable. Once the time to solution comes into play, the picture changes. The mixed-discretization formulations suffer from the issue of increased computational effort. The choice of the best formulation is, hence, not obvious; especially since the choice of the CF/CS weighting factor χ also influences the accuracy for the less accurate equations.

4.6 The Trade-Off between Accuracy and Conditioning

In a world with just the classical versions of the RWG EFIE, MFIE, and CFIE, one will employ the CFIE necessarily for the computation of large scattering scenarios since the accurate EFIE does not converge on its own due to the conditioning problems associated with interior resonances, dense meshes, and HFs. However, one will also fear the negative impact of the MFIE on the solution accuracy. Hence, the CFIE combination factor is commonly chosen rather large in order to reduce the influence the impact of the MFIE solution. Typical values might be $\chi_{CF} = 0.99$ or even $\chi_{CF} = 0.999$ —values which we have also considered when calculating (HO) reference solutions (on refined meshes).

In this chapter, two approaches to solve the MFIE accuracy issues and the interior resonance problem simultaneously with only RWG functions have been discussed so far: the RWG CSIE and the CFIE with a WF weighting scheme for the discretization of the identity inside the RWG-MFIE. Furthermore, the mixed discretization schemes of the BC-CFIE and the BC-CSIE also solve both issues. As we have seen in the previous section in particular, all of these discussed approaches are able to cope excellently with the interior resonance problem. However, differences in the iterative solver convergence behavior, the involved computational effort, and the accuracy have been observed. The choice between the four IEs—or just the CSIE and the WF-CFIE with RWG functions only—is hence not really obvious since the WF-CFIE comes out on top regarding conditioning but the CSIE shows the superior accuracy; the two IEs with a mixed discretization combine the best accuracy with best conditioning but exhibit higher computational effort; all with $\chi = 0.5$. In the following, we analyze the optimal choice of the respective combination factors χ_{CS} and χ_{WF-CF} when the goal is to maintain EFIE-alike accuracy levels for electrically large scattering and radiation scenarios. One insight is already known from the discussion so far: All four discussed approaches offer far better trade-offs between solution accuracy and time to convergence than the classical CFIE.

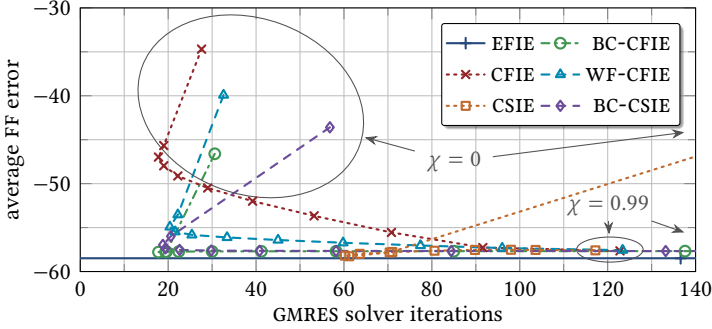


Fig. 4.39: Analysis of CFIE, WF-CFIE, CSIE, BC-CSIE, and BC-CFIE error levels and iterative solver convergences for varying weighting factors χ , scattering from a sphere around the first interior resonances.⁴

4.6.1 Electrically Smaller Sphere

As a first scenario, we look at the 1-m diameter PEC sphere with 999 RWG unknowns which was already investigated previously. The same scenario is the same as in Subsection 4.5.2 and we consider three frequencies, which are not affected by interior resonances, -2 GHz, 3 GHz, and 4 GHz—and two further frequencies which are close to interior resonances, cf. Fig. 4.35 on p. 98— 2.635 GHz and 3.72 GHz. The error levels and GMRES solver iterations are geometrically/arithmeticly averaged for the results obtained at those five frequencies.

Figure 4.39 shows the solver iterations and (twice) averaged error levels of the five interior-resonance free IEs for weighting factors χ ranging from 0 to 0.9 in steps of 0.1 and one additional data point at 0.99 . The maximum and average EFIE errors are at -52.0 dB and -58.5 dB, and its average iteration count to convergence is 136.6 —which is included as a baseline in Fig. 4.39. The versions with only the MFIE operators are included at $\chi = 0$. The fastest convergence of the CFIE is observed at $\chi_{CF} = 0.2$ with 17.8 iterations and maximum/average errors of -35.7 dB/ -47.0 dB. The WF-CFIE converges a bit slower but is generally more accurate: The fastest convergence is observed also at $\chi_{WF-CF} = 0.2$ with 20.4 iterations (about 15% more) and a maximum/average errors of -44.5 dB/ -54.9 dB (about 8 dB better). The CSIE shows its fastest convergence at $\chi_{CS} = 0.3$ with 60.2 iterations (238% more than the

4. Note that the convergence of the two BC-based IEs is slower than the one of the EFIE for large values of χ ; the reason being the BEAST implementation in particular around interior-resonance frequencies. In particular for the highlighted value of $\chi = 0.99$, the BC-CSIE converges only within 372.6 iterations on average and the BC-CFIE converges within 435 iterations. The pure EFIE—with the same code as used for the CFIE, WF-CFIE, and CSIE—converges in just 122.8 iterations to the same residual of $1 \cdot 10^{-5}$. The other SIEs take fewer iterations to convergence than the EFIE, except for the CSIE at $\chi = 0$, which suffers from the non-trivial null space of $\mathbf{G}_{\alpha,\beta}$.

CFIE) and errors of -49.7 dB/ -58.3 dB—about more than 10 dB better than the CFIE and very close to the EFIE error. Note that the CSIE with only the MFIE operator does not converge well due to the non-trivial null space in the matrix—the average number of iterations to convergence is 378.4 and the error goes up to -9.5 dB.

It is not fully clear yet whether the minor accuracy advantage of the CSIE over the WF-CFIE is systematic or just “noise.” The latter achieves the same number of iterations (close to 60) at $\chi_{\text{WF-CF}} = 0.7$, with errors of -47.8 dB/ -56.4 dB—that is only 2 dB worse than the CSIE/EFIE. Accepting an additional error of 1 dB, the iteration count is reduced to a third.

For this electrically small scenario, the BC-CFIE and the BC-CSIE are also included in the analysis. For larger scenarios, this is not possible due to missing acceleration in the employed Julia package BEAST. Just as the CSIE, the BC-CFIE stays close to the EFIE error level except for $\chi_{\text{BC-CF}} = 0$, i.e., the pure MFIE solution. The fastest convergence is found with $\chi_{\text{BC-CF}} = 0.2$ and 17.8 iterations to convergence, where the solution exhibits maximum/average errors of -49.6 dB/ -57.8 dB. The BC-CSIE shows a comparable behavior but with a slightly worse accuracy and slightly slower solver convergence. The fastest convergence is observed again at $\chi_{\text{BC-CS}} = 0.2$ and with 18.8 iterations to convergence. The maximum/average errors at this weighting read -48.8 dB/ -57.0 dB. As mentioned previously, the matrix setup and each MVP are computationally more costly than for the other IEs and the look at the iteration count favors the BC-CFIE spuriously. If we assume a six-fold increase in computational effort as a reasonable estimate for an accelerated solver, both mixed-discretization formulations perform clearly worse than the RWG CSIE.

4.6.2 Stealth Object Flamme

The next scattering scenario is the stealth object Flamme first discussed in Subsection 4.5.1. We consider the incident plane wave with $\mathbf{k} = k\mathbf{u}_x$ at the frequencies 8 GHz, 9 GHz, 10 GHz, 11 GHz, and 12 GHz; and the incident plane wave with $\mathbf{k} = -k\mathbf{u}_z$ at the frequencies 8.5 GHz, 9.5 GHz, 10.5 GHz, and 11.5 GHz. As a baseline, the EFIE converges within an average of 5057.4 iterations and shows an average error of -72.9 dB.

Figure 4.40 shows the simulation results for varying χ from 0 to 0.9 in steps of 0.1 and the additional points 0.94 and 0.98. The CFIE shows the fastest convergence for $\chi_{\text{CF}} = 0.2$ with 281.3 iterations and an average FF error of -51.6 dB. The WF-CFIE shows the fastest convergence at $\chi_{\text{WF-CF}} = 0.4$ with 304.7 iterations and an average FF error of -58.8 dB. The CSIE also shows the fastest convergence at $\chi_{\text{CS}} = 0.3$ with 323.2 iterations and an FF error of -67.1 dB. Overall, the WF-CFIE is about 5 dB (or slightly more) more accurate as the CFIE, and the CSIE shows an improvement of another 10 dB.

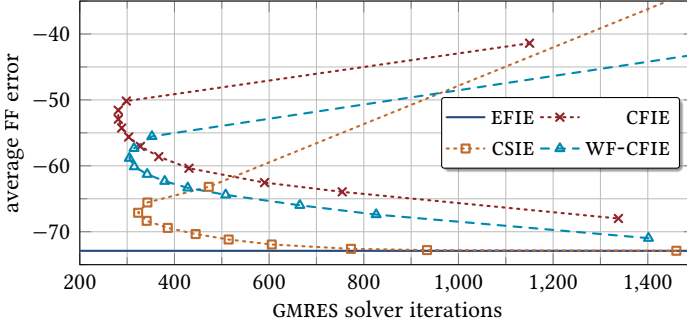


Fig. 4.40: Analysis of CFIE, WF-CFIE, and CSIE accuracies and iterative solver convergences for varying weighting factors χ , scattering from Flamme.

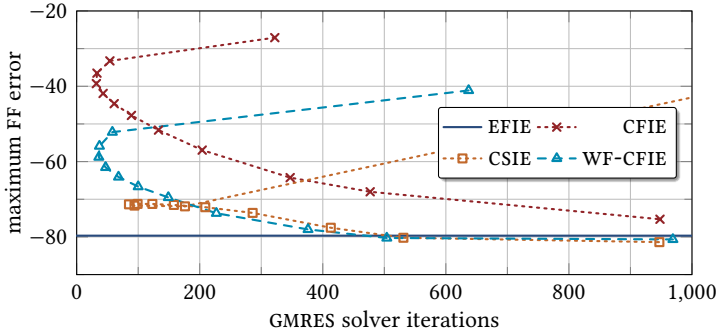


Fig. 4.41: Analysis of CFIE, WF-CFIE, and CSIE accuracies and iterative solver convergences for varying weighting factors χ , scattering from a sphere with 16.7λ diameter.

4.6.3 Electrically Larger Sphere

The next scattering scenario is the sphere from Subsection 4.5.2 with 242 238 RWG unknowns at a simulation frequency of 5 GHz, i.e., the sphere exhibits a diameter of 16.7λ . Since the accuracy in general is limited by the MLFMM settings, see Tab. 4.3, we look at the more meaningful maximum error. Figure 4.41 shows the simulation results for varying χ from 0 to 0.9 in steps of 0.1 and the additional points 0.94 and 0.98. The choices for the fastest convergences are as follows. The CFIE with $\chi_{CF} = 0.3$ converges within 32 iterations and shows a maximum/average FF errors of -39.3 dB/ -72.8 dB. The WF-CFIE with $\chi_{WF-CF} = 0.3$ converges within 36 iterations and shows a maximum/average FF errors of -58.3 dB/ -83.7 dB—about twenty and ten decibels lower. The CSIE with $\chi_{CS} = 0.3$ converges within 85 iterations and shows an maximum/average FF errors of -71.4 dB/ -100.1 dB—about twenty and

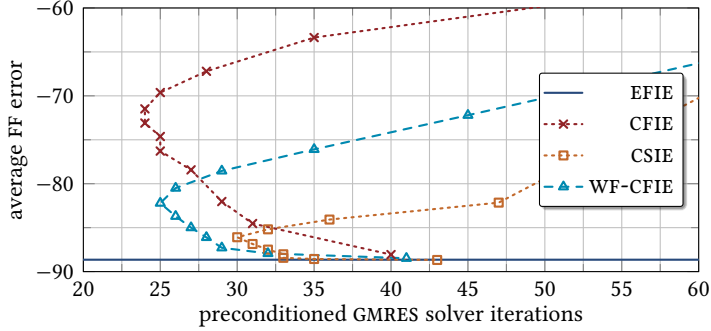


Fig. 4.42: Analysis of CFIE, WF-CFIE, and CSIE accuracies and iterative solver convergences for varying weighting factors χ , scattering from the airplane.

ten decibels lower. Except for the choice $\chi_{\text{CS}} = 0$, the CSIE offers the most accurate solution. The WF-CFIE is able to catch up in terms of accuracy and iterations for $\chi_{\text{WF-CF}} \geq 0.7$.

4.6.4 Airbus Airplane

Scattering from a PEC airplane with 756 288 RWG unknowns has already been discussed in Subsection 4.5.1. We re-investigate the scenario with the same settings. We recall that the GMRES solver is preconditioned with an inner-outer scheme and that the EFIE did only converge to $2 \cdot 10^{-5}$ within 300 iterations. This EFIE solution gives -88.6 dB as baseline for the average error of the solution. The weighting parameter χ is swept from 0.0 to 0.9 in steps of 0.1, and in steps of 0.04 up to $\chi = 0.98$. In Fig. 4.42, the results of this sweep are shown.

The CFIE shows the fastest iterative solver convergence between $\chi_{\text{CF}} = 0.4$ and 0.5 with 24 iterations for convergence to 10^{-5} . For $\chi_{\text{CF}} = 0.5$ (the better case), it exhibits an average RCS error of -73.1 dB. The WF-CFIE takes 25 iterations with $\chi_{\text{WF-CF}} = 0.5$, leading to an average error of -82.2 dB. The CSIE converges slower but does show the fastest convergence with $\chi_{\text{CS}} = 0.5$ (30 iterations), too. The error is a bit smaller with -86.1 dB but still 2.5 dB worse than the EFIE error. The fact that all three IEs show the fastest convergence at $\chi = 0.5$ clearly hints at the fact that, for large and overmoded objects, the equal weighting of EFIE and MFIE operators is more important than the better conditioning of the MFIE operator since the interior resonance problem becomes more severe.

The CFIE only achieves CSIE error levels with $\chi_{\text{CF}} = 0.96$ and 33 iterations to convergence, i.e., slower than the CSIE. The WF-CFIE is able to “beat” the CSIE with $\chi_{\text{WF-CF}} = 0.8$ and 28 iterations. Also for the considered values $\chi_{\text{WF-CF}}$ above

0.8, the WF-CFIE beats the CSIE in the combined consideration of error level and conditioning.

4.6.5 Summary

Overall, the CSIE and the WF-CFIE show comparable accuracy improvements over the classical RWG CFIE. The choices of $\chi_{\text{WF-CF}} \geq 0.8$ and $\chi_{\text{CS}} \geq 0.5$ seem reasonable in order to come close to EFIE accuracy at a much faster convergence rate. Both offer a more balanced approach than the classical CFIE, which may not even provide an accurate solution with $\chi_{\text{CF}} \geq 0.98$. If implemented efficiently (one full operator for the (WF-)CFIE and two symmetric ones for the CSIE), not only the iteration count to convergence but also the computational effort are comparable for appropriate choices of $\chi_{\text{WF-CF}}$ and χ_{CS} . From an implementation perspective, the WF-CFIE may offer the advantage that the involved singular integrals are the same as for the classical CFIE.

There is one major advantage to the use of the WF-CFIE. Retrieving a Love current solution offers a wider range of applications, for instance concerning the SIE part of the hybrid FE-BI method. The CSIE on the other hand has its own two potential benefits. One, the CSIE is able to cope better with inaccuracies of the MFIE operator for challenging scenarios (objects with sharp edges). Two, it does not suffer from the severe LF breakdown of the RWG-MFIE.

The theoretically more sound mixed-discretization schemes leading to the BC-CFIE and the BC-CSIE are favorable when looking just at accuracies and solver iteration counts, but they lose this advantage once the increased effort for the barycentric refinement of the mesh is considered.

4.7 Higher-Order Rao-Wilton-Glisson Discretization Schemes

In Subsection 3.2.2, we have mentioned employing HO expansion functions as one among many reported approaches to tackle the MFIE inaccuracy problem. Trintinalia and Ling [2001], Sun et al. [2001], Ismatullah and Eibert [2009b], L. Li et al. [2014b], Ylä-Oijala et al. [2005], Ergül and Gürel [2007], Gil and Conde-Pumpido [2020], and Kornprobst et al. [2021c] have demonstrated that div-conforming HO expansion approaches may improve the accuracy of both the EFIE and MFIE, where it remains unclear whether the MFIE inaccuracy issues are really completely resolved or only partially. Notably, Kornprobst et al. [2021c] have proposed to fix the HF RWG-MFIE by applying the WF discretization scheme for the discretized identity operator while working with classical div-conforming RWG testing functions and a hierarchical HO basis [Ismatullah and Eibert 2009a, 2009b; Ismatullah 2010; L.

Li et al. 2014b; L. Li 2016], which is only capable of fixing the MFIE inaccuracy in part. In this section, we propose hierarchical HO discretizations for the CSIE and the WF-MFIE. Just as for the LO case, numerical studies for various scattering demonstrate the accuracy, well-conditioning and the effectiveness to deal with the problem of interior resonances.

4.7.1 Higher-Order Combined-Source Integral Equation

It is straight-forward to extend the RWG CSIE implementation to the HO case. Ismatullah and Eibert [2009a, 2009b] have proposed a similar approach for the MFIE and the EFIE with a Leontovich IBC—both with the same HO expansion functions as discussed here. However, this implementation was done by a SC for the CS condition. As we have demonstrated in Subsection 4.1.3, this is a suboptimal implementation. Hence, we only consider the CSIE with an explicit inversion of the CS condition in each MVP according to (4.18). This equation reads, for the sake of completeness,

$$\left[\mathbf{T}_{\alpha,\beta} + \frac{1-\chi}{\chi} \left(\frac{1}{2} \mathbf{G}_{\alpha,\beta} - \mathbf{K}_{\alpha,\beta} \right) \mathbf{G}_{\beta,\beta}^{-1} \mathbf{G}_{\alpha,\beta} \right] \mathbf{i} = \mathbf{e}_{\alpha}. \quad (4.54)$$

Of course, the set of div-conforming basis functions β includes all HO functions up to order p ; and the rotated curl-conforming counterparts are denoted as α . The full set of magnetic currents is mapped onto a 90° rotated version by a WF rotation.

Such a discretization scheme for the CSIE is feasible for any set of HO expansion functions. There is no need to employ the particular set of hierarchical HO functions which we consider in this work.

4.7.2 Higher-Order Weak-Form Scheme for the Magnetic Field Integral Equation

The following investigations for the HO MFIE are tailored to the employed hierarchical HO functions. Other HO approaches, especially interpolatory ones, may not directly contain an RWG-alike subset of the functions. However, identifying and isolating the anisotropic influence of the RWG functions is crucially important to improve the accuracy of the HF MFIE as considered in this work.

Revisiting the Low-Order Case

The foundation of the proposed formulation is the WF identity operator discretization scheme for the RWG-MFIE, which was proposed in Section 4.3. In order to integrate this scheme with the hierarchical HO basis functions, we have to revisit the basic equations and name the occurring matrices more specifically as designated

for the RWG or LO part β_{LO} with $p = 0.5$. First, we have the WF basis transformation matrix based on (4.27)

$$\mathbf{W}_\gamma^{\text{LO}} = \gamma \mathbf{I}_{\text{LO}} + (1 - \gamma) \mathbf{R}_{\text{LO}} \quad (4.55)$$

with the identity matrix $\mathbf{I}_{\text{LO}} \in \mathbb{R}^{N_{\text{LO}} \times N_{\text{LO}}}$ as well as the twice-rotated WF identity matrix

$$\mathbf{R}_{\text{LO}} = -\mathbf{G}_{\beta_{\text{LO}}, \beta_{\text{LO}}}^{-1} \mathbf{G}_{\alpha_{\text{LO}}, \beta_{\text{LO}}} \mathbf{G}_{\beta_{\text{LO}}, \beta_{\text{LO}}}^{-1} \mathbf{G}_{\alpha_{\text{LO}}, \beta_{\text{LO}}}. \quad (4.56)$$

This is used to build the RWG/LO WF-MFIE in (4.45) as

$$\left[\frac{1}{2} \mathbf{G}_{\beta_{\text{LO}}, \beta_{\text{LO}}} \mathbf{W}_\gamma^{\text{LO}} + \mathbf{K}_{\beta_{\text{LO}}, \beta_{\text{LO}}} \right] i_{\text{LO}} = \mathbf{h}_{\beta_{\text{LO}}} \quad (4.57)$$

The Higher-Order Case

We assume that the anisotropy of the RWG functions is the major cause of the problems of the identity operator discretization. Hence, we investigate two different approaches to cope with the RWG anisotropy inside the hierarchical HO basis. First, we apply the WF discretization scheme to all HO functions as a whole. This means that we can re-use (4.45) (just as for the CSIE)

$$\left[\frac{1}{2} \mathbf{G}_{\beta, \beta} \mathbf{W}_\gamma + \mathbf{K}_{\beta, \beta} \right] i = \mathbf{h}_\beta, \quad (4.58)$$

where β includes the whole set of hierarchical HO expansion functions.

Second, we tackle only the RWG part of the Gram matrix. Here, the whole Gram matrix $\mathbf{G}_{\beta, \beta}$ is split into LO/RWG and HO interaction blocks in the way of

$$\mathbf{G}_{\beta, \beta}, i = \begin{bmatrix} \mathbf{G}_{\beta_{\text{LO}}, \beta_{\text{LO}}} & \mathbf{G}_{\beta_{\text{LO}}, \beta_{\text{HO}}} \\ \mathbf{G}_{\beta_{\text{HO}}, \beta_{\text{LO}}} & \mathbf{G}_{\beta_{\text{HO}}, \beta_{\text{HO}}} \end{bmatrix} \begin{bmatrix} i_{\text{LO}} \\ i_{\text{HO}} \end{bmatrix}. \quad (4.59)$$

The respective LO/RWG expansion coefficients are represented by the vector i_{LO} , the HO part by i_{HO} . Then, the WF basis transformation scheme including two WF rotations is employed only for the LO subset of the basis functions as described in (4.55). This alters the Gram matrix to

$$\mathbf{G}_{\beta, \beta}^{\text{WF-LO}} i = \begin{bmatrix} \mathbf{G}_{\beta_{\text{LO}}, \beta_{\text{LO}}} \mathbf{W}_\gamma^{\text{LO}} & \mathbf{G}_{\beta_{\text{LO}}, \beta_{\text{HO}}} \\ \mathbf{G}_{\beta_{\text{HO}}, \beta_{\text{LO}}} & \mathbf{G}_{\beta_{\text{HO}}, \beta_{\text{HO}}} \end{bmatrix} \begin{bmatrix} i_{\text{LO}} \\ i_{\text{HO}} \end{bmatrix}, \quad (4.60)$$

where the weighting factor γ depends on the polynomial order p of the expansion functions but is fixed for the whole matrix otherwise. Note that the basis transformation (4.55) is in fact not even employed for the LO functions as a whole set of basis functions but just for the self-interaction Gram matrix block, i.e., for the inner products $\langle \beta_{\text{LO}}, \beta_{\text{LO}} \rangle$ of LO with LO functions themselves. In consequence, the

hierarchical HO MFIE including a WF identity operator representation follows as

$$\left[\frac{1}{2} \mathbf{G}_{\beta, \beta}^{\text{WF-LO}} + \mathbf{K}_{\beta, \beta} \right] i = h_{\beta}. \quad (4.61)$$

In the hierarchical HO discretization, a part of the RWG anisotropy is already taken care of by the expansion functions themselves. This effect should increase with increasing order of the expansion functions. Hence, we expect that γ has to come closer to one with a higher order of the expansion functions. This means that the discretization might come closer to the classical one overall.

4.7.3 Analyzing the Weighting Factor for Both Proposed HO WF-MFIEs

In Subsection 4.4.1, extensive studies for choosing the weighting factor γ for the case $p = 0.5$ have been carried out. There, it became clear that the weighting factor γ certainly exhibits some dependence on the considered scenario. For instance, the optimal choice was found to be $\gamma \approx 0.4$ for a cube with 0.5λ edge length and $\gamma \approx 0.55$ for a smooth sphere. Here, we carry out a similar analysis over a set of scattering scenarios in order to determine what a suitable choice of γ might look like—as problem-independent as feasible.

A 0.5 λ Cube

We consider once again plane-wave scattering from a 0.5λ square cuboid, with all simulation settings just as discussed in Subsection 4.4.1 for the RWG case. Figure 4.43 shows the analysis of the weighting factor γ for the WF scheme concerning all HO functions. For the RWG discretization, we compute the solutions on 14 different triangular meshes ranging from 0.28λ to 0.035λ average edge lengths h . The number of RWG unknowns goes from 72 up to 4302 on the finest mesh. For the full first-order expansion functions ($p = 1$), we have 144 up to 8604 unknowns; for the 1.5th order functions, we have 240 up to 14 340 unknowns. Just as before, the RCS of the PEC cube scattering for plane-wave incidence is evaluated in the FF for the MFIE, the EFIE, the BC-tested MFIE, the M-CSIE (again with $\chi_{\text{CS}} = 1/11$) as well as the proposed WF-MFIE. Then, the relative (arithmetic) average FF error with respect to the reference solution (a 2.5th order EFIE solution on the finest among the considered meshes) is computed for each choice of the mesh and also for each choice of γ and $p = \{0.5, 1, 1.5\}$ in the WF-MFIE.⁵ Among these mesh variations, the geometric average τ of the individual arithmetically averaged FF errors is calculated.

⁵ It has been analyzed previously that accuracy improvements of the WF-MFIE occur also in the NF and not only in the FF.

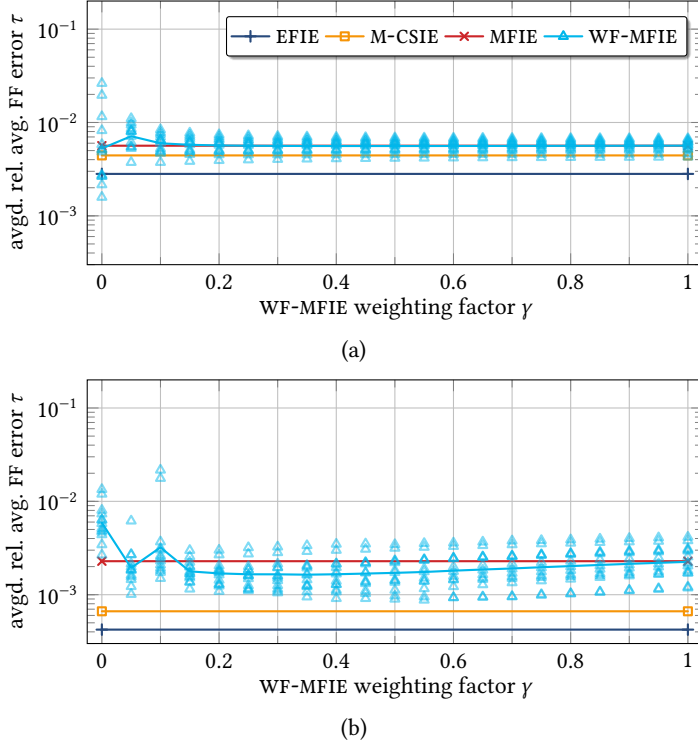


Fig. 4.43: Optimal WF-MFIE weighting factor for scattering from the mesh refinement models of a 0.5λ cube, HO basis functions, for the WF scheme for all HO functions according to (4.58). (a) Order $p = 1$. (b) Order $p = 1.5$.

The geometric mean is chosen since the individual (already averaged) errors vary by orders of magnitude, and, unlike the arithmetic average, the geometric average is not dominated by large values. For more details, see (4.48). The scatter marks denote the error ratio of EFIE and WF-MFIE solutions, see (4.49).

In Fig. 4.43, no improvement is observed for full first-order basis functions. At values below 0.15, the WF schemes show their slightly negative influence and the error is slightly increased. For the case $p = 1.5$, the error is improved by a couple of decibels in a stable manner, with the optimal value at $\gamma = 0.35$: Here, the average WF-MFIE error goes down to -55.7 dB (from -53.0 dB for the classical MFIE).

For comparison, the optimum value found for this scenario and the RWG WF-MFIE is $\gamma = 0.4$ as shown in Fig. 4.44(a). Figure 4.44 shows the results for the WF scheme focusing on the RWG part according to (4.61). We observe significant improvements.

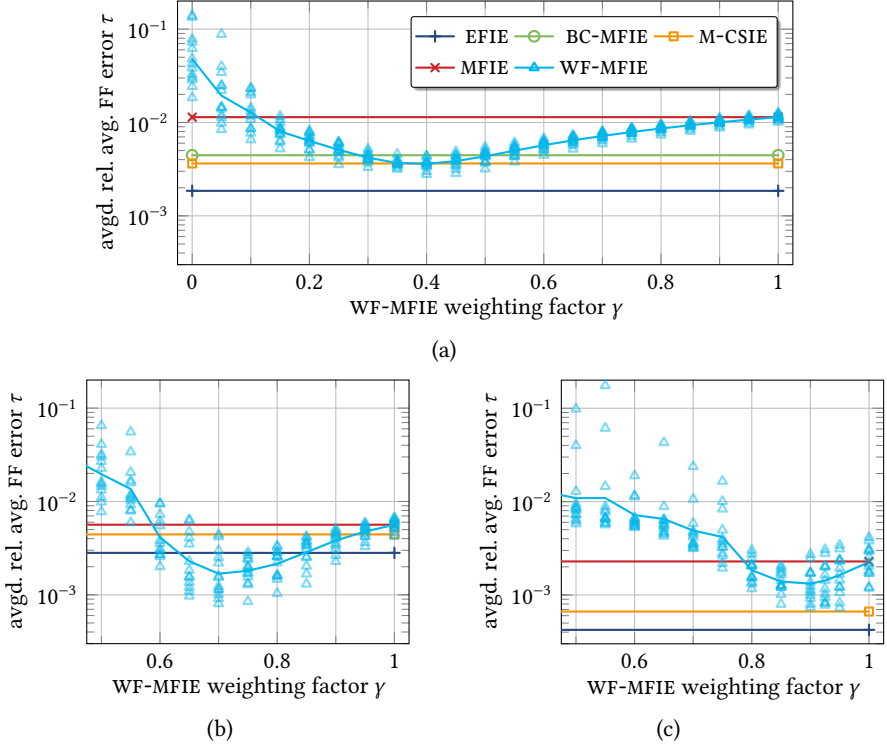
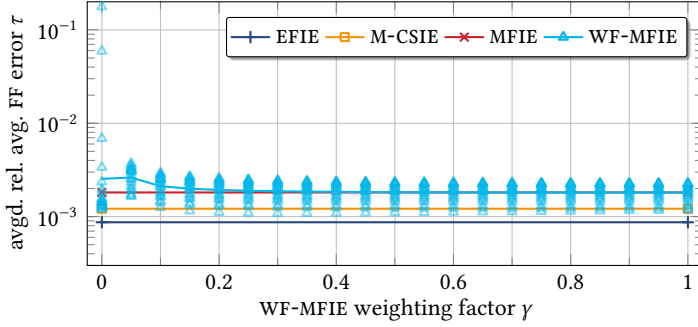


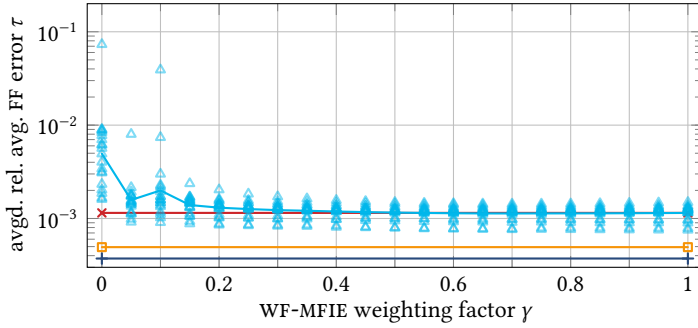
Fig. 4.44: Optimal WF-MFIE weighting factor for scattering from the mesh refinement models of a 0.5λ cube, HO basis functions, for the WF scheme focusing on the RWG part according to (4.61). (a) Order $p = 0.5$, same as Fig. 4.15. (b) Order $p = 1$. (c) Order $p = 1.5$.

For $p = 1$, the lowest error of -55.5 dB is found at $\gamma = 0.7$, which is more than 10 dB better than the error -45.0 dB of the classical MFIE. For $p = 1.5$, the error goes down from -53.0 dB to -57.6 dB at $\gamma = 0.9$. These accuracy improvements are larger than for the scheme applied for all functions. However, the deterioration of the solution below the optimal value of γ is rather severe for the HO cases.

It is important to analyze further scenarios in order to consider the observations as robust. Just as in Subsection 4.4.1 for the RWG case, we investigate an electrically larger cube with 1λ edge length first and then a sphere with 0.5λ diameter.



(a)



(b)

Fig. 4.45: Optimal WF-MFIE weighting factor γ for scattering from the mesh refinement models of a 1λ cube, HO basis functions, for the WF scheme for all HO functions according to (4.58). (a) $p = 1$. (b) $p = 1.5$.

A 1λ Cube

For the 1λ cube, 20 meshes with h ranging from 0.37λ to 0.027λ are considered. These meshes exhibit between 162 and 30 240 RWG unknowns, between 324 and 60 480 full first-order unknowns and between 540 and 100 800 1.5th order unknowns. The results for the WF scheme for all HO functions according to (4.58) are shown in Fig. 4.45. The accuracy improvements for the 1.5th order expansion functions are not confirmed in this scenario. The best case is found at $\gamma = 0.7$, but the error is only improved by a negligible tenth of a decibel. For both sets of HO functions, the solutions deteriorate below $\gamma = 0.25$. Since there are no stable accuracy improvements, this WF method seems to be rather useless to reduce the MFIE error levels in general.

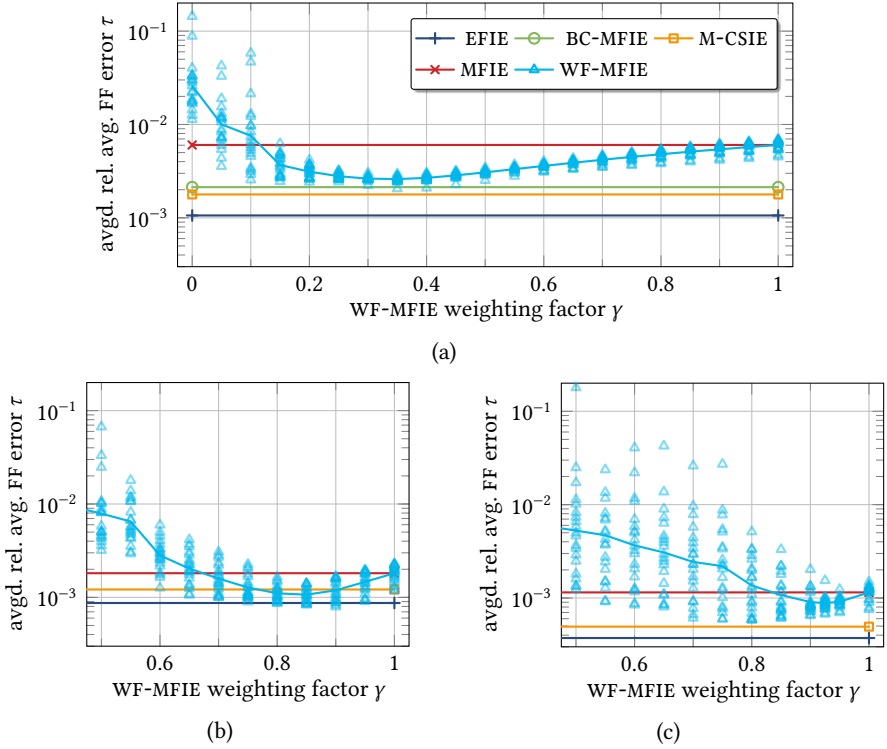
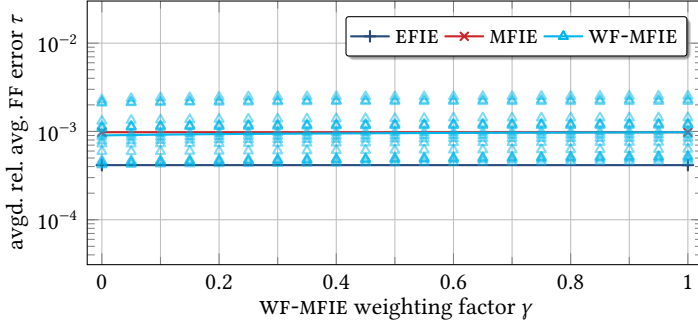
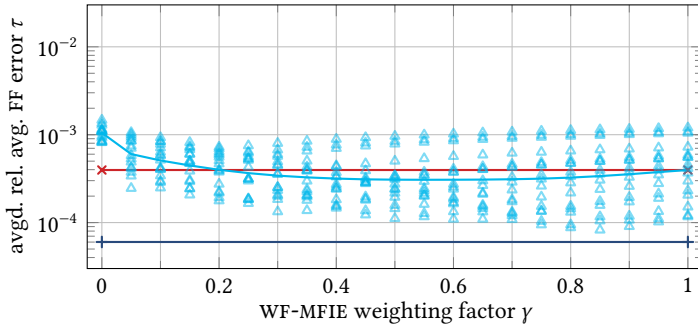


Fig. 4.46: Optimal WF-MFIE weighting factor γ for scattering from the mesh refinement models of a 1λ cube, HO basis functions, for the WF scheme focusing on the RWG part according to (4.61). (a) $p = 0.5$, same as Fig. 4.16. (b) $p = 1$. (c) $p = 1.5$.

Looking at the results of the WF scheme focusing on the RWG part according to (4.61) in Fig. 4.46, the improved error levels are also observed in this scattering scenario. For the RWG-only case, the lowest error of -51.7 dB is found at $\gamma = 0.35$, which is an improvement over the error of -44.4 dB of the classical MFIE. For the full first-order functions, the difference between the best solution at $\gamma = 0.85$ and the classical MFIE is 4.6 dB—with the error reduced from -54.8 dB to -59.4 dB. The improvement for the 1.5th order functions is not as large with an error of the classical MFIE of -58.8 dB and the lowest error of -61.1 dB at $\gamma = 0.925$.



(a)



(b)

Fig. 4.47: Optimal WF-MFIE weighting factor γ for scattering from the mesh refinement models of a 0.5λ sphere, HO basis functions, for the WF scheme for all HO functions according to (4.58). (a) $p = 1$. (b) $p = 1.5$.

A 0.5λ Sphere

The last scenario is a 0.5λ -diameter PEC sphere, which has been analyzed in Subsection 4.4.1 for LO functions. For the LO case, larger values for γ have been observed to be optimal. Here, we consider 16 triangular meshes with h ranging from 0.14λ to 0.034λ . These meshes exhibit 126 to 2388 RWG unknowns, 252 to 4776 first-order unknowns, or 420 to 7960 1.5th order unknowns. The reference solution is a 2.5th order EFIE solution on a refined version of each of the individual meshes, where the surfaces of the respective reference matches with the original one.

The results for the WF scheme for all HO functions according to (4.58) are shown in Fig. 4.47. Again, the influences on the error are minor. For $p = 1.5$, the most improvement of just 2.2 dB is found at $\gamma = 0.5$.

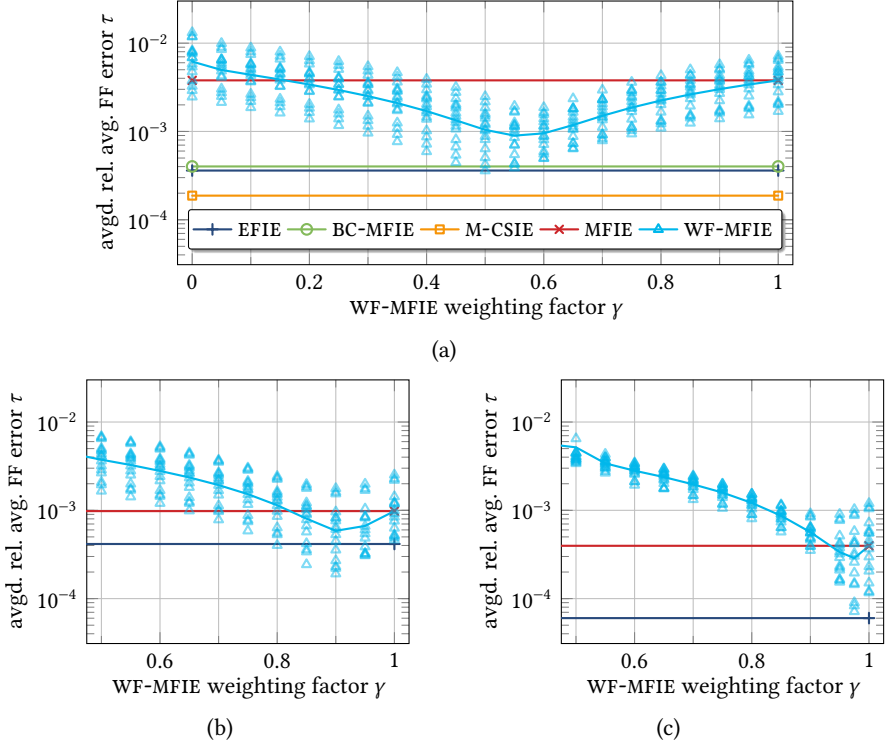


Fig. 4.48: Optimal WF-MFIE weighting factor γ for scattering from the mesh refinement models of a 0.5λ sphere, HO basis functions, for the WF scheme focusing on the RWG part according to (4.61). (a) $p = 0.5$, same as Fig. 4.21(b). (b) $p = 1$. (c) $p = 1.5$.

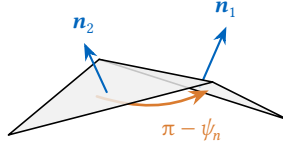
Figure 4.48 shows the weighting analysis for the WF scheme focusing on the RWG part according to (4.61), including the RWG-only case. Here, we find an improvement of 4.5 dB at $\gamma = 0.9$ for $p = 1$ and 2.8 dB at $\gamma = 0.975$ for $p = 1.5$. These γ values are very close to 1 (the classical MFIE) and the observed improvements are not as large as for the two cubes.

Tackling Geometrical Singularities

Overall, the WF scheme applied only to the RWG part of the Gram matrix yields better results, particularly for the first-order functions. This scheme seems hence more promising and will be investigated further. In any case, the observed HO

Tab. 4.4: Comparison of the optimal HO weighting factors γ regarding the improvement of the average FF error.

order	0.5 λ cube		1 λ cube		0.5 λ sphere	
	γ	improvement	γ	improvement	γ	improvement
$p = 0.5$	0.4	10.0 dB	0.35	7.3 dB	0.55	12.5 dB
$p = 1$	0.7	10.5 dB	0.85	4.6 dB	0.9	4.5 dB
$p = 1.5$	0.9	4.6 dB	0.925	2.3 dB	0.975	2.8 dB

Fig. 4.49: Illustration of the angle ψ associated with the edge between two adjacent triangles.

accuracy improvements are smaller for the sphere than for the two cubes, the optimal values of γ are shifted to larger values for the (smoother) sphere, and the choice of a suitable value for γ becomes more sensitive with increasing basis function order p . This insight is summarized in Tab. 4.4. In order to be safe from the negative influence of the non-trivial kernel of $\mathbf{G}_{\alpha_{l.o}, \beta_{l.o}}$, the following investigations are based on the values found for the sphere.

One way to improve the WF scheme might be to adjust γ as presented in [Kornprobst and Eibert 2018b, 2019]. Since we do not need to take action for smooth surfaces, the first step is to identify sharp edges in the discretized geometry. This is done by calculating the angles associated with each n th interior edge or, more specifically, each RWG function. The definition of these angles ψ_n is illustrated in Fig. 4.49. We construct a diagonal matrix $\mathbf{\Gamma}$ with the entries

$$[\mathbf{\Gamma}]_{nn} = w(\boldsymbol{\psi}, n), \quad (4.62)$$

where each edge is associated with a weighting function dependent on the vector of the angles $\boldsymbol{\psi}$ associated with the edges of the mesh, i.e., $[\boldsymbol{\psi}]_n = \psi_n = \arccos(\mathbf{n}_1 \cdot \mathbf{n}_2)$. The most simple choice would be $w(\boldsymbol{\psi}, n) \propto \psi_n$. However, it is rather clear that this does not yield satisfactory results. Such a weighting would only affect RWG functions with a current across each edge. It is even more important to take care of currents flowing in parallel to sharp edges, though, since these currents may

become singular, cf. Fig. 4.27(d) on p. 88. Hence, we employ a moving average filter

$$h_{\text{MAV}}(\boldsymbol{\psi}, n) = \frac{1}{5} \left[[\boldsymbol{\psi}]_n + \sum_{m \in \text{neighbors}(n)} [\boldsymbol{\psi}]_m \right] \quad (4.63)$$

spreading the effect of the edge on all four adjacent edges, too, whether they themselves exhibit $\psi_n > 0$ or not. If two triangles are in a flat area, the respective entry is zero. The matrix entry is increased proportionally to the averaged angle with the weighting function

$$w(\boldsymbol{\psi}, n) = \begin{cases} \nu, & \text{for } \psi_{\text{th}} \leq |h_{\text{MAV}}(\boldsymbol{\psi}, n)| \\ \nu |h_{\text{MAV}}(\boldsymbol{\psi}, n)| / \psi_{\text{th}}, & \text{for } 0 < |h_{\text{MAV}}(\boldsymbol{\psi}, n)| < \psi_{\text{th}} \\ 0, & \text{for } 0 = |h_{\text{MAV}}(\boldsymbol{\psi}, n)| \end{cases} \quad (4.64)$$

up to a threshold ψ_{th} . A reasonable choice is $\pi/10$, which occurs for a single geometrical angle of $\psi = \pi/2$. With this choice, the maximum effect occurs whenever the sum of the adjacent angles reaches $\pi/2$. The maximum weighting is done by the factor ν . We can integrate this diagonal matrix and augment the effect of γ where suitable. This yields the WF approximated identity matrix for the RWG part only

$$\mathbf{W}_{\gamma, \nu, \psi_{\text{th}}}^{\text{LO}} = \gamma \mathbf{I}_{\text{LO}} - \boldsymbol{\Gamma} + [(1 - \gamma) \mathbf{I}_{\text{LO}} + \boldsymbol{\Gamma}] \mathbf{R}_{\text{LO}} \quad (4.65)$$

Finally, we plug this matrix into the WF-MFIE, i.e., into (4.60) and (4.61).

For the WF weighting factor γ , we choose the conservative values for the sphere. The choice of ν is analyzed briefly, again for the two cubes. The results are shown in Fig. 4.50. The observed error improvements are summarized in Tab. 4.5 for $\gamma \in \{0.55, 0.9, 0.975\}$ and $\nu = 0$ as well as for the respective optimal choice for ν . Overall, the accuracy improvements observed with the best choice of ν are on the same level as the ones given for the optimal choice of γ in Tab. 4.4. However, the version with ν , i.e., tackling geometrical edges individually, seems to be more stable regarding the choice of the weighting factor ν . As we can see in the comparison of Fig. 4.50 with the previous analyses for the choice of γ , a too large weighting of the WF scheme has less negative influence here. In the following, we consider the choice $\nu = 0$ as well as the choices $\nu = \{0.2, 0.1, 0.075\}$ for $p = \{0.5, 1, 1.5\}$.

Going into a more in-depth analysis, we find that the best value of γ increases with increasing p . For the considered scenarios, we have chosen $\gamma \in \{0.55, 0.9, 0.975\}$. The additional WF weighting factor ν has the opposite sign in (4.65) and decreases with p . Not only are the WF weighting factors reduced, there are also diminishing gains for HO expansions, i.e., the error is reduced to a lesser extent. For $p > 0.5$, the gains are only on a smaller level and the required value of the overall WF weighting factor comes closer to 1, i.e., the choice for the pure classical MFIE. For

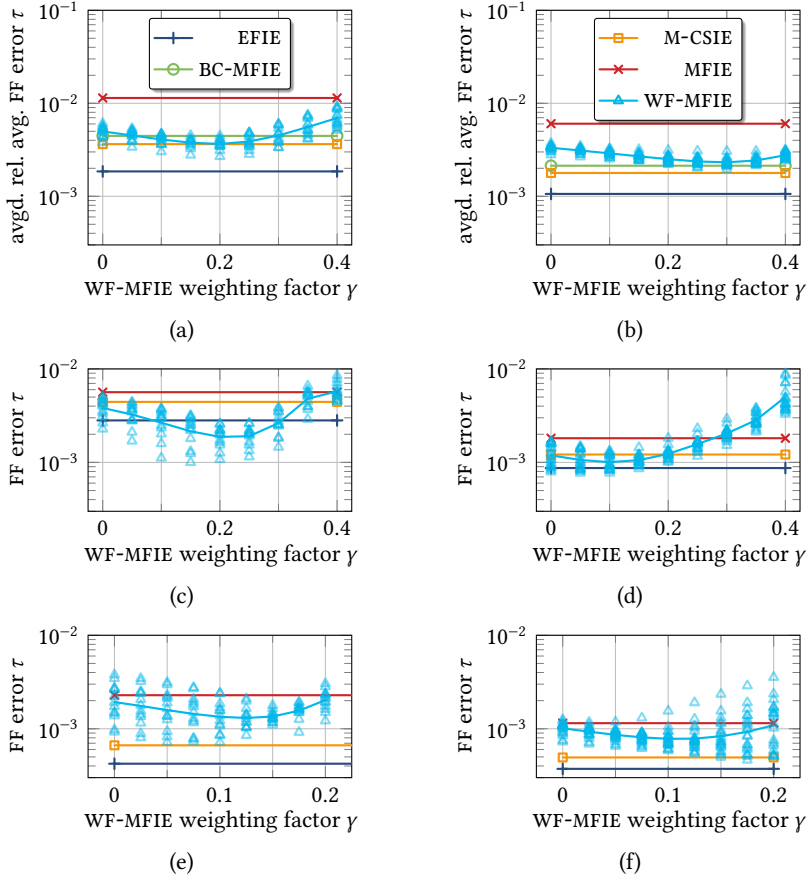


Fig. 4.50: Analysis of the weighting factor ν for scattering from the two discussed cubes, $\gamma \in \{0.55, 0.9, 0.95\}$ for $p \in \{0.5, 1, 1.5\}$. (a) $p = 0.5$, 0.5λ cube. (b) $p = 0.5$, 1λ cube. (c) $p = 1$, 0.5λ cube. (d) $p = 1$, 1λ cube. (e) $p = 1.5$, 0.5λ cube. (f) $p = 1.5$, 1λ cube.

Tab. 4.5: Comparison of the optimal HO weighting factors ν regarding the improvement of the average FF error, $\gamma \in \{0.55, 0.9, 0.975\}$ for $p \in \{0.5, 1, 1.5\}$.

order	0.5 λ cube				1 λ cube			
	ν	improv.	ν	improv.	ν	improv.	ν	improv.
$p = 0.5$	0	7.2 dB	0.2	9.9 dB	0	5.2 dB	0.3	8.3 dB
$p = 1$	0	3.4 dB	0.2	9.6 dB	0	3.7 dB	0.1	5.1 dB
$p = 1.5$	0	1.5 dB	0.125	4.9 dB	0	1.1 dB	0.1	3.3 dB

the three scattering scenarios analyzed in Tab. 4.4, the average error improvements as compared to the classical MFIE are 9.9 dB for $p = 0.5$, 6.5 dB for $p = 1.0$, and 3.2 dB for $p = 1.5$. Furthermore, the error spread increases with increasing p ; this is observed both for the MFIE and the WF-MFIE. The meaning of this is best investigated by showing the underlying errors in more detail in the following Subsection 4.7.4.

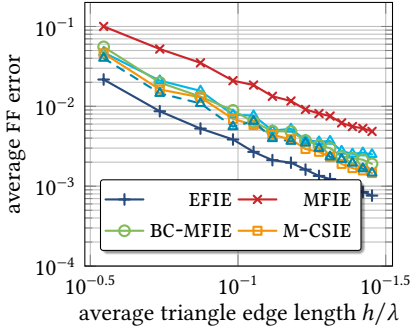
Another interesting observation is that all three of the RWG WF-MFIE, the BC-MFIE, and the classical full first-order MFIE are on a very similar accuracy level. This is consistently observed for all our analyzed scenarios, with minor advantages for one or another in each specific instance. Such observations have led to the conclusion that the HO MFIE fixes the MFIE accuracy problems. Nonetheless, we have demonstrated that further improvements are indeed possible, and also how to achieve these improvements for HF scenarios.

4.7.4 Numerical Investigations of the HO Schemes

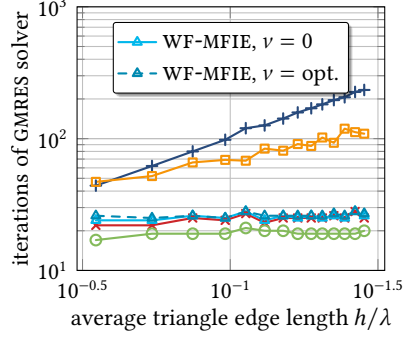
Mesh Refinement Analysis

In this section, we discuss one particular mesh refinement study in more detail for all HO IEs. The RWG case for the cube with 0.5λ edge length has been discussed already in Fig. 4.14, there with $\gamma = 0.5$. The error levels and GMRES iterations to a residual of 10^{-6} are shown in Fig. 4.51. For the RWG basis functions, the observations are the same as in Fig. 4.14 with $\gamma = 0.5$. Here, $\gamma = 0.55$ exhibits a slightly higher (geometrically) averaged error of -46.0 dB instead of -47.2 dB. Choosing $\nu = 0.2$ lowers the error to -48.7 dB. The RWG M-CSIE with $\chi_{CS} = 1/11$ and the BC-MFIE show about the same average error with -48.8 dB and -47.0 dB, respectively. None of these IEs involving the MFIE operator comes close to the EFIE, which exhibits an error of only -54.6 dB. The WF-MFIEs and the BC-MFIE are able to retain the excellent conditioning of the classical MFIE independent of h whereas the M-CSIE exhibits a slight dependence on h and barely beats the EFIE in terms of iterations to convergence.

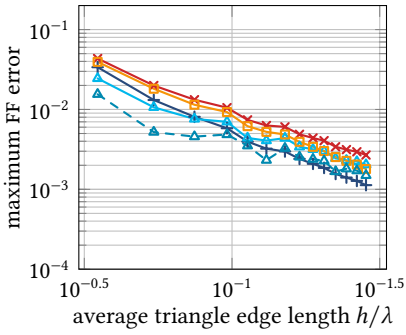
The full first-order WF-MFIE with $\gamma = 0.9$ exhibits an average error of -48.3 dB, clearly better than the MFIE with -45.0 dB. With a local emphasis on the WF scheme with $\nu = 0.1$, the error is decreased to even -51.5 dB, beating the EFIE error of -51.0 dB for the coarser meshes and on average. The HO CSIE is doing only slightly better than the classical MFIE with an error of -47.0 dB. It exhibits a worse iterative solver convergence than the EFIE, though. The WF schemes are again able to almost retain the excellent, mesh-size independent conditioning of the MFIE. Note that the first-order EFIE surprisingly shows a larger error than RWG EFIE. This is not a recurring observation, though, and dependent on object size and frequency. Yet, it is clear that the HF MFIE, which suffers from the anisotropy of the RWG functions



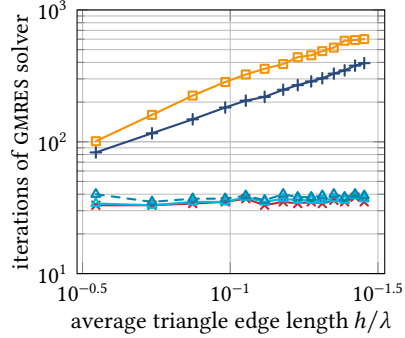
(a)



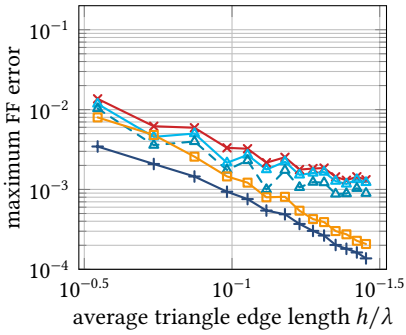
(b)



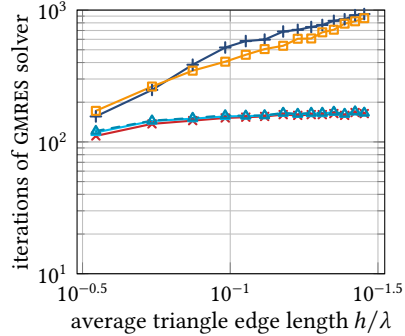
(c)



(d)



(e)



(f)

Fig. 4.51: Mesh refinement analysis for a 0.5λ cube. Average FF error in the left column, iterations for convergence to a residual of 10^{-6} in the right column. (a), (b) $p = 0.5$, $\gamma = 0.55$, $\nu = \{0, 0.2\}$. (c), (d) $p = 1$, $\gamma = 0.9$, $\nu = \{0, 0.15\}$. (e), (f) $p = 1.5$, $\gamma = 0.975$, $\nu = \{0, 0.075\}$.

and the singularity of the identity operator, potentially benefits more from HO expansion functions.

For the 1.5th order expansion functions, the classical MFIE exhibits an average error of -52.8 dB. The WF-MFIE with $\gamma = 0.975$ is able to lower this to -54.3 dB. The additional WF weighting with $\nu = 0.075$ lowers the error further to -56.8 dB. The M-CSIE and EFIE exhibit clearly lower error levels of -63.5 dB and -67.5 dB, though. As for the first-order case, the CSIE does not offer a significant improvement in the iteration count to convergence over the EFIE, whereas the number of WF-MFIE iterations is only marginally above that of the classical MFIE.

Overall, the HO WF-MFIE seems to promise accuracy improvements, while the CSIE shows a worse error than the EFIE and also a worse iterative solver convergence. It remains to be studied whether the CSIE offers any benefits at all, in particular at the presence of interior resonances.

Stability at Interior Resonances

We investigate the first two interior resonances of a sphere discretized with 666 triangles. The IEs with RWG expansion functions have been studied in Fig. 4.35. In Fig. 4.52, the iterative solver convergence and error levels as compared to a HO EFIE reference on a refined mesh are analyzed with the same simulation settings and frequency sampling as in Fig. 4.35.

Looking at the full first-order functions ($p = 1$), we find that the EFIE and the IEs with dominant MFIE operator show an increased number of iterations for convergence to a threshold of 10^{-5} at the interior resonances. The CF/CS IEs do not show such a behavior. The WF-CFIE retains the excellent conditioning of the CFIE, whereas the CSIE shows about the same convergence rate as the EFIE but neglecting the increase at the interior-resonance frequencies. The classical MFIE, the WF-MFIE with $\gamma = 0.9$ and $\nu = 0$, and the M-CSIE with $\chi_{cs} = 1/11$ show an increased error around these frequencies. The MFIEs' errors go up to -12 dB (not shown, truncated). As observed previously, the EFIE error is rather large and mostly above the RWG EFIE error of about -58 dB. The WF-CFIE beats the CFIE by about one decibel, whereas the WF-MFIE performs better than the MFIE up to 300 MHz and slightly worse above. In the lower frequency range, the CSIE is a couple of decibels better than the WF-CFIE.

For the 1.5th order functions, most observations regarding the GMRES solver iterations are similar. The most significant difference is that the CSIE converges slightly faster than the EFIE. Albeit the picture changes when we look at the error levels. The error of the M-CSIE is about 5 dB larger than of the MFIE, while the WF-MFIE beats the MFIE handily by another 5 dB. This translates to the CF/CS solutions: The CSIE is about half a decibel less accurate than the CFIE. The WF-CFIE is, on average, about 4 dB more accurate than the CFIE.

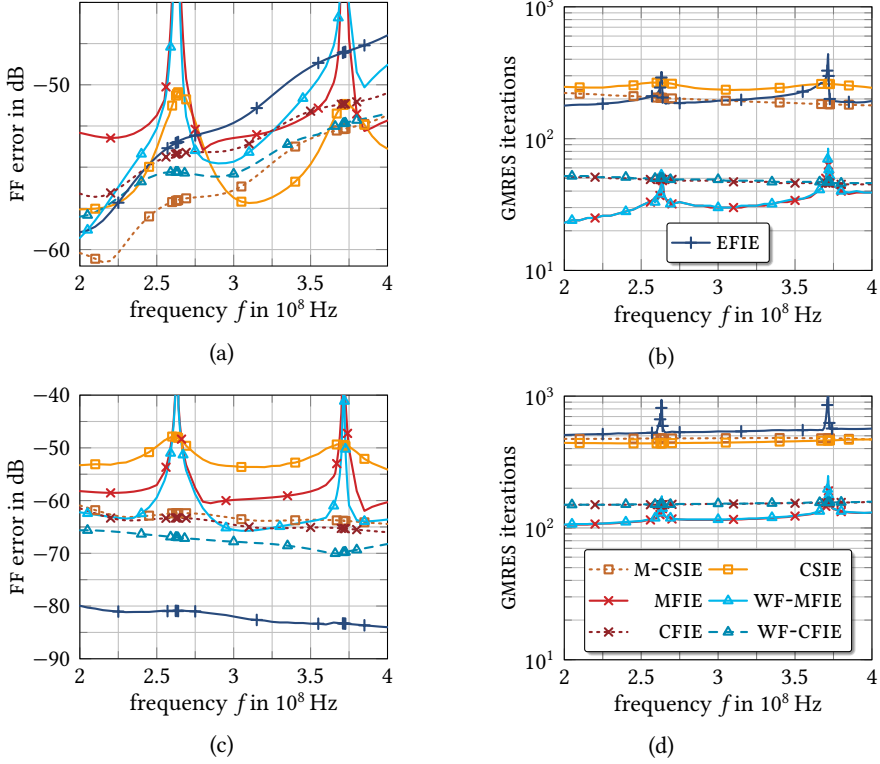


Fig. 4.52: Analysis of the HO IEs at the first two interior resonances of a 1-m PEC sphere. Maximum FF error on the left, iterations for convergence to a residual of 10^{-5} on the right. (a), (b) $p = 1$, $\gamma = 0.9$. (c), (d) $p = 1.5$, $\gamma = 0.975$.

While both the HO WF-CFIE and the HO CSIE have been able to cope with the problem of interior resonances, the HO CSIE's improvements regarding accuracy and conditioning are marginal or non-existent. For $p = 1$, part of the reason might be the rather poor performance of the EFIE itself. This stands in contrast to the RWG case, where both IEs have been on a comparable accuracy level for scatterers with smooth surfaces and the CSIE has been clearly advantageous for scatterers with sharp edges. The latter aspect is investigated in the following.

Electrically Larger Scattering Scenario

Once again, we study the scaled stealth object Flamme since it has proven to be one of the most challenging scattering scenario from the ones studied in Section 4.6.

Tab. 4.6: Error level comparison with Mie and HO references for the 1-m diameter PEC sphere at 5 GHz. (a) $p = 0.5$, $\chi_{\text{cf/cs}} = 0.5$, $\gamma = 0.55$, $\nu = \{0, 0.2\}$. (b) $p = 0.5$, $\chi_{\text{cf/cs}} = 0.5$, $\gamma = 0.9$, $\nu = \{0, 0.1\}$. (c) $p = 1.5$, $\chi_{\text{cf/cs}} = 0.5$ unless otherwise stated, $\gamma = 0.975$, $\nu = \{0, 0.075\}$.

(a)				(b)		
	its.	$\epsilon_{\text{avg}}^{\text{FF}}$	$\epsilon_{\text{max}}^{\text{FF}}$	its.	$\epsilon_{\text{avg}}^{\text{FF}}$	$\epsilon_{\text{max}}^{\text{FF}}$
CFIE	267	-22.7 dB	-45.3 dB	349	-34.8 dB	-57.8 dB
WF-CFIE	287	-28.7 dB	-51.6 dB	407	-36.8 dB	-60.8 dB
$\nu > 0$	394	-29.8 dB	-51.5 dB	542	-31.2 dB	-54.3 dB
CSIE	340	-36.9 dB	-60.7 dB	896	-34.8 dB	-58.7 dB
EFIE	9508	-37.0 dB	-61.6 dB	9459	-36.3 dB	-59.3 dB

(c)			
	its.	$\epsilon_{\text{avg}}^{\text{FF}}$	$\epsilon_{\text{max}}^{\text{FF}}$
CFIE	955	-34.8 dB	-57.9 dB
WF-CFIE	1969	-35.4 dB	-58.9 dB
$\nu = 0.2$	1026	-36.9 dB	-59.2 dB
$\nu = 0.2, \gamma = 0.85$	1924	-39.6 dB	-62.2 dB
CSIE	1918	-42.5 dB	-65.2 dB
EFIE	>10 000	-41.9 dB	-66.9 dB

The bi-static RCS is evaluated for a plane wave incidence with polarization $\mathbf{p} = \mathbf{u}_y$ and wave vector $\mathbf{k} = k\mathbf{u}_x$, now at a frequency of 15 GHz. The electrical length is 30λ and $h \approx 0.15\lambda$; this is a rather coarse mesh for RWG functions. As a reference, we employ a 1.5th order CFIE solution with $\chi_{\text{CF}} = 0.999$ on a refined mesh. The simulation results are summarized in Tab. 4.6.

The RWG-only results confirm the observations from earlier investigations: The CSIE is on the same accuracy level as the EFIE and all other IEs exhibit larger errors. The WF-CFIE is a couple of decibels better than the classical CFIE, though.

For full first-order expansion functions with $p = 1$, the EFIE and CSIE accuracies are worse than for RWG functions. All studied IEs show similar error levels. The best one is the WF-CFIE with $\nu = 0$. Surprisingly, choosing $\nu = 0.1$ is detrimental here.

With $p = 1.5$ expansions functions, the EFIE and the EFIE are able to show their superior accuracy again. Just as for the RWG case—cf. also Fig. 4.40—the CSIE is able to deliver its superior error levels also at low weightings of the EFIE operator with $\chi_{\text{sc}} < 0.5$, which leads to a faster iterative solver convergence.

Summary

The CSIE and the WF-MFIE have been integrated with a set of hierarchical HO functions. For the CSIE, the WF rotation of the electric currents was implemented for all functions just as in the RWG case. The WF-MFIE shows its greatest benefit when the WF identity scheme is only employed for the Gram matrix of RWG functions, which are a subset of the employed hierarchical HO functions. The benefits over the classical testing of the MFIE with div-conforming functions, which is prone to accuracy issues, are in general comparable to the RWG case but minor differences are observed. We have demonstrated that the accuracy issues of the classical MFIE persist in a HO discretization in a decreasing manner even though the accuracy is improved—in contrast to how the results may appear at first glance. This can be seen by looking at the results of the full first-order MFIE solved on the same mesh as the RWG MFIE. The accuracy is improved, and the improvement is on a similar level with accurate discretization schemes for the LO MFIE—namely, the BC-tested mixed-discretization MFIE, the CSIE, and the WF-MFIE; all with an RWG basis. Taking into account the increased number of DOFs provided by HO expansion functions, it becomes clear that the HO MFIE is still not as accurate as it should be possible with the increased number of DOF.

The WF scheme for the MFIE takes care of the anisotropy of the RWG part of the HO functions and is, thus, able to mitigate the accuracy issues in part. The resulting full first-order discretization can be more accurate than the classical one, which only achieves about the same accuracy as the BC-tested MFIE or the RWG WF-MFIE.

The CSIE shows contradictory results. For most results, the error levels were on the same level as for the EFIE and the same holds for the iterative solver convergence. However, for scattering from a PEC sphere, the FF RCS error was slightly worse than the error of the classical CFIE. The CSIE seems to be a viable option for HO scattering solutions to challenging geometries, while the WF-CFIE offers some improvements whenever Love current solutions are needed, for instance for FE-BI approaches.

Surface-Source Reconstruction for Antenna Measurements

Science is the belief in the ignorance of experts.

– Richard Feynman, *What is Science?*

EQUIVALENT SURFACE-SOURCE MODELS offer a great deal of versatility as a basis for NFFFTs and related post-processing methods, which constitute the overarching theme of this chapter. Section 5.1 discusses linear surface-source reconstruction approaches when complex field measurement data is available, with the focus on the fact that in general the number of observations and unknowns do not match. This section and subsequent results in Section 5.3 are based on [Kornprobst et al. 2019e; Kornprobst et al. 2019f; Kornprobst et al. 2019b; Kornprobst et al. 2019g; Kornprobst et al. 2019c; Kornprobst et al. 2020; Mauermayer et al. 2019; Kornprobst et al. 2021a; Mauermayer and Kornprobst 2022]. Four different approaches to retrieve the special Love currents are presented in Section 5.2, which are founded on the work in [Kornprobst et al. 2019e; Kornprobst et al. 2019f; Kornprobst et al. 2019b; Kornprobst et al. 2021a]. The algorithms of the first two sections are put into practice in Section 5.3, where source reconstruction results and NFFFTs based on such retrieved surface sources are discussed in detail. The following Section 5.4 touches the subject of echo suppression from two directions. The inverse equivalent source approach is combined with the PEC MOM in order to get rid of the influence of echo objects [Paulus et al. 2019; Kornprobst et al. 2019d] and the current distributions altered by mutual coupling with scatterers are cured by time-gating [Knapp et al. 2020; Knapp et al. 2019b]. Another application of equivalent-source based NFFFTs, magnitude-only source reconstruction, is discussed in Section 5.5, which is based upon [Paulus et al. 2020; Knapp et al. 2021; Kornprobst et al. 2021d; Paulus et al. 2021; Paulus et al. 2022a; Kornprobst et al. 2022].

5.1 Linear Equivalent Source Reconstruction

In the ideal case, we consider a boundary value radiation problem as shown in Fig. 2.6. The radiation originates from the source region v_1 enclosing the AUT and

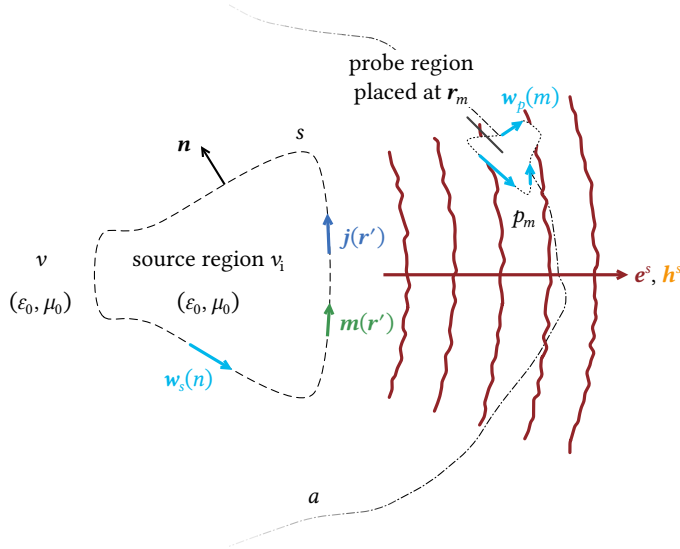


Fig. 5.1: A general equivalent source scenario with equivalent electric and magnetic surface current densities \mathbf{j} and \mathbf{m} on the Huygens surface s enclosing the AUT © 2021 IEEE [Kornprobst et al. 2021a].

is described by equivalent sources on its surface s (or inside this region for other source types) according to the Huygens principle. Prescribed boundary values may be defined anywhere on s (e.g., for a scattering problem) or outside of v_i . Figure 2.6 includes a second closed observation surface a , where the measurements are taken. For real-world NF antenna measurements, boundary values are defined in the form of measurement values of a probe antenna, i.e., the continuous fields on the ideally closed surface a are sampled and evaluated with an appropriate weighting function representing the probe. Such an equivalent scenario is depicted in Fig. 5.1. Then, the measurement surface a is not closed any more since there might be holes between the different probe measurement locations \mathbf{r}_m and, additionally, a might be truncated due to geometrical restrictions of the measurement setup.

5.1.1 General Discretization Strategy

With a triangular mesh on s , the surface current densities are modeled by RWG functions as

$$\mathbf{j} = \sum_{n=1}^N [j]_n \boldsymbol{\beta}_n, \quad \mathbf{m} = \sum_{n=1}^N [v]_n \boldsymbol{\beta}_n \quad (5.1)$$

on pairs of neighboring triangles. The electric current unknowns i and the magnetic ones \mathbf{v} may be, if used at the same time, concatenated to the unknowns vector $\mathbf{x} = [i^T \ \mathbf{v}^T]^T$. In a rather general way, the field evaluation is then performed by surface density testing functions $\mathbf{w}(\mathbf{r})$, see Fig. 5.1. These surface testing functions are either defined as \mathbf{w}_s directly on the surface s enclosing the AUT or as \mathbf{w}_p on a surface around a probe somewhere in v (placed on a). Evaluating $\mathbf{n} \times \mathbf{e}$ radiated by an electric surface current density basis function \mathbf{v} (or $\mathbf{n} \times \mathbf{h}$ for a magnetic current basis function) with one specific testing function \mathbf{w} , we obtain one element of a forward operator matrix as

$$[\mathbf{T}_{\mathbf{w},\mathbf{v}}]_{mn} = \langle \mathbf{w}_m, \mathcal{T} \mathbf{v}_n \rangle \quad \text{for } m \in \{1, 2, \dots, M\}, n \in \{1, 2, \dots, N\} \quad (5.2)$$

For the other matrices $\mathbf{K}_{\mathbf{w},\mathbf{v}}$ and $\mathbf{G}_{\mathbf{w},\mathbf{v}}$, we follow the notation, which has already been introduced in Chapter 3. The inner-product alike interaction integral is evaluated according to (3.3). The matrix entries are defined in (3.6), (3.28), and (3.29). Furthermore, the involved radiation operators are described by (2.41), (2.44), and (2.45).

In the following, we assume that there are N RWG functions on s and M probe measurements taken on a . One important detail is different for antenna measurements: Testing the radiated electric field gives a right-hand side vector of the system of equations with the entries

$$[\mathbf{b}]_m = \langle \mathbf{w}_m, \mathbf{n} \times \mathbf{e}^s \rangle + [\epsilon_{\text{OE}}]_m \quad \text{for } m \in \{1, 2, \dots, M\}, \quad (5.3)$$

where the vector ϵ_{OE} includes the observation error (OE) arising for instance from noise or imperfectly known probe positioning or behavior.

5.1.2 Description of the Forward Operator

For the source reconstruction, the received power wave at the probe is evaluated in the presented formulation by testing the radiated electric fields with an equivalent current representation of the probe or, equivalently, with a spectral representation in the accelerated implementation of the fast irregular antenna field transformation algorithm (FIAFTA). We have full freedom to choose any current representation of the probe. The following equations employ a current discretization with RWG functions β without loss of generality. Then, the discretized inverse problem reads

$$\mathbf{A} \mathbf{x} = \begin{bmatrix} \mathbf{T}_{\mathbf{w}_p,\beta} & \mathbf{K}_{\mathbf{w}_p,\beta} \end{bmatrix} \mathbf{x} = \mathbf{b}, \quad (5.4)$$

where $\mathbf{w}_p(m)$ is chosen to be an equivalent electric surface current description of the probe antenna employed for the m th measurement, correctly rotated and shifted in space to the measurement location \mathbf{r}_m . Of course, the employed probe for

different measurement samples may differ, as it is often the case for dual-polarized probes.

For the equivalent current description, the AUT geometry is enclosed by the Huygens surface exactly as depicted in Fig. 5.1. According to the equivalence principle, we can choose a source description with both \mathbf{j} and \mathbf{m} or, alternatively, one with \mathbf{j} only, dropping the \mathbf{m} unknowns (or vice versa).

Assuming we know a true solution $\boldsymbol{\xi}$ of the inverse problem, imperfect measurements cause the OE in the NF

$$\epsilon_{\text{OE}} = \frac{\|\mathbf{A} \boldsymbol{\xi} - \mathbf{b}\|_2}{\|\mathbf{b}\|_2} = \frac{\|\epsilon_{\text{OE}}\|_2}{\|\mathbf{b}\|_2}. \quad (5.5)$$

Some part of this error may be reconstructed by a false solution contribution, which is linearly superimposed to the correct solution. The remainder of the OE is not attributable to any \mathbf{x} . Solving (5.4) retrieves thus a solution \mathbf{x} , but at the observation locations, there remains a reconstruction deviation (RD)

$$\epsilon_{\text{RD}} = \frac{\|\mathbf{A} \mathbf{x} - \mathbf{b}\|_2}{\|\mathbf{b}\|_2}, \quad (5.6)$$

which estimates the OE and helps to suppress errors not attributable to a reconstructed source.

The total number of unknowns N_{un} equals either N or $2N$ and defines the length of the vector \mathbf{x} and the number of columns of \mathbf{A} . The number of observation points M , which is the number of rows in \mathbf{A} and at the same time the number of entries in \mathbf{b} , does not match to N_{un} in general, but the matrix \mathbf{A} is wide for common antenna NF measurement setups with subsequent equivalent current NFFFTs, i.e., $M < N_{\text{un}}$. This is due to the fact that the number of measurements necessary for a correct NF reconstruction M is approximately chosen according to the number of DOFs N_{DOF} of the radiation fields which in turn solely depend on the size, shape, and excitation of the AUT. For instance, if a field representation with spherical modes is chosen, the number of radiating modes (i.e., the possible DOFs in the fields) is limited by the minimum sphere centered around the AUT [J. E. Hansen 1988]. Often, M is chosen a bit larger than N_{DOF} to avoid aliasing in the AUT mode spectrum and to cope with measurement errors.

In other words, a typical observation is that \mathbf{A} is quasi band-limited, the reason being the finite AUT size. In real-world scenarios, the number of reconstructable DOFs may be even further limited by the measurement error; this can be pictured as a threshold to the decaying spectrum of radiating modes [Piestun and D. A. B. Miller 2000; Stupfel and Morel 2008]. Going below this threshold does not add meaningful information but distorts the solution.

This property of the forward operator certainly leads to a nontrivial cokernel

(also called left nullspace) $\ker \mathbf{A}^H$, since $\text{rank } \mathbf{A} \approx N_{\text{DOF}}$. We find the reconstructed solution in the image $\text{im } \mathbf{A}$. Any part of \mathbf{b} in $\ker \mathbf{A}^H$ cannot be reconstructed and leads to a RD. This is desired, since the RD should contain all measurement errors and noise, i.e., contributions which cannot be mapped onto the equivalent sources and which are thus suppressed. With $M > N_{\text{DOF}}$, we have a non-vanishing cokernel dimension and the system of equations in (5.4) can be considered to be overdetermined despite \mathbf{A} being wide.

In addition to the oversampling of observations, the inverse equivalent surface source problem exhibits another totally unrelated kind of oversampling in the unknowns space. The equivalent currents are modeled on a (possibly non-convex) mesh where $\lambda/10$ is a typical discretization density for the lowest-order RWG functions. This source representation is by far oversampled due to a large N_{un} as compared to the DOFs of the AUT, which can be roughly approximated by $\lambda/2$ -spaced measurements on the minimum sphere or a smaller AUT hull. A similar oversampling is present in a distributed spherical harmonics (DSH) expansion. Due to this oversampling, evanescent modes are possibly excited. However, they are impossible to reconstruct even with infinitely precise algorithms since they are typically not observable at the measurement distance due to various types of uncertainties. In a MLFMM-accelerated forward operator, strongly evanescent modes are typically not propagated to the measurement locations due to the inherent low-pass filtering. All of this implies a non-trivial null space $\ker \mathbf{A}$, i.e., the solution of (5.4) cannot be unique and the inverse problem is thus mildly ill-posed. This non-uniqueness does not affect the reconstructed exterior fields at a sufficiently large distance, though.¹

Additionally, various surface current representations (purely electric or magnetic, both, etc.) exist which obviously differ by non-radiating currents, i.e., they differ by solutions of the corresponding interior problem. Changing the retrieved solution by non-radiating currents has no effect on any fields outside of s for reasonably chosen shapes of v_i if numerical issues are under control; neither on radiating nor on evanescent modes. Such an inverse problem can be seen as severely ill-posed.

Both effects cause a non-trivial $\ker \mathbf{A}$ (with a larger dimension for ambiguous electric and magnetic currents). Unknown vectors with an effect on the reconstruction are only found in $\text{im } \mathbf{A}^H$. In the sense of $N_{\text{un}} \gg N_{\text{dof}}$, we conclude that the system of equations (5.4) is underdetermined. Typically, some kind of regularization is employed to get rid of negative effects of $\ker \mathbf{A}$.

1. If the Huygens surface is too large or a spherical harmonics (SH) expansion is utilized, the number of DOFs of the equivalent source representation is larger than the number of DOFs supported by the AUT. However, this does not cause an increased dimensionality of $\ker \mathbf{A}$ since such an equivalent source representation exhibits additional (spurious) radiating modes which do propagate to the observation location. This is not a uniqueness issue but can lead to false solutions when the OE is mapped to radiating modes not supported by the real AUT.

The unknowns ambiguity is commonly removed by minimizing a certain norm of the currents or NF residuals. A common way is the solution of (5.4) in a least-squares sense by minimizing an ℓ^2 -norm, which is discussed in the following subsection. Only in special scenarios, other norms might be of interest [Hofmann et al. 2019]. In summary, we find that the band-limited forward operator of inverse surface-source problems with oversampled measurements exhibits a non-trivial kernel and a non-trivial cokernel. Both have to be kept in mind to appropriately solve the inverse surface-source problem. Due to the typical surface-source oversampling and the existence of non-radiating currents, we commonly have to deal with $\dim(\ker \mathbf{A}) \gg \dim(\ker \mathbf{A}^H)$.

5.1.3 The Normal Equations

In order to solve (5.4), direct methods are not suitable due to their high complexity and incompatibility with fast algorithms. To reduce the computational complexity, iterative solvers are the method of choice in conjunction with well-conditioned fast formulations to obtain a solution with $\mathcal{O}(N_{it}N_{un} \log N_{un})$ complexity, where $N_{it} \ll N_{un}$. Since standard iterative solvers such as the CG method [Hestenes and Stiefel 1952] or the GMRES method [Saad and Schultz 1986] have been initially proposed for square matrices, which are commonly not encountered for measurement scenarios, normal systems of equations (NEs) are the method of choice to resolve this issue and to obtain a square system matrix [Saad 1996]. The common formulation employed in antenna NF measurements is the normal-residual system of equations (NRE)

$$\mathbf{A}^H \mathbf{A} \mathbf{x} = \mathbf{A}^H \mathbf{b}, \quad (5.7)$$

where the adjoint of the forward operator \mathbf{A}^H is multiplied from the left-hand side. Eq. (5.7) is well suited for overdetermined systems of equations [Saad 1996]. The overdeterminedness of the inverse problem is resolved by minimizing the ℓ^2 -norm of the residual of (5.4), i.e., by minimizing the RD $\|\mathbf{A} \mathbf{x} - \mathbf{b}\|_2$ [Saad 1996]. Hence, the NRE takes care of a possibly non-trivial $\ker \mathbf{A}^H$. The problem of a non-trivial $\ker \mathbf{A}$ for underdetermined problems persists and additional regularization is necessary for a stable solution. The employed solver may impose additional regularization constraints to remove any ambiguity in the solution. In the case of GMRES, we observe an $\|\mathbf{x}\|_2$ regularization with a suitable termination threshold [Calvetti et al. 2002; Eldén and Simoncini 2012]. A truncated singular value decomposition (SVD) has a similar effect. Notably, this regularization of the unknowns norm $\|\mathbf{x}\|_2$ contains no information about the behavior of the associated currents \mathbf{j} and \mathbf{m} or about the reconstructed interior fields. The exterior fields are theoretically the same anyhow.

Although the NRE is quite commonly found in the literature for efficient iterative

inverse source solvers, the typical equivalent-current NFFFT scenario resembles more an underdetermined system than an overdetermined one, see the discussion in the previous Subsection 5.1.2. Accordingly, the better suited normal-error system of equations (NEE) [Saad 1996]

$$\mathbf{A}\mathbf{A}^H\mathbf{y} = \mathbf{b}, \quad (5.8)$$

multiplies the adjoint operator prior to the standard forward operator. To retrieve the solution of the inverse problem, the post-processing step

$$\mathbf{x} = \mathbf{A}^H\mathbf{y} \quad (5.9)$$

has to be carried out. Several important differences are listed in the following. First, the iterative solution works with the vector \mathbf{y} , an auxiliary NF vector at the locations of the observation samples. Second, the NF RD ℓ^2 -norm is evaluated during the solution process – and not the ℓ^2 -norm of the current residual. This is advantageous since no termination criterion for the current residual has to be defined. Au contraire, the iterative solution stops on its own if the NF error approaches the possible minimum, limited by the OE. From a theoretical point of view, this kind of NE finds a different least-squares solution since it takes care of a non-trivial $\ker \mathbf{A}$: It minimizes the ℓ^2 -error norm of the unknowns vector, i.e., the norm $\|\mathbf{A}^H\mathbf{y} - \boldsymbol{\xi}\|_2$ for any correct solution $\boldsymbol{\xi}$ of (5.4), where $\boldsymbol{\xi}$ is not necessarily unique for common surface-source models. Additional regularization of \mathbf{y} may also be employed; however, this does not influence the solution except for negligible numerical effects since any contribution to the retrieved solution in the column null-space of \mathbf{A} is suppressed by the post-processing step in (5.9).

Both NEs give similar solutions since the difference only consists of current components which cause no difference in the fields at the observation locations. However, the NEE offers advantages in the iterative solution process [Kornprobst et al. 2019c]. For direct solutions, the two solutions

$$\mathbf{x}_{\text{NRE}} = (\mathbf{A}^H\mathbf{A})^+\mathbf{A}^H\mathbf{b}, \quad (5.10)$$

$$\mathbf{x}_{\text{NEE}} = \mathbf{A}^H(\mathbf{A}\mathbf{A}^H)^+\mathbf{b} \quad (5.11)$$

to the NRE and NEE are mostly interchangeable when the same pseudo-inverse $(\cdot)^+$ is used both times, for instance by a reasonably truncated SVD.

5.2 Zero-Field Enforcement

The equivalent source description on any closed Huygens surface is unique (unambiguous) if one type of currents is utilized, i.e., either electric or magnetic surface current densities.² Choosing both electric and magnetic surface current densities, additional constraints can be enforced to restrict the solution space and arrive at a mildly ill-posed problem. One possible constraint is the Love condition according to (2.34) and (2.35), where the surface current densities

$$\mathbf{j}_L = \mathbf{n} \times \mathbf{h}, \quad \mathbf{m}_L = \mathbf{e} \times \mathbf{n} \quad (5.12)$$

are represented by the total tangential fields on the Huygens surface s . This Love-current representation produces zero fields inside the source region, i.e., the AUT volume. All other surface current solutions result from a superposition of non-radiating currents³ with interior fields only. Araque Quijano and Vecchi [2009, 2010a, 2010b] and Jørgensen et al. [2011a] have claimed that enforcing the Love condition exhibits a better conditioning and a more stable and accurate solution behavior than other equivalent current methods. The improved solution stability might hold true dependent on the solver and its implicit regularization properties [Araque Quijano and Vecchi 2010a]. Unconstrained current solutions may vary arbitrarily as compared to Love currents and may, thus, depend strongly on measurement errors. However, according to the equivalence principle, the external fields (both near and far) of all equivalent current scenarios are indistinguishable. This concerns both evanescent and radiating fields. Hence, the solution stability of the retrieved currents is not very meaningful for the field reconstruction problem as long as the current variations do not cause additional numerical errors in the solution process, e.g., by numerical cancellation.

In the following, four (two approximate and two exact) possibilities for the zero-field enforcement are described. In the subsequent source reconstruction and NFFFT results, we analyze which benefits are observed when such reconstruction methods are employed, regarding the reconstruction accuracy and the interior zero-field quality, i.e., the accuracy of the Love condition.

2. Except for interior resonances, of course. Since the exterior fields are enforced to match the observations, there are no accuracy issues/parasitic exterior solutions associated with interior resonances as it might happen for the PEC MFIE; and the additional nullspace dimension also does not play any role since the non-trivial $\ker \mathbf{A}$ dominates the system matrix anyhow.

3. Note that the term “non-radiating currents” is used with different meanings in literature. Careful attention has to be paid to the particular definition in each source. Here, we employ the term „non-radiating currents“ to distinguish between purely exterior, mixed interior/exterior, and purely interior solutions. The unique exterior solution is expressed by Love currents lacking the non-radiating part. Non-radiating currents constitute a purely interior Love current solution. Another frequently encountered meaning is that of current coefficients with minimum (ℓ^2) norm, which exhibit—at least in some abstract sense—minimum energy and are not directly related to any fields.

5.2.1 Combined Source Approximation

An approximation of the Love condition is given by the CS condition, which enforces locally outward-oriented radiation for the sources placed on s [Mautz and Harrington 1979; Eibert et al. 2016]. This works if the surface under consideration contains all sources of the scenario⁴ and if the surface is convex and sufficiently smooth.

We briefly discuss the CS equivalent surface current representation since it is employed for comparison to the other methods. Assuming general equivalent surface currents according to (5.1) [and ignoring (5.12)], the magnetic surface current densities are obtained via the CS condition (2.36)

$$\mathbf{m}_{\text{CS}} = \mathbf{n} \times \mathbf{j}_{\text{CS}} \quad (5.13)$$

from the electric surface current densities. Due to the directive, outward-oriented radiation characteristic of the resulting sources, a null field inside the source region is approximated for convex Huygens surfaces.

The discretization of (5.13) is achieved either by enforcing the \mathbf{n} -rotation of one type of surface current density or by a mapping between two sets of the same basis functions, for instance for RWG functions [Eibert et al. 2016; Eibert and T. B. Hansen 2017; Kornprobst and Eibert 2018a]. We follow the latter strategy since it was demonstrated by Eibert and T. B. Hansen [2017] to be more accurate for inverse equivalent surface-source scenarios. The very same approach has been proposed for tackling PEC scattering scenarios with a WF implementation of the CS condition in Section 4.1.

5.2.2 Love-Current Retrieval via Post-Processing

After retrieving any kind of arbitrary equivalent surface current densities—for instance unconstrained electric and magnetic surface currents \mathbf{j} and \mathbf{m} —, we can change this solution to an entirely exterior Love current solution by evaluating the interior fields \mathbf{e}_i and \mathbf{h}_i of these currents on s and then subtracting the currents associated with this purely interior solution from the arbitrary solution. Alternatively, the exterior fields can be also evaluated. Since the Love current solution is related to specific (zero) fields inside v_i , the resulting equivalent currents, which are altered by a solution for the interior fields only, are Love currents according to (2.32) and (2.33), which are related to the total exterior fields.

One way to achieve this is to calculate the fields slightly outside of s for each triangle and map them back on the basis functions for \mathbf{j} and \mathbf{m} . Hence, the inverse

4. For more general scenarios with an impinging field, it is not a zero-field approximation any more, see the analysis related to Fig. 2.5 on p. 25.

problem is solved and (5.12) is fulfilled. Alternatively, the Love-current mapping proposed in the following Subsection 5.2.3 can be performed as a post-processing step just after we have obtained an unconstrained solution [Kornprobst et al. 2019b].

5.2.3 Love-Current Mapping via Calderón Projection

It is possible to obtain Love currents by evaluating the tangential electric and magnetic fields on the Huygens surface, which in turn relate to the Love surface current densities \mathbf{j}_L and \mathbf{m}_L . This mapping is known as the Calderón projector (CP), written in the form of [Calderón 1963; Hsiao and Kleinman 1997; Nédélec 2001; Kornprobst et al. 2019e]

$$\begin{bmatrix} \mathbf{j}_L \\ \mathbf{m}_L \end{bmatrix} = \begin{bmatrix} \mathbf{n} \times \mathbf{h} \\ \mathbf{e} \times \mathbf{n} \end{bmatrix} = \begin{bmatrix} \frac{1}{2}\mathbf{I} - \mathcal{K} & \mathcal{T} \\ -\mathcal{T} & \frac{1}{2}\mathbf{I} - \mathcal{K} \end{bmatrix} \begin{bmatrix} \mathbf{j} \\ \mathbf{m} \end{bmatrix}, \quad (5.14)$$

which consists of the suitably arranged equations (2.39) and (2.40). Discretized as a mapping matrix, we have

$$\mathbf{G} \mathbf{x}_L = \begin{bmatrix} \mathbf{G}_{\beta,\beta} & \mathbf{0} \\ \mathbf{0} & \mathbf{G}_{\beta,\beta} \end{bmatrix} \begin{bmatrix} \mathbf{i}_L \\ \mathbf{v}_L \end{bmatrix} = \begin{bmatrix} \frac{1}{2}\mathbf{G}_{\beta,\beta} - \mathbf{K}_{\beta,\beta} & \mathbf{T}_{\beta,\beta} \\ -\mathbf{T}_{\beta,\beta} & \frac{1}{2}\mathbf{G}_{\beta,\beta} - \mathbf{K}_{\beta,\beta} \end{bmatrix} \begin{bmatrix} \mathbf{i} \\ \mathbf{v} \end{bmatrix} = \mathbf{L}_m \mathbf{x} \quad (5.15)$$

with β testing functions for the rotated fields $\mathbf{e} \times \mathbf{n}$ and $\mathbf{n} \times \mathbf{h}$. The diagonal blocks of \mathbf{L}_m are a well-conditioned MFIE-alike matrix. Even if RWGs might not be the optimal choice of testing functions, this kind of testing is necessary since the mapping from the evaluated fields back to the currents is only possible due to the Gram matrices on the left-hand side of (5.15).⁵ The Gram matrix $\mathbf{G}_{\beta,\beta}$ on the left side of (5.15) is easily inverted iteratively, cf. Subsection 4.1.4. The conditioning of this formulation is excellent due to the dominant Gram matrices on the matrix diagonal and the typically smooth and convex reconstruction surfaces, for which the mesh quality is well under control.

However, it might happen that this MFIE-alike discretization of the mapping operator may suffer from the discretization inaccuracies of the standard MFIE, cf. Chapter 4 [Cools et al. 2011; Kornprobst and Eibert 2018a, 2018e]. We investigate the accuracy improvement attained in an improved discretization of the identity operator, which was presented in Section 4.3. Transferring this approach to the present case, the WF discretization of the identity operator inside the surface field evaluation reads

$$\mathbf{G}_{\beta,\beta,\text{WF}} = \frac{1}{2}\mathbf{G}_{\beta,\beta} - \frac{1}{2}\mathbf{G}_{\beta,\alpha}\mathbf{G}_{\beta,\beta}^{-1}\mathbf{G}_{\beta,\alpha}, \quad (5.16)$$

5. BC testing functions are also feasible, $\mathbf{n} \times$ RWGs are not.

$$\mathbf{G}_{\text{WF}} = \begin{bmatrix} \mathbf{G}_{\beta,\beta,\text{WF}} & \mathbf{0} \\ \mathbf{0} & \mathbf{G}_{\beta,\beta,\text{WF}} \end{bmatrix} \quad (5.17)$$

which changes the WF-CP matrix to

$$\mathbf{L}_{\text{m,WF-CP}} = \begin{bmatrix} \frac{1}{2}\mathbf{G}_{\text{WF}} - \mathbf{K}_{\beta,\beta} & \mathbf{T}_{\beta,\beta} \\ -\mathbf{T}_{\beta,\beta} & \frac{1}{2}\mathbf{G}_{\text{WF}} - \mathbf{K}_{\beta,\beta} \end{bmatrix}. \quad (5.18)$$

Both CPs are applied to the NRE (5.7) in the form of a left preconditioner as

$$\mathbf{G}^{-1} \mathbf{L}_{\text{m}} \mathbf{A}^{\text{H}} (\mathbf{A} \mathbf{x} - \mathbf{b}) = \mathbf{0}. \quad (5.19)$$

The NRE maps the field residual ($\mathbf{A} \mathbf{x}_i - \mathbf{b}$) of the i th solver iteration back to the currents by the adjoint operator \mathbf{A}^{H} . Then, the CP has the effect that the residual

$$\mathbf{r}_i = \mathbf{G}^{-1} \mathbf{L}_{\text{m}} \mathbf{A}^{\text{H}} (\mathbf{A} \mathbf{x}_i - \mathbf{b}) \quad (5.20)$$

of the i th search vector \mathbf{x}_i —and, thus, also the final solution composed of search vectors only of that kind—mostly contain Love currents with zero field inside the source region, where the inner-field suppression is limited by the current discretization and the accuracy of the CP.

An important effect of the CP is that the ambiguity of choosing both electric and magnetic equivalent currents is eliminated. Possible benefits are analyzed in the following results section. For the NEE, the very same mapping is introduced as

$$\mathbf{A} \mathbf{G}^{-1} \mathbf{L}_{\text{m}} \mathbf{A}^{\text{H}} \mathbf{y} = \mathbf{b} \quad (5.21)$$

and the post-processing step for retrieving the equivalent currents is adapted as

$$\mathbf{x} = \mathbf{G}^{-1} \mathbf{L}_{\text{m}} \mathbf{A}^{\text{H}} \mathbf{y}. \quad (5.22)$$

5.2.4 Love-Current or Zero-Field Side Constraint

The second possibility to enforce the zero-field condition in an exact manner is to set up a system of equations just for the Love currents without any mapping. The assumption that all currents occurring in (5.14) are Love currents yields⁶

$$\mathbf{0} = \begin{bmatrix} -\frac{1}{2}\mathbf{I} - \mathbf{K} & \mathcal{T} \\ -\mathcal{T} & -\frac{1}{2}\mathbf{I} - \mathbf{K} \end{bmatrix} \begin{bmatrix} \mathbf{j}_{\text{L}} \\ \mathbf{m}_{\text{L}} \end{bmatrix}. \quad (5.23)$$

6. The resulting operator in (5.23) is just an interior CP, which is employed to ideally enforce a null field inside of \mathbf{v}_i .

This equation is utilized as a SC and no mapping back to the current unknowns is required as for the CP. Thus, the testing functions can be chosen freely. Testing as for the PEC MFIE with β -functions leads to

$$\mathbf{o} = \begin{bmatrix} -\frac{1}{2}\mathbf{G}_{\beta,\beta} - \mathbf{K}_{\beta,\beta} & \mathbf{T}_{\beta,\beta} \\ -\mathbf{T}_{\beta,\beta} & -\frac{1}{2}\mathbf{G}_{\beta,\beta} - \mathbf{K}_{\beta,\beta} \end{bmatrix} \begin{bmatrix} \mathbf{i} \\ \mathbf{v} \end{bmatrix} = \mathbf{L}_{\text{SC-MF}} \mathbf{x} \quad (5.24)$$

with diagonal matrix blocks as known from the classical MFIE. Flipping the magnetic-field with the electric-field equations in (5.23) and testing with α -functions results in

$$\mathbf{o} = \begin{bmatrix} -\mathbf{T}_{\alpha,\beta} & -\frac{1}{2}\mathbf{G}_{\alpha,\beta} - \mathbf{K}_{\alpha,\beta} \\ -\frac{1}{2}\mathbf{G}_{\alpha,\beta} - \mathbf{K}_{\alpha,\beta} & \mathbf{T}_{\alpha,\beta} \end{bmatrix} \begin{bmatrix} \mathbf{i} \\ \mathbf{v} \end{bmatrix} = \mathbf{L}_{\text{SC-EF}} \mathbf{x} \quad (5.25)$$

with the well-tested EFIE matrix blocks $\mathbf{T}_{\alpha,\beta}$, as known from the classical PEC EFIE.

As we have seen in the analyses in Chapter 4, the LO RWG discretization of the EFIE is very accurate, whereas this is not the case for the MFIE. This may affect the Love-condition discretization and, thus, the achievable level of field suppression inside the AUT volume v_i . Since the numbers of side conditions in (5.24) or (5.25) are actually twice as many as theoretically required, it is possible to enforce only $N = N_{\text{un}}/2$ of the equations in (5.24) or (5.25) with the drawback of interior resonances or, in order to avoid interior resonances, to combine (5.24) and (5.25) in the manner of a CFIE approach. The most comprehensive approach with equal weighting of (5.24) and (5.25) and of the electric field and magnetic field leads to

$$\mathbf{o} = [\mathbf{I} \quad \mathbf{I}] (\mathbf{L}_{\text{SC-MF}} + \mathbf{L}_{\text{SC-EF}}) \mathbf{x} = \mathbf{L}_{\text{SC-CF}} \mathbf{x} \quad (5.26)$$

with the identity matrices $\mathbf{I} \in \mathbb{R}^{N \times N}$.

5.2.5 Scaling of the Zero-Field Side Conditions

The proper scaling of a SC with respect to the forward operator is a challenging task. A detailed investigation is necessary to arrive at a problem-independent method. In literature, the weighting is never discussed in detail with respect to NFFFTs. Either no satisfying solution is proposed in previously reported NFFFTs with a SC matrix [Paulus et al. 2019], or the L-curve method is mentioned to find the optimal weighting factor [Jørgensen et al. 2010; P. C. Hansen 1992; Kornprobst et al. 2019b], which does not seem to be very practical. The L-curve method means that the (Tikhonov-regularized) inverse problem is solved for a wide range of weighting factors for the SC. For a weak weighting of the SC, this yields a small residual. A sharp increase of the residual is observed at some value of an increased weighting factor. This gives a typically L-shaped curve if the norm of the residual

is plotted versus the norm of the regularization term. The desired weighting and its associated solution is found at the knee of the L. We perform a similar analysis in the following with the goal of determining an almost problem-independent weighting factor, or at least with the goal of obtaining a rule of thumb which does not require to solve the inverse problem multiple times.

In order to find a suitable weighting, we have to discuss the conditioning,⁷ and hence the SVDs of the two matrices under consideration, the forward operator \mathbf{A} and the SC matrix $\mathbf{L}_{\text{SC-}i}$. Both matrices are expected to exhibit a non-trivial null space. The formulation with electric and magnetic current unknowns is ill-posed per se as mentioned in Subsection 5.1.3. All Love constraint equations

$$\mathbf{L}_{\text{SC-}i} \mathbf{x} = \mathbf{0} \quad (5.27)$$

must also exhibit a (discretization-limited) nullspace which contains the sought solution. All non-Love currents are filtered out by nonzero SVs. It is worth noting that a wrong scaling does not only influence the conditioning of the system matrix, but also determines how accurately the inverse problem on the one hand and the SC on the other hand are solved for a certain residual stopping threshold. It might even occur that the weighting of the SC determines the achievable residual threshold.

At this point, we have to distinguish between the NRE and the NEE, whose differences have been analyzed in detail in Subsection 5.1.3. The NRE preserves the nullspace of \mathbf{A} and an additional regularization is both possible and necessary for a unique solution. This is a starting point for a meaningful regularization by the Love SC to eliminate the null-space of \mathbf{A} . The SC receives the scaling factor ξ , yielding the systems of equations

$$\begin{bmatrix} \mathbf{A} \\ \sqrt{\xi} \mathbf{L}_{\text{SC-}i} \end{bmatrix} \mathbf{x} = \begin{bmatrix} \mathbf{b} \\ \mathbf{0} \end{bmatrix} \quad (5.28)$$

and, subsequently, we attain the modified NRE

$$[\mathbf{A}^H \mathbf{A} + \xi \mathbf{L}_{\text{SC-}i}^H \mathbf{L}_{\text{SC-}i}] \mathbf{x} = \mathbf{A}^H \mathbf{b} \quad (5.29)$$

augmented by a Tikhonov regularization term.

In the NEE, the ill-posedness of the current unknowns \mathbf{x} is already mitigated. Employing the SC as a regularization term is not required anymore and is also not required for a unique solution. Nevertheless, having (5.28) in mind, the formulation

7. The conditioning of a singular matrix is just related to the nonzero SVs of a (truncated) SVD.

of the NEE including a SC is still possible as

$$\begin{bmatrix} \mathbf{A}\mathbf{A}^H & \sqrt{\tilde{\xi}}\mathbf{A}\mathbf{L}_{\text{SC}-i}^H \\ \sqrt{\tilde{\xi}}\mathbf{L}_{\text{SC}-i}\mathbf{A}^H & \tilde{\xi}\mathbf{L}_{\text{SC}-i}\mathbf{L}_{\text{SC}-i}^H \end{bmatrix} \begin{bmatrix} \mathbf{y} \\ \tilde{\mathbf{y}} \end{bmatrix} = \mathbf{b} \quad (5.30)$$

where $\tilde{\mathbf{y}}$ are additional unknowns in the space of the Love condition equations, constructed by a mapping

$$\mathbf{x} = \begin{bmatrix} \mathbf{A}^H & \sqrt{\tilde{\xi}}\mathbf{L}_{\text{SC}-i}^H \end{bmatrix} \begin{bmatrix} \mathbf{y} \\ \tilde{\mathbf{y}} \end{bmatrix} \quad (5.31)$$

similar to the one in (5.9). Further detailed investigations on the SC weighting are carried out for the NRE only and should be easily transferable to the NEE.

Side Condition Scaling for the NRE

The L-curve approach shows high computational cost and is highly problem-specific [P. C. Hansen 1992]. Hence, we propose a weighting based on the SVD properties of the matrices \mathbf{A} and $\mathbf{L}_{\text{SC}-i}$, which can be stated for any measurement setup. Employing an iterative solver with residual-limited accuracy, the smaller SVs are more likely to be “ignored” dependent on the stopping threshold. Thereby, the key is that neither the relevant SVs of the forward operator nor of the Love SC are neglected. The decay of the SVs of \mathbf{A} is much stronger than for $\mathbf{L}_{\text{SC}-i}$, since the observability of the various propagating modes decreases with the measurement or observation distance, whereas the observation distance for the Love condition is zero.

For an empirical study, we employ a small synthetic example, see Fig. 5.2. A dipole model of an open-ended waveguide (OEWG), size $\lambda/4 \times \lambda/2 \times \lambda/4$, is employed to generate 300 ideal measurements with Fibonacci sampling on a sphere with radius 3λ [Keinert et al. 2015]. The source reconstruction mesh is $\lambda/2 \times 3\lambda/4 \times \lambda/2$ in size and features 477 RWG electric and magnetic current unknowns each. In Fig. 5.3, the SV spectra of the forward operator \mathbf{A} , of the SC matrices $\mathbf{L}_{\text{SC}-\text{MF}}$ (MFIE-alike), $\mathbf{L}_{\text{SC}-\text{EF}}$ (EFIE-alike), $\mathbf{L}_{\text{SC}-\text{CF}}$ (CFIE-alike), and of the CP mapping matrix \mathbf{L}_{m} are shown. While the matrix \mathbf{A} exhibits a clear null space after $M = 300$ and a strong decay beforehand, the SV decay of the Love-current conditions is weaker. Interior and exterior solutions are clearly separated with the SC-CF constraint (drop of SVs to zero after $N = 477$), but this is not as clearly observed with the SC-MF and SC-EF constraints. Here, the discretization errors of the overdetermined sets of equations do not allow to clearly separate the non-radiating from the strongly evanescent modes. The SVs are interpreted as follows. For the CP, Love currents are found at large SVs, while for the SCs, Love currents are found for the small, close to vanishing SVs.

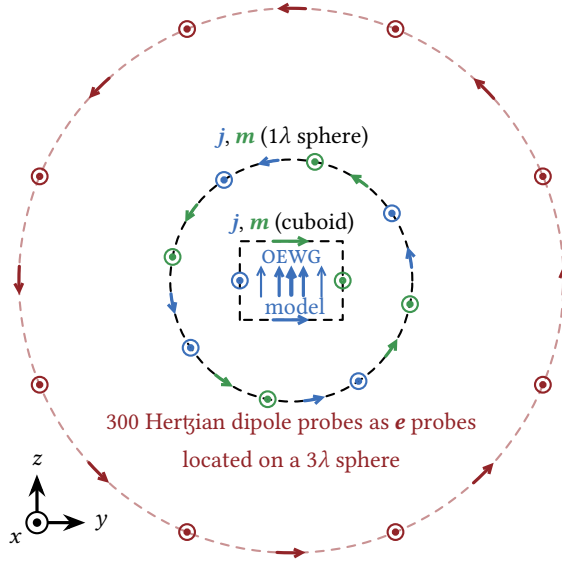


Fig. 5.2: Setup of synthetic measurements with Hertzian dipole probes and reconstruction surfaces for equivalent electric and magnetic surface currents © 2021 IEEE [Kornprobst et al. 2021a].

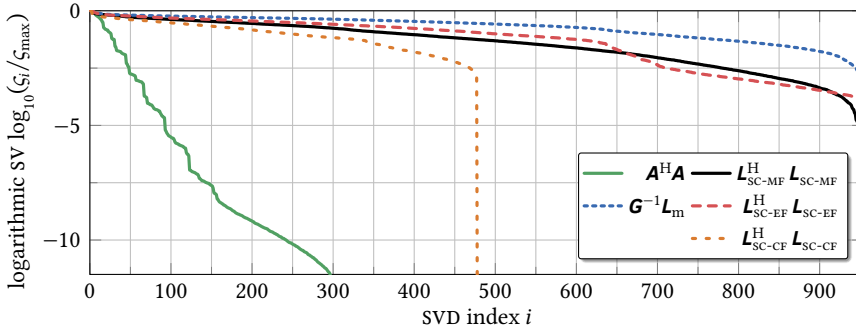


Fig. 5.3: Comparison of SV spectra of the forward operator, the differently tested Love SCs, and the CP © 2021 IEEE [Kornprobst et al. 2021a].

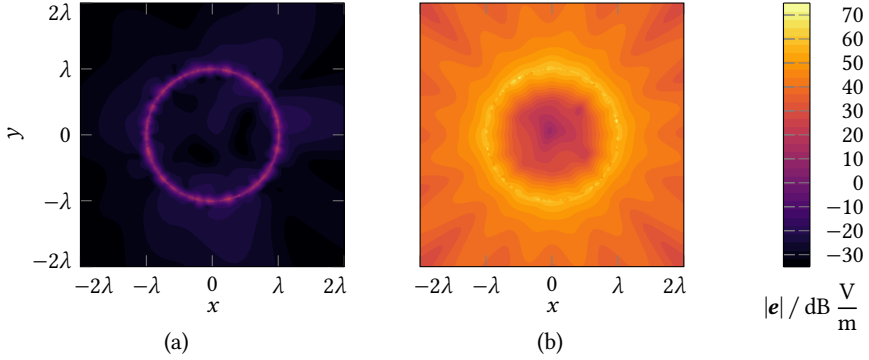


Fig. 5.4: Absolute electric field of singular vectors corresponding to (a) ζ_{\max} of $\mathbf{L}_{\text{SC-EF}}^{\text{H}} \mathbf{L}_{\text{SC-EF}}$ (non-Love current, evanescent) and to (b) ζ_{\min} of $\mathbf{P}_{\mathbf{A}} \mathbf{L}_{\text{SC-EF}}^{\text{H}} \mathbf{L}_{\text{SC-EF}} \mathbf{P}_{\mathbf{A}}$ (Love current, strongly radiating) © 2021 IEEE [Kornprobst et al. 2021a].

This small example is mostly intended to be an illustration of the fact that the decay of the SV spectrum of \mathbf{A} is steeper than of the SC spectra. This key property stems from the different interaction distances between the sources and the observation locations in the forward operator and in the SC operators, respectively. Larger and more realistic test cases follow in the subsequent subsections.

Since the AUT box with dimensions $3\lambda/4 \times \lambda/2 \times \lambda/2$ cannot provide a particularly strong field suppression inside, we repeat the same investigation with a sphere with radius 1λ and about 13 000 electric and magnetic current unknowns each. Only the first 300 SVs and corresponding singular vectors are efficiently computed [Martinson et al. 2011], since the smallest SVs cannot be evaluated realistically due to the matrix size. The spectra (not shown) look very similar to Fig. 5.3 with the only difference of a slightly smaller decay of the SVs of \mathbf{A} , since more modes are excitable on the enlarged equivalent surface—however, still steeper than the SV decay of the SCs of course. The spherical AUT hull is employed to illustrate the meanings of the SVs in the SC. The electric field in a cut plane is evaluated for several singular vectors related to specific SVs of the SC-EF matrix in Fig. 5.4. Figure 5.4(a) shows the electric field of the singular vector related to the largest SV ζ_{\max} of the matrix $\mathbf{L}_{\text{SC-EF}}^{\text{H}} \mathbf{L}_{\text{SC-EF}}$, i.e., of the EFIE-alike SC matrix. This large SV corresponds to an evanescent mode from a non-Love current, which is also what can be seen in the field plot. For the smallest SVs, we project the matrices into $\text{im } \mathbf{A}$ by utilizing the projection matrix

$$\mathbf{P}_{\mathbf{A}} = \mathbf{A}^+ \mathbf{A}, \quad (5.32)$$

where $(\cdot)^+$ denotes a generalized inverse. The fields of the singular vector corresponding to the smallest SV of $\mathbf{P}_A \mathbf{L}_{\text{SC-EF}}^H \mathbf{L}_{\text{SC-EF}} \mathbf{P}_A$ are evaluated in Fig. 5.4(b).⁸ The radiated fields are rather strong and a certain suppression of the interior field is observed. Overall, a separation of strongly and weakly radiating currents is observed for the largest and smallest SVs, respectively. For the CP, the meanings of maximum and minimum SVs are of course interchanged.

Note that all considered singular vectors are orthonormal, i.e., their possible influence on the norm $\|\mathbf{x}\|_2$ is the same and non-Love currents are suppressed by the Love condition only at a suitable weighting. A weak weighting has a negligible effect on the inverse problem solution, and a strong weighting limits the achievable solver residual threshold, which has a similar effect as an too early solver termination.

The question remains as how to incorporate these insights in a meaningful way into the transformation process appropriate for any kind of measurement. From the SVD analysis, it is clear that an equal weighting normalized to the maximum SVs—as shown in Fig. 5.3—will lead to a dominant SC and a poor solution quality of the inverse problem. With the knowledge of the achievable accuracy of the algorithm and of the measurement setup,⁹ one can choose a weighting of the SC at a somewhat larger ratio than the expected accuracy. The accuracy, e.g., as a measure for the signal-to-noise ratio (SNR), can be quantified at the maximum of the measured AUT NF as

$$\text{SNR} = \frac{\|\epsilon_{\text{OE}}\|_2 / \sqrt{M}}{\max_{k \in [0, M]} |[\mathbf{b}]_k|} \quad (5.33)$$

scaled according to the number of observation points M and assuming $\|\epsilon_{\text{OE}}\|_2$ is known. The relative ℓ_2 -norm of the OE in the NF is estimated as the RD ϵ_{RD} . As discussed in Subsection 5.1.2, the RD of the retrieved solution ϵ_{RD} is commonly a bit smaller than ϵ_{OE} since parts of the OE are almost inevitably attributed to the solution of the inverse problem. Measurement errors (echoes, positioning uncertainties, etc.) may increase the ϵ_{OE} . These quantities, and the eventually achievable ϵ_{OE} , are commonly known for a measurement setup and determine the iterative solver stopping threshold or the SVD truncation criterion for direct solvers.

The correct weighting of the SC is now apparent: The Love-current SVs—i.e., the smallest SVs of the SC—have to disappear below ϵ_{OE}^2 , and the non-Love current SVs have to be located above ϵ_{OE}^2 . With a suitable iterative solver termination criterion based on ϵ_{OE} , the non-Love parts in the solution are effectively suppressed. Certainly, the full SV spectrum is computationally too costly to compute, but a

8. After the projection into $\text{im} \mathbf{A}$, there are only $M = 300$ non-zero SVs instead of N_{un} SVs. The projector \mathbf{P}_A suppresses non-observable (non-radiating) components at the measurement locations.

9. The FIAFTA itself is limited by numerical errors controllable by the MLFMM accuracy settings; measurements have inherent limitations by the SNR and other measurement errors.

normalization relative to the largest SV is feasible and also reasonable, if we keep in mind that the decay of the SVs related to the Love SC is considerably slower than the decay of the SVs in the forward operator. Estimating the largest SV is easily done with a few so-called power iterations. A repeated evaluation of the matrix-vector product gives a good estimate of the largest SV

$$\hat{\mathbf{S}}_{\mathbf{B},\max} = \frac{\mathbf{x}^H \mathbf{B}^k \mathbf{x}}{\mathbf{x}^H \mathbf{B}^{k-1} \mathbf{x}}, \quad (5.34)$$

assuming a Hermitian matrix \mathbf{B} . This method converges rather fast, for a reasonable residual below 10^{-1} typically with $k < 5$. Other possibilities include Arnoldi iterations or a Rayleigh quotient with the starting vector $\mathbf{A}^H \mathbf{b}$.

In order to attain a normalization according to the largest SVs of \mathbf{A} and the Love SC, respectively, (as seen in Fig. 5.3) we employ the (estimated) ratio

$$v = \frac{\hat{\mathbf{S}}_{\mathbf{A}^H \mathbf{A}}}{\hat{\mathbf{S}}_{\mathbf{L}_{\text{SC}} - i^H \mathbf{L}_{\text{SC}} - i}}. \quad (5.35)$$

The normalization has to be done in a way that, first, the larger SVs of \mathbf{A} influence the reconstruction and, second, the iterative solver termination threshold at ϵ_{OE} coincides with the desired SV threshold within the SV spectrum of the Love SC. This is achieved by choosing the scaling factor ξ according to (5.29) as

$$1 > \frac{\xi}{v} > \epsilon_{\text{OE}}^2. \quad (5.36)$$

For the studied example of an OEWG, the SVs of the combined operator according to (5.29) of several values of ξ/v and for an EFIE-like SC are shown in Fig. 5.5. An ϵ_{OE}^2 range is depicted for each value of ξ/v . The corresponding ϵ_{OE} value is determined as follows. Based on the NRE including an error vector ϵ_{OE} within \mathbf{b} , we recognize that \mathbf{A}^H is multiplied to both the forward operator and the error vector. Hence, the ϵ_{OE} range in Fig. 5.5 has to be considered. We assume that, for the discussed scenario,

$$\xi/v = (10^1 \dots 10^3) \epsilon_{\text{OE}}^2 \quad (5.37)$$

is a good choice. For larger scenarios, the upper bound ξ/v is shifted to slightly larger values. In the following results section, it is demonstrated that this scaling is indeed meaningful. Analyzing this relation in depth for any individual source reconstruction scenario would require the L-curve method.

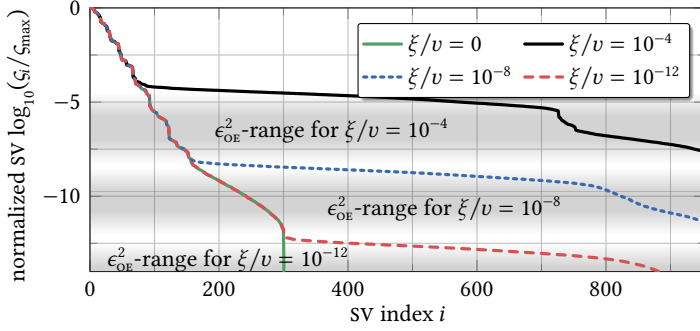


Fig. 5.5: Analysis of the weighting ξ/v by a look at the SVs of (5.29). Gray areas approximately show possible ϵ_{OE}^2 ranges for the given weights.

Tab. 5.1: Summary of equivalent source type notation.

abbreviation	long version
J	purely electric currents
M	purely magnetic currents
JM	unconstrained electric and magnetic currents
CS	weak-form combined sources
SC-MF	Love-current side constraint, MFIE-alike
SC-EF	Love-current side constraint, EFIE-alike
SC-CF	Love-current side constraint, CFIE-alike
CP	Calderón projector
WF-CP	improved weak-form Calderón projector
SH	spherical harmonics expansion
DSH	distributed spherical harmonics expansion

5.3 Source Reconstruction and FF Transformation Results

We consider two types of measurement scenarios. First, accuracy analyses are performed for simulated synthetic data since only in such a case the true solution, which is to be retrieved, is known. Second, we consider real measurement data taken inside an anechoic chamber. In both cases, we investigate two separate issues.

First, we examine the question of which source representation is the most beneficial choice. Table 5.1 summarizes the studied equivalent source types. A standard

version is to expand the fields with SHs, either scalar or vectorial. The number of unknowns N_{un} is determined under the assumption that a certain amount of propagating modes is supported inside the volume of the AUT minimum sphere [J. E. Hansen 1988]. Therefore, N_{un} is usually larger than the real N_{DOF} if the AUT shape is not spherical but with this source representation, it is not that simple to really separate these two numbers. As an alternative, we consider a DSH expansion. The AUT surface is subdivided into smaller pieces, which are assigned to the typical (non-empty) boxes of the MLFMM on a certain level. Then, SHs are employed as expansion functions in each non-empty box individually. This allows for a better source localization than with a single SH expansion, and furthermore, geometrical information about the AUT shape is incorporated into the transformation algorithm. Commonly, $N_{\text{un}} \gg N_{\text{DOF}}$ and the forward operator is band-limited subject to the MLFMM settings. This DSH expansion may be improved by considering combinations of SHs which show an outward-oriented radiation similar to CSs [Eibert et al. 2022b; Ostrzyharczik et al. 2023; Eibert et al. 2022a].

In contrast, a source representation with even better source localization is a surface-source representation on a Huygens surface (closed or open) around the AUT. Geometrical details can be described as granularly as desired. We consider electric and magnetic surface current densities (JM) with RWG discretization. Thus, the surface currents are oversampled and, again, $N_{\text{un}} \gg N_{\text{DOF}}$ holds. These JM currents have inherently even another ambiguity (leading to an increased kernel dimension) between electric and magnetic current solutions, as discussed in this work in detail. To avoid these ambiguities, we also consider just electric surface current densities (J), just magnetic ones (M), and restricted combinations of both as proposed in Section 5.2. A clear downside of the enforcement of a Love current solution is the considerably increased computational effort, which can exceed the effort required for the solution of the actual inverse equivalent surface-source problem. It remains to be investigated whether this effort is worth it in terms of its influence in the solution process.

Second, we investigate the related question of how to regularize the inverse source solution effectively without sacrificing accuracy. To this end, not only the constraints on the retrieved surface current densities are studied but also the choice between the NREs and the NEEs.

5.3.1 Results with Synthetic Near Field Data

Transformation Results for the Small Synthetic OEFG

For the discussed OEFG example, we consider the equivalent source types listed in Tab. 5.1, the various types of surface current densities, but also—for completeness regarding (surface) source representations—SH and DSH sources. For the latter, the

MLFMM-octree is built for the AUT hull and SH expansions are employed in the non-empty lowest-level boxes with a size of 0.15λ .

White Gaussian noise with $\epsilon_{\text{OE}} = 10^{-2}$ is added to the ideal synthetic data. All the solvers except the SC ones have been analyzed for the small cube mesh with regard to their properties and the results are summarized in Tab. 5.2. Excellent results are highlighted in **bright green**, good ones in **blue**, worse ones in **darkish orange**, and the underwhelmingly poor ones in **dark red**. Cells without a judgment are **gray**. To put these ratings into perspective, the following should be considered. An iteration count N_{it} below ten is rather good, while hundreds of iterations are too many. The solver residual ϵ_{res} only conveys information for the NEE case. The normalized RD $\epsilon_{\text{RD}}/\epsilon_{\text{OE}}$ has an ideal value of 1, with lower values indicating over-fitting and larger values indicating a wrong solution. The zero field quality inside v_1 $\epsilon_{\text{ZF,avg}}$ is judged by averaging the field inside s at 100 observation points, normalized to the JM-NEE case, which shows a strong but not excessive interior field. This is visualized in Fig. 5.6 for various different solutions. The relative FF error between the reconstructed \mathbf{e}^{FF} and the reference $\mathbf{e}_{\text{ref}}^{\text{FF}}$ is calculated as per (4.46).

Iterative solver settings are chosen as the residual thresholds $\epsilon_{\text{res,th}} = 10^{-4}$ for the NRE and $\epsilon_{\text{res,th}} = \epsilon_{\text{RD}} = 10^{-2}$ for the NEE. We further investigate a somewhat relaxed, relative termination criterion¹⁰ dependent on the iterative solver convergence ratio: The solver stops if the relative residual improvement $\Delta\|r\|$ becomes worse than 0.99 three times in a row. This is demonstrated to work almost as well as the absolute stopping for the NEE in Tab. 5.2(d), whereas the NRE struggles to prevent overfitting without an absolute stopping, cf. Tab. 5.2(a) and (b). Overfitting leads to a solution which is numerically contaminated by the null space of \mathbf{A} . Furthermore, we note that the NEE version always converges in fewer iterations than the NRE for any specific source type or stopping criterion.

Various values of ξ/v for both the SC-MF and the SC-EF discretizations are investigated in Tab. 5.3, again for the same absolute and relative stopping criteria. We observe that the SC with increasing weighting i) slows down the iterative solver (undesired), ii) increases the FF error if the weighting becomes too strong (undesired), and iii) increases the RD (up to a certain limit, desirable). The RD limitation is observed even though the solver performs hundreds of iterations and reaches a residual of 10^{-9} —if the correct weight of about $\xi/v = 10^1 \dots 10^2$ is set in Tab. 5.3(b) and (d). The same is observed, to a certain degree, for the CP and for the WF-CP in Tab. 5.2(b).

Overall, the only ensured and meaningful effect of enforcing a Love-current solution is a zero field inside s , see Fig. 5.6(e) and (f). The second effect of influencing the iterative solver residual threshold is achieved much more conveniently—and

¹⁰. The advantage of a relative stopping criterion is that no pre-knowledge about the measurement setup (i.e., knowledge of the OE) is required.

Tab. 5.2: Comparison of various source types for the two NEs, $\epsilon_{\text{oe}} = 10^{-2}$. (a) NRE with $\epsilon_{\text{res,th}} = 10^{-4}$. (b) NRE with $\Delta\|\mathbf{f}\| = 0.99$. (c) NEE with $\epsilon_{\text{res,th}} = 10^{-2}$. (d) NEE with $\Delta\|\mathbf{f}\| = 0.99$.

type	N_{it}	$\epsilon_{\text{res,th}}$	$\epsilon_{\text{RD}}/\epsilon_{\text{oe}}$	$\epsilon_{\text{FR,avg}}$	$\epsilon_{\text{FR,max}}$
SH	5	$6.1 \cdot 10^{-5}$	0.64	—	-43.2 dB
DSH	24	$9.9 \cdot 10^{-5}$	0.77	—	-44.6 dB
J	41	$7.8 \cdot 10^{-5}$	0.92	8.5 dB	-48.4 dB
M	32	$9.8 \cdot 10^{-5}$	1.02	2.0 dB	-44.9 dB
JM	32	$8.2 \cdot 10^{-5}$	0.94	0.0 dB	-48.6 dB
CS	32	$9.2 \cdot 10^{-5}$	0.94	-5.8 dB	-48.2 dB
CP	31	$9.6 \cdot 10^{-5}$	0.99	-16.6 dB	-49.4 dB
WF-CP	32	$9.9 \cdot 10^{-5}$	0.98	-21.1 dB	-48.8 dB

(a)

type	N_{it}	$\epsilon_{\text{res,th}}$	$\epsilon_{\text{RD}}/\epsilon_{\text{oe}}$	$\epsilon_{\text{FR,avg}}$	$\epsilon_{\text{FR,max}}$
SH	16	$5.0 \cdot 10^{-8}$	0.64	—	-43.2 dB
DSH	208	$1.6 \cdot 10^{-7}$	0.12	—	-40.6 dB
J	134	$8.9 \cdot 10^{-5}$	0.62	30.4 dB	-43.6 dB
M	139	$4.4 \cdot 10^{-8}$	0.58	24.1 dB	-42.9 dB
JM	152	$3.8 \cdot 10^{-8}$	0.45	40.0 dB	-43.4 dB
CS	121	$1.9 \cdot 10^{-7}$	0.69	18.1 dB	-43.6 dB
CP	48	$3.2 \cdot 10^{-5}$	0.87	-11.8 dB	-48.0 dB
WF-CP	48	$4.9 \cdot 10^{-5}$	0.87	-11.8 dB	-46.7 dB

(b)

type	N_{it}	$\epsilon_{\text{res,th}}$	$\epsilon_{\text{RD}}/\epsilon_{\text{oe}}$	$\epsilon_{\text{FR,avg}}$	$\epsilon_{\text{FR,max}}$
SH	2	$6.9 \cdot 10^{-3}$	0.69	—	-43.3 dB
DSH	5	$9.7 \cdot 10^{-3}$	0.97	—	-40.4 dB
J	37	$9.9 \cdot 10^{-5}$	0.99	8.5 dB	-45.1 dB
M	32	$9.6 \cdot 10^{-3}$	0.96	2.0 dB	-45.0 dB
JM	26	$9.7 \cdot 10^{-3}$	0.97	0.0 dB	-48.0 dB
CS	28	$9.8 \cdot 10^{-3}$	0.98	-7.7 dB	-47.2 dB
CP	30	$9.9 \cdot 10^{-3}$	0.99	-21.2 dB	-47.5 dB
WF-CP	30	$9.9 \cdot 10^{-3}$	0.99	-21.6 dB	-47.7 dB

(c)

type	N_{it}	$\epsilon_{\text{res,th}}$	$\epsilon_{\text{RD}}/\epsilon_{\text{oe}}$	$\epsilon_{\text{FR,avg}}$	$\epsilon_{\text{FR,max}}$
SH	7	$6.4 \cdot 10^{-3}$	0.64	—	-43.3 dB
DSH	14	$8.0 \cdot 10^{-3}$	0.80	—	-45.3 dB
J	45	$8.7 \cdot 10^{-5}$	0.87	8.6 dB	-47.6 dB
M	38	$8.9 \cdot 10^{-3}$	0.89	2.1 dB	-48.3 dB
JM	33	$9.2 \cdot 10^{-3}$	0.92	5.2 dB	-47.6 dB
CS	34	$9.1 \cdot 10^{-3}$	0.91	-3.7 dB	-48.2 dB
CP	35	$9.5 \cdot 10^{-3}$	0.95	-21.3 dB	-47.9 dB
WF-CP	35	$9.5 \cdot 10^{-3}$	0.95	-21.7 dB	-47.7 dB

(d)

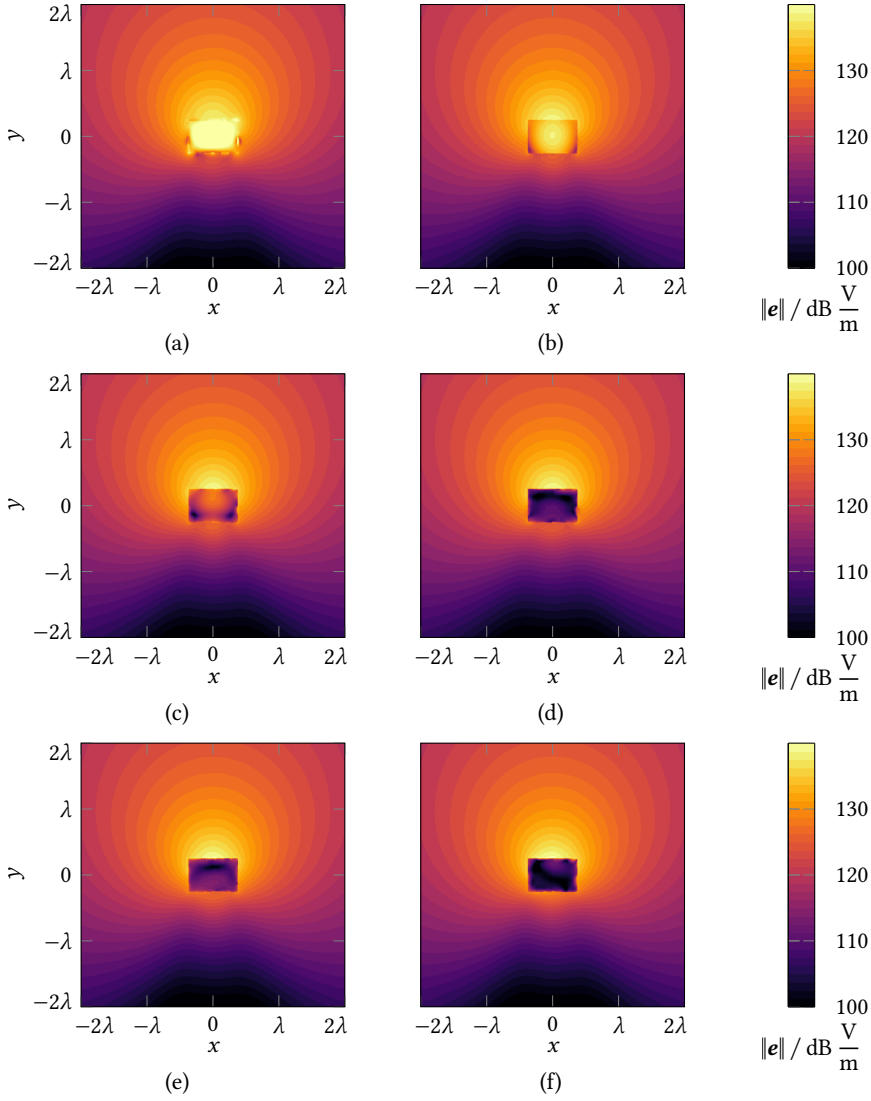


Fig. 5.6: Reconstructed electric field in a cut plane of the (a) J – NEE, (b) JM – NEE, (c) CS – NEE, and (d) CP – NEE solutions with $\epsilon_{\text{res,th}} = 10^{-2}$ termination criterion as well as (e) SC-MF – NRE ($\xi/v = 10^2$) and (f) SC-EF – NRE ($\xi/v = 10^1$) solutions with $\epsilon_{\text{res,th}} = 10^{-4}$ termination criterion. © 2021 IEEE [Kornprobst et al. 2021a].

Tab. 5.3: Analysis of Love SC weighting ξ/ν , NRE, ϵ_{OE} = 10^{-2} . (a) SC-MF, $\epsilon_{res,th}$ = 10^{-4} . (b) SC-MF, $\Delta\|r\|$ = 0.99. (c) SC-EF, $\epsilon_{res,th}$ = 10^{-4} . (d) SC-EF, $\Delta\|r\|$ = 0.99.

$\xi/(u\epsilon_{OE}^2)$	N_H	$\epsilon_{res,th}$	$\epsilon_{RD}/\epsilon_{OE}$	ϵ_{Z}		$\epsilon_{F,max}$
				$\epsilon_{Z,avg}$	$\epsilon_{F,min}$	
10^0	32	$8.8 \cdot 10^{-5}$	0.94	-0.23 dB	-48.7 dB	-48.7 dB
$10^{0.5}$	36	$9.9 \cdot 10^{-5}$	0.92	-1.0 dB	-49.2 dB	-49.2 dB
10^1	40	$9.3 \cdot 10^{-5}$	0.89	-9.7 dB	-49.0 dB	-49.0 dB
$10^{1.5}$	39	$9.6 \cdot 10^{-5}$	0.90	-16.7 dB	-49.4 dB	-49.4 dB
10^2	39	$9.4 \cdot 10^{-5}$	0.92	-18.3 dB	-48.1 dB	-48.1 dB
10^3	49	$9.9 \cdot 10^{-5}$	0.98	-18.2 dB	-41.4 dB	-41.4 dB
10^4	101	$9.7 \cdot 10^{-5}$	2.33	-16.9 dB	-41.4 dB	-41.4 dB

(a)

$\xi/(u\epsilon_{OE}^2)$	N_H	$\epsilon_{res,th}$	$\epsilon_{RD}/\epsilon_{OE}$	ϵ_{Z}		$\epsilon_{F,max}$
				$\epsilon_{Z,avg}$	$\epsilon_{F,min}$	
10^0	225	$1.1 \cdot 10^{-9}$	0.76	-11.9 dB	-44.7 dB	-44.7 dB
$10^{0.5}$	226	$1.4 \cdot 10^{-9}$	0.78	-14.5 dB	-45.3 dB	-45.3 dB
10^1	238	$1.2 \cdot 10^{-9}$	0.80	-16.2 dB	-45.9 dB	-45.9 dB
$10^{1.5}$	249	$1.2 \cdot 10^{-9}$	0.82	-17.2 dB	-46.3 dB	-46.3 dB
10^2	268	$1.2 \cdot 10^{-9}$	0.84	-17.5 dB	-45.9 dB	-45.9 dB
10^3	326	$1.7 \cdot 10^{-9}$	1.03	-17.2 dB	-43.2 dB	-43.2 dB
10^4	409	$3.3 \cdot 10^{-9}$	2.35	-16.5 dB	-38.2 dB	-38.2 dB

(b)

$\xi/(u\epsilon_{OE}^2)$	N_H	$\epsilon_{res,th}$	$\epsilon_{RD}/\epsilon_{OE}$	ϵ_{Z}		$\epsilon_{F,max}$
				$\epsilon_{Z,avg}$	$\epsilon_{F,min}$	
10^{-1}	32	$8.3 \cdot 10^{-5}$	0.94	-0.03 dB	-48.6 dB	-48.6 dB
10^0	32	$9.2 \cdot 10^{-5}$	0.93	-0.33 dB	-48.7 dB	-48.7 dB
$10^{0.5}$	40	$9.9 \cdot 10^{-5}$	0.89	-3.7 dB	-49.2 dB	-49.2 dB
10^1	40	$9.5 \cdot 10^{-5}$	0.89	-21.5 dB	-49.0 dB	-49.0 dB
$10^{1.5}$	39	$8.1 \cdot 10^{-5}$	0.91	-15.7 dB	-49.4 dB	-49.4 dB
10^2	38	$9.8 \cdot 10^{-5}$	0.94	-14.8 dB	-48.1 dB	-48.1 dB
10^3	68	$9.9 \cdot 10^{-5}$	1.18	-12.5 dB	-41.4 dB	-41.4 dB
10^4	128	$9.7 \cdot 10^{-5}$	3.63	-11.6 dB	-27.0 dB	-27.0 dB

(c)

$\xi/(u\epsilon_{OE}^2)$	N_H	$\epsilon_{res,th}$	$\epsilon_{RD}/\epsilon_{OE}$	ϵ_{Z}		$\epsilon_{F,max}$
				$\epsilon_{Z,avg}$	$\epsilon_{F,min}$	
10^{-1}	236	$1.5 \cdot 10^{-9}$	0.72	-2.1 dB	-44.0 dB	-44.0 dB
10^0	262	$1.4 \cdot 10^{-9}$	0.76	-9.3 dB	-44.9 dB	-44.9 dB
$10^{0.5}$	266	$1.5 \cdot 10^{-9}$	0.78	-10.9 dB	-45.7 dB	-45.7 dB
10^1	304	$1.5 \cdot 10^{-9}$	0.81	-11.6 dB	-46.6 dB	-46.6 dB
$10^{1.5}$	309	$2.2 \cdot 10^{-9}$	0.84	-11.8 dB	-46.6 dB	-46.6 dB
10^2	329	$1.6 \cdot 10^{-9}$	0.88	-11.7 dB	-46.8 dB	-46.8 dB
10^3	360	$4.1 \cdot 10^{-9}$	1.19	-11.6 dB	-42.0 dB	-42.0 dB
10^4	392	$1.0 \cdot 10^{-8}$	3.60	-11.5 dB	-27.2 dB	-27.2 dB

(d)

at a much lower computation cost—with an ambiguous JM solution or a unique CS solution by choosing an appropriate stopping criterion for the selected NE, with a clear preference for the NEE.

Interestingly, no significant differences in the solution quality between MFIE- and EFIE-alike discretizations of the Love SC can be identified—while this classical MFIE discretization causes accuracy problems for scattering problems, see Chapter 4. Even the zero-field quality is comparable, with slight advantages for the SC-MF. A similar lack of influence is observed for the CP, where the potentially accuracy-improved WF-CP does not perform better in any of the considered measures.

The SH approach shows the fastest iterative solver convergence, however, also an about 3 dB to 8 dB larger FF error. However, this is by no means a *fair* comparison.¹¹ It is listed for the sake of completeness. The second-fastest source type is DSH, again without the full diagnostic capabilities. The fastest surface-current solutions are obtained either with ambiguous JM or unique CS currents. The use of the NEE speeds up the solution process from 32 to 26 and 28 iterations. Furthermore, we observe that the JM and CS solutions are among the most accurate ones.

In this investigation, the JM-NEE and CS-NEE are the fastest-convergent (i.e., best conditioned) and most accurate (in the NF and FF) surface-current formulations. Hence, JM or CS currents with the NEE seem to be the most reasonable choice for best accuracy and best conditioning. Diagnostics capabilities can be easily enhanced in the post-processing, cf. Subsection 5.2.2.

Finally, we analyze the weighting of the Love SC-MF for different SNRs in Fig. 5.7. An acceptably suppressed interior field is observed with weightings larger than $\xi/v = 10^1 \epsilon_{\text{OE}}^2$, and the reconstructed FF deteriorates with a too strong weighting above $\xi/v = 10^3 \epsilon_{\text{OE}}^2$. Note that the FF error is given with reference to the OE; the processing gain is therefore included. As seen in Tab. 5.3, a similar behavior is observed for the SC-EF variant. However, the zero-field quality is more sensitive especially to the choice of the stopping criterion.

A More Realistic Antenna Model

In the following, a simulation model of a DRH400 antenna at 6 GHz is considered [RFspin 2021b]. The integral equation solver of the simulation software Feko was employed to generate synthetic NF data (3754 measurement samples) for a spiral scan with 20% oversampling in relation to the minimum sphere of the AUT [Altair 2021; J. E. Hansen 1988; Bucci et al. 2003]. The advantage compared to measurements is that the real solution (i.e., a reference) is known from simulation.

11. Since the measurement distance of this example is quite large (beneficial for SH), the iterative solver convergence of the SH NFFFT is extremely fast. Yet, the SH solution exhibits the drawback that it cannot offer the same diagnostic information and source localization as an equivalent current approach and, thus, exhibits larger NF and FF errors.

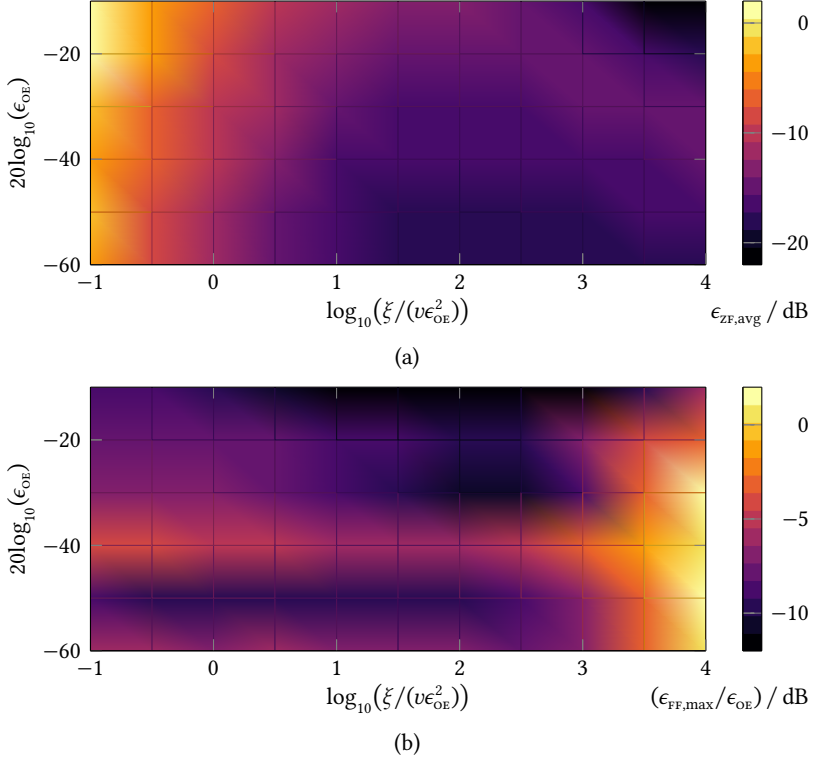


Fig. 5.7: Love SC-MF weighting analysis regarding (a) zero-field quality and (b) maximum FF error for varying OE levels, for the OEWG simulation model © 2021 IEEE [Kornprobst et al. 2021a].

First, we perform an analysis of the Love SC weighting (for the case of SC-MF) in Fig. 5.8. The results are similar to the OEWG case. Deterioration of the solution is observed at larger weights of the SC, at about $\xi/v = 10^5 \epsilon_{\text{OE}}^2$. The lower limit for obtaining an acceptable zero field again depends on the SNR. Also, the GMRES stopping criterion heavily influences the SC fulfillment. For the high-SNR/low-weighting region, the weighting needs to be relaxed to obtain a Love-current solution. In the following, we choose $\xi/v = 10^3 \epsilon_{\text{OE}}^2$.

For further investigations, white Gaussian noise with $\epsilon_{\text{OE}} = 10^{-3}$ is added to the simulated NF. The inverse problem is solved for three different equivalent surfaces of the AUT: the minimum sphere, a tight hull (close to the smallest convex hull) around the AUT, and an exact geometrical representation, see Fig. 5.9. The

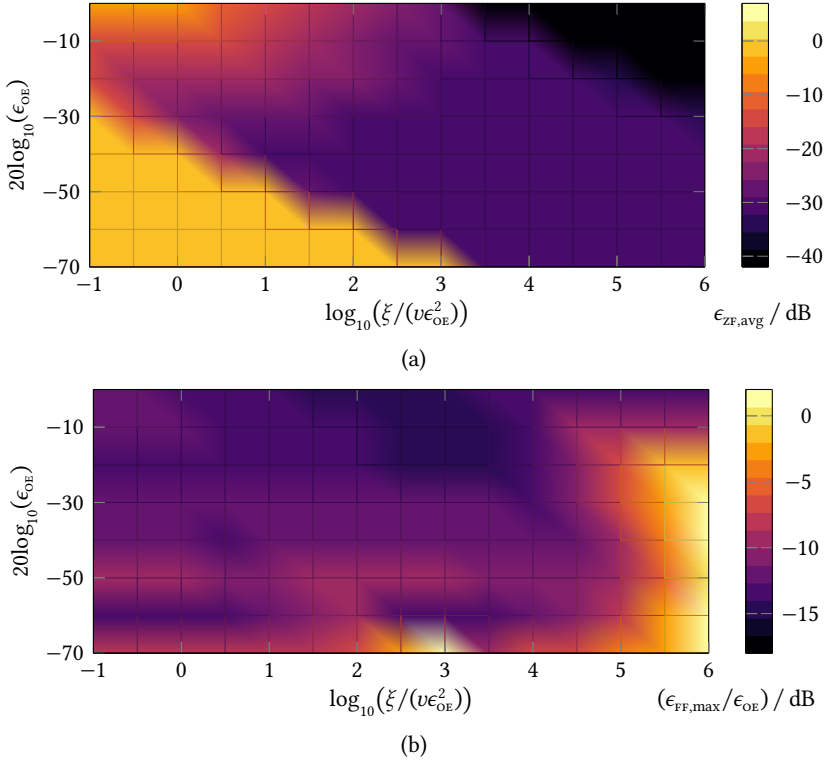


Fig. 5.8: Love SC-MF weighting analysis regarding (a) zero-field quality and (b) maximum FF error for varying OE levels, for the DRH400 simulation model © 2021 IEEE [Kornprobst et al. 2021a].

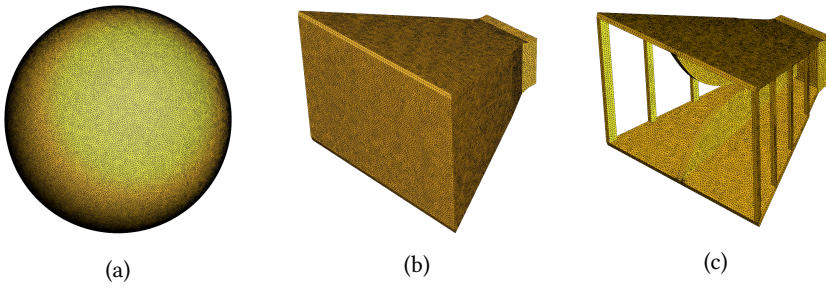


Fig. 5.9: Huygens surfaces for the DRH400 simulation model: (a) a sphere, (b) a tight, close to convex hull, and (c) an exact model © 2021 IEEE [Kornprobst et al. 2021a].

Tab. 5.4: Source type comparison on a convex hull around the AUT, $\epsilon_{\text{OE}} = 10^{-3}$, for (a) the NRE with $\Delta\|r\| = 0.995$ and (b) the NEE with $\Delta\|r\| = 0.999$.

(a)

type	N_{it}	$\epsilon_{\text{res,th}}$	$\epsilon_{\text{RD}}/\epsilon_{\text{OE}}$	$\epsilon_{\text{ZF,avg}}$	$\epsilon_{\text{FF,max}}$
J	402	$2.6 \cdot 10^{-6}$	0.81	7.0 dB	-70.8 dB
M	451	$1.6 \cdot 10^{-6}$	0.74	6.7 dB	-72.0 dB
JM	336	$1.2 \cdot 10^{-6}$	0.70	0.0 dB	-73.1 dB
CS	336	$1.2 \cdot 10^{-6}$	0.71	-6.8 dB	-72.5 dB
CP	157	$1.2 \cdot 10^{-5}$	0.99	-27.4 dB	-66.5 dB
WF-CP	153	$1.3 \cdot 10^{-5}$	1.02	-27.2 dB	-66.1 dB
SC-MF	451	$1.7 \cdot 10^{-5}$	0.69	-30.0 dB	-73.0 dB
SC-EF	357	$3.3 \cdot 10^{-6}$	0.72	-9.4 dB	-71.7 dB

(b)

J	368	$7.4 \cdot 10^{-4}$	0.74	6.8 dB	-71.1 dB
M	330	$8.0 \cdot 10^{-4}$	0.80	6.7 dB	-69.0 dB
JM	222	$7.3 \cdot 10^{-4}$	0.73	0.0 dB	-73.3 dB
CS	228	$7.5 \cdot 10^{-4}$	0.75	-6.8 dB	-71.5 dB
CP	127	$1.0 \cdot 10^{-3}$	1.04	-28.1 dB	-66.4 dB
WF-CP	128	$1.0 \cdot 10^{-3}$	1.05	-27.8 dB	-66.6 dB

respective number of triangles is 100 238, 53 286, and 64 508. The distance of the hull and the (slightly enlarged) exact equivalent model to the simulation model is about 1 mm, which is about $\lambda/50$ at the simulation frequency. As previous investigations and Kornprobst et al. [2019c], Kornprobst et al. [2019g], Kornprobst et al. [2019b], and Kornprobst et al. [2021a] have shown, the solver residual of the NRE is rather meaningless. Hence, we evaluate the NF RD in each step of the iterative solver while the stopping is still based on the NRE residual. We consider the same surface-source types as before and a relative solver stopping criterion, for the NRE if $\Delta\|r\| > 0.995$ three times in a row, and for the NEE a somewhat relaxed version with $\Delta\|r\| > 0.999$. In order to estimate the accuracy and conditioning of the source representations, the iterative solution process is studied in Fig. 5.10. A summary of results is given in Tab. 5.4 for the convex hull model.

The number of solver iterations and the convergence rate give some insight into the conditioning. The NF RD and FF error provide insight into the achievable accuracy levels. The largest differences in the solution behavior are observed between the three choices of the reconstruction surface: The sphere leads to the fastest convergence (i.e., the best conditioning), the convex hull performs worse for any

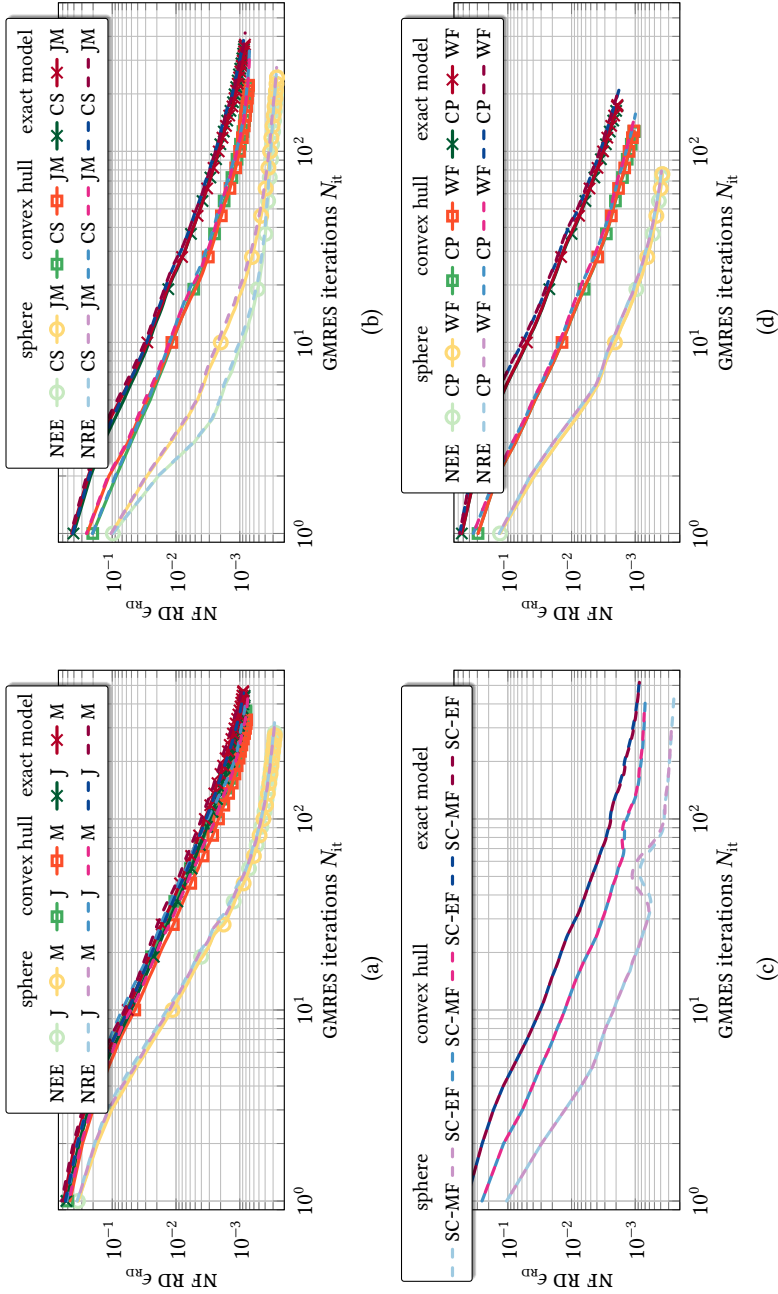


Fig. 5.10: Iterative solver convergence of the FIAFTA with equivalent surface currents. (a) J and M solutions. (b) JM and CS solutions. (c) Love SCs. (d) CP and WF-CP solutions © 2021 IEEE [Kornprobst et al. 2021a].

source type, and the exact geometrical representation is even slower. Investigations on the shape of the reconstruction surface have already been performed by Araque Quijano et al. [2010], Leone et al. [2018], Knapp and Eibert [2019], and Leone et al. [2021], in part for echo suppression applications. The shape of the equivalent source surface may introduce weakly radiating currents (evanescent modes) if the surface is non-convex. Hence, the reconstruction surface has to be chosen accordingly. In the comparison at hand including various equivalent source types, the influence of the Huygens surface shape is certainly also an interesting factor of influence. Notably, the convergence curves of Love-current representations and pure electric-current solutions are very similar if the reconstruction surface comes close to the conducting antenna model. From a physical point of view, this kind of similar behavior is expected due to the fact that both systems of equations yield the same solution of purely electric currents for the same right-hand side, hence the matrices have to be very similar.

Looking at the accuracy of the equivalent surface choices, we can state that the sphere leads to overfitting (NF RD below the noise level of 10^{-3} , see Fig. 5.10) and, hence, reduced accuracy. The FF errors of the sphere model are in the range of -44 dB to -54 dB—the worst results are obtained for J and M solutions. The convex hull offers a RD of about 10^{-3} and FF errors of mostly below -70 dB, which is a significant improvement (the so-called *processing gain*). The exact model is able to provide better diagnostic information, but requires a lot of detailed information about the AUT. The optimal reconstruction deviation of 10^{-3} is reached, see Fig. 5.10, and the FF errors are about one to two decibels worse than for the convex hull—i.e., absolutely comparable. Overall, for best accuracy and reasonable conditioning (fast iterative solver convergence), a convex hull is the reasonable choice.

A Large Reflector Antenna

To showcase the differences between the NEs, we consider an electrically large simulation model, see Fig. 5.11, of a real-world reflector antenna located in Raisting, Germany [Paulus et al. 2018]. The simulation frequency is 1.1 GHz, the reflector diameter is 92λ and the height in z -direction including the feed and the support structure in the back is almost 41λ . Subject to the electrical size of the minimum sphere, we choose a spiral sampling with $M = 700\,000$ measurement samples on a sphere of radius 55λ [J. E. Hansen 1988; Keinert et al. 2015]. The measurement vector is superimposed with white Gaussian noise ϵ_{OE} , with $\|\epsilon_{\text{OE}}\|_2 = 10^{-2}\|\mathbf{b}\|_2$.

With the NEE formulation, the number of unknowns obviously equals M , whereas for the NRE, there are 17 248 275 DSH unknowns or 7 725 366 JM unknowns. Both source types are placed according to the reconstruction surface s , i.e., the mesh shown in Fig. 5.11(b). Assuming that the (intentionally introduced) OE is unknown, we consider a relative solver stopping criterion: If the residual decreases three times

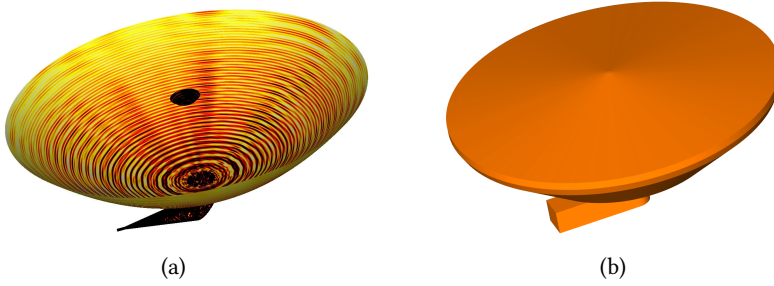


Fig. 5.11: Simulation model of a large reflector antenna located in Raisting, Germany. (a) The real part of the simulated electric surface current density. (b) Closed source reconstruction surface around the simulation model © 2019 IEEE [Kornprobst et al. 2019c].

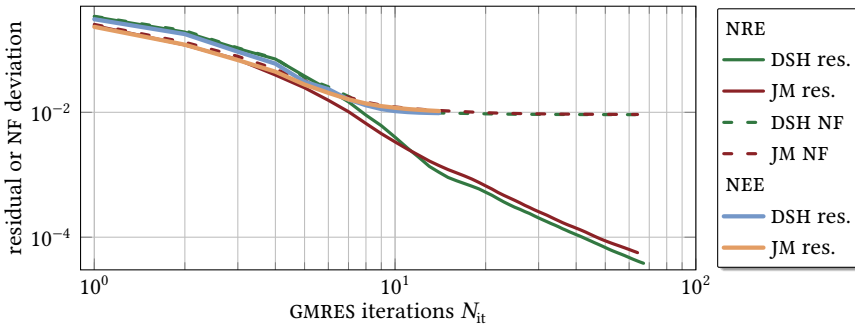


Fig. 5.12: Iterative solver convergence of the reflector antenna source reconstruction © 2019 IEEE [Kornprobst et al. 2019c].

in a row by less than 3%, the solver halts. The convergence curves of the residuals and NF reconstruction deviations for all cases are given in Fig. 5.12. Both NEE versions converge to an NF RD of 10^{-2} after 15 iterations, while the NRE ones take nearly 70 iterations and go slightly below the error-induced 10^{-2} NF RD—meaning a part of the error is mistakenly fitted to a contribution in the retrieved currents.

It has to be highlighted that the NRE version was modified to output the NF deviation in each solver step, i.e., a 50% extra effort of one MVP per iteration (about 15 s on a Intel Xeon E5-1650 v4 running at 3.60 GHz). This information is in general not available since only incremental changes in the residual are evaluated, and cannot be used without additional effort to control the solver termination criterion. What is surprising in this example (and not a general rule) is that, in the beginning of the solution process, the NRE residual resembles the NEE NF deviation. Later in

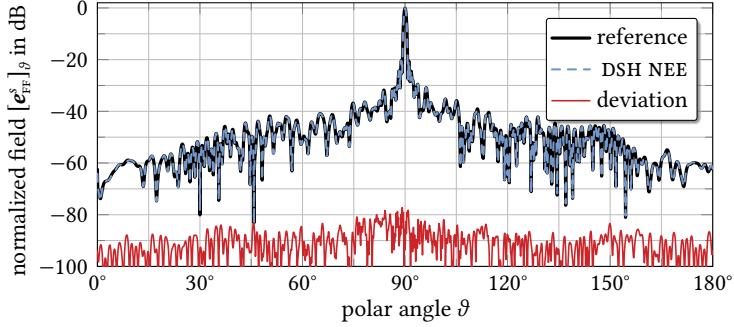


Fig. 5.13: Comparison of reference and reconstructed FF of the Raisting reflector antenna model, for the DSH NEE, $\varphi = 270^\circ$ cut © 2019 IEEE [Kornprobst et al. 2019c].

the solution process, the residual becomes arbitrary and also differs between the source representations even when the NF RDs are on a comparable level.

Finally, the reconstructed FF is compared to the simulated reference in Fig. 5.13 exemplarily for the DSH NEE solution. The complex deviation between the fields normalized to their respective maxima is below -77 dB in all cuts and for both polarizations. The source localization helps to suppress the additive noise in the reconstructed sources to a great extent. In this specific scenario, the additional iterations carried out for the NRE solution have no detrimental effect on the accuracy but also lack any other positive impact on the solution process.

5.3.2 Results for Measurement Data

Source Reconstruction for a Reflector Antenna

Spherical NF measurements of a parabolic reflector antenna have been conducted at 18 GHz with a DRH18 probe in the measurement facilities of Rohde & Schwarz [Neitz et al. 2017; Steatite Ltd. 2021; RFspin 2021a]. The AUT exhibits a diameter of 1.23 m and the measurement distance was 5 m. Based on our previous insights, only a convex hull is considered as reconstruction surface. The AUT inside the anechoic chamber and the reconstruction surface are shown in Fig. 5.14.

The number of NF measurement samples is 812 702 (for two orthogonal polarizations), which also equals the number of unknowns for all NEE variants. For the NRE, the DSH formulation has 14 143 275 unknowns. The employed mesh comprises 4 289 139 RWG unknowns, with double the number for the JM approach.

An iterative solver convergence study is shown in Fig. 5.15. The stopping criterion was chosen relative with a residual decrease slower than 0.997 three times in a row. Additionally, the NRE solver was stopped once a residual threshold of

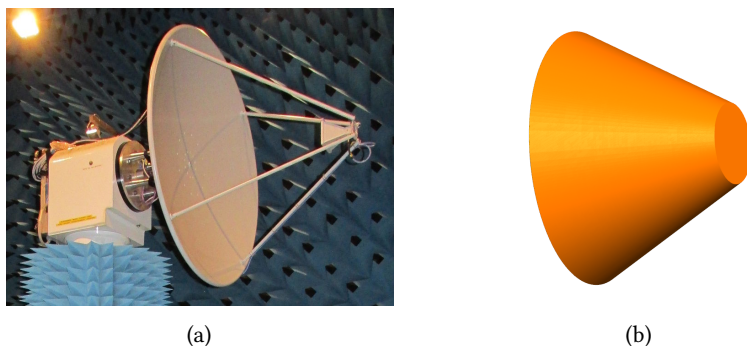


Fig. 5.14: Measured reflector antenna (a) inside the anechoic chamber and (b) as a reconstruction model © 2021 IEEE [Kornprobst et al. 2021a].

10^{-5} was reached. The RD estimates the OE to about 2% consistently among all solvers. All formulations show a comparable convergence behavior with a slight advantage for the NEE. The control of the solver termination, once a stagnating NF RD is reached, works much better for the NEE. For instance, the JM NEE version stops at an NF RD of 1.96% after 36 iterations, while the JM NRE version stops after 141 iterations at a residual of $9.9 \cdot 10^{-6}$ and an NF RD of 1.89%. The NRE reaches the same NF RD as the NEE with convergence at 39 iterations. The JM, CS, and DSH variants perform very similarly. The J and M versions show a worse convergence.

The Love-current SC formulations show a worse convergence than the JM, CS, and DSH formulations. The CP and WF-CP variants show a comparable convergence. However, keep in mind that each iteration is computationally more costly.

For comparison, a fully probe-corrected spherical transformation according to Mauermayer and Eibert [2018] with the NRE takes 35 iterations for a residual of 10^{-4} and stops at an NF RD of 1.67%, i.e., it suffers from a bit of overfitting due to the inherently limited source localization.

Transformed FFs of the spherical transformation and the CS NEE source reconstruction are shown in Fig. 5.16, with the relative magnitude deviation reaching up to -48.5 dB. The deviation between the various surface-source formulations is below this level. Hence, an accuracy analysis for measurement data is not feasible. We can, however, compare some of the deviations. The maximum deviation between the CS solutions with the NEE and the NRE is at -59.0 dB, between the JM and the CS solutions with the NEE at -72.1 dB, between the J NRE and the CS NEE solutions is at -53.8 dB, between the CP NRE and the CP NEE solutions at -59.0 dB, and between the SC-MF NRE and the CS NEE solutions at -59.9 dB. All these values are below the measurement accuracy.

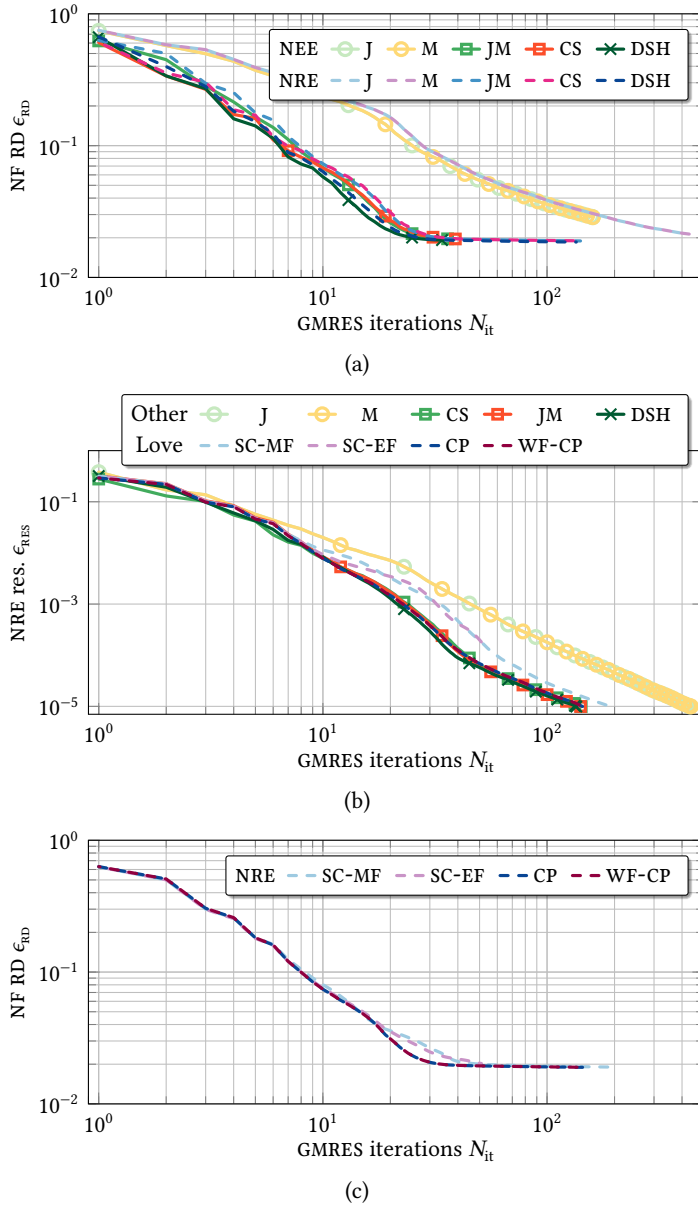


Fig. 5.15: Iterative solver convergence for the source reconstruction of reflector antenna NF measurements. (a) NF RD of non-physical surface source representations, for both the NRE and the NEE. (b) NF RD of Love-current formulations, for the NRE. (c) Solver residual of the NRE solvers © 2021 IEEE [Kornprobst et al. 2021a].

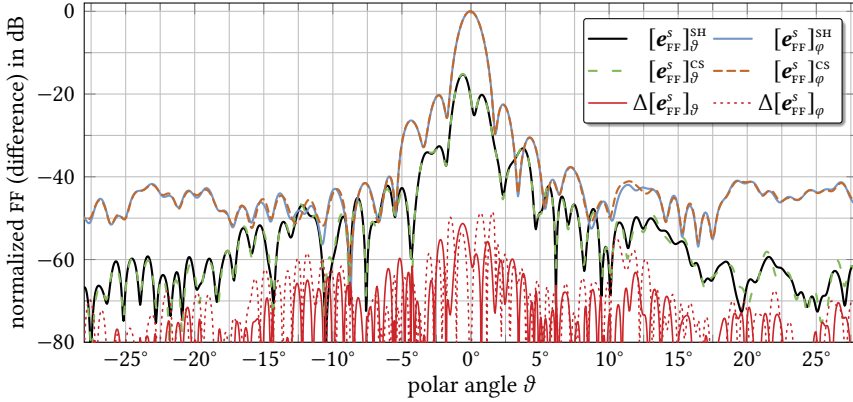


Fig. 5.16: Transformed FFs of a SH expansion solved with the NRE and a CS surface-source solution of the NEE © 2021 IEEE [Kornprobst et al. 2021a].

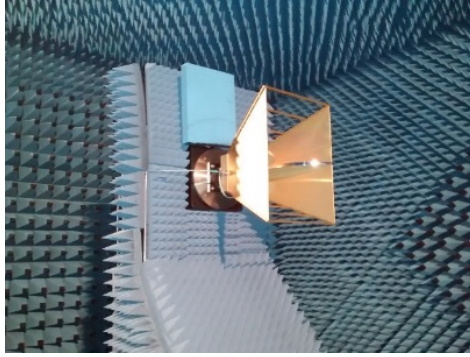


Fig. 5.17: DRH400 AUT mounted for a spherical NF scan inside an anechoic chamber.

NF Measurements of a DRH400 AUT

The dual-ridged DRH400 horn antenna, which has been employed as a simulation model in Subsection 5.3.1, has been measured in the anechoic chamber of the Chair of High-Frequency Engineering, Technical University of Munich [RFspin 2021b]. This AUT as mounted during the NF measurement is shown in Fig. 5.17. Spherical near-field measurements are performed at a frequency of 6 GHz with a roll-over-azimuth positioner and a DRH18 probe antenna [RFspin 2021a]. $M = 58\,322$ measurements have been collected.

First, we investigate the benefits of the NEE over the NRE. We only consider DSH

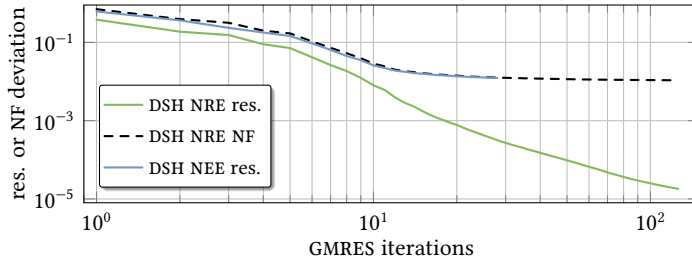


Fig. 5.18: Comparison of the NRE and NEE convergences for DRH400 NF measurements [Kornprobst et al. 2019c].

equivalent sources, which are located on a closed surface tightly fitted around the AUT. This leads to a DSH expansion with 160 272 coefficients. We consider a relative GMRES convergence criterion of the residual decrease, i.e., a relative decrease by less than 1% three times in row. The convergence results for NF RD and GMRES solver residual are given in Fig. 5.18. The NEE converges in 29 iterations to an NF RD of 1.24%, whereas the NRE takes 127 iterations to converge to a residual of $1.8 \cdot 10^{-5}$. In this scenario, a slight benefit for the NEE in terms of iterative solver convergence is observed. The 1.24% NF RD is reached at iteration 32 with the NRE (instead of 29). Furthermore, the NRE residual is—as expected—totally unrelated to the NF RD. We can state that the NRE exhibits one of two disadvantages. One either needs to put extra effort into the evaluation of the NF RD or one needs to trust a residual stopping criterion which can only be based on experience and is checked ex-post. The latter is highly unreliable: In the two considered scenarios, the NEE stopping threshold of about 1% NF RD was reached at residuals of 0.0109 and $2.5 \cdot 10^{-4}$, respectively—orders of magnitude apart.

In order to evaluate the reconstruction quality of both the NRE and the NEE solutions, we compare the reconstructed FF patterns in Fig. 5.19. The deviation is mostly below -50 dB, which is better than the estimated measurement error of about -40 dB in this measurement setup. We conclude that both algorithms exhibit a comparable accuracy.

Second, we analyze the diagnostic capabilities of a Love current reconstruction, in particular with a CP. In the iterative solution of the NRE, a solver residual of 10^{-4} is used as termination criterion. We consider three different source types: generic JM unknowns, the CP Love current solution, and the SC-EF Love condition. Without the Love current mapping, but with the non-unique electric and magnetic equivalent currents, 61 GMRES iterations are necessary to reach this residual. The solution achieves a relative NF RD of 1.40%. With Love current mapping, only 53 iterations are performed, while the relative NF RD is comparable with 1.44%. The

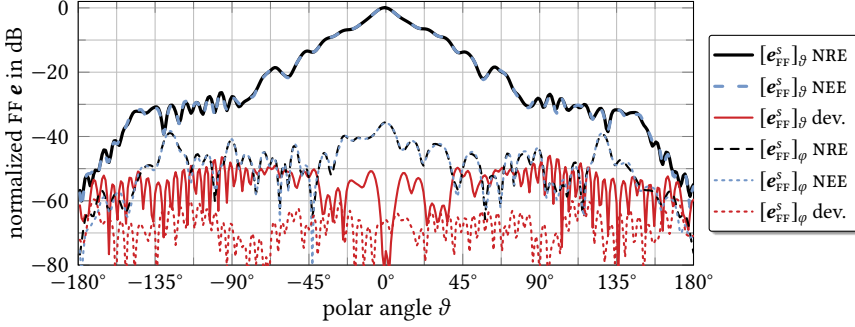


Fig. 5.19: Comparison of the FF patterns for the DRH400 measurements, DSH sources for the NRE and NEE, $\varphi = 0^\circ$ cut [Kornprobst et al. 2019c].

Love current SC, however, takes 86 iterations to convergence (and shows then about the same NF RD). As we can see here, the residuals in the NRE solution process are meaningless. The system matrices are different in every case. Hence, the residuals

$$r_{JM,i} = \mathbf{A}^H(\mathbf{A}x_i - \mathbf{b}), \quad (5.38)$$

$$r_{CP,i} = \mathbf{G}^{-1}\mathbf{L}_m\mathbf{A}^H(\mathbf{A}x_i - \mathbf{b}), \quad (5.39)$$

$$r_{SC,i} = [\mathbf{A}^H\mathbf{A} + \xi\mathbf{L}_{SC}^H\mathbf{L}_{SC}]x_i - \mathbf{A}^H\mathbf{b} \quad (5.40)$$

cannot be meaningfully compared and choosing the same iterative solver threshold based upon $\|r\|$ is not really sensible.

The difference in the field solutions is analyzed in Fig. 5.20, where the zero field inside the source region is clearly visible up to a level of -60 dB in the case of the Love current solution. The radiated NFs around the AUT look, by visual inspection, identical. This is also confirmed in the field difference plot in Fig. 5.20(c).

Furthermore, we show the magnitude distributions of the equivalent currents in Fig. 5.21. For the solution without the Love condition, the currents are concentrated on the rear side of the antenna and radiate through the antenna volume, as already observed in the corresponding near-field plot in Fig. 5.20(a). If the Love current solution is retrieved, the radiating currents concentrate on the front side—in the aperture of the horn antenna—, where the electromagnetic waves are expected to detach from the AUT.

Finally, we look at the radiated fields in Fig. 5.22 to check whether the retrieved equivalent currents behave similar. This is done by determining the FF patterns of both current distributions. An excellent agreement of below -60 dB is observed in Fig. 5.22, which is lower than typical measurement accuracies.

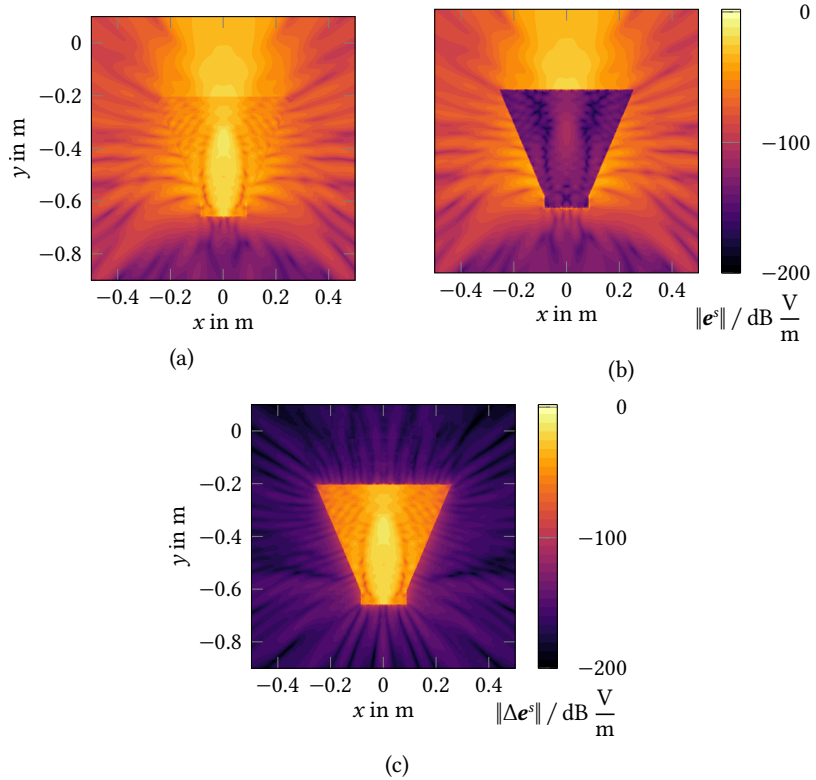


Fig. 5.20: Electric field of the equivalent currents obtained for DRH400 NF measurements at $y = 0$. The black line marks the outline of the Huygens surface s . (a) Field of the generic JM solution. (b) Field of the Love current CP solution. (c) Difference between the two reconstructed fields [Kornprobst et al. 2019e].

UAV-Based Diagnostics

The diagnostic features of Love current reconstructions are an excellent extension for specialized measurement applications. For instance, García-Fernández et al. [2018a] have performed outdoor measurements of a base station AUT with an unmanned aerial system. Such kind of in-situ measurements, possibly with highly specialized measurement hardware such as unmanned aerial vehicles (UAVs) and radio-frequency over fiber (RFOF) connections, can benefit greatly from the flexibility of FIAFTA (since the observation samples are typically taken on an irregular grid), from phaseless field transformation algorithms as discussed in Section 5.5,

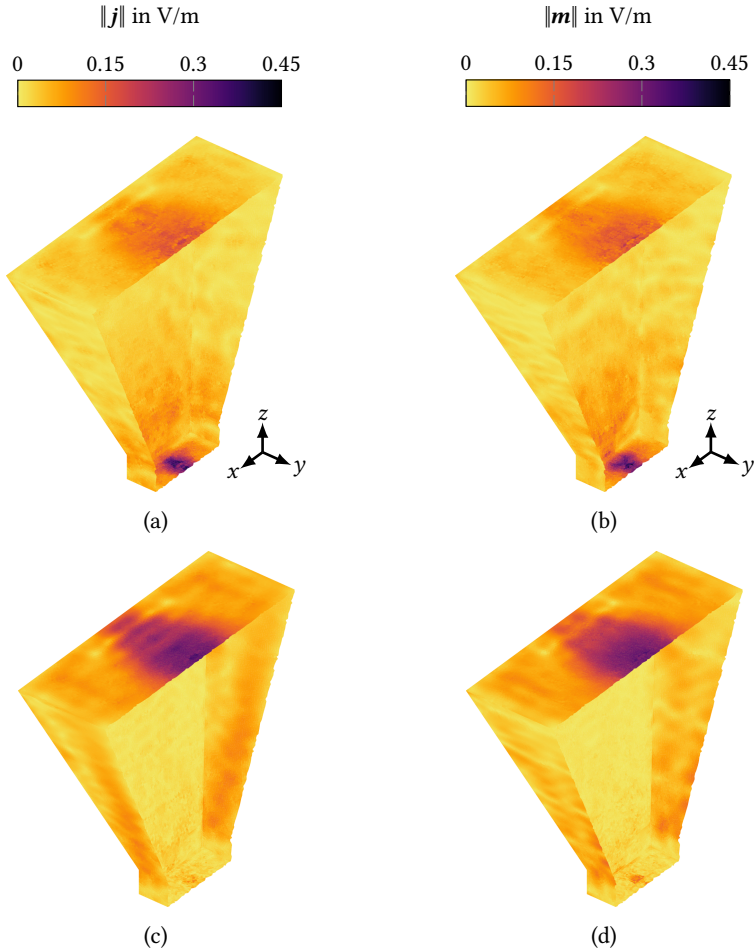


Fig. 5.21: Magnitudes of the generic JM equivalent (a) electric and (b) magnetic surface current densities, and of the (c) electric and (d) magnetic Love currents obtained with the CP, both on s for $y < 0$ [Kornprobst et al. 2019e].

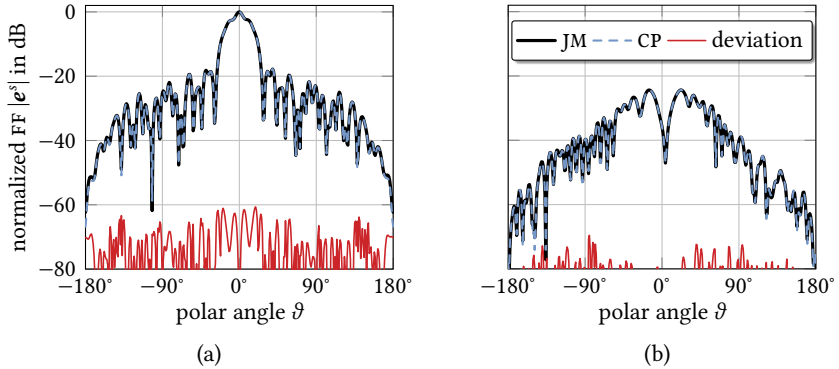


Fig. 5.22: $\varphi = 90^\circ$ cut of the retrieved FFs. (a) Co-polar $[e^s_{FF}]_\varphi$ component. (b) Cross-polar $[e^s_{FF}]_\theta$ component [Kornprobst et al. 2019e].

and from the diagnostic source-localization capabilities of a Love current reconstruction. In this work, we consider an NF measurement conducted by Mauermayer and Kornprobst [2022] (preliminary measurement results have been presented in [Mauermayer et al. 2019]) in the controlled environment of the anechoic chamber of the Chair of High-Frequency Engineering, Technical University of Munich.

Figure 5.23 shows the measurement hardware in action. The UAV position and orientation is tracked with the help of four base station of a HTC Vive tracking system. The visible cable connects the UAV to a ground station, which supplies the necessary power, is able to configure the flight trajectory and measurement settings, and collects the measurement data. The HF measurement itself is performed with a low-cost software-defined radio (SDR) board LimeSDR mounted on the UAV and features two synchronous measurement channels (utilized for two polarizations of a dual-polarized patch antenna probe). The AUT is fed synchronously by the same SDR via a custom RFOF connection to the ground station and then via a coaxial cable to the AUT. The trajectory of a cylindrical scan including the magnitude of the collected NF of the co-polarized patch probe antenna port is depicted in Fig. 5.24, where maneuver paths are omitted. Figure 5.25 shows the Love currents, which have been reconstructed with the CP approach for NF measurement data taken at a frequency of 1.8 GHz. Clearly, the reconstructed currents look like the currents of a horn antenna should like: We can identify the radiation coming from the aperture. Hence, UAV-based measurements concepts combined with Love-current reconstruction algorithms offer valuable diagnostics for on-site measurement and troubleshooting scenarios.

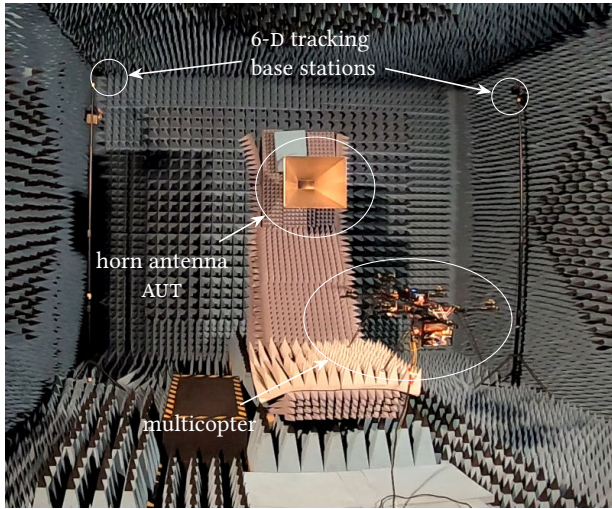


Fig. 5.23: Photograph of the measurement setup in the anechoic chamber, showing two of the four tracking base stations in the background, as well as the horn AUT in the center and the hovering drone in the front.

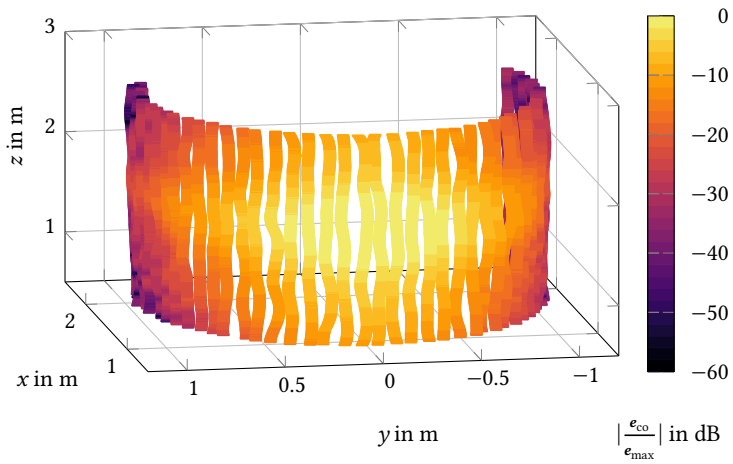


Fig. 5.24: Magnitude of the measured NF for the first (co-polarized) probe antenna port along the cylindrical flight trajectory.

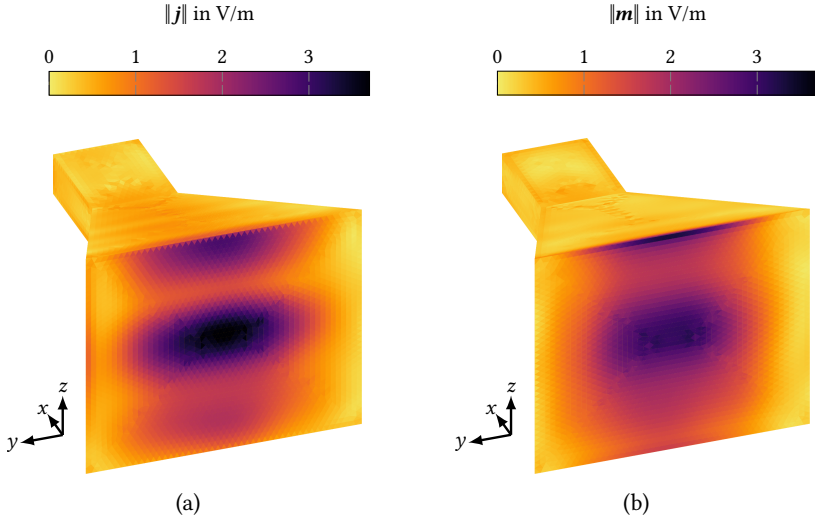


Fig. 5.25: Equivalent (a) electric and (b) magnetic Love surface current densities on s reconstructed from the UAV-based NF measurement.

Post-Processing Based Love-Current Calculation

As a final step, we investigate how enforcing the Love condition during the solution process compares to calculating Love currents in a post-processing step—where the latter choice implies significantly reduced computational effort. To this end, we consider an HF907 double-ridged waveguide horn antenna [Rohde & Schwarz 2021]. $M = 90902$ spherical NF measurements have been collected in the anechoic chamber at the Chair of High-Frequency Engineering, Technical University of Munich, at a frequency of 18 GHz with an OEWG probe. For the surface-source reconstruction, we employ a tightly fitted mesh with 282 135 RWG unknowns for electric and magnetic currents each. We calculate one solution with a Love current SC (with the EFIE-alike testing), one solution with a Love CP, and one with unconstrained JM currents, both for the NEE and with a stopping threshold of a relative NF RD improvement of worse than 0.999 three times. The convergence of the solution with the Love SC is slower than the other two approaches but reaches the same residual eventually; in addition, each MVP of the Love solutions is of course more costly to compute [Kornprobst et al. 2019b].

As compared to a spherical NFFFT, all three solutions show about the same relative deviations (up to -47 dB), which is below the measurement accuracy of the setup. Figure 5.26(a) visualizes the retrieved Love currents of the CP approach. In addition, Fig. 5.26(b) shows the Love currents which are obtained with the CP, after

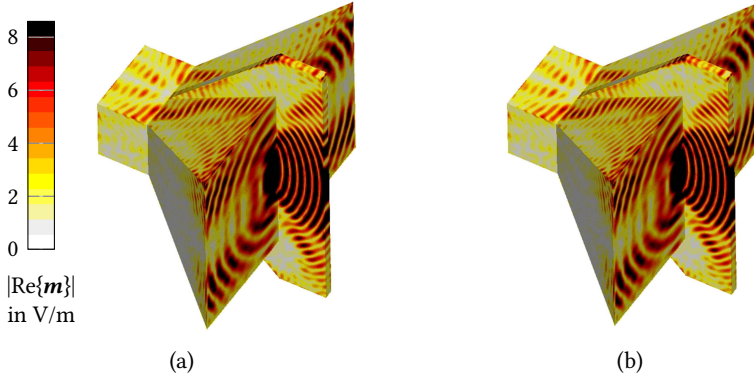


Fig. 5.26: $|\text{Re}\{\mathbf{m}\}|$ of the reconstructed Love current on the Huygens surface of a HF907 AUT, colormapping clipped with $\max |\text{Re}\{\mathbf{m}\}| \approx 21 \text{ V/m}$. (a) Retrieved with the NEE and CP. (b) Love currents attained by post-processing a JM NEE solution. Reproduced courtesy of The Electromagnetics Academy [Kornprobst et al. 2019b].

unconstrained JM currents have been retrieved in the iterative solution process. The differences of both Love current representations are insignificant, both show the same behavior and suffice for antenna diagnostics. Certainly, the post-processing method is preferred due to the lower computational effort.

5.3.3 Summary

Based on the theoretical analyses in Sections 5.1 and 5.2, we have analyzed the the inverse surface-source problem related to NF antenna measurements in detail. The first aspect is the *regularization* of the ill-posed inverse problem. The use of fast methods such as the MLFMM or the adaptive cross-approximation (ACA) already requires to employ an inherently regularized iterative solver (such as GMRES) and an NE with regularizing properties. In addition to that, the various source representations have almost no measurable influence. The only noticeable effect is that enforcing a Love current solution prevents overfitting to some extent, which can be achieved computationally cheaper with the appropriate choice of the NEE over the NRE.

In combination with the superior NEE, which makes the choice of the iterative solver stopping criterion much simpler, the ambiguous unconstrained JM solution or the unique CS solution are the sensible choices for equivalent surface currents. This is due to the importance of making use of both radiation operators \mathcal{T} and \mathcal{K} , e.g., employing electric and magnetic currents simultaneously, in order to arrive at the best possible *conditioning* of the inverse source problem with the most reasonable

computational effort. Additionally, we found that a close to convex hull around the AUT without too much geometrical details offers the best conditioning at the best possible accuracy.

The third side of the investigation is that for the best reconstruction *accuracy*, it is crucial to choose a source representation working with a close to convex hull around the AUT in order to avoid the excitation of spurious radiating modes. This basically excludes a plain SH expansion for most (non-spherical) AUTs if the best accuracy is desired. The choice of a specific (surface) source representation is, however, not critical, since all of them are identical from both a practical and theoretical point of view—they all offer (in practice only approximately) the same number of DOFs for the reconstruction of radiated fields. This brings us back to the first issue of solver regularization: Despite the theoretical equivalence, preventing overfitting remains important no matter which source representation is employed.

A further aspect are the *diagnostic capabilities* of surface source methods. In this respect, the various surface-source representations indeed differ. However, the largest distinction is found in the computational effort associated with the calculation of the Love currents. Since there are no observable benefits over a computationally cheaper post-processing step, the Love current solutions via a SC or CP seem to be generally not worth the effort. In most cases, the reconstruction of a unique CS solution should suffice. Post-processing techniques for the field visualization on the AUT surface also seem to be a viable method if desired.

5.4 Echo Suppression

Typically, NF antenna measurements are performed in a controlled environment, for instance in anechoic chambers, to avoid spurious signals which do not propagate along the line-of-sight between the AUT and the measurement probe. There are circumstances in which the environment is not completely under control, such as outdoor/on-site measurements [Faul and Eibert 2021], or in which an echoic environment is not avoidable for other sound reasons, such as the use of metallic thermal vacuum chambers investigated by Knapp and Eibert [2019] and Knapp et al. [2019a]. The processing methods and specific measurement hardware to cope with negative influences of echoic measurement environments work either with time-domain or time-harmonic data. Inverse surface-source algorithms are typically concerned with the latter case. These algorithms, similar to ones based on spectral properties, already provide spatial filtering capabilities by source localization [Hess 2010; Araque Quijano et al. 2011; Gregson et al. 2012; Jørgensen et al. 2012b; Mauermayer et al. 2013; Foged et al. 2013a; Kozan et al. 2014; Cappellin and Pivnenko 2014]. However, source localization for the AUT might not suffice to separate the radiation of reconstructed equivalent surface current densities for the

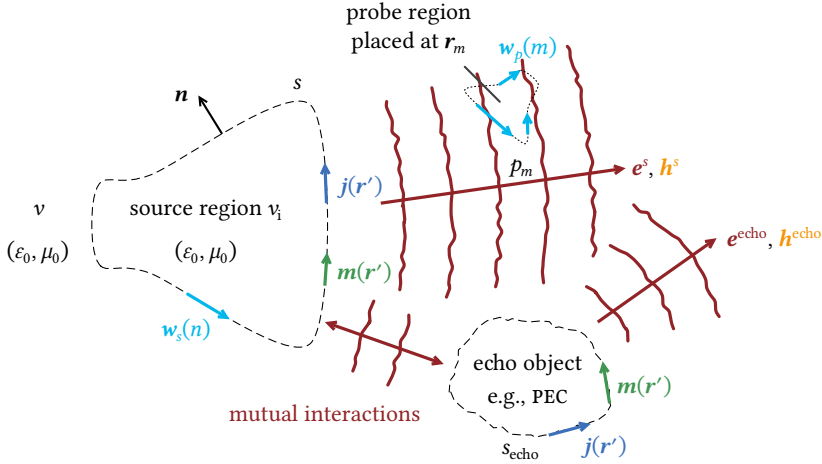


Fig. 5.27: A variation of the general equivalent inverse surface-source scenario depicted in Fig. 5.1, which involves echo source localization on the surface s_{echo} .

AUT from echo contributions. Source reconstruction algorithms based on equivalent surface current densities can be enhanced by modeling echo contributions with separate equivalent sources and by software time-gating for multi-frequency measurement data [Araque Quijano et al. 2010; Yinusa and Eibert 2013; Mauermayer and Eibert 2015, 2017; Knapp and Eibert 2018; Paulus et al. 2019; Knapp et al. 2019b; Knapp et al. 2019a; Kornprobst et al. 2019d; Knapp et al. 2020]. Contributions to both of these approaches are discussed in the following.

5.4.1 Echo Source Localization with a MOM Side Constraint

We are not restricted to modeling the AUT sources but can also include echo objects in the equivalent source representation, as depicted in Fig. 5.27. In principle, it is sufficient to place sources at all locations where radiation or scattering occurs as long as the relative positions of radiating and scattering sources do not change, i.e., measuring a stationary AUT. However, to restrict the number of DOFs in the reconstruction (and reduce the number of required NF measurement samples), it can be beneficial to incorporate knowledge about the material properties and exact shapes of scattering objects. One way to do this is to link the solver of the NFFFT inverse problem to a forward problem for scattering objects, which has been reported both for dielectric objects by Mitharwal and Andriulli [2015] and Omi et al. [2019] and for PEC objects by Giordanengo et al. [2013], Giordanengo et al. [2016], Ciorba et al. [2019], Paulus et al. [2019], and Kornprobst et al. [2019d].

The topic of echo suppression is related to an important challenge of NF antenna measurements: Measurements shall be sped-up significantly, which is a particularly severe topic for electrically large antennas and for measurements with scatterers, since the mode spectrum increases significantly due to a larger minimum sphere. Hence, efforts have been made to directly integrate electromagnetic models of objects close to the AUT into the transformation problem in two different ways. Giordanengo et al. [2013], Giordanengo et al. [2016], and Ciorba et al. [2019] have pre-computed basis functions before the measurement which include the influence of the scatterer, i.e., they have solved the scattering problem for any possible or expected variation of the AUT. This poses a tremendous computational overhead. Paulus et al. [2019] and Kornprobst et al. [2019d] have proposed a more efficient approach which is discussed in the following.

From electromagnetic theory, the most efficient sampling methods and traditional sampling limits due to the spatial bandwidth of the radiated fields are well-known, with the most practical method being spiral sampling in various fashions [J. E. Hansen 1988; Bucci et al. 2003; Keinert et al. 2015]. More aggressive approaches to reduce the number of samples and, thus, the measurement time, seem to be rather unstable and unreliable if the made assumptions are not met; for instance in the case of compressed sampling, no speed-up is gained with random measurement locations [Hofmann et al. 2019]. To be more reliable, the approaches to reduce measurement samples and time need to incorporate additional information such as geometrical data of the AUT.

Theoretical Description

We pursue an approach to incorporate knowledge about the exact geometry and material parameters of certain objects close to the AUT into the NFFFT and, subsequently, reduce the required field samples due to a significantly shrunk minimum sphere of the AUT. However, some measurement efforts are transferred into the spatial domain: To save NF measurement time, the geometrical shape of some objects, which are part of or surrounding the AUT, can be captured using a high-accuracy 3-D laser scanner. This geometry information, combined with the knowledge of the material parameters, is utilized to treat the objects not as unknown radiation sources within the NFFFT inverse problem but as a standard scattering problem. This is implemented as a MOM SC within the standard inverse problem of the NFFFT—just as it has been done for the Love SC in Subsection 5.2.4 and 5.2.5. By doing so, we are able to model any known scattering object or any part of the AUT as PEC or whatever boundary condition is enforced by the SIE SC.

The basis is the typical RWG modeling of electric and magnetic surface current densities according to (5.1). The according unknowns are represented by the vector \mathbf{x} , the field observations are collected in the vector \mathbf{b} , and the forward operator

from the sources to the unknowns is written in discretized form as the matrix \mathbf{A} . This allows us to write the source reconstruction problem as the standard linear system of equations $\mathbf{A}\mathbf{x} = \mathbf{b}$. For the treatment of additional echo sources with a known boundary condition, whose unknowns are also contained in \mathbf{x} , we split the unknowns vector and the forward operator

$$\mathbf{A}\mathbf{x} = [\mathbf{A}_{\text{AUT}} \quad \mathbf{A}_{\text{echo}}] \begin{bmatrix} \mathbf{x}_{\text{AUT}} \\ \mathbf{i}_{\text{echo}} \end{bmatrix} = \mathbf{b} \quad (5.41)$$

into separate parts for sources placed on the AUT hull and on the PEC echo object, which only exhibits electric surface current unknowns. Furthermore, we need to evaluate the radiation of the AUT sources on the echo object's surface, which is done by the MVP $\mathbf{A}_{\text{A} \rightarrow \text{e}} \mathbf{x}_{\text{AUT}}$, which contains the submatrices

$$\mathbf{A}_{\text{A} \rightarrow \text{e}} \mathbf{x}_{\text{AUT}} = \begin{bmatrix} \mathbf{T}_{\alpha, \beta}^{\text{A} \rightarrow \text{e}} & \mathbf{K}_{\alpha, \beta}^{\text{A} \rightarrow \text{e}} \\ -\mathbf{K}_{\beta, \beta}^{\text{A} \rightarrow \text{e}} & \mathbf{T}_{\beta, \beta}^{\text{A} \rightarrow \text{e}} \end{bmatrix} \begin{bmatrix} \mathbf{i}_{\text{AUT}} \\ \mathbf{v}_{\text{AUT}} \end{bmatrix} = \begin{bmatrix} -\mathbf{e}_{\alpha}^{\text{echo}} \\ -\mathbf{h}_{\beta}^{\text{echo}} \end{bmatrix} \quad (5.42)$$

with the matrix entries

$$[\mathbf{T}_{\mathbf{w}, \beta}^{\text{A} \rightarrow \text{e}}]_{mn} = \langle \mathbf{w}_m, \mathcal{T} \beta_n \rangle \quad \text{for } m \in \{1, 2, \dots, N_{\text{echo}}\}, n \in \{1, 2, \dots, N_{\text{AUT}}\} \quad (5.43)$$

for electric currents and, similarly, for magnetic currents

$$[\mathbf{K}_{\mathbf{w}, \beta}^{\text{A} \rightarrow \text{e}}]_{mn} = \langle \mathbf{w}_m, \mathcal{K} \beta_n \rangle \quad \text{for } m \in \{1, 2, \dots, N_{\text{echo}}\}, n \in \{1, 2, \dots, N_{\text{AUT}}\}, \quad (5.44)$$

where $\mathbf{w}_m \in \{\alpha_m, \beta_m\}$ are located on s_{echo} , and β_n on s . Knowing the electric and magnetic fields $\mathbf{e}_{\alpha}^{\text{echo}}$ and $\mathbf{h}_{\beta}^{\text{echo}}$ on the surface of the echo object, we can employ a suitable scattering IE, for instance the CFIE (3.34) written compactly as

$$\mathbf{C}_{0.5} \mathbf{i}_{\text{echo}} = \frac{1}{2} (\mathbf{e}_{\alpha}^{\text{echo}} + \mathbf{h}_{\beta}^{\text{echo}}). \quad (5.45)$$

In terms of the complete RWG unknowns vector \mathbf{x} , the SC matrix reads

$$\mathbf{S}\mathbf{x} = \begin{bmatrix} -\frac{1}{2} [\mathbf{I} \quad \mathbf{I}] \mathbf{A}_{\text{A} \rightarrow \text{e}} & \mathbf{C}_{0.5} \end{bmatrix} \begin{bmatrix} \mathbf{x}_{\text{AUT}} \\ \mathbf{i}_{\text{echo}} \end{bmatrix} = \mathbf{0} \quad (5.46)$$

Employing this system of equations as a SC in (5.28) and (5.29) yields the Tikhonov-regularized source reconstruction equation

$$[\mathbf{A}^{\text{H}} \mathbf{A} + \xi \mathbf{S}^{\text{H}} \mathbf{S}] \mathbf{x} = \mathbf{A}^{\text{H}} \mathbf{b} \quad (5.47)$$

The weighting factor ξ is set according to the procedure described in Subsection 5.2.5.

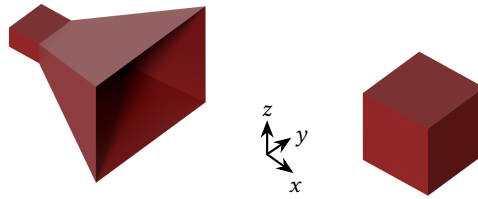


Fig. 5.28: Feko simulation model of a horn antenna with a PEC cube echo object in front [Kornprobst et al. 2019d].

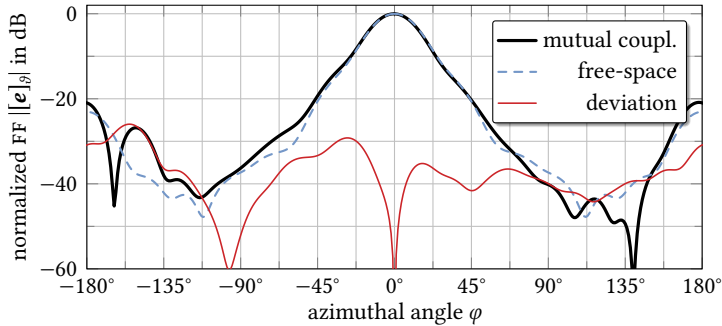


Fig. 5.29: Co-polar $[\mathbf{e}]_\theta$ component of the horn antenna FF in the comparison of free-space solution and the antenna currents influenced by mutual coupling with the cube in the $\vartheta = 90^\circ$ cut [Kornprobst et al. 2019d].

This regularized NRE can of course be further augmented by a Love SC.

Transformation Results

We consider the simulation setup in Fig. 5.28 including a horn antenna and a scatterer in front, a square PEC cube as a known echo object. In the simulation with Altair Feko [Altair 2021], we extract the FF of the horn antenna part and compare it to the horn simulated in free space. The mutual coupling with the cube distorts the FF up to a level of -26 dB, see Fig. 5.29, if the complex deviation between the maximum-normalized FFs is considered. For the case of “mutual coupling,” only the currents on the AUT are taken to calculate the FF. In the following, the task is to retrieve these AUT currents influenced by mutual coupling and filter out the currents on the echo object.¹² We consider three different source-reconstruction

¹² Reconstructing the free-space solution poses a more challenging task and requires, for instance, knowledge about the material composition and shape of the horn antenna itself. An approach for this

techniques for the scenario in Fig. 5.28. For all of them, we extract the same $M = 14\,640$ electric NF samples around the AUT including the cube with a spiral sampling proposed by Bucci et al. [2003] at a frequency of 3 GHz. This is about a ten-fold oversampling according to the minimum sphere of the horn antenna only and about a four-fold oversampling with respect to the sphere with minimum diameter enclosing the AUT plus echo object. Hence, the sampling suffices to capture more than the DOFs of the AUT alone, which is reasonable in the presence of an echo object which increases the DOFs in the radiated fields.

The first approach is just a simple source localization for the AUT, i.e., exploiting the spatial filtering capabilities of a surface-source method. Only the unknowns \mathbf{x}_{AUT} are retrieved and employed for the calculation of NFs and FFs. This simplistic spatial filtering is equivalent to the work done by Hess [2010], Gregson et al. [2012], Mauermayer et al. [2013], and Kozan et al. [2014] from a theoretical point of view, as Knapp [2021] has pointed out. The second approach considers additional electric and magnetic Love currents \mathbf{x}_{echo} on the scatterer *without* enforcing a boundary condition on the scatterer. We refer to this method as a reconstruction of unconstrained (Love) currents, which resembles the methodology proposed by Araque Quijano et al. [2010], Araque Quijano et al. [2011], and Yinusa et al. [2012a, 2012b]. The third approach incorporates the PEC boundary condition on the echo object and introduces the additional electric current unknowns i_{echo} for the solution of the Tikhonov-regularized NRE (5.47). In all three solutions, a Love current SC with MFIE-alike testing is considered.

The simple source localization approach converges to a residual of 10^{-4} within 221 iterations and a large NF RD of 24.2% remains after the solution is found. The reconstruction of unconstrained currents on both AUT and scatterer converges within 84 iterations and exhibits an NF RD of 0.25%, much lower than in the first case. The approach including the CFIE SC for the PEC echo object converges within 67 GMRES iterations to the same threshold. Here, the equivalent currents placed additionally on the scatterer are able to reproduce the observed fields even better, leading to an NF RD of only 0.18%.

Next, we look at the reconstructed electric NFs. Figure 5.30(a) shows the NF of the reconstructed currents on the AUT and the echo object including the MOM SC and the Love SC for the AUT. These fields are visually almost indistinguishable from the simulated reference fields. In Fig. 5.30(b), the radiation contributions of the echo object are effectively removed and we evaluate the radiation of the currents on the AUT only. However, we still observe the effect of mutual coupling: While the (symmetric) horn antenna in free space shows a symmetric radiation with respect to the x -axis, we can identify unsymmetrical contributions in particular for the backradiation. This effect is inherent in the considered model and cannot be “cured”

is discussed in the following Subsection 5.4.2.

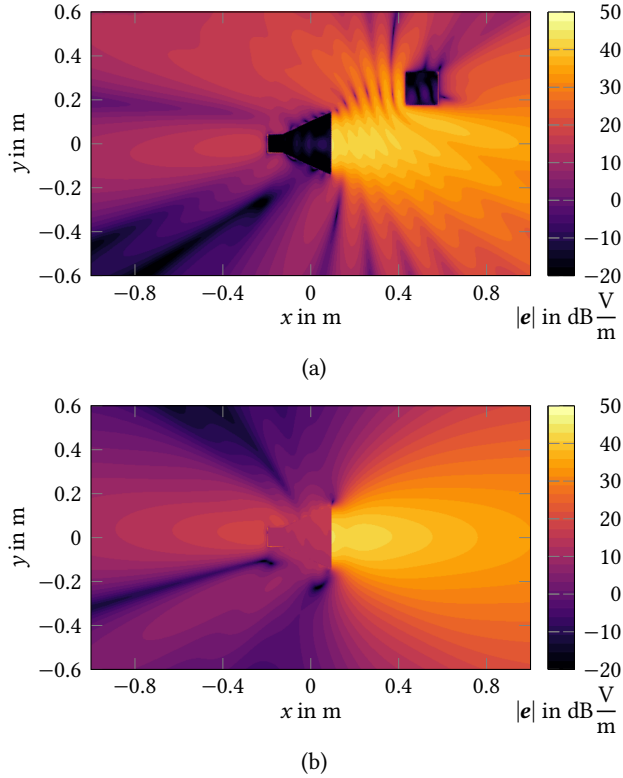


Fig. 5.30: Electric NF magnitude in the $z = 0$ cut plane for the reconstruction with a MOM SC. (a) Fields of all reconstructed currents. (b) Fields of AUT currents only.

with mono-frequent measurements. Furthermore, the Love current property of a zero field inside the AUT is lost since this condition was enforced together with the equivalent sources placed on the echo object. Without the radiation from the scatterer, the radiated fields do not cancel any more.

The reconstructed NF of the unconstrained Love currents are shown in Fig. 5.31, for the whole set of reconstructed currents in Fig. 5.31(a) and evaluating only the currents on the AUT in Fig. 5.31(b). The differences to the fields shown in Fig. 5.30 for the PEC boundary SC are few and far between. However, when looking at the difference of the fields between the reconstruction with unconstrained currents and with the MOM SC in Fig. 5.31(c)—both cases for the AUT currents only—, we observe two noteworthy details. First, evanescent modes along the Huygens surface enclosing the AUT are excited more pronouncedly. Second, the evanescent fields between

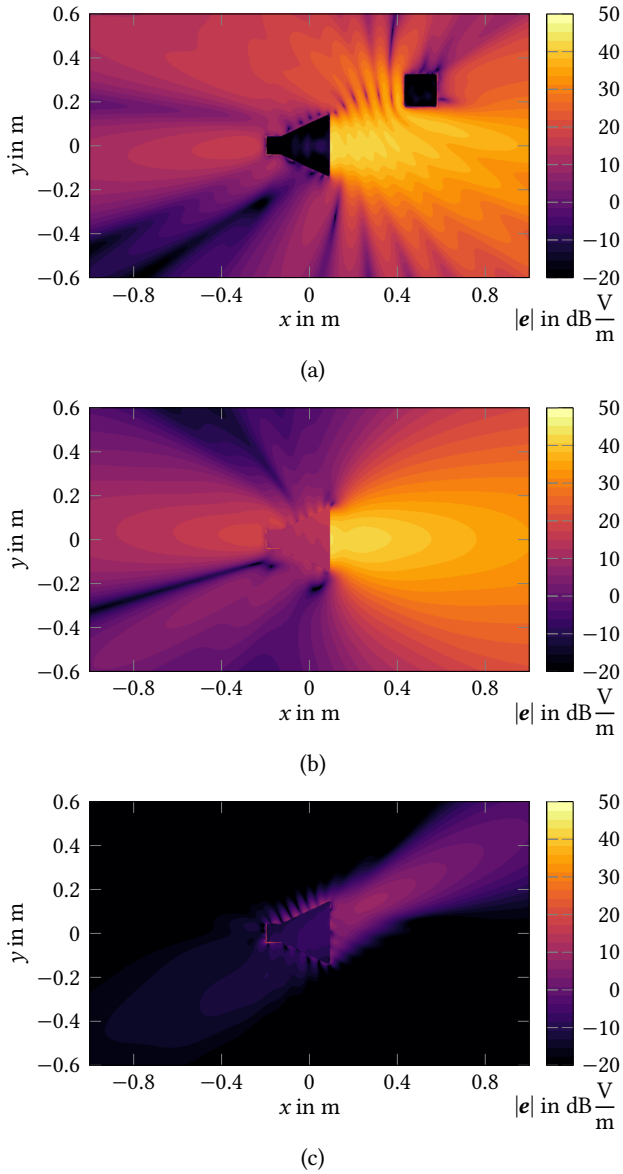


Fig. 5.31: Electric NF magnitude in the $z = 0$ cut plane for the reconstructed Love currents on both the AUT and the scatterer. (a) Fields of all reconstructed currents. (b) Fields of AUT currents only. (c) Field difference to the solution including the MOM SC, for AUT currents only.

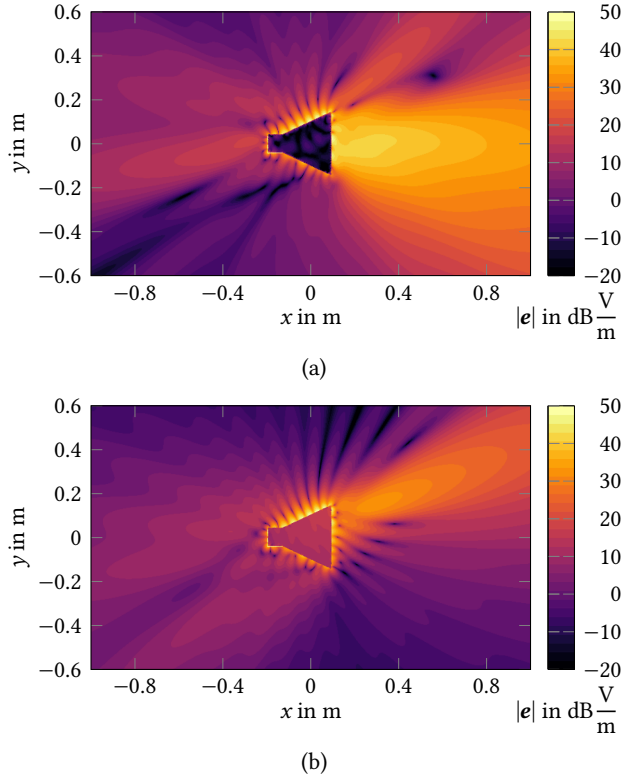


Fig. 5.32: Electric NF magnitude in the $z = 0$ cut plane for spatial filtering with an AUT model only. (a) Reconstructed fields. (b) Field difference to the solution including the MOM SC, for AUT currents only.

the AUT and the cube are not resolved as well with unconstrained currents; the reason being that the reconstruction of unconstrained currents exhibits more DOFs. This makes the separation of the radiation originating from two closely placed objects more challenging and requires extreme measurement accuracy and/or extreme oversampling [Klinkenbusch 2009; Knapp 2021] or, alternatively, measurements taken at the locations of strongly evanescent fields [Paulus et al. 2019].

Finally, Fig. 5.32 shows the electric NF of the reconstructed currents for the spatial filtering with the AUT hull only. In this case, the evanescent modes on the AUT hull are strongly excited, the reason being that HO modes are necessary in order to reconstruct the observations which originate from a different location (i.e., the echo). This is also apparent in the difference plot in Fig. 5.32(b). In comparison

with Figs. 5.30(a) and 5.31(a), the equivalent currents of the simple spatial filtering approach in Fig. 5.32(a) try to mimic the fields of the other cases (i.e., the real solution) as well as possible. For instance, the fields exhibit a minimum at the position of the cube. The radiation contributions leading to these field distortions cannot be removed. They deteriorate the equivalent current distribution on the AUT.

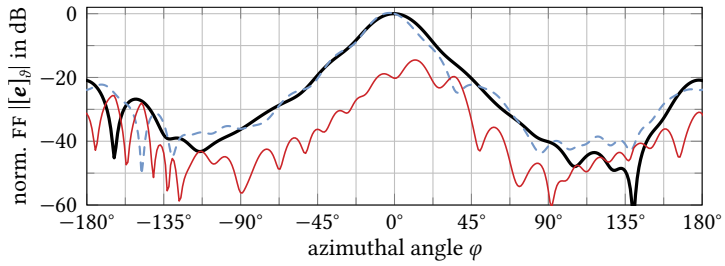
In the last step of the NFFFT, we evaluate the FF of the currents on the horn antenna for all three reconstructions. The resulting patterns are shown in Fig. 5.33 and compared to the Feko reference solution from Fig. 5.29, which is influenced by mutual coupling. The simple source localization approach fares clearly the worst with a maximum error of -14.5 dB. The reconstruction of unconstrained currents achieves a maximum error of -38.5 dB, and the MOM SC solution even -60.8 dB. Clearly, introducing additional knowledge about the inverse problem helps to improve the reconstruction accuracy.

In order to investigate the benefits of the MOM SC, we reduce the number of measurements to about twice the number required by the minimum sphere of the AUT, i.e., $M = 2928$. This sampling would in theory be sufficient to capture the DOFs of the AUT radiation. For the considered setup, this is, however, just an 80% undersampling regarding to the minimum sphere around AUT plus scatterer. Hence, it does not completely suffice for the whole DOFs of AUT plus echo object. The retrieved FFs of the two more accurate methods which include the echo object are shown in Fig. 5.34. The simple source localization approach is not included since it works even worse than with the ten-fold oversampling. The method including the MOM SC comes close to its performance before with a maximum error of -56.5 dB (about 4 dB worse). Compared to that, the unconstrained-currents solution exhibits a larger error of -24.9 dB (about 14 dB worse).

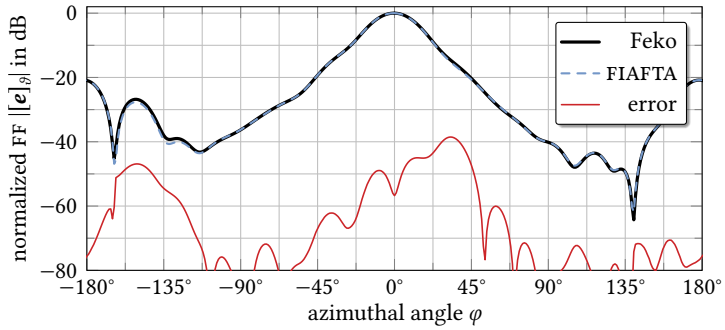
Again, introducing knowledge about the boundary condition of the echo sources helps to improve accuracy since the (evanescent) modes can be separated better between the two source locations and, hence, retrieving the AUT currents works with fewer measurement samples.

The knowledge about the behavior, in particular the boundary condition, of the echo object helps to achieve an improved accuracy since the (evanescent) modes can be separated better between the two source locations. Put differently, this knowledge allows us to reduce the number of measurements compared to the case without this knowledge because less DOFs are to be determined. The measurement effort is, however, shifted to the spatial domain since the surfaces of conducting objects should be known with at least about $\lambda/10$ accuracy or even lower [Paulus et al. 2019].

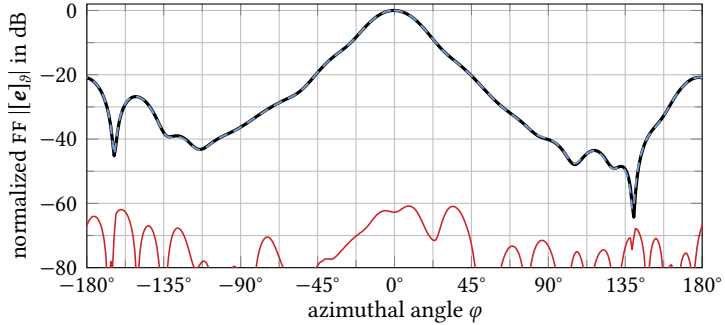
One issue remains when echo sources are introduced in order to separate AUT and echo contributions in the source reconstruction, though. As illustrated in Fig. 5.29, the retrieved solution is still influenced by mutual coupling since the current



(a)



(b)



(c)

Fig. 5.33: Co-polar $[\mathbf{e}]_\phi$ FF component of the AUT currents only, compared to the Feko reference influenced by mutual coupling on the horn antenna. (a) Source localization for the AUT hull only. (b) Additional unconstrained currents on the scatterer, which are neglected for the FF evaluation. (c) Currents obtained with MOM SC, scatterer currents neglected for the FF evaluation.

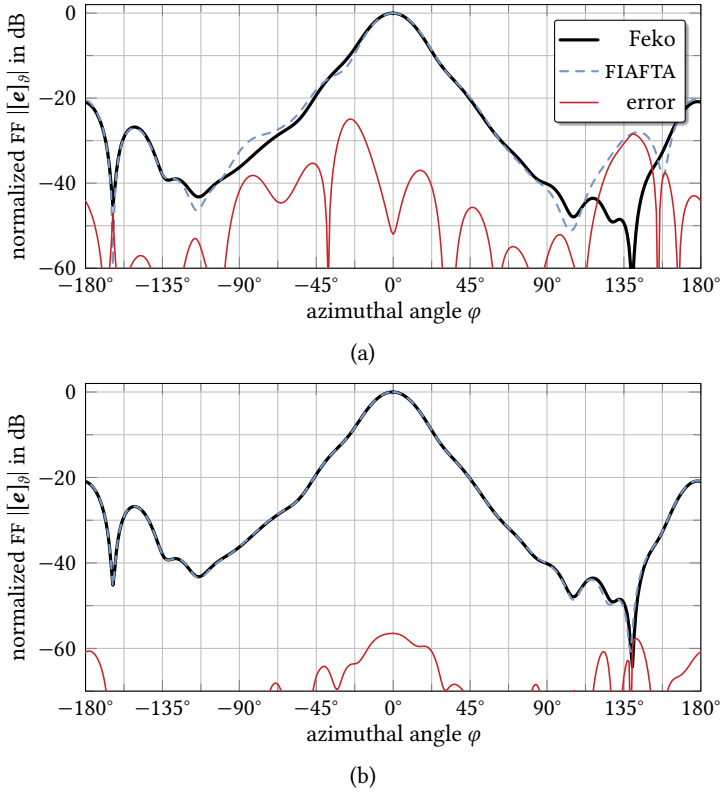


Fig. 5.34: Co-polar $[\mathbf{e}]_{\theta}$ FF component of the AUT currents only, compared to the Feko reference influenced by mutual coupling on the horn antenna. (a) Unconstrained currents on the scatterer, which are neglected for the FF evaluation. (b) Currents with MOM SC, scatterer neglected for the FF evaluation.

distribution on the AUT is changed in reality in close vicinity to a scattering object. In some scenarios, this is indeed the desired solution since the echo comes from the AUT mounting structures which might be present in the real-world application [Saporetti et al. 2019]. In other cases, mutual coupling is seen as a degradation of the “true” free-space solution. Then, broadband measurements and software-based time-gating for the surface sources are able to remove the influence of mutual coupling [Knapp et al. 2019b; Knapp et al. 2020].

5.4.2 Time-Gating for Equivalent Sources & Mutual Coupling

In general, the equivalent surface currents obtained from NF measurements and source reconstruction techniques are only valid in the environment the measurements have been taken. That is why we commonly aim for a controlled measurement environment such as anechoic chambers. In scenarios where this is not feasible, the measurements are inferred by coupling effects, cf. Fig. 5.29. One of the approaches to reduce the influence of coupling/echo effects on the reconstructed NFs and FFs is (possibly software-based) time-gating [Henderson et al. 1989; Levitas and Ponomarev 1996; De Jough et al. 1997; Leather et al. 2004; Loredó et al. 2004; Leibfritz et al. 2007; Loredó et al. 2009]. When we work with time-harmonic measurements, the NF samples are collected over a broad bandwidth and transformed into the time-domain via an inverse Fourier transform. Then, the desired contributions are identified via an analysis of the path length of the line-of-sight connection of the AUT and the field probe and the longer path lengths of parasitic paths involving echo objects. After windowing the desired pulse, another Fourier transform yields the filtered broadband time-harmonic measurement data, which may be employed in subsequent post-processing steps such as a surface-source reconstruction. Special care has to be taken of the ringing at the edges of the measurement bandwidth, for instance by the use a frequency-extension technique or sparsity-base time-gating [Mauermayer and Eibert 2016, 2017; Knapp et al. 2019a].

If the path lengths of the direct, line-of-sight connection and indirect paths including reflections are close to each other or whenever multiple interactions play a role, time-gating of the probe signals may be unfeasible for some configurations of AUT and probe positions since the time-domain signals overlap. This poses a crucial limitation to time-gating of the NF at the observation locations for scenarios where mutual coupling changes the AUT current distribution due to multiple interactions between AUT and scatterer. Time-gating of the reconstructed currents is able to cope with such scenarios [Knapp et al. 2019b; Knapp et al. 2020].

We consider a source reconstruction approach similar to the one introduced in Subsection 5.4.1. One particular difference is that multi-frequency time-harmonic measurements are required. At each single frequency f , equivalent currents $\mathbf{x}_{\text{AUT}}(f)$ are reconstructed on a hull enclosing the AUT. The same is done for any echo objects,

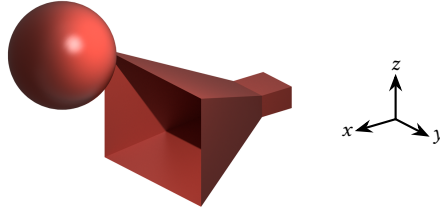


Fig. 5.35: The horn antenna as simulated in Feko, with a PEC sphere in front [Paulus et al. 2019].

where currents $\mathbf{x}_{\text{echo}}(f)$ are retrieved. Since we process the multi-frequency data simultaneously, choosing a unique solution might be important. In the following, we retrieve the computationally efficient and unique WF CS solution [Eibert and T. B. Hansen 2017].

This has been done for the simulation setup shown in Fig. 5.35, which includes the same simulation model of a horn antenna as discussed previously but now with a PEC sphere as an echo object in front. The fields of this echoic antenna configuration have been simulated from 1.7 GHz to 5.7 GHz in steps of 50 MHz, allowing a time resolution of a standard Fourier transform of $\Delta t = 1/4 \text{ GHz} = 0.25 \text{ ns}$. This corresponds to a “length resolution” in free space of about 0.075 m. The sphere was placed with a distance of about 0.3 m to the aperture of the horn antenna, which should give us the possibility to identify mutual interactions reliably.

In the following, we evaluate the FF for the reconstructed currents on the AUT \mathbf{x}_{AUT} only. The reconstructed FF pattern of these currents is compared to the free-space radiation of the horn antenna in Fig. 5.36, at the center frequency 3.7 GHz of the considered bandwidth. The deviation between the two solutions goes up to -27 dB in this scenario. If we want to get rid of the mutual coupling influence on the AUT and reconstruct the behavior in free space, this deviation is an error in the solution.

In the next step, we calculate the time-domain signal for each n th RWG function

$$x_n(t) = \mathcal{F}^{-1}\{\mathbf{x}(f)_n\} \quad (5.48)$$

attained by an inverse Fourier transform. The resulting time-domain signal—as the summed absolute-value signal of all coefficients $\log_{10}(\sum_n |x_n(t)|^2)$ —is given in Fig. 5.37. The dominant main pulse has its maximum shortly after 1 ns. The excitation of the currents on the sphere (the echo object) occurs at around 3 ns. The dispersion of those currents on the scatterer stems from the fact that the detaching wave coming from the AUT takes some time to pass the sphere. Beginning at 4 ns, we observe the arrival of backscattered fields at the AUT. After 7 ns to 8 ns, we

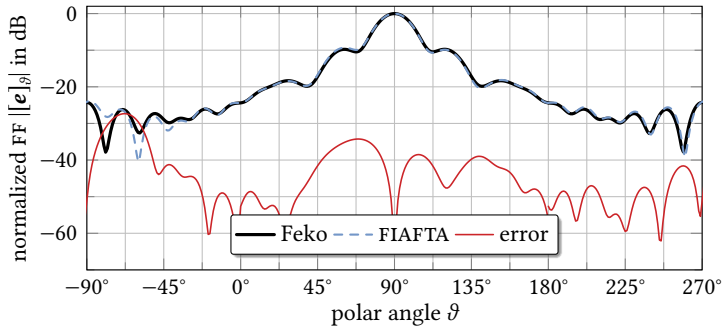


Fig. 5.36: Co-polar $[e]_{\vartheta}$ component of the horn antenna FF in the comparison of free-space reference solution and the reconstructed AUT currents influenced by mutual coupling in the $\varphi = 0^\circ$ cut at 3.7 GHz [Knapp et al. 2020].

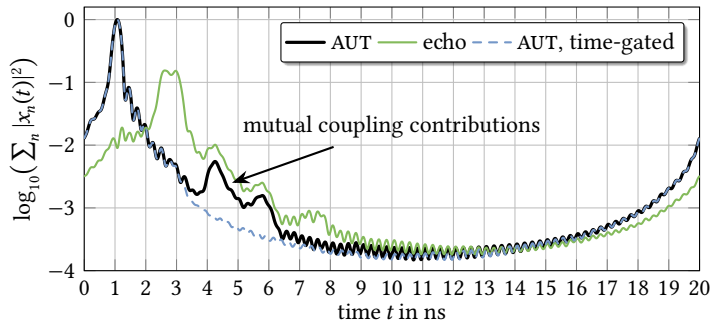


Fig. 5.37: Time-domain current signal on the AUT and on the echo object, presented by Knapp et al. [2019b] and Knapp et al. [2020].

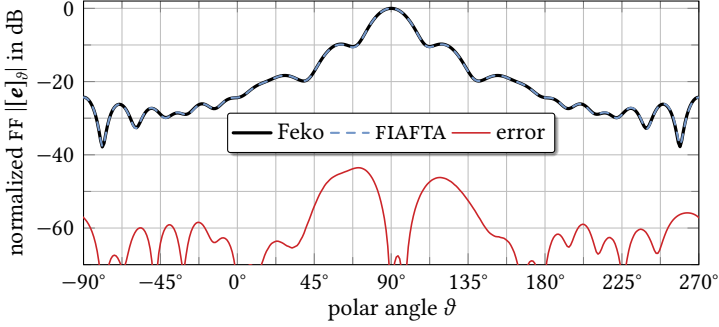


Fig. 5.38: Co-polar $[\mathbf{e}]_\vartheta$ component of the horn antenna FF in the comparison of free-space solution and the time-gated AUT currents in the $\varphi = 0^\circ$ cut at 3.7 GHz [Knapp et al. 2020].

see another interaction with the echo object. With each interaction, the pulse becomes more dispersed since the fields of the already broadened pulse traverse the complete volume of the AUT or echo object and are scattered at different places. According to the distance of AUT and echo object of 0.3 m, a time gate was applied to the AUT currents 2.5 ns after the main peak. The resulting current time signal $\log_{10}(\sum_n |x_n^{\text{AUT}}(t)|^2)$ is also contained in Fig. 5.37.

After another Fourier transform for every time-gated signal $\hat{x}_n(t)$ associated with an RWG function on the AUT

$$\hat{\mathbf{x}}_{\text{AUT}}(f) = \mathcal{F}\{\hat{x}_n(t)\}, \quad (5.49)$$

we evaluate the FF of the processed coefficients of the AUT currents $\hat{\mathbf{x}}_{\text{AUT}}(f)$ in Fig. 5.38. The detrimental effect of mutual coupling is reduced and the agreement to the free-space Feko solution has increased significantly with an maximum error of below -40 dB.

In conclusion, echo sources and time-gating of the observed NF samples do not suffice for a full echo suppression in many NF antenna measurement scenarios where the measurement environment is not ideal free space or anechoic. In such cases, augmenting a surface-source reconstruction technique with software-base time-gating of the currents helps to improve the reconstruction quality and effectively reduces the undesired impact of mutual coupling and multiple interactions between echo objects and the AUT.

5.5 Phase Retrieval for Source Reconstruction Problems

Yet another challenging source reconstruction scenario is encountered when the measurement hardware is restricted to measure only the magnitude $|\mathbf{b}|$ of the radiated fields of an AUT, where $|\cdot|$ operates element-wise. Then, the task of an NFFFT is expanded by an initial step of phase retrieval, i.e., reconstructing the complex observations for which the standard algorithms may be employed. In the scope of source reconstruction techniques, this may be formulated as the non-linear inverse problem

$$|\mathbf{A}\mathbf{x}| = |\mathbf{b}| \quad (5.50)$$

or including an unknown phase vector $\boldsymbol{\phi}$ with the entries

$$[\boldsymbol{\phi}]_m = e^{j\phi_m} \quad (5.51)$$

in addition to the unknown source coefficients \mathbf{x}

$$\mathbf{A}\mathbf{x} = \text{diag}(\boldsymbol{\phi})|\mathbf{b}| \quad \text{s. t. } |[\boldsymbol{\phi}]_m| = 1 \quad \text{for } m \in \{1, 2, \dots, M\}, \quad (5.52)$$

where $\text{diag}(\cdot)$ creates a diagonal matrix from a vector (or a vector from the diagonal of a matrix).

Besides the field of HF engineering, the inverse problem of phase retrieval comes up in many other research fields [Isernia et al. 1996; Yaccarino and Rahmat-Samii 1999; Paulus et al. 2017b; Knapp et al. 2019c; Paulus et al. 2020; Kornprobst et al. 2021d; Knapp et al. 2021; Paulus et al. 2021]: including optics [Gerchberg and Saxton 1972; Shechtman et al. 2015], X-ray crystallography [Miao et al. 2012; Pfeiffer et al. 2006], transmission electron microscopy [Coene et al. 1992; Faulkner and Rodenburg 2004], coherent diffraction imaging [Guizar-Sicairos and Fienup 2008; Candès et al. 2015b; Bacca et al. 2020], applied mathematics [Candès et al. 2013; Candès et al. 2015a; Candès et al. 2015c; Netrapalli et al. 2015; Iwen et al. 2019; Grohs et al. 2020; Cheng et al. 2021; Grohs and Rathmair 2021], and ptychography [Iwen et al. 2016; Ramos et al. 2019; Sissouno et al. 2019].

For most practical scenarios, phase retrieval cannot be proven to work with certainty and convergence analyses are mostly probabilistic. In order to improve the convergence chances, additional information may be incorporated into the phase retrieval problem—with or without renouncing pure magnitude-only measurements. If feasible, the observation kernel can be changed (masking [Pohl et al. 2014], exploiting multiple measurement distances [Isernia et al. 1996; Yaccarino and Rahmat-Samii 1999; Schmidt and Rahmat-Samii 2009]), one may attempt to measure spatial derivatives [Paulus and Eibert 2020], or one may enforce sparsity [Jaganathan et al. 2017; Qiu and Palomar 2017; Pauwels et al. 2018; G. Wang et al. 2018; Baechler et al. 2019]. Two approaches working with additional relative

phase information are discussed in the following.

The implementation of the surface sources is done a bit different for the numerical results in this section. While we have considered div-conforming basis functions for the surface current densities so far (with MLFMM acceleration for both the BEM solver and the FIAFTA), we work with point sources in the following. Hertzian dipoles are placed tangentially on the AUT Huygens surface. Apart from the excitation of evanescent modes close to the AUT hull, this is an equivalent description to employing electric surface currents \mathbf{j} only; offering the same radiation properties and also the same DOFs as any other sensible surface description. The implementation is sped up only by parallelization, possibly on a GPU [Paulus and Eibert 2018].

5.5.1 Multi-Frequency Phase Retrieval and the Problem of Local Minima

One way to incorporate additional information for antenna measurements is to transmit a modulated signal during the NF measurement setup and acquire knowledge of relative phases among the spectral components of the modulated signal at all individual measurement locations [Paulus et al. 2020; Knapp et al. 2021]. The implementation of a possible setup working with modulated signals was described and put into practice by Knapp et al. [2021]. In the following, we focus on the algorithmic challenges of phase retrieval.

Observation Model and Phase Reconstruction Algorithm

The observation model is extended in a way where we formulate the phase retrieval problem at an i th frequency as

$$|\mathbf{A}_i \mathbf{x}_i| = |\mathbf{b}_i|. \quad (5.53)$$

At each other considered k th of K frequencies, we measure not only the magnitudes $|\mathbf{b}_k|$ but also the relative phases with respect to the observation at the i th frequency. This relation between the data of the k th and i th measurement frequency is collected in a diagonal matrix with the entries

$$[\mathbf{U}_{k,i}]_{\ell\ell} = \frac{[|\mathbf{b}_k|]_{\ell}}{[|\mathbf{b}_i|]_{\ell}} e^{j(\phi_{k,\ell} - \phi_{i,\ell})}. \quad (5.54)$$

Knowing the complex data at the i th frequency, we can calculate the complex observation data as $\mathbf{b}_k = \mathbf{U}_{k,i} \mathbf{b}_i$. Unfortunately, we do not know this complex data. Hence, we employ an equivalent source model of the AUT to represent \mathbf{b}_i as the MVP $\mathbf{A}_i \mathbf{x}_i$. The mapping matrices $\mathbf{U}_{k,i}$ allow us to enforce additional restrictions on

the problem via the data at other frequencies. In order to ensure physically correct solutions at those frequencies during the solution process, the projection matrices $\mathbf{P}_{\mathbf{A},k} = \mathbf{A}_k \mathbf{A}_k^+$ are employed. Overall, the task is to solve the non-linear system of equations

$$\begin{bmatrix} |b_1| \\ \vdots \\ |b_i| \\ \vdots \\ |b_K| \end{bmatrix} = \begin{bmatrix} \mathbf{P}_{\mathbf{A},1} \mathbf{U}_{1,i} \\ \vdots \\ \mathbf{I} \\ \vdots \\ \mathbf{P}_{\mathbf{A},K} \mathbf{U}_{K,i} \end{bmatrix} \mathbf{A}_i \mathbf{x}_i \quad (5.55)$$

for \mathbf{x}_i , the unknowns at one i th frequency which is picked arbitrarily. Subsequently, the knowledge of the phase information allows us to solve the inverse problem at all other frequencies.

Transformation Results for Measurement Data

For a real-world measurement setup, we consider spherical measurements of the horn antenna shown in Fig. 5.23 taken with a DRH18 probe [RFspin 2021a]. The NF was captured at four distances with radii 2.512 m, 2.642 m, 2.892 m, and 3.092 m on a 1° grid. From this enormous amount of measurements, 20 000 samples were picked on a regular grid, which is still a strong oversampling for this AUT with several thousand DOFs. The equivalent source representation is implemented as 5000 tangential Hertzian dipoles on a conformal hull around the AUT. Measurements have been taken at various frequencies. In the following, we consider the measurement data at 2.8 GHz, 3.0 GHz, and 3.2 GHz. The non-convex cost functions were minimized with a solver based on the memory limited L -BFGS method [D. C. Liu and Nocedal 1989; Nocedal and Wright 2006], by Broyden, Fletcher, Goldfarb, and Shannon. For the initial guess of the single-frequency solutions, we employ a spectral method by Candès et al. [2015c].

The FF of a magnitude-only NFFFT at 3.2 GHz is shown in Fig. 5.39(a). The phase reconstruction does not work satisfactorily despite employing measurement data on four surfaces with varying distance to the AUT. The FF error goes up to -10.3 dB. For the multi-frequency approach, the single frequency solution at 2.8 GHz is solved first and taken as a starting point for the multi-frequency solver. Then, the complex problem for the reconstructed observations at 3.2 GHz is solved. The resulting FF pattern is given in Fig. 5.39(b). The error is significantly smaller, with the maximum error being -26.1 dB.

While this is a significant improvement, it still is clearly worse than a solution with full phase information. The underlying issue is that the non-convex minimization might get stuck in local minima. Not only is this problem getting worse with increasing size—electrical size as well as number of DOFs—, but also local

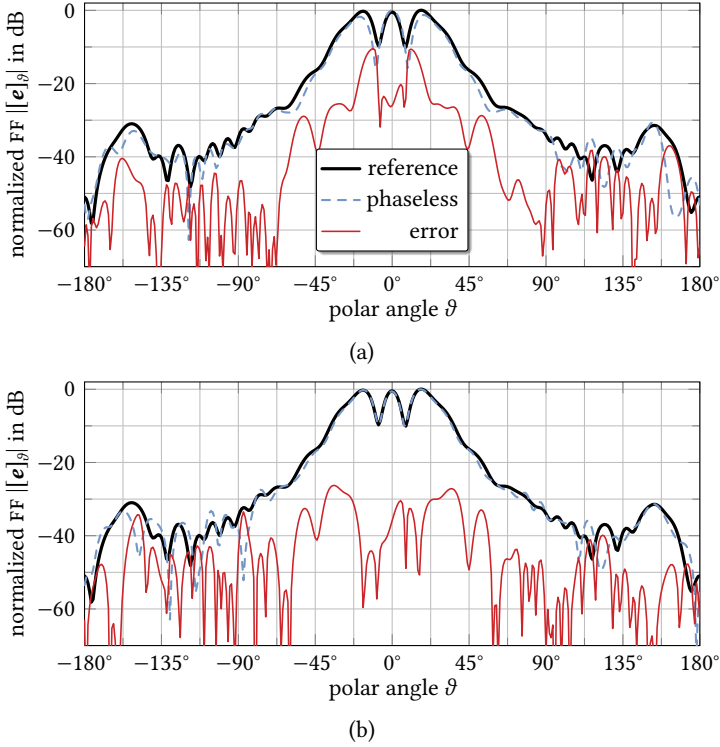


Fig. 5.39: Reconstructed FF patterns in the $\varphi = 0^\circ$ cut at 3.2 GHz. (a) Magnitude-only approach. (b) Augmented by relative phase data at 2.8 GHz and 3.0 GHz. © 2021 IEEE [Knapp et al. 2021].

minima might not be identifiable with magnitude-only information even though only the unique global minimum should exhibit a cost function value of zero in the ideal noise-free case. Whenever the observations are contaminated, the OE gives a limit to the RD, and local minima with cost function values below the error floor become indistinguishable from the true solution. While the FF does not reveal such information, this becomes evident when looking at achievable magnitude-only and complex NF RDs. The complex NF RD is, of course, not available in a true phaseless measurement setup but can be used here to judge the reliability of the algorithms. Since we have this possibility with the fully coherent measurement data, for which we consider a suitable phaseless/phase-restricted portion for phase retrieval, both kinds of NF RD are given in Fig. 5.40. Here, we analyze the impact of the initial guess on the solution quality and, at the same time, observe how severe

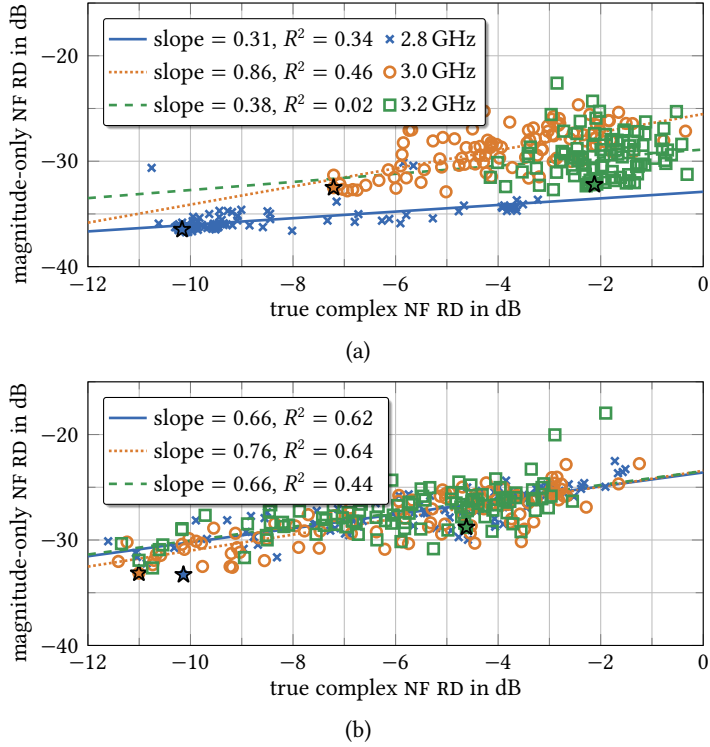


Fig. 5.40: Comparison of magnitude-only and complex NF RDs for 20 000 measurements on a regular grid and four distances. (a) Standard single-frequency approach. (b) Multi-frequency minimization. © 2021 IEEE [Knapp et al. 2021].

the problem of local minima is. 100 random initial guesses are considered for the non-convex optimization. In the single-frequency case, we additionally consider the initial guess according to the mentioned spectral method, which is marked with a star. In the multi-frequency case, this single frequency solution employed as an initial guess is highlighted by a star.

For the single-frequency approach, we observe that there is no way to know whether a lower magnitude-only RD $\|b - |A x|\|$ correlates with a better true complex RD $\|b - A x\|$, since lots of perhaps good, perhaps poor solutions with similar magnitude-only NF RD exist. With the good initial guess provided by the mentioned spectral method, the magnitude-only solver is also stuck in a local minimum.

An advantage of the multi-frequency method is found in the fact that the quality of the solution can be judged to some extent by looking at the reconstruction

deviation of the multi-frequency solution. We observe that local minima with rather low magnitude deviation are still present, but most of the local minima are shifted to much larger NF RD values. While this is a probabilistic statement about the convergence, there is no reliable way to ensure convergence to the global minimum—which is not achieved by any of the random 100 initial guesses.

Non-convex solvers for phase retrieval in antenna measurements struggle with the convergence to the correct solution even when additional information is available, for instance sampling at multiple measurement distances and multi-frequency data. Even though more information certainly helps for convergence, the non-linear problem is hard to solve. Given the current capabilities of local optimization algorithms, one should avoid these kind of problems, since local minima may prevent to retrieve a reasonable solution at all—and this is not even noticeable with magnitude-only data.

5.5.2 Linear Phase Retrieval for Partially Coherent Observations

As seen in the previous Subsection 5.5.1, phase retrieval is a non-convex optimization problem in practice¹³ and the corresponding algorithms generally struggle to find the true global solution—if it exists and is unique. Here, we consider the special case of having coherently linked subsets of measurements which relaxes the phase retrieval problem and allows to develop a linear phase reconstruction algorithm which inherently avoids the problem of local minima.

To this end, we propose to use a special measurement equipment which allows to observe (possibly small) sets of observations coherently. Such measurement configurations have been already employed for NF antenna measurements with multi-probe measurements by Costanzo et al. [2001], Costanzo and Di Massa [2001], Costanzo et al. [2005], Costanzo and Di Massa [2008], Paulus et al. [2017a, 2017b, 2018], Tena-Sánchez et al. [2020], and Tena-Sánchez et al. [2021b] and with multi-frequency measurements by Paulus et al. [2020] and Knapp et al. [2021]. Related measurement configurations are found for the stitching of holographic images, which is relevant to antenna measurements [Junkin et al. 2000; Castaldi and Pinto 2000; Laviada and Las-Heras 2013; Laviada Martinez et al. 2014; Arboleya et al. 2015; Arboleya et al. 2018; Tena-Sánchez and Sierra-Castafier 2018; Berlt et al. 2020] and optics [Gabor 1949; Leith and Upatnieks 1962; Barmherzig et al. 2019]. These two scenarios of a multi-probe and holographic antenna measurement setup

13. In theory, phase retrieval can be formulated as a linear problem once sufficient information is available. However, practically speaking, this is close to impossible to achieve for antenna NF measurements: It is unclear how to “design” the measurement in order to capture the necessary information content, the linear formulation requires enormous oversampling of order $\mathcal{O}(N_{\text{dof}}^2)$, and it involves tremendous computational complexity of inverting a system of equations of the according size. Each of these aspects alone causes us to consider phase retrieval as non-linear and non-convex in any realistic implementation [Knapp et al. 2019c].

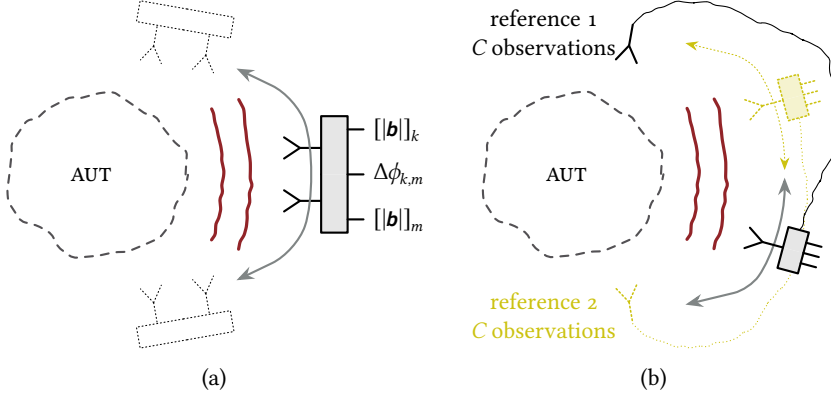


Fig. 5.41: Antenna measurement setups with partially coherent observations. (a) A multi-probe approach, $C = 2$. (b) A holographic approach with two coherent data sets, $M = 2$ and C is large. © 2021 IEEE [Kornprobst et al. 2021d].

are depicted in Fig. 5.41. A third possibility is to measure multiple frequencies coherently with one probe antenna, i.e., a slight variation of the setup in Fig. 5.41(a) [Knapp et al. 2021]. As shown, we collect an additional phase measurement $\Delta\phi_{k,m}$ as

$$[\phi]_k / [\phi]_m = e^{j(\phi_k - \phi_m)} = e^{j\Delta\phi_{k,m}} \quad (5.56)$$

between the k th and m th entry of the observation vector. In the case of multi-probe systems, see Fig. 5.41(a), the phase retrieval task is harder since C is typically rather small, e.g., $C = 2$ in the measurement systems proposed by Costanzo and Di Massa [2001], Costanzo et al. [2001, 2005], Costanzo and Di Massa [2008], and Paulus et al. [2017b]. Having such a measurement setup, localized and generally disconnected “isles” of coherent observations are captured on the observation surface a . This may be achieved with vector and scalar receivers. The particular phase differences of interest are observed either directly by multi-channel receivers with shared oscillator signals or via distinct magnitude observations in the form of $[\mathbf{b}]_k$, $[\mathbf{b}]_m$, $[\mathbf{b}]_k + [\mathbf{b}]_m$, $[\mathbf{b}]_k + j[\mathbf{b}]_m$, which allows to numerically reconstruct the phase differences as [Paulus et al. 2017b]

$$\Delta\phi_{k,m} = \text{atan} \frac{[\mathbf{b}]_k + [\mathbf{b}]_m|^2 - [\mathbf{b}]_k^2 - [\mathbf{b}]_m^2}{[\mathbf{b}]_k + j[\mathbf{b}]_m|^2 - [\mathbf{b}]_k^2 - [\mathbf{b}]_m^2}. \quad (5.57)$$

Other sets of at least four independent linear combinations of $[\mathbf{b}]_k$ and $[\mathbf{b}]_m$ can reconstruct the same phase difference. In the following, we abstract from the

hardware implementation and assume the $C - 1$ phase differences of each set of C measurement samples to be known. Furthermore, we constrain the way of how these observations are taken when studying the effect of such partially coherent observations. A special observation probe shall be able to capture C independent observations coherently whenever it performs a measurement.¹⁴ For instance, Fig. 5.41(a) shows a setup with fixed $C = 2$.

Phase retrieval for partially coherent observations is certainly a less challenging task than the general phase retrieval problem since additional but limited information about relative phases is available. Nevertheless, the algorithms found in literature, which tackle this particular problem, are limited to solving non-convex non-linear minimization problems, which is known to be unreliable [Paulus et al. 2017b; Knapp et al. 2017; Tena-Sánchez et al. 2020; Tena-Sánchez et al. 2021b; Rodríguez Varela et al. 2021b; Tena-Sánchez et al. 2021a] (also for the case of classical magnitude-only observations [Bangun et al. 2019; Moretta and Pierri 2019; Pierri et al. 2020; Varela et al. 2021] and possibly with multiple measurement surfaces [Varela et al. 2019; Fuchs et al. 2020; Rodríguez Varela et al. 2021a]) or they utilize restrictive, unrealistic, or even practically unfeasible sampling strategies [Costanzo et al. 2001; Pohl et al. 2017; Tena-Sánchez et al. 2020].

A Linear Phase Retrieval Algorithm

It is possible to incorporate the information in (5.56) about phase differences into (5.52) as an additional SC. This yields different formulations of the same underlying non-linear optimization problem, which all continue to struggle with the problem of getting stuck in local minima [Kornprobst et al. 2021d]. For the linear formulation presented in the following, Kornprobst et al. [2021d], Paulus et al. [2021], and Paulus et al. [2022a] have proposed several formulations, which exhibit slightly different constraints and benefits. The approach has also been generalized for measurement signals with unstable magnitude reference [Paulus et al. 2022b]. One of the linear formulations for phase retrieval is discussed in detail [Kornprobst et al. 2021d].

In order to exploit the structured information of the partially coherent measurements, we use the block-structured partially-coherent observation matrix

$$\mathbf{B} = [\mathbf{B}_1 \quad \mathbf{B}_2 \quad \dots \quad \mathbf{B}_c \quad \dots \quad \mathbf{B}_C]^\top, \quad \mathbf{B} \in \mathbb{C}^{CM \times M}. \quad (5.58)$$

Here, M denotes the number of measurement locations, at each of which C measurements are taken. The diagonal submatrices contain all available information:

¹⁴. While this restriction is not required to profit from the presented phase-retrieval algorithm, it facilitates the notation and enables us to predict at which oversampling ratio phase retrieval becomes reliable. In the more general case, C may change rather arbitrarily from one observation to another but all methods and insights presented here are still applicable [Paulus et al. 2021].

They are built from the magnitude-only observations vector

$$|\mathbf{b}| = [|\mathbf{b}_1^T| \quad |\mathbf{b}_2^T| \quad \dots \quad |\mathbf{b}_c^T| \quad \dots \quad |\mathbf{b}_C^T|]^T, \quad (5.59)$$

where the c th subvector $\mathbf{b}_c \in \mathbb{R}^M$ contains the observed magnitudes of the c th probe of the overall C probes at all M location. In this notation, $|\mathbf{b}| \in \mathbb{R}^{CM}$, $\mathbf{b} \in \mathbb{C}^{CM}$, and $\mathbf{A} \in \mathbb{C}^{CM \times N}$. Furthermore, the diagonal submatrices \mathbf{B}_c contain the additionally measured phase differences $\Delta\phi_{m+cM,m}$ between the first and the c th subset of measurements. This means that the first submatrix

$$\mathbf{B}_1 = \text{diag}(|\mathbf{b}_1|) \quad (5.60)$$

only contains magnitudes, lacking a globally connected phase. The other submatrices are defined via their entries on the diagonal

$$[\mathbf{B}_c]_{mm} = [|\mathbf{b}_c|]_m e^{j\Delta\phi_{m+cM,m}} \quad (5.61)$$

and contain the relative phases to the observations of the first part of the observations in \mathbf{B}_1 . Obviously, we have reduced the number of phase unknowns to M from CM in ϕ . This can be formalized by introducing the reduced phase unknowns vector $\psi \in \mathbb{C}^M$ in (5.52), yielding the partial-coherent phase retrieval problem with both source coefficient unknowns and observation phase unknowns

$$\mathbf{A} \mathbf{x} = \mathbf{B} \psi \quad \text{s. t. } |[\psi]_m| = 1 \quad \text{for } m \in \{1, 2, \dots, M\}. \quad (5.62)$$

After retrieving the phase ψ , we reconstruct the complex observations vector as

$$\mathbf{b} = \mathbf{B} \psi. \quad (5.63)$$

We know that this reconstructed vector has to be generated by the AUT source model. The effect of these sources are evaluated by the MVP $\mathbf{A} \mathbf{x}$. With the projection matrix $\mathbf{P}_A = \mathbf{A} \mathbf{A}^+$, we are able to enforce an observation vector

$$\mathbf{b} = \mathbf{P}_A \mathbf{b} = \mathbf{P}_A \mathbf{B} \psi \quad (5.64)$$

matching the source model, even if the retrieved complex vector $\mathbf{B} \psi$ contains parts which cannot be attributed to AUT sources. So far, we have not yet revealed how to retrieve ψ in the first place.

With the above considerations, we are able to calculate the difference between any guess of a complex vector $\mathbf{B} \psi$ and its associated projection into $\text{im } \mathbf{A}$, i.e., the part of a guess representable by sources on s . We want minimize this difference to

retrieve a reasonable solution, and aim to solve the system of equations

$$\mathbf{R}\boldsymbol{\psi} = [\mathbf{P}_A - \mathbf{I}]\mathbf{B}\boldsymbol{\psi} = \mathbf{0}, \quad \text{s. t. } |[\boldsymbol{\psi}]_m| = 1 \quad \text{for } m \in \{1, 2, \dots, M\} \quad (5.65)$$

including a non-linear SC for $\boldsymbol{\psi}$. If the submatrices \mathbf{B}_c and accordingly defined submatrices \mathbf{A}_c fulfill certain requirements [Kornprobst et al. 2021d], we posit the necessary but not sufficient condition

$$M(C - 1) \geq N - 1 \quad (5.66)$$

for a unique solution, which allows to drop the non-linear SC. Then, the phase retrieval problem is solved once the unique vector $\boldsymbol{\psi}$ in the one-dimensional null-space of \mathbf{R} is retrieved.¹⁵ This can be either achieved by computing an SVD of \mathbf{R} or by constraining the i th phase unknown (i.e., defining the irrelevant global phase) and solving the inhomogeneous and invertible linear system

$$\mathbf{R}_\star \boldsymbol{\psi} = \mathbf{u}_{CM+1} \quad \text{with } \mathbf{R}_\star = [\mathbf{R}^\top \quad \mathbf{u}_i]^\top, \quad (5.67)$$

where \mathbf{u}_i refers to the i th unit vector. This offers the additional advantage that the generalized inverse \mathbf{A}^+ can be approximated iteratively and, thus, the implementation can be done computationally much more efficiently.

After retrieving the phase vector, the complex observations

$$\mathbf{b} = \mathbf{B} \text{diag}(|\boldsymbol{\psi}|)^{-1} \boldsymbol{\psi}, \quad (5.68)$$

are reconstructed similarly to (5.63) but taking into account that the magnitude-one constraint has been dropped. The standard source-reconstruction problem may be solved subsequently, and the quantities of interest such as the AUT FF can be calculated afterwards from the retrieved vector \mathbf{x} .

Numerical Results

First, we consider Gaussian Random matrices \mathbf{A} . For each realization, we randomly pick a true solution $\boldsymbol{\xi}$ and a right-hand side $\mathbf{b}' = \mathbf{A}\boldsymbol{\xi}$. We evaluate the true RD

$$\epsilon_b = \|\mathbf{A}\mathbf{x} - \mathbf{A}\boldsymbol{\xi}\|_2 / \|\mathbf{A}\boldsymbol{\xi}\|_2, \quad (5.69)$$

where, however, the solution \mathbf{x} is obtained for a noise-contaminated vector \mathbf{b} with the SNR $\|\mathbf{b}\|_2 / \|\mathbf{b}' - \mathbf{b}\|_2$.¹⁶ We consider $N = 3000$ unknowns and $CM = 2.1N = 6300$

¹⁵. Suitable measures have to be taken in scenarios where the null-space of \mathbf{R} is inherently not one-dimensional, for instance for truncated measurement surfaces [Paulus et al. 2022a].

¹⁶. This is an alternative definition to (5.33), which fits better to the quantity ϵ_b . Eq. (5.33), on the other hand, fits well to measurement scenarios for which the SNR is known per measurement sample.

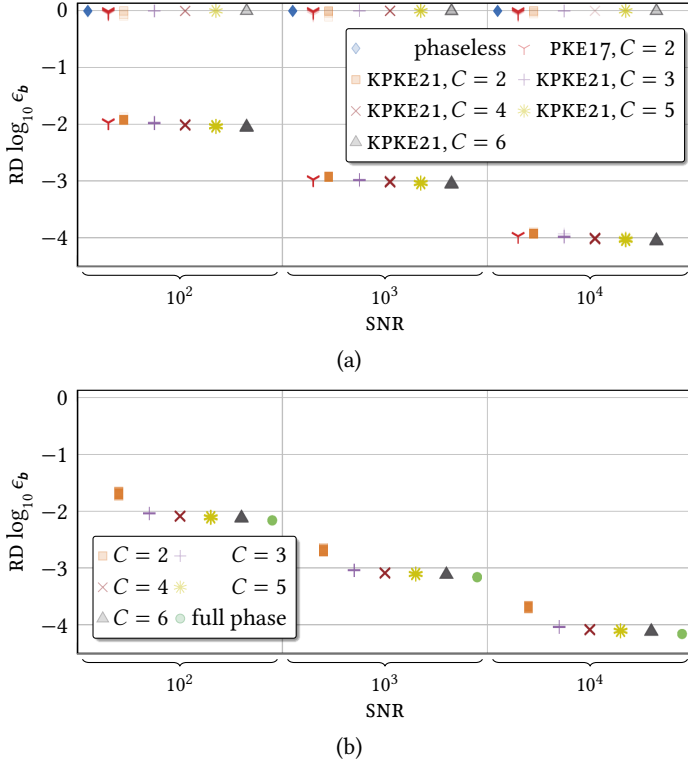


Fig. 5.42: 100 random simulations for an SNR analysis, $N = 3000$, $CM = 2.1N$. (a) Non-linear solvers for phaseless and partially coherent data, KPKE21 by Kornprobst et al. [2021d] and PKE17 by Paulus et al. [2017b]. (b) Linear solvers for partially coherent data and also with full phase information © 2021 IEEE [Kornprobst et al. 2021d].

observations, which is above the success threshold (5.66) for any $C \geq 2$. Apart from the linear phase retrieval algorithm, we consider several non-convex solvers. The most basic one is of course a pure magnitude-only solver. Additionally, one non-linear solver proposed by Kornprobst et al. [2021d] (KPKE21) and another one by Paulus et al. [2017b] (PKE17). For all of these, the initial guess is computed with a spectral method by Candès et al. [2015c].

For each of the SNRs $\{10^2, 10^3, 10^4\}$, we have performed 100 Monte Carlo simulations. The resulting RDs ϵ_b are shown in Fig. 5.42. All non-convex solvers, see Fig. 5.42(a), fail to converge reliably to the correct solution and get stuck in local minima for some realizations of the inverse problem. The standard phaseless solver

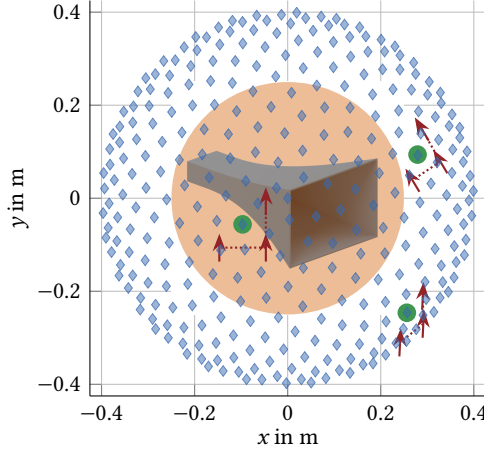


Fig. 5.43: Synthetic NF antenna measurement setup for capturing partially coherent observations with L-shaped multi-probe arrays on a closed spherical surface © 2021 IEEE [Kornprobst et al. 2021d].

(a non-convex minimization of the magnitude-only cost functional) fails to retrieve a good solution at all. The solver from PKE17 achieves a “success rate” of just 65% for the case $C = 2$. The non-linear solvers from KPKE21 fare better with 94.14% success rate on average over all C and SNRs. In contrast, we do not observe such an issue for the linear algorithms studied in Fig. 5.42(b), which all show a “success rate” of 100%. Differences are only observed regarding the achievable RD: The solution with full phase information to the standard complex inverse problem offers the best accuracy and the best reliability. For the chosen scenario, we see an increasing RD with decreasing C —which is somewhat expected since the phase information content is reduced with decreasing C .

Eventually, we employ the linear phase retrieval in a (synthetic) NF antenna measurement setup, which is depicted in Fig. 5.43. The equivalent-source sphere enclosing the AUT and a measurement sphere, exhibit diameters of 5λ and 8λ , respectively. As equivalent sources, $N = 1200$ tangential Hertzian dipoles are utilized, whose coefficients form the solution vector \mathbf{x} and which are placed tangentially on the smallest (orange) sphere enclosing the horn antenna. An L-shaped probe array (consisting of Hertzian dipoles indicated by red arrows in Fig. 5.43) is placed at each the measurement position, whose center is denoted by a green dot. The horizontal as well as the vertical spacing between the probe-array elements is 1λ . This array is used to acquire magnitude and local phase difference information with $C = 2$ and $C = 3$ at all sample locations visualized by blue diamonds. For the case $C = 2$,

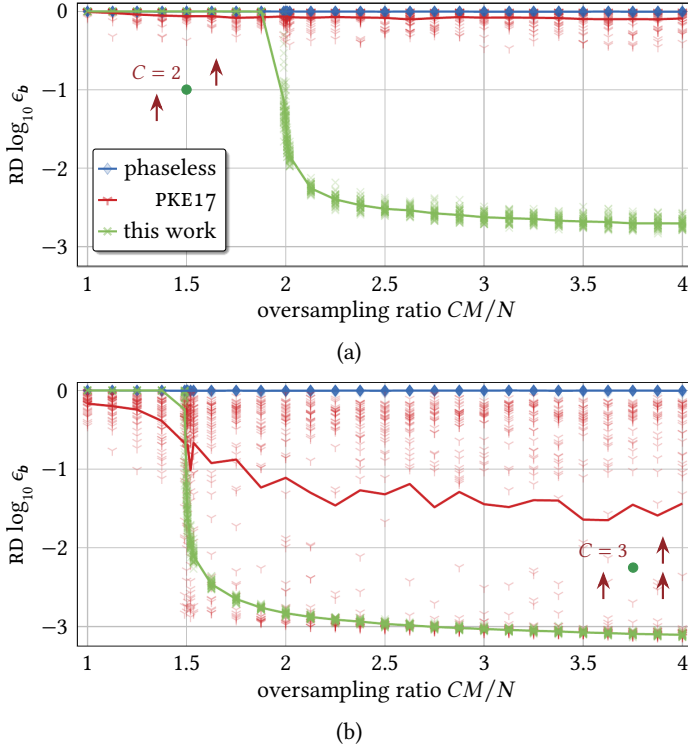


Fig. 5.44: Analysis for the RD of the inverse problem solved for a synthetic NF measurement setup, including the non-linear solver PKE17 by Paulus et al. [2017b]. (a) Using the two diagonal elements of the L-shaped probe array, $C = 2$. (b) Using the full L-shaped probe array, $C = 3$. © 2021 IEEE [Kornprobst et al. 2021d].

we pick the measurement samples of the two diagonal probe elements only.

The obtainable RDs for the two phase retrieval formulations from literature (non-convex minimization for phaseless data and PKE17) as well as the proposed linear algorithm are shown in Fig. 5.44. For every ratio of CM/N , 50 random orientations of the AUT were simulated, resulting in different measurement vectors. All results were obtained for an SNR of 10^3 . The magnitude-only approach fails completely to retrieve any solution close to the global solution. This problem persists if multiple measurement distances are considered, which is one of the most famous approaches to the phase retrieval problem [Gerchberg and Saxton 1972; Isernia et al. 1996; Yaccarino and Rahmat-Samii 1999; Schmidt and Rahmat-Samii 2009; Varela et al. 2019; Fuchs et al. 2020]. The non-convex optimization from PKE17

also mostly fails to retrieve a good solution and there is certainly no guarantee for overcoming the problem of local minima. Looking at the proposed linear phase retrieval algorithm, we observe a sharp transition from complete failure at about $CM/N = 2$ for $C = 2$ and $CM/N = 1.5$ for $C = 3$. This matches the condition given in (5.66). Notably, the non-linear solver from PKE17 achieves better results below this threshold, where the linear approach is doomed to fail—albeit with an unacceptable convergence rate.

Looking at the behavior of the linear phase retrieval algorithm above the success threshold, we further observe that the approach with the L-shaped probe and $C =$ gives a systematically lower RD. The root cause is found in the behavior of electromagnetic fields. Observations have to be made on a two-dimensional surface a which is closed around the AUT in the ideal case. In terms of an orthogonal expansion, there are always two independent directions on a two-dimensional surface. Connections between the observed fields have to be made accordingly in at least two independent directions, just as it was implemented with the L-shaped probe array. However, there is one more aspect to consider. Radiated electromagnetic fields may exhibit two independent polarizations. Both need to be captured and coherently linked for each (or at least most) set of measurement samples. Without infinite measurement accuracy or without matching polarizations between probe and AUT as done in Fig. 5.43, Paulus et al. [2022a] and Kornprobst et al. [2022] have advised to use at least four probe antennas with individually differing polarizations. Working with fewer antennas (say three) is only reasonable if they are dual-polarized and the polarization may be switched from sample to sample. None of these two requirements have been met in practical multi-probe measurement setups so far [Costanzo et al. 2001; Costanzo and Di Massa 2001; Costanzo et al. 2005; Costanzo and Di Massa 2008; Paulus et al. 2017a, 2017b; Tena-Sánchez et al. 2020; Tena-Sánchez et al. 2021b; Rodríguez Varela et al. 2021b; Tena-Sánchez et al. 2021a] but they are certainly feasible in future work.

With the presented linearized phase retrieval algorithm, accurate and reliable phase reconstruction for partially coherent observations is possible. There are two major advantages over any other state-of-the-art phase retrieval algorithms for NF antenna measurements. The solution process for a linear system of equations is reliable as opposed to previous non-convex algorithms and tedious optimization procedures. Additionally, the solution quality and the success of the algorithm can be judged by looking into the null space of the linear system of equations—a great benefit over non-linear optimization methods, where noise may conceal local minima as false solutions which prevents a judgment of the solution quality. Under ideal, noise-free conditions, the required sampling density of the proposed

algorithm is less than two times the number of unknowns.¹⁷ Noise and other observation errors increase this value slightly. This seems acceptable given the benefits of the method.

¹⁷ The number of required measurement locations M remains the same or even decreases, but C partially coherent measurements are necessary at each location. The total number MC of necessary measurements is, under ideal conditions, in the range of $N < MC < 2N$.

Contributions & Conclusion

“I don’t think it was for reading. It was for having written.”

— Terry Pratchett, *A Collegiate Casting-Out of Devilish Devices*

SURFACE SOURCE REPRESENTATIONS have been employed in this thesis for handling electromagnetic scattering, radiation, and source reconstruction problems. The analyzed aspects include the achievable accuracy, the well-posedness (at least partially by avoiding false solutions & enforcing uniqueness), the well-conditioning, as well as the computational effort.

The theoretical foundations for these topics are closely related. In Chapter 2, the continuous description of the involved IEs has been derived based upon the time-harmonic Maxwell’s equations. Chapter 3 gave an overview over the MOM and the classical RWG discretizations of the EFIE, the MFIE, and the CFIE.

Simulation of PEC Scattering and Radiation Scenarios

Boundary IEs for PEC bodies were the core theme of Chapter 4. The tackled challenge was in particular the classical MFIE discretized with div-conforming functions which shows severe inaccuracies both at LFs and HF. The first part was focused on the LO/RWG case, for which two RWG-based discretization strategies have been presented. The proposed WF discretization scheme for the identity operator inside the WF-MFIE improves the accuracy for HF scattering and radiation problems significantly and may also be employed inside the interior-resonance free and well-posed WF-CFIE, while the conditioning is almost not compromised as compared to the standard RWG CFIE. The proposed CSIE, based on a pure RWG discretization and a WF implementation of the CS condition, achieves an even better accuracy, which reaches EFIE levels for smooth objects and comes close to it when the geometry exhibits sharp edges. It is also able to avoid the problem of interior resonances. While the conditioning is worse than for the classical RWG CFIE, the CSIE and the better-conditioned WF-CFIE are mostly on par once a CF/CS weighting targeting a pre-defined accuracy is considered. Conformal mixed discretization schemes have also been considered as comparison algorithms. The CFIE with a mixed discretization—using an MFIE with RWG basis and BC testing functions—shows an accuracy comparable to that of the RWG CSIE. While the conditioning is good

(almost as good as for the classical CFIE), the extra computational effort of working with the barycentric refinement of the mesh reduces this advantageous property so far that the time to solution may as well be longer. The observations for a mixed-discretization CSIE with RWG functions for the electric currents and BC functions for the magnetic currents are fairly similar to the ones for the mixed-discretization CFIE. Overall, the proposed RWG-only discretization schemes offer decent accuracy improvements at a reasonable conditioning whenever the barycentric refinement of the mesh is undesirable and the radiation or scattering scenario is posed as an HF problem. The RWG CSIE works better for challenging geometries, while the WF-CFIE exhibits the advantage of working with Love currents.

Furthermore, the discretization schemes for the CSIE and the WF-CFIE have been extended for the use with hierarchical HO functions. It was demonstrated that the inaccuracy of the MFIE discretized with div-conforming functions in a Galerkin approach persists for HO functions and that extra measures need to be taken. However, the impact of the RWG anisotropy is lower once HO functions are considered and the positive impact of the WF schemes on the accuracy is, hence, reduced—and more sensitive to parameter choices inside the WF-CFIE. Both the HO CSIE and the HO WF-CFIE have been demonstrated to be interior-resonance free and to work well for electrically larger scattering scenarios.

Source Reconstruction for Antenna Measurements

The embrative topic of Chapter 5 was surface-source reconstruction for (NF) antenna measurements and subsequent NFFFTs, where three distinct problems have been discussed.

First, the linear inverse equivalent surface-source problem arising from complex time-harmonic field observations has been analyzed in detail. In general, this problem is ill-posed. Different approaches to the necessary regularization and their impact on accuracy and conditioning have been investigated. This concerns, on a superordinate level, the choice of the NEE over the NRE, and on a more detailed level, the choice of a possibly unique and well-conditioned equivalent source representation. The NEE combined with unconstrained JM or unique and computationally cheap CS currents is found to be the most universal approach. Other approaches have the disadvantages of an unclear stopping criterion, worse conditioning, or increased computational effort. The achievable accuracy of all surface-source representations is similar since it is dominated by the measurement configuration and observation errors. However, one critical choice concerns the reconstruction surface. Enlarging the Huygens surface compared to a close to convex hull is detrimental to accuracy. This happens inherently with a SH expansion, which is hence less accurate than surface-source based approaches.

While the impact of the choice of the source representation and the choice of

the basis and testing functions were important for the IEs considered in the first part, such an effect is not observed when the source and observation surfaces are separated, as it is the case for antenna measurements. It remains important though to employ both radiation operators (e.g., of the electric field of both electric and magnetic currents) in order to achieve the best possible conditioning of the inverse problem.

Second, echo suppression is of concern whenever the measurement environment is not fully under control or when external circumstances dictate an echoic environment. Echo source localization was demonstrated to work much better than simple spatial filtering, and incorporating additional knowledge about the behavior of echo objects helps to reduce the required number of measurements and to increase accuracy since the DOFs which have to be measured are reduced. Even with source localization, multiple interactions between the AUT and scatterers in close vicinity cause a changed current distribution on the AUT, so-called mutual coupling. It was proposed to solve this problem with broadband time-harmonic measurements and software time-gating of the reconstructed equivalent currents. Hence, the accuracy of the equivalent-current echo suppression methods is further increased.

Third, phase retrieval is a particularly challenging task where only magnitudes of the AUT field are observable. The state of the art approach to this inverse problem with non-convex minimization is unreliable. Even with additional information from multiple surfaces and an proposed approach incorporating relative phase information from multiple frequencies, local minima may prevent retrieving the true solution to the phase retrieval problem. Moreover, local minima become false solutions in the presence of observation errors: They are not identifiable when working with magnitude-only data. Overall, non-linear phase retrieval with local minimization does not and cannot work reliably for NF antenna measurements in the current non-linear formulation. In order to solve this problem, a linearized phase retrieval algorithm was presented, which augments the magnitude-only data with partially coherent observations, i.e., multi-frequency data, multi-antenna probes, or holographic measurement systems. This approach leverages a projection into the space of physically possible solutions, which offers a promising way forward for phaseless source reconstruction techniques. All involved operations are inherently linear and are thus able to circumvent at least some or even all of the problems associated with classical phase retrieval. Thus, reliable phase retrieval becomes possible. It remains to be seen whether such an approach can be transferred to magnitude-only measurements without relative phase information.

Glossary

Notation

- A** A matrix in $\mathbb{C}^{(\cdot) \times (\cdot)}$; bold, italic and sans-serif
- e* A mathematical constant, roman and serif
- $h(x)$ A scalar function with a scalar argument, font-style and -weight accordingly
- L*** A dyadic operator in \mathbb{C}^3 ; bold, italic and serif
- x* A scalar quantity, italic and serif
- x*** A “physical” vector in \mathbb{C}^3 ; bold, italic and serif
- $\|\mathbf{x}\|$ The magnitude (ℓ^2 -norm) of a “physical” or “linear algebra” vector
- x*** A “linear algebra” “column” vector in $\mathbb{C}^{(\cdot)}$; bold, italic and sans-serif
- $[\mathbf{x}]_{(\cdot)}$ (\cdot) th entry or component of the vector \mathbf{x} or of a matrix
- $|\mathbf{x}|$ Element-wise absolute value operator, here applied to a “linear algebra” vector

Physical Quantities and Mathematical Symbols

- a* Observation surface; may coincide with *s*
- a*** Magnetic vector potential, $[\mathbf{a}] = \text{V}$
- ã*** Dual curl-conforming rotated BC functions
- α*** Curl-conforming basis functions, rotated versions of RWG or HO functions
- A** Forward operator of an inverse (surface) source problem
- \mathbf{A}^{-1}** Inverse of a matrix
- \mathbf{A}^+** Generalized inverse or Moore-Penrose pseudoinverse of a matrix
- β̃*** Dual div-conforming BC functions
- β*** Div-conforming basis functions, RWG or HO
- b*** Generic right-hand side vector
- b*** Magnetic flux density, $[\mathbf{b}] = \text{V s m}^{-2}$
- $C(\vartheta, \varphi)$ Antenna radiation pattern
- c* Speed of light in a medium, $[c] = \text{m s}^{-1}$

PHYSICAL QUANTITIES AND MATHEMATICAL SYMBOLS

- c_0 Speed of light in free space
- χ Weighting factor for the CFIE and CSIE with $0 \leq \chi \leq 1$
- curl** \mathbf{x} Curl of a vector \mathbf{x} ; also $\nabla \times \mathbf{x}$
- $D(\vartheta, \varphi)$ Directivity of an antenna
- $\delta(\cdot)$ Dirac delta distribution with $[\delta(\cdot)] = [\cdot]^{-1}$
- $\text{div } \mathbf{x}$ Divergence of a vector \mathbf{x} ; also $\nabla \cdot \mathbf{x}$
- \mathbf{d} Electric displacement field, $[\mathbf{d}] = \text{A s m}^{-2}$
- \mathbf{e}_w Tested electric field vector
- e Euler's number
- ϵ Relative error; maximum, average, or norm of ϵ
- ϵ Relative error of a vector quantity
- ϵ_{OE} Relative (norm of) observation error
- ϵ_{RD} Relative NF RD of a source reconstruction
- ϵ Permittivity, $[\epsilon] = \text{A s V}^{-1} \text{m}^{-1}$
- η Wave impedance of a homogeneous medium, $[\eta] = \Omega$
- η_s Normalized surface wave impedance
- \mathbf{e} Electric field, $[\mathbf{e}] = \text{V m}^{-1}$
- \mathbf{e}^s Scattered or radiated electric field (equivalent sources on s)
- \mathbf{e}^v Incident electric field (sources in v)
- f Frequency variable, $[f] = \text{s}^{-1}$
- f Electric vector potential, $[f] = \text{V}$
- $G(\vartheta, \varphi)$ Antenna gain
- $g(\mathbf{r}, \mathbf{r}')$ Scalar Green's function
- γ Weighting factor of WF identity scheme
- $\mathbf{G}_{w,v}$ (Gram) matrix for \mathcal{I} operator discretized with basis \mathbf{v}_m and trial functions \mathbf{w}_m
- grad** g Gradient of a scalar function g ; also ∇g
- h The average edge length of a mesh
- $H^{-1/2}(\text{curl}_s, s)$ Curl-conforming Sobolev space on s
- $H^{-1/2}(\text{div}_s, s)$ Div-conforming Sobolev space on s
- \mathbf{h}_w Tested magnetic field vector
- \mathbf{h} Magnetic field, $[\mathbf{h}] = \text{V m}^{-1}$
- \mathbf{h}^s Scattered or radiated magnetic field (equivalent sources on s)
- \mathbf{h}^v Incident magnetic field (sources in v)

- i Electric current unknowns vector
 $\text{Im}\{z\}$ Imaginary part of a complex quantity
 \mathbf{I} Identity operator
 j Imaginary unit with $j^2 = -1$
 j Electric surface current density, $[\mathbf{j}] = \text{V m}^{-1}$
 j_v Electric volume current density, $[\mathbf{j}] = \text{V m}^{-2}$
 k Wavenumber $\|\mathbf{k}\|$, $[k] = \text{m}^{-1}$
 κ_e Electrical conductivity, $[\kappa_e] = \text{A V}^{-1} \text{m}^{-1}$
 κ_m Magnetic conductivity, $[\kappa_m] = \text{V A}^{-1} \text{m}^{-1}$
 $\mathbf{K}_{w,v}$ Matrix for \mathcal{K} operator discretized with basis \mathbf{v}_m and trial functions \mathbf{w}_m
 \mathcal{K} Magnetic field integral operator for electric currents
 \mathbf{k} Wavevector
 λ Wavelength $c/f = 2\pi/k$
 λ_i Barycentric coordinates on a triangle, $\lambda_1 + \lambda_2 + \lambda_3 = 1$
 \mathbf{L} Love current SC or CP matrix
 M Number of observations
 m Running index for observations
 μ Permeability, $[\mu] = \text{V s A}^{-1} \text{m}^{-1}$
 \mathbf{m} Magnetic surface current density, $[\mathbf{m}] = \text{V m}^{-1}$
 \mathbf{m}_v Magnetic volume current density, $[\mathbf{m}] = \text{V m}^{-2}$
 N Number of RWG/basis functions
 n Running index for unknowns
 ∇ Nabla-operator, containing component-wise derivatives
 N_{DOF} Number of DOFs
 N_{it} Number of iterative solver iterations to convergence
 v Weighting factor of WF identity scheme associated with edges in the geometry
 N_{un} Number of unknowns
 \mathbf{n} Outward unit normal vector on a surface
 ω Angular frequency $2\pi f$
 p Polynomial order of basis functions
 φ The azimuthal angle in a spherical coordinate system
 ϕ Electric scalar potential
 $\mathbf{P}_{(\cdot)}$ Matrix for the projection into the range indicated by the subscript

PHYSICAL QUANTITIES AND MATHEMATICAL SYMBOLS

- \mathbf{p} Electric field polarization of a plane wave
- r The radial distance in a spherical coordinate system, $[r] = \text{m}$
- \mathbf{r}' Source coordinate vector
- $\text{Re}\{z\}$ Real part of a complex quantity
- \mathbf{r} Iterative solver residual vector
- ρ_e Electric surface charge density, $[\rho_e] = \text{A s m}^{-2}$
- $\rho_{e,v}$ Electric volume charge density, $[\rho_{e,v}] = \text{A s m}^{-3}$
- ρ_m Magnetic surface charge density, $[\rho_m] = \text{V s m}^{-2}$
- $\rho_{m,v}$ Magnetic volume charge density, $[\rho_{m,v}] = \text{V s m}^{-3}$
- r_{th} Iterative solver stopping threshold
- \mathbf{r} Position in three-dimensional space; mostly employed for the observation coordinate
- s Source or Huygens surface, $s = \partial v_i$
- $\sigma(\vartheta, \varphi)$ Bi-static radar cross section, $[\sigma] = \text{m}^2$
- ζ_i The i th SV of an SVD
- \mathbf{s} Poynting vector, $[\mathbf{s}] = \text{V A m}^{-2}$
- t Time variable (time convention $e^{j\omega t}$), $[t] = \text{s}$
- ϑ The polar angle in a spherical coordinate system
- $\mathbf{T}_{\mathbf{w},\mathbf{v}}$ Matrix for \mathcal{T} operator discretized with basis \mathbf{v}_m and trial functions \mathbf{w}_m
- \mathcal{T} Electric field integral operator for electric currents
- v Weighting factor to shift the Tikhonov SC scaling ξ above the OE
- $\mathbf{u}_{(\cdot)}$ Unit normal vector in the direction of the subscript
- v Exterior volume
- v_i Source region
- \mathbf{v} Magnetic current unknowns vector
- \mathbf{v} Generic basis function
- \mathbf{w} Generic trial function
- ξ Weighting factor of Tikhonov regularization term
- \mathbf{x} Generic unknowns vector
- ζ Antenna efficiency, radiation or total
- z^* Complex conjugate of a complex quantity

Abbreviations

ACA	Adaptive cross-approximation 173
AI	Aproximate inverse 58–60
AUT	Antenna under test 26, 27, 131–135, 138, 142, 146, 147, 150, 151, 155, 156, 158, 160, 162, 165–168, 170, 171, 173–192, 198, 199, 201–203, 207
BC	Buffa-Christiansen 44, 47–54, 62, 64, 66, 68, 70–75, 77–79, 81, 82, 89, 99–101, 105–108, 111, 114, 124, 129, 140, 205, 206, 209
BEAST	Boundary element analysis and simulation toolkit 47, 53, 100, 107, 108
BEM	Boundary element method 14, 191
BIM	Boundary integral method 14
CEM	Computational electromagnetics 2, 7
CF	Combined field 22, 50, 88, 90, 95, 100, 105, 106, 126, 144, 205
CFIE	Combined field integral equation 22–24, 31, 44, 45, 47–50, 56, 89–91, 93, 94, 96, 97, 100–103, 105–111, 126–129, 142, 144, 149, 177, 179, 205, 206, 210
CG	Conjugate gradient method 58–60, 74, 88, 91, 93, 136
CP	Calderón projector 140–142, 144, 145, 147, 149, 151–153, 155, 158, 159, 163, 166, 168–170, 172–174, 211
CS	Combined source 12, 13, 23–25, 28, 50–56, 58, 60, 61, 69, 90, 95, 100, 105, 106, 112, 126, 139, 150, 152, 153, 155, 158, 159, 163, 165, 173, 174, 187, 205, 206
CSIE	Combined source integral equation 22–25, 47, 49, 50, 52, 53, 55–58, 61, 62, 69, 73–75, 77, 79, 81–84, 89–91, 93–97, 100, 101, 103, 105–114, 124, 126–129, 205, 206, 210
DOF	Degree of freedom 26–28, 46, 129, 134, 135, 174, 175, 179, 182, 183, 191, 192, 207, 211
DSH	Distributed spherical harmonics 135, 149, 150, 152, 155, 160, 162, 163, 165–167
EFIE	Electric field integral equation 18, 19, 21–25, 31, 32, 34, 35, 37, 39–44, 46–51, 53, 55, 56, 58, 61, 65, 70–75, 77, 79–82, 84–91, 94, 95, 97–101, 103, 105–108, 110–112, 114, 115, 119, 124, 126–129, 142, 144, 146, 148, 149, 155, 172, 205
FE-BI	Finite-element boundary-integral 17, 111, 129
FEM	Finite element method 2, 31, 34, 39
FF	Far field 15, 17, 26, 44, 52, 65–67, 70–74, 76–86, 88, 97–99, 102–105, 108, 109, 114, 121, 123, 125, 127, 129, 151, 155–158, 160, 162, 163, 165–167, 170, 178, 179, 183–189, 192, 193, 199
FIAFTA	Fast irregular antenna field transformation algorithm 133, 147, 159, 168, 191
GMRES	Generalized minimum residual method 56, 74, 75, 79, 83, 86, 89–91, 94, 96–100, 102–105, 107, 110, 124, 126, 136, 156, 166, 173, 179
HF	High-frequency 41, 44–48, 61, 69, 82, 85, 97, 106, 111, 112, 124, 170, 190, 205, 206
HO	Higher-order 39, 40, 46, 49, 50, 53, 71, 79, 81, 91, 98, 99, 102, 105, 106, 111–124, 126–129, 182, 206, 209
IBC	Impedance boundary condition 10, 13, 23, 47, 50, 52, 54, 112
IE	Integral equation 3, 14, 17, 18, 20, 24, 31, 48, 49, 52, 58, 61, 75, 79, 84, 85, 89–97, 101, 103, 105–108, 110, 124, 126–128, 177, 205, 207

ABBREVIATIONS

LF	Low-frequency 40, 44, 45, 47, 48, 69, 73, 82–85, 111, 205
LO	Low-order 39, 49, 88, 112, 113, 119, 129, 142, 205
MFIE	Magnetic field integral equation 3, 19–22, 24, 31, 34, 41–53, 55, 56, 61, 62, 64, 69–75, 77–79, 81–91, 93–95, 99–101, 103, 105–108, 110–120, 122, 124, 126, 129, 138, 140, 142, 144, 149, 155, 179, 205, 206
MLFMM	Multi-level fast multipole method 2, 3, 89–91, 94, 96, 97, 103, 105, 109, 135, 147, 150, 151, 173, 191
MOM	Method of moments 3, 14, 31–33, 37, 97, 131, 176, 179–185, 205
MVP	Matrix-vector product 3, 59, 60, 75, 91, 93, 94, 96, 101, 103, 108, 112, 161, 172, 177, 191, 198
NE	Normal system of equations 136, 137, 152, 155, 160, 173
NEE	Normal-error system of equations 137, 141, 143, 144, 150–153, 155, 158, 160–167, 172, 173, 206
NF	Near field 15, 17, 24–26, 52, 66–68, 73, 79–81, 85–87, 91, 114, 132, 134, 136, 137, 147, 155, 156, 158, 160–168, 170–176, 179–182, 186, 189, 191–195, 201–203, 206, 207
NFFFT	Near-field far-field transformation 26, 131, 134, 137, 138, 142, 155, 172, 175, 176, 183, 190, 192, 206
NRE	Normal-residual system of equations 136, 137, 141, 143, 144, 148, 150–154, 158, 160–167, 173, 178, 179, 206
OE	Observation error 133–135, 137, 147, 151, 155–157, 160, 163, 193, 212
OEWG	Open-ended waveguide 144, 148, 150, 156, 172
PEC	Perfect electric conductor 3, 9, 10, 13, 17–22, 24, 43, 47–52, 56, 57, 70, 73, 75, 79, 82, 83, 89, 91–99, 102, 104, 105, 107, 110, 114, 119, 127–129, 131, 138, 139, 142, 175–180, 187, 205
PMC	Perfect magnetic conductor 20–22
RCS	Radar cross-section 16, 17, 70–72, 74, 75, 77, 79, 82, 83, 86, 88, 90–99, 102, 104, 110, 114, 128, 129
RD	Reconstruction deviation 134–137, 147, 151, 158, 160–164, 166, 167, 172, 179, 193–195, 199–203
RFOF	Radio-frequency over fiber 168, 170
RWG	Rao-Wilton-Glisson 24, 37–40, 42–56, 58–73, 76–82, 84–86, 88–91, 94, 96–100, 103, 105–122, 124, 126–129, 132, 133, 135, 139, 140, 142, 144, 150, 162, 172, 176, 177, 187, 189, 205, 206, 209
SC	Side constraint 54–56, 58, 112, 142–149, 151, 153–159, 163, 166, 167, 172, 174, 176–185, 197, 199, 211, 212
SDR	Software-defined radio 170
SH	Spherical harmonics 135, 149–152, 155, 165, 174, 206
SIE	Surface integral equation 14, 17, 18, 33, 34, 37, 43, 54, 64, 71–75, 77–79, 82, 83, 97–99, 102, 104, 107, 111, 176
SNR	Signal-to-noise ratio 147, 155, 156, 199–202
SV	Singular value 56, 57, 100, 143–149, 212
SVD	Singular value decomposition 136, 137, 143, 144, 147, 199, 212
UAV	Unmanned aerial vehicle 168, 170, 172

ABBREVIATIONS

WF Weak-form 49, 50, 52, 54-56, 61, 62, 64, 66-79, 81-91, 93, 94, 96-101, 103, 105-122, 124, 126-129, 139-141, 149, 151, 152, 155, 158, 159, 163, 187, 205, 206, 210, 211

Bibliography

- Adams, R. J. 2004. "Physical and analytical properties of a stabilized electric field integral equation." *IEEE Trans. Antennas Propag.* 52, no. 2 (February): 362–372. <https://doi.org/10.1109/tap.2004.823957>. Cited on p. 41.
- Adana, F. S. de, O. Gutiérrez, I. González, M. F. Cátedra, and L. Lozano. 2011. *Practical Applications of Asymptotic Techniques in Electromagnetics*. Norwood, MA, US: Artech House. Cited on p. 2.
- Adrian, S. B. 2018. "Rapidly Converging Boundary Integral Equation Solvers in Computational Electromagnetics." Doctoral diss., Munich, DE: Tech. Univ. Munich. <https://mediatum.ub.tum.de/?id=1388176>. Cited on pp. 37, 48.
- Adrian, S. B., F. P. Andriulli, and T. F. Eibert. 2014. "Hierarchical bases preconditioners for the electric field integral equation on multiply connected geometries." *IEEE Trans. Antennas Propag.* 62 (11): 5856–5861. <https://doi.org/10.1109/tap.2014.2347392>. Cited on p. 41.
- . 2016. "On the hierarchical preconditioning of the combined field integral equation." *IEEE Antennas Wireless Propag. Lett.* 15:1897–1900. <https://doi.org/10.1109/lawp.2016.2542828>. Cited on p. 48.
- . 2017. "A hierarchical preconditioner for the electric field integral equation on unstructured meshes based on primal and dual haar bases." *J. Comput. Phys.* 330 (February): 365–379. <https://doi.org/10.1016/j.jcp.2016.11.013>. Cited on p. 41.
- . 2019. "On a refinement-free Calderón multiplicative preconditioner for the electric field integral equation." *J. Comput. Phys.* 376 (January): 1232–1252. <https://doi.org/10.1016/j.jcp.2018.10.009>. Cited on p. 41.
- Adrian, S. B., A. Dely, D. Consoli, A. Merlini, and F. P. Andriulli. 2021. "Electromagnetic integral equations: insights in conditioning and preconditioning." *IEEE Open J. Antennas Propag.* 2:1143–1174. <https://doi.org/10.1109/ojap.2021.3121097>. Cited on p. 48.
- Alaydrus, M., V. Hansen, and T. F. Eibert. 2002. "Hybrid²: Combining the three-dimensional hybrid finite element-boundary integral technique for planar multilayered media with the uniform geometrical theory of diffraction." *IEEE Trans. Antennas Propag.* 50, no. 1 (January): 67–74. <https://doi.org/10.1109/8.992563>. Cited on p. 17.
- Altair. 2021. "Altair Feko." <https://www.feko.info>. Cited on pp. 155, 178.
- Alvarez, Y., F. Las-Heras, and M. R. Pino. 2007. "Reconstruction of equivalent currents distribution over arbitrary three-dimensional surfaces based on integral equation algorithms." *IEEE Trans. Antennas Propag.* 55, no. 12 (December): 3460–3468. <https://doi.org/10.1109/tap.2007.910316>. Cited on pp. 26, 27.
- Alvarez, Y., F. Las-Heras, M. R. Pino, and J. A. López. 2008. "Acceleration of the sources reconstruction method via the fast multipole method." In *Proc. IEEE Antennas Propag. Soc. Int. Symp. (APS)*. San Diego, CA, US, July. <https://doi.org/10.1109/aps.2008.4619598>. Cited on p. 28.

BIBLIOGRAPHY

- Andreasen, M. 1964. "Scattering from parallel metallic cylinders with arbitrary cross sections." *IEEE Trans. Antennas Propag.* 12, no. 6 (June): 746–754. <https://doi.org/10.1109/tap.1964.1138303>. Cited on p. 19.
- Andreasen, M., and K. Mei. 1964. "Comments on 'scattering by conducting rectangular cylinders.'" *IEEE Trans. Antennas Propag.* 12, no. 2 (March): 235–236. <https://doi.org/10.1109/tap.1964.1138184>. Cited on p. 19.
- Andriulli, F. P. 2012. "Loop-star and loop-tree decompositions: analysis and efficient algorithms." *IEEE Trans. Antennas Propag.* 60, no. 5 (May): 2347–2356. <https://doi.org/10.1109/tap.2012.2189723>. Cited on p. 41.
- Andriulli, F. P., K. Cools, H. Bagci, F. Olyslager, A. Buffa, S. Christiansen, and E. Michielssen. 2008. "A multiplicative Calderón preconditioner for the electric field integral equation." *IEEE Trans. Antennas Propag.* 56, no. 8 (August): 2398–2412. <https://doi.org/10.1109/tap.2008.926788>. Cited on pp. 41, 47.
- Andriulli, F. P., K. Cools, I. Bogaert, and E. Michielssen. 2013. "On a well-conditioned electric field integral operator for multiply connected geometries." *IEEE Trans. Antennas Propag.* 61, no. 4 (April): 2077–2087. <https://doi.org/10.1109/tap.2012.2234072>. Cited on p. 41.
- Andriulli, F. P., A. Tabacco, and G. Vecchi. 2010. "Solving the EFIE at low frequencies with a conditioning that grows only logarithmically with the number of unknowns." *IEEE Trans. Antennas Propag.* 58, no. 5 (May): 1614–1624. <https://doi.org/10.1109/tap.2010.2044325>. Cited on p. 41.
- Andriulli, F. P., and G. Vecchi. 2012. "A Helmholtz-stable fast solution of the electric field integral equation." *IEEE Trans. Antennas Propag.* 60, no. 5 (May): 2357–2366. <https://doi.org/10.1109/tap.2012.2189693>. Cited on p. 41.
- Araque Quijano, J. L., L. Scialacqua, J. Zackrisson, L. J. Foged, M. Sabbadini, and G. Vecchi. 2011. "Suppression of undesired radiated fields based on equivalent currents reconstruction from measured data." *IEEE Antennas Wireless Propag. Lett.* 10:314–317. <https://doi.org/10.1109/lawp.2011.2135831>. Cited on pp. 174, 179.
- Araque Quijano, J. L., and G. Vecchi. 2009. "Improved-accuracy source reconstruction on arbitrary 3-D surfaces." *IEEE Antennas Wireless Propag. Lett.* 8:1046–1049. <https://doi.org/10.1109/lawp.2009.2031988>. Cited on pp. 27, 138.
- . 2010a. "Field and source equivalence in source reconstruction on 3D surfaces." *Prog. Electromagn. Res.* 103:67–100. <https://doi.org/10.2528/pier10030309>. Cited on pp. 26, 27, 138.
- . 2010b. "Near- and very near-field accuracy in 3-D source reconstruction." *IEEE Antennas Wireless Propag. Lett.* 9:634–637. <https://doi.org/10.1109/lawp.2010.2055032>. Cited on pp. 27, 138.
- Araque Quijano, J. L., G. Vecchi, L. Li, M. Sabbadini, L. Scialacqua, B. Bencivenga, F. Mioc, L. J. Foged, and P. O. Iversen. 2010. "3D spatial filtering applications in spherical near field antenna measurements." In *Proc. Annu. Meeting Symp. Antenna Meas. Techn. Assoc. (AMTA)*. Atlanta, GA, US, October. Cited on pp. 160, 175, 179.
- Arboleya, A., J. Laviada, J. Ala-Laurinaho, Y. Alvarez, F. Las-Heras, and A. V. Räsänen. 2015. "Phaseless characterization of broadband antennas." *IEEE Trans. Antennas Propag.* 64, no. 2 (February): 484–495. <https://doi.org/10.1109/tap.2015.2511789>. Cited on p. 195.
- Arboleya, A., J. Laviada, and F. Las-Heras. 2018. "Scalar calibration for broadband phaseless antenna measurements based on indirect off-axis holography." *IEEE Trans. Antennas Propag.*, no. 6 (June): 3241–3246. ISSN: 0018-926X. <https://doi.org/10.1109/tap.2018.2819881>. Cited on p. 195.

- Ayyalasomayajula, R., A. Arun, C. Wu, S. Sharma, A. R. Sethi, D. Vasisht, and D. Bharadia. 2020. "Deep learning based wireless localization for indoor navigation." In *Proc. 26th Ann. Int. Conf. Mobile Comput. Netw. (MobiCom)*. London, UK, April. <https://doi.org/10.1145/3372224.3380894>. Cited on p. 1.
- Bacca, J., S. Pinilla, and H. Arguello. 2020. "Super-resolution phase retrieval from designed coded diffraction patterns." *IEEE Trans. Image Process.* 29:2598–2609. <https://doi.org/10.1109/tip.2019.2949436>. Cited on p. 190.
- Baechler, G., M. Krekovic, J. Ranieri, A. Chebira, Y. M. Lu, and M. Vetterli. 2019. "Super resolution phase retrieval for sparse signals." *IEEE Trans. Signal Process.* 67, no. 18 (September): 4839–4854. ISSN: 1053-587X. <https://doi.org/10.1109/tsp.2019.2931169>. Cited on p. 190.
- Balanis, C. A. 2012. *Advanced Engineering Electromagnetics*. 2nd ed. Hoboken, NJ, US: Wiley. Cited on pp. 2, 6, 8, 10, 11.
- . 2016. *Antenna Theory: Analysis and Design*. 4th ed. Hoboken, NJ, US: Wiley. Cited on p. 15.
- Bangun, A., A. Behboodi, and R. Mathar. 2020. "Sensing matrix design and sparse recovery on the sphere and the rotation group." *IEEE Trans. Signal Process.* 68:1439–1454. <https://doi.org/10.1109/tsp.2020.2973545>. Cited on p. 28.
- Bangun, A., C. Culotta-López, A. Behboodi, R. Mathar, and D. Heberling. 2019. "On phaseless spherical near-field antenna measurements." In *Proc. 13th Eur. Conf. Antennas Propag. (EuCAP)*. Krakow, PL, April. <https://ieeexplore.ieee.org/document/8740316>. Cited on p. 197.
- Barmherzig, D. A., J. Sun, P.-N. Li, T. J. Lane, and E. J. Candès. 2019. "Holographic phase retrieval and reference design." *Inverse Problems* 35, no. 9 (August): 094001. <https://doi.org/10.1088/1361-6420/ab23d1>. Cited on p. 195.
- Beghein, Y., K. Cools, H. Bagci, and D. De Zutter. 2012. "A space-time mixed Galerkin marching-on-in-time scheme for the time-domain combined field integral equation." *IEEE Trans. Antennas Propag.* 61, no. 3 (March): 1228–1238. <https://doi.org/10.1109/tap.2012.2226553>. Cited on p. 48.
- Berlt, P., C. Bornkessel, and M. A. Hein. 2020. "Accurate 3D phase recovery of automotive antennas through LTE power measurements on a cylindrical surface." In *Proc. 14th Eur. Conf. Antennas Propag. (EuCAP)*. Copenhagen, DK, April. <https://doi.org/10.23919/eucap48036.2020.9135443>. Cited on p. 195.
- Betz, J. W. 2013. "Signal structures for satellite-based navigation: past, present, and future." In *Proc. ION 2013 Pacific PNT Meeting*, 131–137. Honolulu, HI, US, April. Cited on p. 1.
- Bilik, I., O. Bialer, S. Villeval, H. Sharifi, K. Kona, M. Pan, D. Persechini, M. Musni, and K. Geary. 2016. "Automotive mimo radar for urban environments." In *Proc. IEEE Radar Conf. (RadarConf)*. Philadelphia, PA, US: IEEE, May. <https://doi.org/10.1109/radar.2016.7485215>. Cited on p. 1.
- Bladel, J. G. van. 1991. *Singular Electromagnetic Fields and Sources*. Oxford, UK: Clarendon. Cited on p. 46.
- . 2007. *Electromagnetic Fields*. 2nd ed. Piscataway, NJ, US: IEEE Press. Cited on pp. 8, 34.
- Bogaert, I., F. P. Andriulli, and K. Cools. 2013. "Low-frequency stability of the razor blade tested MFIE." In *Proc. Int. Conf. Electromagn. Adv. Appl. (ICEAA)*, 620–623. Torino, IT, September. <https://doi.org/10.1109/iceaa.2013.6632317>. Cited on p. 44.

BIBLIOGRAPHY

- Bogaert, I., K. Cools, F. P. Andriulli, and H. Bağcı. 2014. "Low-frequency scaling of the standard and mixed magnetic field and Müller integral equations." *IEEE Trans. Antennas Propag.* 62, no. 2 (February): 822–831. <https://doi.org/10.1109/tap.2013.2293783>. Cited on pp. 44, 84.
- Bogaert, I., K. Cools, F. P. Andriulli, and D. De Zutter. 2011a. "Low frequency scaling of the mixed MFIE for scatterers with a non-simply connected surface." In *Proc. Int. Conf. Electromagn. Adv. Appl. (ICEAA)*, 951–954. Turin, IT, September. <https://doi.org/10.1109/iceaa.2011.6046467>. Cited on p. 45.
- Bogaert, I., K. Cools, F. P. Andriulli, J. Peeters, and D. De Zutter. 2011b. "Low frequency stability of the mixed discretization of the MFIE." In *Proc. 5th Eur. Conf. Antennas Propag. (EuCAP)*, 2463–2465. Rome, IT, April. <https://ieeexplore.ieee.org/document/5782047>. Cited on pp. 44, 84.
- Bogdanov, F. G., D. D. Karkashadze, and R. S. Zaridze. 1999. "The method of auxiliary sources in electromagnetic scattering problems." In *Generalized Multipole Techniques for Electromagnetic and Light Scattering*, edited by T. Wriedt, 143–172. Amsterdam, NL: Elsevier. Cited on p. 32.
- Bolomey, J.-C., and W. Tabbara. 1973. "Numerical aspects on coupling between complementary boundary value problems." *IEEE Trans. Antennas Propag.* 21, no. 3 (May): 356–363. <https://doi.org/10.1109/tap.1973.1140500>. Cited on pp. 12, 23.
- Bouche, D., F. Molinet, and R. Mittra. 1997. *Asymptotic Methods in Electromagnetics*. Berlin/Heidelberg, DE: Springer-Verlag. <https://doi.org/10.1007/978-3-642-60517-8>. Cited on p. 2.
- Brakhage, H., and P. Werner. 1965. "Über das Dirichletsche Außenraumproblem für die Helmholtzsche Schwingungsgleichung." *Archiv der Mathematik* 16 (1): 325–329. <https://doi.org/10.1007/bf01220037>. Cited on pp. 12, 23.
- Brown, W. J., and D. R. Wilton. 1999. "Singular basis functions and curvilinear triangles in the solution of the electric field integral equation." *IEEE Trans. Antennas Propag.* 47, no. 2 (February): 347–353. <https://doi.org/10.1109/8.761075>. Cited on p. 46.
- Bucci, O. M., F. D'Agostino, C. Gennarelli, G. Riccio, and C. Savarese. 2003. "Near-field-far-field transformation with spherical spiral scanning." *IEEE Antennas Wireless Propag. Lett.* 2:263–266. <https://doi.org/10.1109/lawp.2003.820710>. Cited on pp. 155, 176, 179.
- Bucci, O. M., and T. Isernia. 1997. "Electromagnetic inverse scattering: retrievable information and measurement strategies." *Radio Science* 32 (6): 2123–2137. <https://doi.org/10.1029/97rs01826>. Cited on p. 28.
- Bucci, O. M., and C. Gennarelli. 1988. "Use of sampling expansions in near-field-far-field transformation: The cylindrical case." *IEEE Trans. Antennas Propag.* 36, no. 6 (June): 830–835. <https://doi.org/10.1109/8.1185>. Cited on p. 28.
- Bucci, O. M., C. Gennarelli, and C. Savarese. 1991. "Fast and accurate near-field-far-field transformation by sampling interpolation of plane-polar measurements." *IEEE Trans. Antennas Propag.* 39, no. 1 (January): 48–55. <https://doi.org/10.1109/8.64434>. Cited on p. 28.
- Bucci, O. M., M. D. Migliore, G. Panariello, and D. Pinchera. 2013. "Plane-wave generators: design guidelines, achievable performances and effective synthesis." *IEEE Trans. Antennas Propag.* 61, no. 4 (April): 2005–2018. <https://doi.org/10.1109/tap.2012.2233453>. Cited on p. 28.
- Buffa, A., and S. Christiansen. 2007. "A dual finite element complex on the barycentric refinement." *Math. Comput.* 76, no. 260 (October): 1743–1769. <https://doi.org/10.1090/s0025-5718-07-01965-5>. Cited on pp. 37, 44, 47.

- Buffa, A., and R. Hiptmair. 2005. "Regularized combined field integral equations." *Numerische Mathematik* 100 (1): 1–19. <https://doi.org/10.1007/s00211-004-0579-9>. Cited on p. 12.
- Calderón, A.-P. 1963. "Boundary value problems for elliptic equations." In *Proc. Soviet-American Conf. Partial Differential Equations*, 303–304. Novosibirsk, RU. Cited on p. 140.
- Calvetti, D., B. Lewis, and L. Reichel. 2002. "On the regularizing properties of the GMRES method." *Numerische Mathematik* 91, no. 4 (June): 605–625. <https://doi.org/10.1007/s002110100339>. Cited on p. 136.
- Candès, E. J., Y. C. Eldar, T. Strohmer, and V. Voroninski. 2015a. "Phase retrieval via matrix completion." *SIAM Rev.* 57 (2): 225–251. <https://doi.org/10.1137/151005099>. Cited on p. 190.
- Candès, E. J., X. Li, and M. Soltanolkotabi. 2015b. "Phase retrieval from coded diffraction patterns." *Appl. Comput. Harmonic Anal.* 39, no. 2 (September): 277–299. <https://doi.org/10.1016/j.acha.2014.09.004>. Cited on p. 190.
- . 2015c. "Phase retrieval via Wirtinger flow: theory and algorithms." *IEEE Trans. Inf. Theory* 61, no. 4 (April): 1985–2007. <https://doi.org/10.1109/tit.2015.2399924>. Cited on pp. 190, 192, 200.
- Candès, E. J., T. Strohmer, and V. Voroninski. 2013. "Phaselift: exact and stable signal recovery from magnitude measurements via convex programming." *Commun. Pure Appl. Math.* 66 (8): 1241–1274. <https://doi.org/10.1002/cpa.21432>. Cited on p. 190.
- Canning, F. X. 1991. "Protecting EFIE-based scattering computations from effects of interior resonances." *IEEE Trans. Antennas Propag.* 39, no. 11 (November): 1545–1552. <https://doi.org/10.1109/8.102767>. Cited on p. 22.
- . 1995. "Robust use of supplementary conditions for moment method solution near internal resonances." *IEEE Trans. Antennas Propag.* 43, no. 3 (March): 264–269. <https://doi.org/10.1109/8.371995>. Cited on p. 22.
- Caorsi, S., A. Massa, and M. Raffetto. 1996. "Critical frequencies for solving electromagnetic scattering problems by the moment/finite-element method." *Microw. Opt. Techn. Lett.* 11, no. 4 (March): 222–228. [https://doi.org/10.1002/\(sici\)1098-2760\(199603\)11:4<222::aid-mop16>3.0.co;2-d](https://doi.org/10.1002/(sici)1098-2760(199603)11:4<222::aid-mop16>3.0.co;2-d). Cited on p. 22.
- Cappellin, C., and S. Pivnenko. 2014. "Filtering of measurement noise with the 3D reconstruction algorithm." In *Proc. 36th Annu. Meeting Symp. Antenna Meas. Techn. Assoc. (AMTA)*. Tucson, AZ, US, October. Cited on p. 174.
- Castaldi, G., and I. M. Pinto. 2000. "Well-posed well-conditioned phase retrieval technique using a known reference source." In *Proc. IEEE Antennas Propag. Soc. Int. Symp. USNC/URSI Nat. Radio Sci. Meeting (APSURSI)*, 1780–1782. Salt Lake City, UT, USA, July. <https://doi.org/10.1109/aps.2000.874589>. Cited on p. 195.
- Cessenat, M. 1996. *Mathematical Methods in Electromagnetism: Linear Theory and Applications*. Vol. 41. Adv. Math. Appl. Sci. Singapore, SG: World Scientific. Cited on pp. 35–37.
- Chang, R., and V. Lomakin. 2013. "Quadrilateral barycentric basis functions for surface integral equations." *IEEE Trans. Antennas Propag.* 61, no. 12 (December): 6039–6050. <https://doi.org/10.1109/tap.2013.2280472>. Cited on p. 47.
- Chang, Y., and R. F. Harrington. 1977. "A surface formulation for characteristic modes of material bodies." *IEEE Trans. Antennas Propag.* 25, no. 6 (June): 789–795. <https://doi.org/10.1109/tap.1977.1141685>. Cited on p. 17.

BIBLIOGRAPHY

- Chen, Q. 1990. "Electromagnetic Modeling of Three-Dimensional Piecewise Homogeneous Material Bodies of Arbitrary Composition and Geometry." PhD diss., Houston, TX, US: Univ. Houston. Cited on pp. 37, 44, 47.
- Chen, Q., and D. R. Wilton. 1990. "Electromagnetic scattering by three-dimensional arbitrary complex material/conducting bodies." In *Proc. Antennas Propag. Soc. Int. Symp.* 590–593. Dallas, TX, US, May. <https://doi.org/10.1109/aps.1990.115179>. Cited on pp. 37, 44, 47.
- Chen, R.-S., J. Ding, D. Z. Ding, Z. H. Fan, and D. Wang. 2009. "A multiresolution curvilinear Rao-Wilton-Glisson basis function for fast analysis of electromagnetic scattering." *IEEE Trans. Antennas Propag.* 57, no. 10 (October): 3179–3188. <https://doi.org/10.1109/tap.2009.2028599>. Cited on p. 41.
- Cheng, C., I. Daubechies, N. Dym, and J. Lu. 2021. "Stable phase retrieval from locally stable and conditionally connected measurements." *Applied and Computational Harmonic Analysis* 55 (November): 440–465. <https://doi.org/10.1016/j.acha.2021.07.001>. Cited on p. 190.
- Chew, W. C. 1995. *Waves and Fields in Inhomogeneous Media*. Piscataway, NJ, US: IEEE Press. Cited on p. 11.
- Chew, W. C., T. J. Cui, and J. M. Song. 2002. "A FAFFA-MLFMA algorithm for electromagnetic scattering." *IEEE Trans. Antennas Propag.* 50, no. 11 (November): 1641–1649. <https://doi.org/10.1109/tap.2002.802162>. Cited on p. 17.
- Chew, W. C., E. Michielssen, J. M. Song, and J.-M. Jin. 2001. *Fast and Efficient Algorithms in Computational Electromagnetics*. Boston, MA, US: Artech House. Cited on pp. 2, 3, 28.
- Chew, W. C., and J. M. Song. 2007. "Gedanken experiments to understand the internal resonance problems of electromagnetic scattering." *Electromagn.* 27, no. 8 (November): 457–471. <https://doi.org/10.1080/02726340701668039>. Cited on p. 21.
- Chew, W. C., M. S. Tong, and B. Hu. 2008. *Integral equation methods for electromagnetic and elastic waves*. San Rafael, CA, US: Morgan & Claypool. Cited on p. 21.
- Chhim, T. L., S. B. Adrian, and F. P. Andriulli. 2018. "On the spectral behavior and normalization of a resonance-free and high-frequency stable integral equation." In *Proc. IEEE Int. Symp. Antennas Propag. & USNC/URSI Nat. Radio Sci. Meeting*, 2447–2448. Boston, MA, US: IEEE, July. <https://doi.org/10.1109/apusncursinrsm.2018.8608769>. Cited on p. 48.
- Chhim, T. L., A. Merlini, L. Rahmouni, J. E. O. Guzman, and F. P. Andriulli. 2020. "Eddy current modeling in multiply connected regions via a full-wave solver based on the quasi-Helmholtz projectors." *IEEE Open J. Antennas Propag.* 1:534–548. <https://doi.org/10.1109/ojap.2020.3027186>. Cited on p. 48.
- Chowdhury, M. Z., M. Shahjalal, S. Ahmed, and Y. M. Jang. 2020. "6G wireless communication systems: applications, requirements, technologies, challenges, and research directions." *IEEE Open J. Commun. Soc.* 1:957–975. <https://doi.org/10.1109/ojcoms.2020.3010270>. Cited on p. 1.
- Ciorba, L., G. Giordanengo, M. Righero, and G. Vecchi. 2019. "Far field evaluation from undersampled near field measurements using numerically built basis functions." In *Proc. 13th Eur. Conf. Antennas Propag. (EuCAP)*. Krakow, PL, April. Cited on pp. 175, 176.
- Coene, W., G. Janssen, M. O. de Beeck, and D. van Dyck. 1992. "Phase retrieval through focus variation for ultra-resolution in field-emission transmission electron microscopy." *Phys. Rev. Lett.* 69, no. 26 (December): 3743–3746. <https://doi.org/10.1103/physrevlett.69.3743>. Cited on p. 190.

- Coifman, R., V. Rokhlin, and S. Wandzura. 1993. "The fast multipole method for the wave equation: a pedestrian prescription." *IEEE Antennas Propag. Mag.* 35, no. 3 (June): 7–12. <https://doi.org/10.1109/74.250128>. Cited on p. 28.
- Colton, D. L., and R. Kress. 2019. *Inverse Acoustic and Electromagnetic Scattering Theory*. 4th ed. Vol. 93. New York, NY, US: Springer-Verlag. Cited on p. 28.
- Contopanagos, H., B. Dembart, M. Epton, J. J. Ottusch, V. Rokhlin, J. L. Visher, and S. M. Wandzura. 2002. "Well-conditioned boundary integral equations for three-dimensional electromagnetic scattering." *IEEE Trans. Antennas Propag.* 50, no. 12 (December): 1824–1830. <https://doi.org/10.1109/tap.2002.803956>. Cited on p. 41.
- Cools, K., F. P. Andriulli, F. Olyslager, and E. Michielssen. 2009. "Improving the MFIE's accuracy by using a mixed discretization." In *Proc. IEEE Antennas Propag. Soc. Int. Symp.* North Charleston, SC, US: IEEE, June. <https://doi.org/10.1109/aps.2009.5172077>. Cited on p. 47.
- Cools, K., F. P. Andriulli, D. De Zutter, and E. Michielssen. 2011. "Accurate and conforming mixed discretization of the MFIE." *IEEE Antennas Wireless Propag. Lett.* 10:528–531. ISSN: 1536-1225. <https://doi.org/10.1109/lawp.2011.2155022>. Cited on pp. 37, 45, 47, 140.
- Cools, K., F. P. Andriulli, P. Ylä-Oijala, H. Bagci, D. D. Zutter, and E. Michielssen. 2010. "Improving the accuracy of the Calderón preconditioned CFIE by using a mixed discretization." In *Proc. IEEE Antennas Propag. Soc. Int. Symp. (APS)*. Toronto, CA, July. <https://doi.org/10.1109/aps.2010.5561897>. Cited on pp. 47, 48.
- Cools, K., R. Voskamp, and S. Lasisi. 2021. "krcools/BEAST:jl: v1.4.0," November. <https://doi.org/10.5281/zenodo.3865279>. Cited on pp. 47, 53.
- Cornelius, R., D. Heberling, N. Koep, A. Behboodi, and R. Mathar. 2016. "Compressed sensing applied to spherical near-field to far-field transformation." In *Proc. 10th Eur. Conf. Antennas Propag. (EuCAP)*. Davos, CH, April. <https://doi.org/10.1109/eucap.2016.7481140>. Cited on p. 28.
- Correia, L. M. 1993. "A comparison of integral equations with unique solution in the resonance region for scattering by conducting bodies." *IEEE Trans. Antennas Propag.* 41, no. 1 (January): 52–58. <https://doi.org/10.1109/8.210115>. Cited on p. 22.
- Costanzo, S., G. Di Massa, and M. D. Migliore. 2001. "Integrated microstrip probe for phaseless near-field measurements on plane-polar geometry." *Electron. Lett.* 37, no. 16 (August): 1018–1020. <https://doi.org/10.1049/el:20010684>. Cited on pp. 195–197, 203.
- . 2005. "A novel hybrid approach for far-field characterization from near-field amplitude-only measurements on arbitrary scanning surfaces." *IEEE Trans. Antennas Propag.* 53, no. 6 (June): 1866–1874. ISSN: 0018-926X. <https://doi.org/10.1109/tap.2005.845218>. Cited on pp. 195, 196, 203.
- Costanzo, S., and G. Di Massa. 2001. "An integrated probe for phaseless plane-polar near-field measurements." *Microw. Opt. Technol. Lett.* 30 (5): 293–295. <https://doi.org/10.1002/mop.1294>. Cited on pp. 195, 196, 203.
- . 2008. "Wideband phase retrieval technique from amplitude-only near-field data." *Radioengineering* 17, no. 4 (December): 8–12. https://www.radioeng.cz/fulltexts/2008/08_o4b_008_012.pdf. Cited on pp. 195, 196, 203.
- D'Agostino, F., F. Ferrara, J. A. Fordham, C. Gennarelli, R. Guerriero, M. Migliozzi, G. Riccio, and C. Rizzo. 2009. "An effective near-field-far-field transformation technique for elongated antennas using a fast helicoidal scan [measurements corner]." *IEEE Antennas Propag. Mag.* 51, no. 4 (August): 134–141. <https://doi.org/10.1109/map.2009.5338700>. Cited on p. 28.

BIBLIOGRAPHY

- Darbas, M. 2006. "Generalized combined field integral equations for the iterative solution of the three-dimensional Maxwell equations." *Appl. Math. Lett.* 19 (8): 834–839. <https://doi.org/10.1016/j.aml.2005.11.005>. Cited on pp. 12, 41.
- Davis, C. P., and K. F. Warnick. 2004. "High-order convergence with a low-order discretization of the 2-D MFIE." *IEEE Antennas and Wireless Propagation Letters* 3:355–358. <https://doi.org/10.1109/lawp.2004.840254>. Cited on pp. 45, 56, 61.
- . 2005. "Error analysis of 2-D MoM for MFIE/EFIE/CFIE based on the circular cylinder." *IEEE Trans. Antennas Propag.* 53, no. 1 (January): 321–331. <https://doi.org/10.1109/tap.2004.838791>. Cited on p. 45.
- De Alwis, C., A. Kalla, Q.-V. Pham, P. Kumar, K. Dev, W.-J. Hwang, and M. Liyanage. 2021. "Survey on 6G frontiers: trends, applications, requirements, technologies and future research." *IEEE Open J. Commun. Soc.* 2:836–886. <https://doi.org/10.1109/ojcoms.2021.3071496>. Cited on p. 1.
- De Jough, R. V., M. Hajian, and L. P. Ligthart. 1997. "Antenna time-domain measurement techniques." *IEEE Antennas Propag. Mag.* 39, no. 5 (October): 7–11. <https://doi.org/10.1109/74.637102>. Cited on p. 186.
- Dély, A., F. P. Andriulli, and K. Cools. 2017. "An impedance boundary condition EFIE that is low-frequency and refinement stable." *IEEE Trans. Antennas Propag.* 65, no. 3 (March): 1259–1266. <https://doi.org/10.1109/tap.2016.2647684>. Cited on pp. 52, 53.
- Dély, A., A. Merlini, S. B. Adrian, and F. P. Andriulli. 2019. "On preconditioning electromagnetic integral equations in the high frequency regime via Helmholtz operators and quasi-Helmholtz projectors." In *Proc. Int. Conf. Electromagn. Adv. Appl. (ICEAA)*, 1338–1341. Granada, ES, September. <https://doi.org/10.1109/iceaa.2019.8879366>. Cited on p. 41.
- Deraemaeker, A., I. Babuška, and P. Bouillard. 1999. "Dispersion and pollution of the fem solution for the helmholtz equation in one, two and three dimensions." *Int. J. Numer. Methods Eng.* 46, no. 4 (October): 471–499. [https://doi.org/10.1002/\(sici\)1097-0207\(19991010\)46:4<471::aid-nme684>3.0.co;2-6](https://doi.org/10.1002/(sici)1097-0207(19991010)46:4<471::aid-nme684>3.0.co;2-6). Cited on p. 2.
- Dölz, J., S. Kurz, S. Schöps, and F. Wolf. 2019. "Isogeometric boundary elements in electromagnetism: rigorous analysis, fast methods, and examples." *SIAM J. Sci. Comput.* 41 (5): B983–B1010. <https://doi.org/10.1137/18M1227251>. Cited on p. 77.
- Duffy, M. G. 1982. "Quadrature over a pyramid or cube of integrands with a singularity at a vertex." *SIAM J. Numer. Anal.* 19 (6): 1260–1262. <https://doi.org/10.1137/0719090>. Cited on p. 33.
- Edemsky, D., A. Popov, I. Prokopovich, and V. Garbatsevich. 2021. "Airborne ground penetrating radar, field test." *Remote Sens.* 13 (4): 667. <https://doi.org/10.3390/rs13040667>. Cited on p. 1.
- Eibert, T. F. 2004. "Iterative-solver convergence for loop-star and loop-tree decompositions in method-of-moments solutions of the electric-field integral equation." *IEEE Antennas and Propagation Magazine* 46, no. 3 (June): 80–85. <https://doi.org/10.1109/map.2004.1374101>. Cited on p. 41.
- . 2005. "A diagonalized multilevel fast multipole method with spherical harmonics expansion of the k-space integrals." *IEEE Trans. Antennas Propag.* 53, no. 2 (February): 814–817. <https://doi.org/10.1109/tap.2004.841310>. Cited on pp. 28, 89.
- . 2007. "Some scattering results computed by surface-integral-equation and hybrid finite-element – boundary-integral techniques, accelerated by the multilevel fast multipole method." *IEEE Antennas Propag. Mag.* 49, no. 2 (April): 61–69. <https://doi.org/10.1109/map.2007.376638>. Cited on p. 90.

- Eibert, T. F., and T. B. Hansen. 2017. "Inverse-source algorithm for antenna-field transformations using the weak form of the combined source condition." In *Proc. 11th Eur. Conf. Antennas Propag. (EuCAP)*. Paris, France, March. <https://doi.org/10.23919/EuCAP.2017.7928265>. Cited on pp. 28, 139, 187.
- Eibert, T. F., and V. Hansen. 1996. "On the interior resonance problem of FEM/BEM-hybrid- and BEM-approaches." In *Proc. IEEE Antennas Propag. Soc. Int. Symp. (APSURSI)*, 1:154–157. Baltimore, MD, US, July. <https://doi.org/10.1109/aps.1996.549564>. Cited on p. 19.
- . 1997. "3-D FEM/BEM-hybrid approach based on a general formulation of Huygens' principle for planar layered media." *IEEE Trans. Microw. Theory Techn.* 45, no. 7 (July): 1105–1112. <https://doi.org/10.1109/22.598448>. Cited on p. 46.
- Eibert, T. F., Ismatullah, E. Kaliyaperumal, and C. H. Schmidt. 2010. "Inverse equivalent surface current method with hierarchical higher order basis functions, full probe correction and multilevel fast multipole acceleration." *Prog. Electromagn. Res.* 106:377–394. <https://doi.org/10.2528/PIER10061604>. Cited on p. 27.
- Eibert, T. F., E. Kılıç, C. Lopez, R. A. M. Mauermayer, O. Neitz, and G. Schnattinger. 2015. "Electromagnetic field transformations for measurements and simulations (invited paper)." *Prog. Electromagn. Res.* 151:127–150. <https://doi.org/10.2528/pier14121105>. Cited on p. 28.
- Eibert, T. F., and R. A. M. Mauermayer. 2018a. "Equivalent sources based near-field far-field transformation above dielectric half space." In *Proc. Antenna Meas. Techn. Assoc. Symp. (AMTA)*. Williamsburg, VA, US, November. <https://ieeexplore.ieee.org/document/8604259>. Cited on p. 28.
- . 2018b. "Near-field far-field transformations for automobile antenna measurements." In *Proc. Appl. Comput. Electromagn. Soc. Conf. (ACES)*. Denver, CO, US, March. <https://ieeexplore.ieee.org/document/8604259>. Cited on p. 28.
- Eibert, T. F., D. Ostrzyharczik, J. Kornprobst, and J. Knapp. 2022a. "On the generation of distributed spherical harmonics expansions for inverse source solutions," TechRxiv: 21330690. Cited on p. 150.
- . 2022b. "Solution of inverse source problems with distributed spherical harmonics expansions." In *Proc. 3rd URSI Atlantic/Asia-Pacific Radio Sci. Meeting (AT-AP-RASC)*. Gran Canaria, ES, June. <https://doi.org/10.23919/at-ap-rasc54737.2022.9814176>. TechRxiv: 20146901. Cited on p. 150.
- Eibert, T. F., C. H. Schmidt, and Ismatullah. 2011. "Investigation of full probe correction and higher order expansion functions in multilevel fast multipole accelerated inverse equivalent current method." In *Proc. 5th Eur Conf. Antennas Propag. (EuCAP)*, 3885–3887. Rome, IT, April. <https://ieeexplore.ieee.org/document/5782418>. Cited on p. 27.
- Eibert, T. F., and C. H. Schmidt. 2009. "Multilevel fast multipole accelerated inverse equivalent current method employing Rao–Wilton–Glisson discretization of electric and magnetic surface currents." *IEEE Trans. Antennas Propag.* 57, no. 4 (April): 1178–1185. <https://doi.org/10.1109/tap.2009.2015828>. Cited on pp. 27, 28.
- Eibert, T. F., and D. Vojvodic. 2016. "Fast inverse equivalent current solutions with surface currents in complex space." In *Proc. URSI Int. Symp. Electromagn. Theory (EMTS)*, 280–283. Espoo, FI, August. <https://doi.org/10.1109/ursi-emts.2016.7571374>. Cited on p. 28.
- Eibert, T. F., D. Vojvodic, and T. B. Hansen. 2016. "Fast inverse equivalent source solutions with directive sources." *IEEE Trans. Antennas Propag.* 64, no. 11 (November): 4713–4724. <https://doi.org/10.1109/tap.2016.2606405>. Cited on pp. 26, 28, 52, 139.

BIBLIOGRAPHY

- Eibert, T. F., J. L. Volakis, D. R. Wilton, and D. R. Jackson. 1999. "Hybrid FE/BI modeling of 3-D doubly periodic structures utilizing triangular prismatic elements and an MPIE formulation accelerated by the Ewald transformation." *IEEE Trans. Antennas Propag.* 47, no. 5 (May): 843–850. <https://doi.org/10.1109/8.774139>. Cited on p. 17.
- Einstein, A. 1905. "Zur Elektrodynamik bewegter Körper." *Annalen der Physik* 322 (10): 891–921. <https://doi.org/10.1002/andp.19053221004>. Cited on p. 1.
- Eldén, L., and V. Simoncini. 2012. "Solving ill-posed linear systems with GMRES and a singular preconditioner." *SIAM J. Matrix Anal. Appl.* 33, no. 4 (December): 1369–1394. <https://doi.org/10.1137/110832793>. Cited on p. 136.
- Ergül, Ö., and L. Gürel. 2004a. "Improving the accuracy of the MFIE with the choice of basis functions." In *Proc. IEEE Antennas Propag. Soc. Symp. (APSURSI)*, 3:3389–3392. Monterey, CA, US, June. <https://doi.org/10.1109/aps.2004.1332107>. Cited on p. 46.
- . 2004b. "Investigation of the inaccuracy of the MFIE discretized with the RWG basis functions." In *Proc. IEEE Antennas Propag. Soc. Symp. (APSURSI)*, 3:3393–3396. Monterey, CA, US, June. <https://doi.org/10.1109/aps.2004.1332108>. Cited on pp. 45, 46.
- . 2006. "The use of curl-conforming basis functions for the magnetic-field integral equation." *IEEE Trans. Antennas Propag.* 54, no. 7 (July): 1917–1926. <https://doi.org/10.1109/tap.2006.877159>. Cited on p. 45.
- . 2007. "Linear-linear basis functions for MLFMA solutions of magnetic-field and combined-field integral equations." *IEEE Trans. Antennas Propag.* 55, no. 4 (April): 1103–1110. <https://doi.org/10.1109/tap.2007.893393>. Cited on p. 46, 111.
- . 2009. "Discretization error due to the identity operator in surface integral equations." *Comput. Phys. Commun.* 180, no. 10 (October): 1746–1752. <https://doi.org/10.1016/j.cpc.2009.04.020>. Cited on pp. 44, 45, 56, 61, 64, 65.
- Erricolo, D. 2017. "Benchmarking computational electromagnetics with exact analytical solutions of canonical electromagnetic scattering problems." In *Proc. IEEE Int. Symp. Antennas Propag. & USNC/URSI Nat. Radio Sci. Meeting (APSURSI)*, 249–250. San Diego, CA, US: IEEE. <https://doi.org/10.1109/apusncursinrsm.2017.8072167>. Cited on p. 2.
- Faul, F. T., J. Kornprobst, T. Fritzel, H. Steiner, R. Strauss, A. Weiss, R. Geise, and T. F. Eibert. 2018. "A concept study of near-field measurements and corresponding field transformations of the modulated fields of air navigation systems." In *Kleinheubacher Tagung*. Miltenberg, DE, September. Cited on p. 28.
- Faul, F. T., J. Kornprobst, T. Fritzel, H.-J. Steiner, R. Strauß, A. Weiß, R. Geise, and T. F. Eibert. 2019. "Near-field measurement of continuously modulated fields employing the time-harmonic near- to far-field transformation." *Adv. Radio Sci.* 17:83–89. <https://doi.org/10.5194/ars-17-83-2019>. Cited on p. 28.
- Faul, F. T., and T. F. Eibert. 2021. "Setup and error analysis of a fully coherent UAV-based near-field measurement system." In *Proc. 15th Eur. Conf. Antennas Propag. (EuCAP)*. Düsseldorf, DE, March. <https://doi.org/10.23919/eucap51087.2021.9411307>. Cited on p. 174.
- Faulkner, H. M. L., and J. M. Rodenburg. 2004. "Movable aperture lensless transmission microscopy: a novel phase retrieval algorithm." *Phys. Rev. Lett.* 93, no. 2 (July): 023903. <https://doi.org/10.1103/physrevlett.93.023903>. Cited on p. 190.

- Fischer, J. 2009. "NFC in cell phones: the new paradigm for an interactive world [near-field communications]." *IEEE Commun. Mag.* 47, no. 6 (June): 22–28. <https://doi.org/10.1109/mcom.2009.5116794>. Cited on p. 1.
- Fock, V. A. 1946. "The distribution of currents induced by a plane wave on the surface of a conductor." *J. Phys* 10 (2): 130–136. Cited on p. 19.
- Foged, L. J., L. Scialacqua, F. Mioc, F. Saccardi, P. O. Iversen, L. Shmidov, R. Braun, J. L. Araque Quijano, and G. Vecchi. 2013a. "Echo suppression by spatial-filtering techniques in advanced planar and spherical near-field antenna measurements [AMTA corner]." *IEEE Antennas Propag. Mag.* 55, no. 5 (October): 235–242. <https://doi.org/10.1109/map.2013.6735525>. Cited on p. 174.
- Foged, L. J., L. Scialacqua, F. Saccardi, J. L. Araque Quijano, and G. Vecchi. 2014. "Application of the dual-equation equivalent-current reconstruction to electrically large structures by fast multipole method enhancement." *IEEE Antennas Propag. Mag.* 56, no. 5 (October): 264–273. <https://doi.org/10.1109/map.2014.6971966>. Cited on pp. 26–28.
- Foged, L. J., L. Scialacqua, F. Saccardi, F. Mioc, P. O. Iversen, L. Shmidov, R. Braun, J. L. Araque Quijano, and G. Vecchi. 2013b. "Comparison of echo suppression techniques in near field antenna measurement applications." In *Proc. 7th Eur. Conf. Antennas Propag. (EuCAP)*, 3988–3992. Gothenburg, SE, April. Cited on p. 28.
- Freethy, S. J., T. Görler, A. J. Creely, G. D. Conway, S. S. Denk, T. Happel, C. Koenen, P. Hennequin, A. E. White, and A. U. Team. 2018. "Validation of gyrokinetic simulations with measurements of electron temperature fluctuations and density-temperature phase angles on ASDEX upgrade." *Phys. Plasmas* 25 (5): 055903. <https://doi.org/10.1063/1.5018930>. Cited on p. 1.
- Fuchs, B., M. Mattes, S. Rondineau, and L. Le Coq. 2020. "Phaseless near-field antenna measurements from two surface scans — numerical and experimental investigations." *IEEE Trans. Antennas Propag.* 68, no. 3 (March): 2315–2322. <https://doi.org/10.1109/tap.2019.2938744>. Cited on pp. 197, 202.
- Gabor, D. 1949. "Microscopy by reconstructed wave-fronts." In *Proc. R. Soc. Lond. A*, 197:454–487. <https://doi.org/10.1098/rspa.1949.0075>. Cited on p. 195.
- García-Fernández, M., Y. Álvarez López, and F. Las-Heras Andrés. 2018a. "On the use of unmanned aerial vehicles for antenna and coverage diagnostics in mobile networks." *IEEE Commun. Mag.* 56, no. 7 (July): 72–78. <https://doi.org/10.1109/mcom.2018.1700991>. Cited on p. 168.
- García-Fernández, M., Y. Á. López, A. A. Arboleya, B. G. Valdés, Y. R. Vaqueiro, F. L.-H. Andrés, and A. P. García. 2018b. "Synthetic aperture radar imaging system for landmine detection using a ground penetrating radar on board a unmanned aerial vehicle." *IEEE Access* 6:45100–45112. <https://doi.org/10.1109/access.2018.2863572>. Cited on p. 1.
- Gedney, S., J.-F. Lee, and R. Mittra. 1992. "A combined FEM/MoM approach to analyze the plane wave diffraction by arbitrary gratings." *IEEE Trans. Microw. Theory Techn.* 40, no. 2 (February): 363–370. <https://doi.org/10.1109/22.120110>. Cited on p. 17.
- Gemmer, T. M., and D. Heberling. 2019. "Generalized test-zone field compensation." In *Proc. Antenna Meas. Techn. Assoc. Symp. (AMTA)*. San Diego, CA, US, October. <https://doi.org/10.23919/amtap.2019.8906330>. Cited on p. 28.
- Gerchberg, R. W., and W. O. Saxton. 1972. "A practical algorithm for the determination of phase from image and diffraction plane pictures." *Optik* 35 (2): 237–246. Cited on pp. 190, 202.

BIBLIOGRAPHY

- Gibson, W. C. 2014. *The Method of Moments in Electromagnetics*. 2nd ed. Boca Raton, FL, US: CRC Press. Cited on p. 31.
- Gil, J. M., and F. Conde-Pumpido. 2020. "Efficient higher-order discretization of the magnetic field integral equation by means of vector spaces with a solenoidal-no solenoidal decomposition." *Microw. Opt. Techn. L.* 62, no. 6 (June): 2168–2173. <https://doi.org/10.1002/mop.32299>. Cited on pp. 46, 111.
- Giordanengo, G., M. Righero, J. L. Araque Quijano, F. Vipiana, and G. Vecchi. 2016. "Fast hybrid antenna testing with probe compensated procedure." In *Proc. 10th Eur. Conf. Antennas Propag. (EuCAP)*. Davos, CH, April. Cited on pp. 175, 176.
- Giordanengo, G., F. Vipiana, L. J. Foged, L. Scialacqua, F. Saccardi, M. Bandinelli, M. Bercigli, G. Guida, M. Sabbadini, and G. Vecchi. 2013. "Time efficient NF technique with application in satellite antenna integration and test/verification." In *Proc. 7th Eur. Conf. Antennas Propag. (EuCAP)*. Gothenburg, SE, April. <https://ieeexplore.ieee.org/document/6546503>. Cited on pp. 175, 176.
- Glisson, A. W. 1984. "An integral equation for electromagnetic scattering from homogeneous dielectric bodies." *IEEE Trans. Antennas Propag.* 32, no. 2 (February): 173–175. <https://doi.org/10.1109/tap.1984.1143279>. Cited on p. 13.
- . 1992. "Electromagnetic scattering by arbitrarily shaped surfaces with impedance boundary conditions." *Radio Sci.* 27 (6): 935–943. <https://doi.org/10.1029/92rs01782>. Cited on pp. 50, 52.
- Gong, Z., and A. W. Glisson. 1990. "A hybrid equation approach for the solution of electromagnetic scattering problems involving two-dimensional inhomogeneous dielectric cylinders." *IEEE Trans. Antennas Propag.* 38, no. 1 (January): 60–68. <https://doi.org/10.1109/8.43590>. Cited on p. 17.
- Gozick, B., K. P. Subbu, R. Dantu, and T. Maeshiro. 2011. "Magnetic maps for indoor navigation." *IEEE Trans. Instrum. Meas.* 60, no. 12 (December): 3883–3891. <https://doi.org/10.1109/tim.2011.2147690>. Cited on p. 1.
- Graglia, R. 1987. "Static and dynamic potential integrals for linearly varying source distributions in two- and three-dimensional problems." *IEEE Trans. Antennas Propag.* 35, no. 6 (June): 662–669. <https://doi.org/10.1109/tap.1987.1144160>. Cited on p. 33.
- Graglia, R. D., and G. Lombardi. 2008. "Singular higher order divergence-conforming bases of additive kind and moments method applications to 3D sharp-wedge structures." *IEEE Trans. Antennas Propag.* 56, no. 12 (December): 3768–3788. <https://doi.org/10.1109/tap.2008.2007390>. Cited on p. 46.
- Graglia, R. D., D. R. Wilton, and A. F. Peterson. 1997. "Higher order interpolatory vector bases for computational electromagnetics." *IEEE Trans. Antennas Propag.* 45, no. 3 (March): 329–342. <https://doi.org/10.1109/8.558649>. Cited on p. 46.
- Gregson, S. F., A. C. Newell, and G. E. Hindman. 2012. "Examination of far-field mathematical absorber reflection suppression through computational electromagnetic simulation." *Int. J. Antennas Propag.* 2012 (May): 1–10. <https://doi.org/10.1155/2012/623268>. Cited on pp. 174, 179.
- Grohs, P., S. Koppensteiner, and M. Rathmair. 2020. "Phase retrieval: uniqueness and stability." *SIAM Rev.* 62 (2): 301–350. <https://doi.org/10.1137/19m1256865>. Cited on p. 190.
- Grohs, P., and M. Rathmair. 2021. "Stable Gabor phase retrieval for multivariate functions." *Journal of the European Mathematical Society*, <https://doi.org/10.4171/jems/1114>. Cited on p. 190.

- Guizar-Sicairos, M., and J. R. Fienup. 2008. "Phase retrieval with transverse translation diversity: a nonlinear optimization approach." *Opt. Express* 16, no. 10 (May): 7264–7278. <https://doi.org/10.1364/oe.16.007264>. Cited on p. 190.
- Güler, S., A. C. Yücel, H. Bağcı, and Ö. Ergül. 2018. "Mixed discretization of CFIE in the framework of MLFMA." In *Proc. Prog. Electromagn. Res. Symp. (PIERS-Toyama)*, 1500–1505. Toyama, JP, August. <https://doi.org/10.23919/piers.2018.8597735>. Cited on pp. 60, 68.
- Gürel, L., H. Bağcı, J. C. Castelli, A. Cheraly, and F. Tardivel. 2003. "Validation through comparison: Measurement and calculation of the bistatic radar cross section of a stealth target." *Radio Sci.* 38, no. 3 (June): 12-1–12-8. <https://doi.org/10.1029/2001rs002583>. Cited on p. 89.
- Gürel, L., and Ö. Ergül. 2009. "Contamination of the accuracy of the combined-field integral equation with the discretization error of the magnetic-field integral equation." *IEEE Trans. Antennas Propag.* 57, no. 9 (September): 2650–2657. <https://doi.org/10.1109/tap.2009.2024529>. Cited on pp. 44, 45.
- Gürel, L. 2017. "Benchmarking the solutions of billion-unknown problems." In *Proc. IEEE Int. Symp. Antennas Propag. & USNC/URSI Nat. Radio Sci. Meeting (APSURSI)*, 251–252. San Diego, CA, US: IEEE. <https://doi.org/10.1109/apusncursinrsm.2017.8072168>. Cited on p. 2.
- Gürel, L., K. Sertel, and İ. K. Şendur. 1999. "On the choice of basis functions to model surface electric current densities in computational electromagnetics." *Radio Sci.* 34 (6): 1373–1387. <https://doi.org/10.1029/1999rs900008>. Cited on pp. 45, 46.
- Guzman, J. E. O., S. B. Adrian, R. Mitharwal, Y. Beghein, T. F. Eibert, K. Cools, and F. P. Andriulli. 2017. "On the hierarchical preconditioning of the PMCHWT integral equation on simply and multiply connected geometries." *IEEE Antennas Wireless Propag. Lett.* 16:1044–1047. <https://doi.org/10.1109/lawp.2016.2619363>. Cited on p. 48.
- Hamberger, G. F., S. Trummer, U. Siart, and T. F. Eibert. 2016. "A planar dual-polarized microstrip 1-D-beamforming antenna array for the 24-GHz band." *IEEE Trans. Antennas Propag.* 65 (1): 142–149. <https://doi.org/10.1109/tap.2016.2618847>. Cited on p. 1.
- Hansen, J. E., ed. 1988. *Spherical Near-field Antenna Measurements*. London, UK: Peter Peregrinus Ltd. Cited on pp. 28, 134, 150, 155, 160, 176.
- Hansen, P. C. 1992. "Analysis of discrete ill-posed problems by means of the L-curve." *Appl. Comput. Harmonic Anal.* 34, no. 4 (December): 561–580. <https://doi.org/10.1137/1034115>. Cited on pp. 142, 144.
- Hansen, T. B., A. Paulus, and T. F. Eibert. 2019. "On the condition number of a normal matrix in near-field to far-field transformations." *IEEE Trans. Antennas Propag.* 67, no. 3 (March): 2028–2033. <https://doi.org/10.1109/tap.2019.2891233>. Cited on p. 27.
- Harrington, R. F. 1961. *Time-Harmonic Electromagnetic Fields*. New York, NY, US: McGraw-Hill. Cited on pp. 2, 6.
- . 1968. *Field Computation by Moment Methods*. Reprinted in 1993 by Wiley-IEEE Press. New York, NY, US: Macmillan. Cited on pp. 2, 31.
- . 1989. "Boundary integral formulations for homogeneous material bodies." *J. Electromagn. Waves Appl.* 3 (1): 1–15. <https://doi.org/10.1163/156939389x00016>. Cited on pp. 13, 17, 24.
- Helmers, S., H.-F. Harms, and H.-K. Gonschorek. 1999. "Analyzing electromagnetic pulse coupling by combining TLT, MoM, and GTD/UTD." *IEEE Trans. Electromagn. Compat.* 41, no. 4 (November): 431–435. <https://doi.org/10.1109/15.809844>. Cited on p. 17.

BIBLIOGRAPHY

- Henderson, A., J. R. James, P. Newham, and G. Morris. 1989. "Analysis of gating errors in time domain antenna measurements." In *IEE Proc. H (Microw. Antennas Propag.)* 136:311–320. 4. <https://doi.org/10.1049/ip-h-2.1989.0058>. Cited on p. 186.
- Hess, D. W. 2010. "The IsoFilter™ technique: a method of isolating the pattern of an individual radiator from data measured in a contaminated environment." *IEEE Antennas Propag. Mag.* 52, no. 1 (February): 174–181. <https://doi.org/10.1109/map.2010.5466422>. Cited on pp. 174, 179.
- Hestenes, M. R., and E. Stiefel. 1952. "Methods of conjugate gradients for solving linear systems." *J. Res. Nat. Bur. Standards* 49, no. 6 (December): 409–435. <https://doi.org/10.6028/jres.049.044>. Cited on pp. 58, 68, 136.
- Hofmann, B., T. F. Eibert, F. P. Andriulli, and S. B. Adrian. 2021. "Towards accurate discretization of arbitrary right-hand side excitations on multiply-connected geometries." In *Proc. Int. Conf. Electromagn. Adv. Appl. (ICEAA)*, 312–312. Honolulu, HI, US: IEEE, August. <https://doi.org/10.1109/iceaa52647.2021.9539627>. Cited on p. 48.
- Hofmann, B., O. Neitz, and T. F. Eibert. 2019. "On the minimum number of samples for sparse recovery in spherical antenna near-field measurements." *IEEE Trans. Antennas Propag.* 67, no. 12 (December): 7597–7610. <https://doi.org/10.1109/tap.2019.2935102>. Cited on pp. 28, 136, 176.
- Hsiao, G. C., and R. E. Kleinman. 1997. "Mathematical foundation for error estimation in numerical solution of integral equations in electromagnetics." *IEEE Trans. Antennas Propag.* 45, no. 3 (March): 326–328. <https://doi.org/10.1109/8.558648>. Cited on p. 140.
- Huang, W.-F., Y. Ren, and Q. H. Liu. 2016. "Solid-angle error in the magnetic-field integral equation for perfectly electric conducting objects." *IEEE Trans. Antennas Propag.* 64, no. 3 (March): 1158–1163. <https://doi.org/10.1109/tap.2016.2518207>. Cited on p. 46.
- Huygens, C. 1690. *Traité de la lumiere*. Translated in 1912 by S. P. Thompson as *Treatise on Light*. Leiden, NL: Pieter van der Aa. Cited on pp. 10, 27.
- IEEE Antennas and Propagation Society. 2014. "IEEE standard for definitions of terms for antennas." *IEEE Std 145-2013 (Revision of IEEE Std 145-1993)*, 1–50. <https://doi.org/10.1109/ieeestd.2014.6758443>. Cited on p. 16.
- Isernia, T., G. Leone, and R. Pierri. 1996. "Radiation pattern evaluation from near-field intensities on planes." *IEEE Trans. Antennas Propag.* 44, no. 5 (May): 701–710. <https://doi.org/10.1109/8.496257>. Cited on pp. 190, 202.
- Ismatullah. 2010. "Analysis of Space-Borne Antennas by Higher-Order Method of Moments and Inverse Equivalent Current Methods." Doctoral diss., Munich, DE: Tech. Univ. Munich. <https://mediatum.ub.tum.de/?id=9772618>. Cited on pp. 39, 111.
- Ismatullah and T. F. Eibert. 2008. "Adaptive singularity cancellation for efficient treatment of near-singular and near-hypersingular integrals in surface integral equation formulations." *IEEE Trans. Antennas Propag.* 56, no. 1 (January): 274–278. ISSN: 0018-926X. <https://doi.org/10.1109/tap.2007.913170>. Cited on p. 33.
- Ismatullah and T. F. Eibert. 2009a. "Higher order surface integral equation solutions employing spherical harmonics based multilevel fast multipole method." In *Proc. IEEE Antennas Propag. Soc. Int. Symp. (APSURSI)*. Charleston, SC, US, June. <https://doi.org/10.1109/aps.2009.5171539>. Cited on pp. 39, 46, 111, 112.

- . 2009b. "Surface integral equation solutions by hierarchical vector basis functions and spherical harmonics based multilevel fast multipole method." *IEEE Trans. Antennas Propag.* 57, no. 7 (July): 2084–2093. <https://doi.org/10.1109/tap.2009.2021932>. Cited on pp. 39, 50, 54, 111, 112.
- Iwen, M. A., S. Merhi, and M. Perlmutter. 2019. "Lower Lipschitz bounds for phase retrieval from locally supported measurements." *Appl. Comput. Harmonic Anal.* 47 (2): 526–538. <https://doi.org/10.1016/j.acha.2019.01.004>. Cited on p. 190.
- Iwen, M. A., A. Viswanathan, and Y. Wang. 2016. "Fast phase retrieval from local correlation measurements." *SIAM J. Imaging Sci.* 9 (4): 1655–1688. <https://doi.org/10.1137/15m1053761>. Cited on p. 190.
- Jaganathan, K., S. Oymak, and B. Hassibi. 2017. "Sparse phase retrieval: uniqueness guarantees and recovery algorithms." *IEEE Trans. Signal Process.* 65, no. 9 (May): 2402–2410. <https://doi.org/10.1109/tsp.2017.2656844>. Cited on p. 190.
- Jakobus, U., and F. M. Landstorfer. 1993. "Novel basis function for the equivalent magnetic current in the method of moments solution of dielectric scattering problems." *Electronic. L.* 29 (14): 1272–1273. <https://doi.org/10.1049/el:19930849>. Cited on p. 46.
- Jiang, B.-N., J. Wu, and L. A. Povinelli. 1996. "The origin of spurious solutions in computational electromagnetics." *J. Comput. Phys.* 125 (1): 104–123. <https://doi.org/10.1006/jcph.1996.0082>. Cited on p. 34.
- Jiang, W., B. Han, M. A. Habibi, and H. D. Schotten. 2021. "The road towards 6G: a comprehensive survey." *IEEE Open J. Commun. Soc.* 2:334–366. <https://doi.org/10.1109/ojcoms.2021.3057679>. Cited on p. 1.
- Jin, J.-M. 2011. *Theory and Computation of Electromagnetic Fields*. 2nd ed. Hoboken, NJ, US: Wiley. Cited on pp. 2, 6, 9, 23, 31, 77.
- Jin, J.-M., and V. V. Liepa. 1988. "Application of hybrid finite element method to electromagnetic scattering from coated cylinders." *IEEE Trans. Antennas Propag.* 36, no. 1 (January): 50–54. <https://doi.org/10.1109/8.1074>. Cited on p. 17.
- Jin, J.-M., J. L. Volakis, and J. Collins. 1991. *A finite element-boundary integral method for scattering and radiation by two-and three-dimensional structures*. Technical report. Ann Arbor, MI, US: Univ. Michigan, Dept. Elect. Eng. Comput. Sci., November. Cited on p. 17.
- Johnson, R. C., H. A. Ecker, and J. S. Hollis. 1973. "Determination of far-field antenna patterns from near-field measurements." *Proc. IEEE* 61, no. 12 (December): 1668–1694. <https://doi.org/10.1109/proc.1973.9358>. Cited on p. 26.
- Johnson, R. C., H. A. Ecker, and R. Moore. 1969. "Compact range techniques and measurements." *IEEE Trans. Antennas Propag.* 17, no. 5 (September): 568–576. <https://doi.org/10.1109/tap.1969.1139517>. Cited on p. 28.
- Jørgensen, E., D. W. Hess, P. Meincke, O. Borries, and C. Cappellin. 2012a. "Antenna diagnostics on planar arrays using a 3D source reconstruction technique and spherical near-field measurements." In *Proc. 6th Eur. Conf. Antennas Propag. (EuCAP)*. Prague, CZ, March. <https://doi.org/10.1109/eucap.2012.6206503>. Cited on p. 27.
- Jørgensen, E., D. W. Hess, P. Meincke, O. Borries, C. Cappellin, and J. Fordham. 2012b. "Antenna diagnostics on planar arrays using a 3D source reconstruction technique and spherical near-field measurements." In *Proc. 6th Eur. Conf. Antennas Propag. (EuCAP)*, 2547–2550. Prague, CZ, March. <https://doi.org/10.1109/eucap.2012.6206503>. Cited on p. 174.

BIBLIOGRAPHY

- Jørgensen, E., P. Meincke, O. Borries, and M. Sabbadini. 2011a. "Processing of measured fields using advanced inverse method of moments algorithm." In *Proc. 33rd ESA Antenna Workshop*. Noordwijk, NL, October. Cited on p. 138.
- Jørgensen, E., P. Meincke, and C. Cappellin. 2011b. "Advanced processing of measured fields using field reconstruction techniques." In *Proc. 5th Eur. Conf. Antennas Propag. (EuCAP)*, 3880–3884. Rome, IT, April. <https://ieeexplore.ieee.org/document/5782417>. Cited on p. 27.
- Jørgensen, E., P. Meincke, C. Cappellin, and M. Sabbadini. 2010. "Improved source reconstruction technique for antenna diagnostics." In *Proc. 32nd ESA Antenna Workshop*. Noordwijk, NL, October. Cited on pp. 26, 27, 142.
- Junkin, G., T. Huang, and J. C. Bennett. 2000. "Holographic testing of terahertz antennas." *IEEE Trans. Antennas Propag.* 48, no. 3 (March): 409–417. ISSN: 0018-926X. <https://doi.org/10.1109/8.841902>. Cited on p. 195.
- Kabir, S., B. M. Rahman, A. Agrawal, and K. T. V. Grattan. 2013. "Elimination of numerical dispersion from electromagnetic time domain analysis by using resource efficient finite element technique." *Prog. Electromagn. Res.* 137:487–512. <https://doi.org/10.2528/pier13012305>. Cited on p. 2.
- Kaklamani, D. I., and H. T. Anastassiou. 2002. "Aspects of the method of auxiliary sources (MAS) in computational electromagnetics." *IEEE Antennas Propag. Mag.* 44, no. 3 (June): 48–64. <https://doi.org/10.1109/map.2002.1028734>. Cited on p. 32.
- Karagounis, G., D. De Zutter, and D. V. Ginste. 2015. "A hybrid MLFMM–UTD method for the solution of very large 2-D electromagnetic problems." *IEEE Trans. Antennas Propag.* 64, no. 1 (January): 224–234. <https://doi.org/10.1109/tap.2015.2501812>. Cited on p. 3.
- Karaosmanoğlu, B., and Ö. Ergül. 2016. "Numerical design of testing functions for the magnetic-field integral equation." In *Proc. 10th Eur. Conf. Antennas Propag. (EuCAP)*. Davos, CH, April. <https://doi.org/10.1109/eucap.2016.7481383>. Cited on p. 45.
- . 2017. "EFIE-tuned testing functions for MFIE and CFIE." *IEEE Antennas and Wireless Propagation Letters* 16:968–970. <https://doi.org/10.1109/lawp.2016.2615362>. Cited on p. 45.
- Keinert, B., M. Innmann, M. Sängler, and M. Stamminger. 2015. "Spherical Fibonacci mapping." *ACM Trans. Graph.* 34, no. 6 (November): 193:1–193:7. <https://doi.org/10.1145/2816795.2818131>. Cited on pp. 144, 160, 176.
- Khayat, M. A., and D. R. Wilton. 2005. "Numerical evaluation of singular and near-singular potential integrals." *IEEE Trans. Antennas Propag.* 53, no. 10 (October): 3180–3190. <https://doi.org/10.1109/tap.2005.856342>. Cited on p. 33.
- Kılıç, E., and T. F. Eibert. 2015. "Solution of 3D inverse scattering problems by combined inverse equivalent current and finite element methods." *J. Comput. Phys.* 288 (May): 131–149. <https://doi.org/10.1016/j.jcp.2015.02.004>. Cited on pp. 27, 28.
- Klein, C., and R. Mittra. 1975. "An application of the 'condition number' concept to the solution of scattering problems in the presence of the interior resonant frequencies." *IEEE Trans. Antennas Propag.* 23, no. 3 (March): 431–435. <https://doi.org/10.1109/tap.1975.1141094>. Cited on p. 19.
- Klinkenbusch, L. 2009. "On the uniqueness of electromagnetic fields and consequences for inverse-scattering problems." In *Proc. Int. Conf. Electromagn. Adv. Appl. (ICEAA)*, 396–399. Turin, IT, September. <https://doi.org/10.1109/iceaa.2009.5297409>. Cited on p. 182.

- Knapp, J. 2021. "Antenna Field Measurements and Transformations in Arbitrary Echoic Environments." Doctoral diss., Munich, DE: Tech. Univ. Munich. <http://mediatum.ub.tum.de/?id=1612760>. Cited on pp. 179, 182.
- Knapp, J., and T. F. Eibert. 2019. "Near-field antenna pattern measurements in highly reflective environments." *IEEE Trans. Antennas Propag.* 67, no. 9 (September): 6159–6169. <https://doi.org/10.1109/tap.2019.2922548>. Cited on pp. 160, 174.
- . 2018. "Accurate determination of radiation patterns from near-field measurements in highly reflective environments." In *Proc. 12th Eur. Conf. Antennas Propag. (EuCAP)*. London, UK, April. <https://doi.org/10.1049/cp.2018.0896>. Cited on p. 175.
- Knapp, J., J. Kornprobst, and T. F. Eibert. 2019a. "Equivalent source and pattern reconstruction from oversampled measurements in highly-reflective environments." *IET Microw. Antennas Propag.* 13 (October): 2232–2241. <https://doi.org/10.1049/iet-map.2019.0171>. Cited on pp. 28, 174, 175, 186.
- . 2020. "Suppressing undesired echoes by sparsity based time gating of reconstructed sources." In *Proc. 14th Eur. Conf. Antennas Propag. (EuCAP)*. Copenhagen, DK, March. <https://doi.org/10.23919/eucap48036.2020.9135733>. TechRxiv: 20127098. Cited on pp. 28, 131, 175, 186, 188, 189.
- Knapp, J., J. Kornprobst, A. Paulus, and T. F. Eibert. 2019b. "Time-gating the sources in inverse equivalent source reconstruction problems to eliminate mutual coupling effects." In *Proc. Int. Conf. Electromagn. Adv. Appl. (ICEAA)*. Granada, ES, September. <https://doi.org/10.1109/iceaa.2019.8878914>. Cited on pp. 28, 131, 175, 186, 188.
- Knapp, J., A. Paulus, and T. F. Eibert. 2019c. "Reconstruction of squared field magnitudes and relative phases from magnitude-only near-field measurements." *IEEE Trans. Antennas Propag.* 67, no. 5 (May): 3397–3409. <https://doi.org/10.1109/tap.2019.2900414>. Cited on pp. 190, 195.
- Knapp, J., A. Paulus, J. Kornprobst, U. Siart, and T. F. Eibert. 2021. "Multifrequency phase retrieval for antenna measurements." *IEEE Trans. Antennas Propag.* 69, no. 1 (January): 488–501. <https://doi.org/10.1109/tap.2020.3008648>. arXiv: 2105.09928. Cited on pp. 28, 131, 190, 191, 193–196.
- Knapp, J., A. Paulus, C. Lopez, and T. F. Eibert. 2017. "Comparison of non-convex cost functionals for the consideration of phase differences in phaseless near-field far-field transformations of measured antenna fields." *Adv. Radio Sci.* 15:11–19. <https://doi.org/10.5194/ars-15-11-2017>. Cited on p. 197.
- Kornprobst, J., J. Knapp, and T. F. Eibert. 2019a. "Approximate inverse of the Rao-Wilton-Glisson basis functions Gram matrix via monopolar representation." In *Proc. IEEE Int. Symp. Antennas Propag. USNC-URSI Radio Sci. Meeting (APSURSI)*. Atlanta, GA, US, July. <https://doi.org/10.1109/apuscursinrsm.2019.8888979>. TechRxiv: 20151677. Cited on pp. 49, 58, 68.
- Kornprobst, J., R. A. M. Mauermayer, O. Neitz, J. Knapp, and T. F. Eibert. 2019b. "On the solution of inverse equivalent surface-source problems." *Prog. Electromagn. Res.* 195:47–65. <https://doi.org/10.2528/pier19050904>. Cited on pp. 26–28, 131, 140, 142, 158, 172, 173.
- Kornprobst, J., and T. F. Eibert. 2017a. "Accurate and stable solutions to electromagnetic scattering problems by means of the electric field integral equation augmented by a weak combined source condition." In *Proc. Int. Conf. Electromagn. Adv. Appl. (ICEAA)*, 1240–1242. Verona, IT, September. <https://doi.org/10.1109/iceaa.2017.8065495>. TechRxiv: 20154170. Cited on p. 49.
- . 2017b. "An accurate combined source integral equation for perfect electrically conducting bodies." In *Proc. IEEE Int. Symp. Antennas Propag. & USNC/URSI Nat. Radio Sci. Meeting (APSURSI)*, 1457–1458. San Diego, CA, US, July. <https://doi.org/10.1109/apuscursinrsm.2017.8072771>. TechRxiv: 20151767. Cited on pp. 49, 103.

BIBLIOGRAPHY

- Kornprobst, J., and T. F. Eibert. 2017c. "RWG discretized combined source integral equation with improved iterative solver convergence." In *Kleinheubacher Tagung*. Miltenberg, DE, September. Cited on p. 49.
- . 2018a. "A combined source integral equation with weak form combined source condition." *IEEE Trans. Antennas Propag.* 66, no. 4 (April): 2151–2155. <https://doi.org/10.1109/tap.2018.2800734>. arXiv: 2010.08797. Cited on pp. 45, 49, 55, 139, 140.
- . 2018b. "A magnetic field integral equation with accurately discretized geometrical singularities." In *Kleinheubacher Tagung*. Miltenberg, DE, September. Cited on pp. 50, 121.
- . 2018c. "A weak-form combined source integral equation with explicit inversion of the combined-source condition." *IEEE Antennas Wireless Propag. Lett.* 17, no. 12 (December): 2174–2178. <https://doi.org/10.1109/lawp.2018.2869926>. arXiv: 2010.08757. Cited on pp. 45, 49, 55, 56.
- . 2018d. "Accurate identity operator discretization for the combined field integral equation." In *Proc. IEEE Int. Symp. Antennas Propag. & USNC-URSI Radio Sc. Meeting (APSURSI)*, 2437–2438. Boston, MA, US, July. <https://doi.org/10.1109/apuscursinrsm.2018.8608501>. TechRxiv: 20151734. Cited on p. 49.
- . 2018e. "An accurate low-order discretization scheme for the identity operator in the magnetic field and combined field integral equations." *IEEE Trans. Antennas Propag.* 66, no. 11 (November): 6146–6157. <https://doi.org/10.1109/tap.2018.2866578>. arXiv: 2010.08436. Cited on pp. 45, 49, 55, 62, 70, 74, 79, 85, 87–89, 94, 140.
- . 2018f. "Improved accuracy combined source and magnetic field integral equations with low-order discretization." In *Proc. 12th Eur. Conf. Antennas Propag. (EuCAP)*. London, UK, April. <https://doi.org/10.1049/cp.2018.0822>. TechRxiv: 20154167. Cited on p. 49.
- . 2019. "Investigations on the solution of the magnetic field integral equation with Rao-Wilton-Glisson basis functions." In *Proc. Int. Conf. Electromagn. Adv. Appl. (ICEAA)*. Granada, ES, September. <https://doi.org/10.1109/iceaa.2019.8879174>. Cited on pp. 49, 50, 121.
- . 2022. "Accuracy analysis of div-conforming hierarchical higher-order discretization schemes for the magnetic field integral equation," TechRxiv: 21153130. Cited on p. 50.
- Kornprobst, J., J. Knapp, R. A. M. Mauermayer, O. Neitz, A. Paulus, and T. F. Eibert. 2021a. "Accuracy and conditioning of surface-source based near-field to far-field transformations." *IEEE Trans. Antennas Propag.* 69, no. 8 (August): 4894–4908. <https://doi.org/10.1109/tap.2020.3048497>. arXiv: 2004.08918. Cited on pp. 26, 28, 131, 132, 145, 146, 153, 156–159, 163–165.
- Kornprobst, J., J. Knapp, O. Neitz, and T. F. Eibert. 2019c. "Measurement-error controlled iterative least-squares solutions of inverse field transformation problems." In *Proc. 41st Ann. Symp. Antenna Meas. Techn. Assoc. (AMTA)*. San Diego, CA, US, October. <https://doi.org/10.23919/amtap.2019.8906459>. TechRxiv: 20126231. Cited on pp. 131, 137, 158, 161, 162, 166, 167.
- Kornprobst, J., R. A. M. Mauermayer, A. Paulus, and T. F. Eibert. 2019d. "Method-of-moments modeling of conducting objects within the fast irregular antenna field transformation algorithm." In *Proc. 41st Ann. Symp. Antenna Meas. Techn. Assoc. (AMTA)*. San Diego, CA, US, October. <https://doi.org/10.23919/amtap.2019.8906355>. TechRxiv: 20126102. Cited on pp. 28, 131, 175, 176, 178.
- Kornprobst, J., R. A. M. Mauermayer, and T. F. Eibert. 2020. "Versatile low-cost and light-weight RF equipment for field measurements." In *Proc. 14th Eur. Conf. Antennas Propag. (EuCAP)*. Copenhagen, DK, March. <https://doi.org/10.23919/eucap48036.2020.9135598>. TechRxiv: 20126489. Cited on pp. 28, 131.

- Kornprobst, J., R. A. M. Mauermayer, E. Kılıç, and T. F. Eibert. 2019e. "An inverse equivalent surface current solver with zero-field enforcement by left-hand side Calderón projection." In *Proc. 13th Eur. Conf. Antennas Propag. (EuCAP)*. Krakow, PL, April. TechRxiv: 20153630. <https://ieeexplore.ieee.org/document/8739983>. Cited on pp. 28, 131, 140, 168–170.
- Kornprobst, J., R. A. M. Mauermayer, E. Kılıç, B. Möhring, and T. F. Eibert. 2019f. "Improved-accuracy Calderón projector with Rao-Wilton-Glisson discretization for inverse equivalent current methods." In *Proc. Photonics Electromagn. Res. Symp. (PIERS)*. Rome, IT, June. Cited on pp. 28, 131.
- Kornprobst, J., T. Mittermaier, P. Schmidbauer, and T. F. Eibert. 2016. "Signal recovery for self-mixing receivers." In *Kleinheubacher Tagung*. Miltenberg, DE, September. Cited on p. 1.
- Kornprobst, J., T. J. Mittermaier, and T. F. Eibert. 2017a. "Orthogonal frequency division multiplexing with amplitude shift keying subcarrier modulation as a reliable and efficient transmission scheme for self-mixing receivers." *Adv. Radio Sci.* 15:99–106. <https://doi.org/10.5194/ars-15-99-2017>. Cited on p. 1.
- . 2018a. "A millimeter-wave self-mixing array with large gain and wide angular receiving range." *IEEE Trans. Antennas Propag.* 66, no. 2 (February): 702–711. <https://doi.org/10.1109/tap.2017.2780897>. arXiv: 2105.08685. Cited on p. 1.
- . 2018b. "A non-reciprocal receive array with large beamwidth and gain." In *Proc. 11th German Microw. Conf. (GeMiC)*, 33–35. Freiburg, DE, March. <https://doi.org/10.23919/gemic.2018.8335021>. TechRxiv: 20153666. Cited on p. 1.
- Kornprobst, J., T. J. Mittermaier, R. A. M. Mauermayer, G. F. Hamberger, M. G. Ehrnsperger, B. Lehmeyer, M. T. Ivrlač, U. Imberg, T. F. Eibert, and J. A. Nossek. 2021b. "Compact uniform circular quarter-wavelength monopole antenna arrays with wideband decoupling and matching networks." *IEEE Transactions on Antennas and Propagation* 69, no. 2 (February): 769–783. <https://doi.org/10.1109/tap.2020.3016422>. arXiv: 2105.09333. Cited on p. 1.
- Kornprobst, J., O. Neitz, J. Knapp, R. A. M. Mauermayer, and T. F. Eibert. 2019g. "Solving inverse equivalent surface source problems by the normal error system of normal equations." In *Proc. Int. Conf. Electromagn. Adv. Appl. (ICEAA)*. Granada, ES, September. <https://doi.org/10.1109/iceaa.2019.8879105>. Cited on pp. 131, 158.
- Kornprobst, J., A. Paulus, and T. F. Eibert. 2021c. "Improved discretization of the full first-order magnetic field integral equation." In *Proc. 15th Eur. Conf. Antennas Propag. (EuCAP)*. Düsseldorf, DE, March. <https://doi.org/10.23919/eucap51087.2021.9410970>. arXiv: 2010.07351. Cited on pp. 50, 111.
- Kornprobst, J., A. Paulus, J. Knapp, and T. F. Eibert. 2021d. "Phase retrieval for partially coherent observations." *IEEE Trans. Signal Process.* 69:1394–1406. <https://doi.org/10.1109/tsp.2021.3057261>. arXiv: 2002.02939. Cited on pp. 28, 131, 190, 196, 197, 199–202.
- . 2022. "Multi-probe array design for partially-coherent phase retrieval in near-field measurements," TechRxiv: 21330702. Cited on pp. 131, 203.
- Kornprobst, J., K. Wang, G. Hamberger, and T. F. Eibert. 2017b. "A mm-wave patch antenna with broad bandwidth and a wide angular range." *IEEE Trans. Antennas Propag.* 65, no. 8 (August): 4293–4298. <https://doi.org/10.1109/tap.2017.2710261>. arXiv: 2105.08162. Cited on p. 1.
- Kozan, T., S. Burgos, L. J. Foged, F. Saccardi, and P. O. Iversen. 2014. "Comparison of a direct low-pass filtering technique with spherical modal filtering applied to the suppression of range reflections in antenna measurements." In *Proc. 8th Eur. Conf. Antennas Propag. (EuCAP)*, 2481–2485. The Hague, NL, April. <https://doi.org/10.1109/eucap.2014.6902322>. Cited on pp. 174, 179.

BIBLIOGRAPHY

- Larsen, F. H. 1977. "Probe correction of spherical near-field measurements." *Electron. Lett.* 13, no. 14 (July): 393–395. Cited on p. 28.
- Laviada, J., and F. Las-Heras. 2013. "Phaseless antenna measurement on non-redundant sample points via Leith-Upatnieks holography." *IEEE Trans. Antennas Propag.* 61, no. 8 (August): 4036–4044. <https://doi.org/10.1109/tap.2013.2262669>. Cited on p. 195.
- Laviada Martinez, J., A. Arboleya, Y. Alvarez-Lopez, C. Garcia-Gonzalez, and F. Las-Heras. 2014. "Phaseless antenna diagnostics based on off-axis holography with synthetic reference wave." *IEEE Antennas Wireless Propag. Lett.* 13:43–46. <https://doi.org/10.1109/lawp.2013.2295735>. Cited on p. 195.
- Leather, P. S. H., J. D. Parsons, and J. Romeu. 2004. "Signal processing techniques improve antenna pattern measurement." In *Proc. IEE Antenna Meas. SAR (AMS)*, 97–100. May. <https://doi.org/10.1049/ic:20040086>. Cited on p. 186.
- Lee, J.-F., R. Lee, and R. J. Burkholder. 2003. "Loop star basis functions and a robust preconditioner for EFIE scattering problems." *IEEE Trans. Antennas Propag.* 51, no. 8 (August): 1855–1863. <https://doi.org/10.1109/tap.2003.814736>. Cited on p. 41.
- Lee, J.-F., R. Lee, and A. Cangellaris. 1997. "Time-domain finite-element methods." *IEEE Trans. Antennas Propag.* 45, no. 3 (March): 430–442. <https://doi.org/10.1109/8.558658>. Cited on p. 2.
- Lee, J., and S. Nam. 2005. "Protecting the method of auxiliary sources (MAS) solutions from the interior resonance problem." *IEEE Microw. Compon. Lett.* 15, no. 3 (March): 186–188. <https://doi.org/10.1109/lmwc.2005.844220>. Cited on pp. 32, 50.
- Leibfritz, M. M., M. D. Blech, F. M. Landstorfer, and T. F. Eibert. 2007. "A comparison of software-and hardware-gating techniques applied to near-field antenna measurements." *Adv. Radio Sci.* 5:43–48. <https://doi.org/10.5194/ars-5-43-2007>. Cited on p. 186.
- Leith, E. N., and J. Upatnieks. 1962. "Reconstructed wavefronts and communication theory." *J. Opt. Soc. America* 52, no. 10 (October): 1123–1130. <https://doi.org/10.1364/josa.52.001123>. Cited on p. 195.
- Leone, G., M. A. Maisto, and R. Pierri. 2018. "Application of inverse source reconstruction to conformal antennas synthesis." *IEEE Trans. Antennas Propag.* 66, no. 3 (March): 1436–1445. <https://doi.org/10.1109/tap.2018.2794397>. Cited on p. 160.
- Leone, G., F. Munno, and R. Pierri. 2021. "Inverse source on conformal conic geometries." *IEEE Trans. Antennas Propag.* 69, no. 3 (March): 1596–1609. <https://doi.org/10.1109/tap.2020.3016375>. Cited on p. 160.
- Leontovich, M. A. 1948. "Approximate boundary conditions for the electromagnetic field on the surface of a good conductor." *Investigations Radiowave Propag.* 2:5–12. Cited on p. 10.
- Leviatan, Y., and Z. Baharav. 1995. "Overcoming the onset of ill conditioning at interior resonances by using generalized formulations." *Microw. Opt. Techn. Lett.* 9, no. 1 (May): 49–52. <https://doi.org/https://doi.org/10.1002/mop.4650090117>. Cited on p. 22.
- Levitas, B. N., and D. M. Ponomarev. 1996. "Antenna measurements in time domain." In *Proc. IEEE Antennas Propag. Soc. Int. Symp. (APS)*, 1:573–576. Baltimore, MD, US, July. <https://doi.org/10.1109/aps.1996.549664>. Cited on p. 186.
- Li, L. 2016. "Singularity Cancellation Transformations and Hierarchical Higher Order Basis Functions for the Hybrid Finite Element Boundary Integral Technique." Doctoral diss., Munich, DE: Tech. Univ. Munich. <https://mediatum.ub.tum.de/?id=1290418>. Cited on pp. 39, 112.

- Li, L., K. Wang, and T. F. Eibert. 2014a. "A projection height independent adaptive radial-angular- R^2 transformation for singular integrals." *IEEE Trans. Antennas Propag.* 62, no. 10 (October): 5381–5386. <https://doi.org/10.1109/tap.2014.2344103>. Cited on p. 33.
- Li, L., K. Wang, H. Li, and T. F. Eibert. 2014b. "Analytical finite element matrix elements and global matrix assembly for hierarchical 3-d vector basis functions within the hybrid finite element boundary integral method." *Advances in Radio Science* 12, no. B. 1 (November): 1–11. <https://doi.org/10.5194/ars-12-1-2014>. Cited on pp. 39, 111.
- Li, W. D., W. Hong, H. X. Zhou, and Z. Song. 2012. "Novel Buffa-Christiansen functions for improving CFIE with impedance boundary condition." *IEEE Trans. Antennas Propag.* 60, no. 8 (August): 3763–3771. <https://doi.org/10.1109/tap.2012.2201121>. Cited on pp. 47, 52.
- Li, Y., J. Wang, and K.-M. Luk. 2017. "Millimeter-wave multibeam aperture-coupled magnetolectric dipole array with planar substrate integrated beamforming network for 5G applications." *IEEE Trans. Antennas Propag.* 65 (12): 6422–6431. <https://doi.org/10.1109/tap.2017.2681429>. Cited on p. 1.
- Liu, D. C., and J. Nocedal. 1989. "On the limited memory BFGS method for large scale optimization." *Math. Program.* 45, no. 1 (August): 503–528. <https://doi.org/10.1007/bf01589116>. Cited on p. 192.
- Liu, Z.-L., X. Wang, and C.-F. Wang. 2014. "Installed performance modeling of complex antenna array mounted on extremely large-scale platform using fast MoM-PO hybrid framework." *IEEE Trans. Antennas Propag.* 62, no. 7 (July): 3852–3858. <https://doi.org/10.1109/tap.2014.2318319>. Cited on p. 3.
- Lopez, Y. A., F. Las-Heras, and M. R. Pino. 2009. "Application of the adaptive cross approximation algorithm to the sources reconstruction method." In *Proc 3rd Eur. Conf. Antennas Propag. (EuCAP)*, 761–765. Berlin, DE, March. <https://ieeexplore.ieee.org/document/5067730>. Cited on p. 28.
- Loredo, S., G. Leon, S. Zapatero, and F. Las-Heras. 2009. "Measurement of low-gain antennas in non-anechoic test sites through wideband channel characterization and echo cancellation [measurements corner]." *IEEE Antennas Propag. Mag.* 51, no. 1 (February): 128–135. <https://doi.org/10.1109/map.2009.4939035>. Cited on p. 186.
- Loredo, S., M. R. Pino, F. Las-Heras, and T. K. Sarkar. 2004. "Echo identification and cancellation techniques for antenna measurement in non-anechoic test sites." *IEEE Antennas Propag. Mag.* 46, no. 1 (February): 100–107. <https://doi.org/10.1109/map.2004.1296154>. Cited on p. 186.
- Lorenz, L. 1867. "XXXVIII. On the identity of the vibrations of light with electrical currents." *London Edinburgh Dublin Phil. Mag. J. Sci.* 34 (230): 287–301. <https://doi.org/10.1080/14786446708639882>. Cited on p. 7.
- Lori, F. S. H., A. Menshov, R. Gholami, J. B. Mojolagbe, and V. I. Okhmatovski. 2018. "Novel single-source surface integral equation for scattering problems by 3-D dielectric objects." *IEEE Trans. Antennas Propag.* 66, no. 2 (February): 797–807. <https://doi.org/10.1109/tap.2017.2781740>. Cited on p. 13.
- Lou, Z., and J.-M. Jin. 2006. "A novel dual-field time-domain finite-element domain-decomposition method for computational electromagnetics." *IEEE Trans. Antennas Propag.* 54, no. 6 (June): 1850–1862. <https://doi.org/10.1109/tap.2006.875922>. Cited on p. 2.
- Love, A. E. H. 1901. "The integration of the equations of propagation of electric waves." *Phil. Trans. R. Soc. A* 197 (287): 1–43. <https://doi.org/10.1098/rsta.1901.0013>. Cited on pp. 10, 27.

BIBLIOGRAPHY

- Ludwig, A. 1971. "Near-field far-field transformations using spherical-wave expansions." *IEEE Trans. Antennas Propag.* 19, no. 2 (March): 214–220. <https://doi.org/10.1109/tap.1971.1139909>. Cited on p. 26.
- Luk, K.-M., and B. Wu. 2012. "The magnetoelectric dipole—A wideband antenna for base stations in mobile communications." *Proc. IEEE* 100 (July): 2297–2307. <https://doi.org/10.1109/jproc.2012.2187039>. Cited on p. 13.
- Ma, J., S.-X. Gong, X. Wang, Y. Liu, and Y.-X. Xu. 2012. "Efficient wide-band analysis of antennas around a conducting platform using MoM-PO hybrid method and asymptotic waveform evaluation technique." *IEEE Trans. Antennas Propag.* 60, no. 12 (December): 6048–6052. <https://doi.org/10.1109/tap.2012.2210272>. Cited on p. 3.
- Mackenzie, A. I., S. M. Rao, and M. E. Baginski. 2009. "Electromagnetic scattering from arbitrarily shaped dielectric bodies using paired pulse vector basis functions and method of moments." *IEEE Trans. Antennas Propag.* 57, no. 7 (July): 2076–2083. <https://doi.org/10.1109/tap.2009.2021891>. Cited on p. 47.
- Mahmood, S. N., A. J. Ishak, T. Saeidi, H. Alsariera, S. Alani, A. Ismail, and A. C. Soh. 2020. "Recent advances in wearable antenna technologies: a review." *Prog. Electromagn. Res. B* 89:1–27. <https://doi.org/10.2528/pierb20071803>. Cited on p. 1.
- Manohar, V., and Y. Rahmat-Samii. 2017. "Benchmarking full wave analysis of periodic structures: non perpendicularity at periodic boundaries." In *Proc. IEEE Int. Symp. Antennas Propag. & USNC/URSI Nat. Radio Sci. Meeting (APSURSI)*. San Diego, CA, US, July. Cited on p. 2.
- Marchand, R., J. van Tonder, M. Bingle, D. le Roux, M. van Rooyen, and U. Jakobus. 2017. "The benefit of simple benchmarks to highlight problems in CEM codes." In *Proc. IEEE Int. Symp. Antennas Propag. & USNC/URSI Nat. Radio Sci. Meeting (APSURSI)*. San Diego, CA, US, July. Cited on p. 2.
- Marin, S. P. 1982. "Computing scattering amplitudes for arbitrary cylinders under incident plane waves." *IEEE Trans. Antennas Propag.* 30, no. 6 (November): 1045–1049. <https://doi.org/10.1109/tap.1982.1142939>. Cited on p. 17.
- Martin, P. A., and P. Ola. 1993. "Boundary integral equations for the scattering of electromagnetic waves by a homogeneous dielectric obstacle." *Proc. Roy. Soc. Edinburgh Section A Math.* 123 (1): 185–208. <https://doi.org/10.1017/s0308210500021296>. Cited on p. 22.
- Martini, E., G. Carli, and S. Maci. 2008. "An equivalence theorem based on the use of electric currents radiating in free space." *IEEE Antennas Wireless Propag. Lett.* 7:421–424. <https://doi.org/10.1109/lawp.2008.2001764>. Cited on p. 27.
- Martinson, P.-G., V. Rohklin, and M. Tygert. 2011. "A randomized algorithm for the decomposition of matrices." *Appl. Comput. Harmonic Anal.* 30, no. 1 (January): 47–69. <https://doi.org/10.1016/j.acha.2010.02.003>. Cited on p. 146.
- Marx, E. 1982. "Single integral equation for wave scattering." *J. Math. Phys.* 23, no. 6 (June): 1057–1065. <https://doi.org/10.1063/1.525494>. Cited on p. 13.
- Massa, A., P. Rocca, and G. Oliveri. 2015. "Compressive sensing in electromagnetics—a review." *IEEE Antennas Propag. Mag.* 57, no. 1 (February): 224–238. <https://doi.org/10.1109/map.2015.2397092>. Cited on p. 1.

- Massey, J. W., and A. E. Yilmaz. 2017. "Austin benchmark suite for computational bioelectromagnetics: AIM performance data." In *Proc. IEEE Int. Symp. Antennas Propag. & USNC/URSI Nat. Radio Sci. Meeting (APSURSI)*, 257–258. San Diego, CA, US: IEEE. <https://doi.org/10.1109/apusncursinrsm.2017.8072171>. Cited on p. 2.
- Massey, J. W. 2018. "A multiregion-integral-equation method for wearable and implantable device design and evaluation: modeling, high-performance algorithms, and postprocessing." Dissertation, Austin, TX, US: Tech. Univ. Texas Austin. Cited on p. 2.
- Massey, J. W., J. T. Kelley, C. C. Courtney, D. A. Chamulak, and A. E. Yilmaz. 2018. "A benchmark suite for quantifying RCS simulation performance on modern computers." In *Proc. IEEE Int. Symp. Antennas Propag. & USNC/URSI Nat. Radio Sci. Meeting (APSURSI)*, 67–68. Boston, MA, US: IEEE, July. <https://doi.org/10.1109/usnc-ursi.2018.8602595>. Cited on p. 2.
- Maue, A.-W. 1949. "Zur Formulierung eines allgemeinen Beugungsproblems durch eine Integralgleichung." *Zeitschrift für Physik* 126, nos. 7-9 (July): 601–618. <https://doi.org/10.1007/bf01328780>. Cited on pp. 18, 19, 34, 46.
- Mauermayer, R. A. M., J. Kornprobst, and T. Fritzel. 2019. "A low-cost multicopter based near-field antenna measurement system employing software defined radio and 6-D laser metrology." In *Proc. 41st Ann. Symp. Antenna Meas. Techn. Assoc. (AMTA)*. San Diego, CA, US, October. <https://doi.org/10.23919/amtap.2019.8906481>. TechRxiv: 20126321. Cited on pp. 28, 131, 170.
- Mauermayer, R. A. M., and T. F. Eibert. 2015. "Combining the fast irregular antenna field transformation algorithm with asymptotic high frequency methods." In *Proc. 9th Eur. Conf. Antennas Propag. (EuCAP)*. Lisbon, PT, April. <https://ieeexplore.ieee.org/document/7228184>. Cited on p. 175.
- . 2016. "Time gating based on sparse time domain signal reconstruction from limited frequency domain information." In *AMTA 2016 Proceedings*. Austin, TX, US, November. <https://doi.org/10.1109/amtap.2016.7806275>. Cited on p. 186.
- . 2017. "Sparse time domain signal representation for echo suppression in antenna measurements." In *Proc. Int. Conf. Electromagn. Adv. Appl. (ICEAA)*, 1247–1249. Verona, IT, September. <https://doi.org/10.1109/iceaa.2017.8065497>. Cited on pp. 175, 186.
- . 2018. "Spherical field transformation above perfectly electrically conducting ground planes." *IEEE Trans. Antennas Propag.* 65 (3): 1465–1478. <https://doi.org/10.1109/tap.2018.2794406>. Cited on pp. 28, 163.
- Mauermayer, R. A. M., and J. Kornprobst. 2022. "A cost-effective tethered-UAV-based coherent near-field antenna measurement system." *IEEE Open J. Antennas Propag.* 3:984–1002. <https://doi.org/10.1109/ojap.2022.3198269>. TechRxiv: 20115938. Cited on pp. 131, 170.
- Mauermayer, R. A. M., G. Schnattinger, and T. F. Eibert. 2013. "Antenna diagnostic, echo suppression and equivalent sources representation capabilities of the fast irregular antenna field transformation algorithm." In *Proc. 35th Annu. Symp. Antenna Meas. Techn. Assoc. (AMTA)*. Columbus, OH, US, October. Cited on pp. 174, 179.
- Mautz, J. R., and R. F. Harrington. 1984. "An E-field solution for a conducting surface small or comparable to the wavelength." *IEEE Trans. Antennas Propag.* 32, no. 4 (April): 330–339. <https://doi.org/10.1109/tap.1984.1143316>. Cited on p. 40.
- Mautz, J. R., and R. F. Harrington. 1977. *Electromagnetic scattering from a homogeneous body of revolution*. Technical report. Syracuse, NY, US: Syracuse Univ., Dept. Elect. Comput. Eng., November. Cited on p. 17.

BIBLIOGRAPHY

- Mautz, J. R., and R. F. Harrington. 1978. "H-field, E-field, and combined-field solutions for conducting bodies of revolution." *A.E.Ü. (Germany)* 32, no. 4 (April): 157–164. Cited on p. 22.
- . 1979. "A combined-source solution for radiation and scattering from a perfectly conducting body." *IEEE Trans. Antennas Propag.* 27, no. 4 (July): 445–454. <https://doi.org/10.1109/tap.1979.1142115>. Cited on pp. 12, 23, 24, 139.
- Maxwell, J. C. 1865. "A dynamical theory of the electromagnetic field." *Phil. Trans. R. Soc. London*, no. 155, 459–512. <https://doi.org/doi.org/10.1098/rstl.1865.0008>. Cited on pp. 1, 6.
- Medgyesi-Mitschang, L., and D.-S. Wang. 1985. "Hybrid solutions at internal resonances." *IEEE Trans. Antennas Propag.* 33, no. 6 (June): 671–674. <https://doi.org/10.1109/tap.1985.1143643>. Cited on p. 22.
- Mei, K., and J. G. van Bladel. 1963. "Scattering by perfectly-conducting rectangular cylinders." *IEEE Trans. Antennas Propag.* 11, no. 2 (March): 185–192. <https://doi.org/10.1109/tap.1963.1137996>. Cited on p. 19.
- Mei, K., and M. Moberg. 1965. "Measurement of surface current distributions on cylindrical obstacles." *Proc. IEEE* 53, no. 8 (August): 1104–1105. <https://doi.org/10.1109/proc.1965.4107>. Cited on p. 19.
- Meixner, J. 1949. "Die Kantenbedingung in der Theorie der Beugung elektromagnetischer Wellen an vollkommen leitenden ebenen Schirmen." *Annalen der Physik* 6:2–9. <https://doi.org/10.1002/andp.19494410103>. Cited on p. 46.
- . 1972. "The behavior of electromagnetic fields at edges." *IEEE Trans. Antennas Propag.* 20, no. 4 (August): 442–446. <https://doi.org/10.1109/tap.1972.1140243>. Cited on p. 46.
- Melenk, J. M. 2012. "Mapping properties of combined field Helmholtz boundary integral operators." *SIAM J. Math. Anal.* 44 (4): 2599–2636. <https://doi.org/10.1137/100784072>. Cited on p. 12.
- Menshov, A., and V. Okhmatovski. 2013. "New single-source surface integral equations for scattering on penetrable cylinders and current flow modeling in 2-D conductors." *IEEE Trans. Microw. Theory Techn.* 61, no. 1 (January): 341–350. <https://doi.org/10.1109/tmtt.2012.2227784>. Cited on p. 13.
- Merlini, A. 2019. "Unified Computational Frameworks Bridging Low to High Frequency Simulations: Fast and High Fidelity Modelling from Brain to Radio-Frequency Scenarios." PhD diss., Brest, FR: Ecole nationale supérieure Mines-Télécom Atlantique. <https://tel.archives-ouvertes.fr/tel-02466106/>. Cited on p. 48.
- Merlini, A., Y. Beghein, K. Cools, E. Michielssen, and F. P. Andriulli. 2020. "Magnetic and combined field integral equations based on the quasi-Helmholtz projectors." *IEEE Trans. Antennas Propag.* 68, no. 5 (May): 3834–3846. <https://doi.org/10.1109/tap.2020.2964941>. Cited on p. 48.
- Miao, J., R. L. Sandberg, and C. Song. 2012. "Coherent X-ray diffraction imaging." *IEEE J. Sel. Topics Quantum Electron.* 18 (1): 399–410. <https://doi.org/10.1109/jstqe.2011.2157306>. Cited on p. 190.
- Michalski, K. A., and A. A. Kucharski. 2014. "On the surface limit in the boundary integral equations of electromagnetics." *IEEE Trans. Antennas Propag.* 62 (1): 257–263. <https://doi.org/10.1109/tap.2013.2287005>. Cited on p. 46.
- Mitharwal, R., and F. P. Andriulli. 2015. "A regularised boundary element formulation for contactless SAR evaluations within homogeneous and inhomogeneous head phantoms." *Comptes Rendus Physique* 16, no. 9 (November): 776–788. <https://doi.org/10.1016/j.crhy.2015.10.003>. Cited on p. 175.

- Modiri, A., S. Goudreau, A. Rahimi, and K. Kiasaleh. 2017. "Review of breast screening: toward clinical realization of microwave imaging." *Med. Phys.* 44, no. 12 (December): e446–e458. <https://doi.org/10.1002/mp.12611>. Cited on p. 1.
- Mohsen, A. A., A.-R. A. Helaly, and H. M. Fahmy. 1995. "The corrected induced surface current for arbitrary conducting objects at resonance frequencies." *IEEE Trans. Antennas Propag.* 43, no. 5 (May): 448–452. <https://doi.org/10.1109/8.384188>. Cited on p. 22.
- Molisch, A. F., V. V. Ratnam, S. Han, Z. Li, S. L. H. Nguyen, L. Li, and K. Haneda. 2017. "Hybrid beamforming for massive MIMO: a survey." *IEEE Commun. Mag.* 55, no. 9 (September): 134–141. <https://doi.org/10.1109/mcom.2017.1600400>. Cited on p. 1.
- Moretta, R., and R. Pierri. 2019. "Performance of phase retrieval via phaselift and quadratic inversion in circular scanning case." *IEEE Trans. Antennas Propag.* 67, no. 12 (December): 7528–7537. <https://doi.org/10.1109/tap.2019.2930127>. Cited on p. 197.
- Morita, N., N. Kumagai, and J. R. Mautz. 1990. *Integral Equation Methods for Electromagnetics: Theory and Practice*. Norwood, MA, US: Artech House. Cited on pp. 12, 23, 31.
- Müller, C. 1948. "Grundprobleme der mathematischen Theorie elektromagnetischer Schwingungen." *Archiv der Mathematik* 1, no. 4 (July): 296–302. Cited on p. 11.
- . 1969. *Foundations of the Mathematical Theory of Electromagnetic Waves*. Berlin/Heidelberg, DE: Springer-Verlag. <https://doi.org/10.1007/978-3-662-11773-6>. Cited on p. 17.
- Murphy, W. D., V. Rokhlin, and M. S. Vassiliou. 1990. "Solving electromagnetic scattering problems at resonance frequencies." *J. Appl. Phys.* 67 (10): 6061–6065. <https://doi.org/10.1063/1.345217>. Cited on p. 22.
- Nayeri, P., F. Yang, and A. Z. Elsherbeni. 2018. *Reflectarray antennas: theory, designs, and applications*. Hoboken, NJ, US: Wiley. Cited on p. 1.
- Nédélec, J.-C. 1980. "Mixed finite elements in \mathbb{R}^3 ." *Numerische Mathematik* 35 (3): 315–341. Cited on pp. 37, 46.
- . 2001. *Acoustic and Electromagnetic Equations: Integral Representations for Harmonic Problems*. New York, NY, US: Springer-Verlag. Cited on pp. 35–37, 140.
- Neitz, O., R. A. M. Mauer Mayer, Y. Weitsch, and T. F. Eibert. 2017. "A propagating plane-wave based near-field transmission equation for antenna gain determination from irregular measurement samples." *IEEE Trans. Antennas Propag.* 65, no. 8 (August): 4230–4238. <https://doi.org/10.1109/tap.2017.2712180>. Cited on p. 162.
- Neitz, O. 2015. "Propagating Plane-Wave Expansions for Microwave Near-Field Imaging and Radar Cross Section Determination." Doctoral diss., Munich, DE: Tech. Univ. Munich. <https://mediatum.ub.tum.de/?id=1523208>. Cited on p. 29.
- Netrapalli, P., P. Jain, and S. Sanghavi. 2015. "Phase retrieval using alternating minimization." *IEEE Trans. Signal Process.* 63, no. 18 (September): 4814–4826. <https://doi.org/10.1109/tsp.2015.2448516>. Cited on p. 190.
- Neumann, F. E. 1845. "Allgemeine Gesetze der inducirten elektrischen Ströme." *Abhandlungen der Königlich Akademie der Wissenschaften zu Berlin* 21 (16): 1–87. <https://archive.org/details/abhandlungenderk1845deut>. Cited on p. 7.

BIBLIOGRAPHY

- Niemi, T., P. Alitalo, A. O. Karilainen, and S. A. Tretyakov. 2012. "Electrically small Huygens source antenna for linear polarisation." *IET Microw. Antennas Propag.* 6 (May): 735–739. <https://doi.org/10.1049/iet-map.2011.0551>. Cited on p. 13.
- Nikolova, N. K. 2011. "Microwave imaging for breast cancer." *IEEE Microw. Mag.* 12, no. 7 (December): 78–94. <https://doi.org/10.1109/mmm.2011.942702>. Cited on p. 1.
- Nocedal, J., and S. J. Wright. 2006. *Numerical Optimization*. 2nd ed. New York, NY, US: Springer-Verlag. Cited on p. 192.
- Ohm, G. S. 1827. *Die galvanische Kette, mathematisch bearbeitet von Dr. G. S. Ohm*. Berlin, DE: T. H. Riemann. Cited on p. 6.
- Omi, S., T. Uno, T. Arima, and J. Wiart. 2019. "Reconstruction of internal field of dielectric objects for noninvasive SAR measurement using boundary integral equation." *IEEE Trans. Electromagn. Compat.* 61, no. 1 (February): 48–56. <https://doi.org/10.1109/temc.2018.2813398>. Cited on p. 175.
- Oshiro, F. K., K. M. Mitgner, S. S. Locus, J. R. Coleman, and H. C. Heath. 1970. *Calculation of Radar Cross Section*. Air Force Avionics Laboratory, AFAL-TR-70-21, Part II, April. Cited on p. 22.
- Ostrzyharczik, D., J. Knapp, J. Kornprobst, and T. F. Eibert. 2023. "Inverse source solutions with huygens-surface conforming distributed directive spherical harmonics expansions." *IEEE Trans. Antennas Propag.* 71 (2): 1684–1696. <https://doi.org/10.1109/tap.2022.3228752>. TechRxiv: 21259221. Cited on p. 150.
- Pan, G. G., M. Jin, L. Zhang, M. Bai, and J. Miao. 2014. "An efficient scattering algorithm for smooth and sharp surfaces: Coiflet-based scalar MFIE." *IEEE Trans. Antennas Propag.* 62, no. 8 (August): 4241–4250. <https://doi.org/10.1109/tap.2014.2322886>. Cited on p. 46.
- Parini, C., S. Gregson, J. McCormick, D. J. van Rensburg, and T. F. Eibert. 2020. *Theory and Practice of Modern Antenna Range Measurements*. 2nd ed. London, UK: IET. <https://doi.org/10.1049/sbra538f>. Cited on p. 26.
- Patel, U. R., P. Triverio, and S. V. Hum. 2017. "A novel single-source surface integral method to compute scattering from dielectric objects." *IEEE Antennas Wireless Propag. Lett.* 16:1715–1718. <https://doi.org/10.1109/lawp.2017.2669183>. Cited on p. 13.
- Paulus, A., and T. F. Eibert. 2018. "Brute-force GPU accelerated evaluation of dipole-dipole interactions." In *Proc. IEEE Int. Symp. Antennas Propag. & USNC-URSI Radio Sc. Meeting (APSURSI)*, 1839–1840. Boston, MA, US, July. <https://doi.org/10.1109/apusncursinrsm.2018.8609189>. Cited on p. 191.
- . 2020. "Exploiting spatial derivative information in phaseless near-field far-field transformations." In *Proc. 14th Eur. Conf. Antennas Propag. (EuCAP)*. Copenhagen, DK, March. <https://doi.org/10.23919/eucap48036.2020.9135672>. Cited on p. 190.
- Paulus, A., J. Knapp, and T. F. Eibert. 2017a. "Utilizing partial knowledge of phase differences in convex optimization for amplitude-only near-field far-field transformation." In *Proc. 11th Eur. Conf. Antennas Propag. (EuCAP)*, 3766–3770. Paris, FR, March. <https://doi.org/10.23919/eucap.2017.7928262>. Cited on pp. 195, 203.
- . 2017b. "Phaseless near-field far-field transformation utilizing combinations of probe signals." *IEEE Trans. Antennas Propag.* 65, no. 10 (October): 5492–5502. <https://doi.org/10.1109/tap.2017.2735463>. Cited on pp. 28, 190, 195–197, 200, 202, 203.

- . 2018. “Nonconvex phaseless near-field far-field transformation for electrically large problems.” In *Proc. 12th Eur. Conf. Antennas Propag. (EuCAP)*. London, UK, April. <https://doi.org/10.1049/cp.2018.0634>. Cited on pp. 160, 195.
- Paulus, A., J. Knapp, J. Kornprobst, and T. F. Eibert. 2022a. “Reliable linearized phase retrieval for near-field antenna measurements with truncated measurement surfaces.” *IEEE Trans. Antennas Propag.* 70, no. 8 (August): 7362–7367. <https://doi.org/10.1109/tap.2022.3145383>. arXiv: 2109.10864. Cited on pp. 131, 197, 199, 203.
- . 2020. “Improved-reliability phase-retrieval with broadband antenna measurements.” In *Proc. 14th Eur. Conf. Antennas Propag. (EuCAP)*. Copenhagen, DK, March. <https://doi.org/10.23919/eucap48036.2020.9135084>. TechRxiv: 20126813. Cited on pp. 28, 131, 190, 191, 195.
- Paulus, A., J. Kornprobst, and T. F. Eibert. 2022b. “Electromagnetic field transformations of near-field data without global reference for magnitude and phase.” In *Proc. 44th Ann. Meeting Symp. Antenna Meas. Techn. Assoc. (AMTA)*. Denver, CO, US, October. TechRxiv: 20352672. Cited on p. 197.
- Paulus, A., J. Kornprobst, J. Knapp, and T. F. Eibert. 2021. “Linear phase retrieval for near-field measurements with locally known phase relations.” In *Proc. 15th Eur. Conf. Antennas Propag. (EuCAP)*. Düsseldorf, DE, March. <https://doi.org/10.23919/eucap51087.2021.9411328>. arXiv: 2011.08980. Cited on pp. 28, 131, 190, 197.
- Paulus, A., J. Kornprobst, R. A. M. Mauermayer, and T. F. Eibert. 2019. “Comparison of source localization and scatterer modeling in near-field antenna measurements.” In *Proc. 13th Eur. Conf. Antennas Propag. (EuCAP)*. Krakow, PL, April. TechRxiv: 20154089. <https://ieeexplore.ieee.org/document/8739513>. Cited on pp. 28, 131, 142, 175, 176, 182, 183, 187.
- Pauwels, E. J. R., A. Beck, Y. C. Eldar, and S. Sabach. 2018. “On Fienup methods for sparse phase retrieval.” *IEEE Trans. Signal Process.* 66, no. 4 (February): 982–991. <https://doi.org/10.1109/tsp.2017.2780044>. Cited on p. 190.
- Peng, Z., K.-H. Lim, and J.-F. Lee. 2013. “A discontinuous Galerkin surface integral equation method for electromagnetic wave scattering from nonpenetrable targets.” *IEEE Trans. Antennas Propag.* 61, no. 7 (July): 3617–3628. <https://doi.org/10.1109/TAP.2013.2258394>. Cited on p. 45.
- Persson, K., and M. Gustafsson. 2005. “Reconstruction of equivalent currents using a near-field data transformation-with radome applications.” *Prog. Electromagn. Res.* 54:179–198. <https://doi.org/10.2528/piero4111602>. Cited on p. 28.
- Persson, K., M. Gustafsson, and G. Kristensson. 2010. “Reconstruction and visualization of equivalent currents on a radome using an integral representation formulation.” *Prog. Electromagn. Res. B* 20:65–90. <https://doi.org/doi:10.2528/pierb10012109>. Cited on p. 28.
- Persson, K., M. Gustafsson, G. Kristensson, and B. Widenberg. 2014. “Radome diagnostics—source reconstruction of phase objects with an equivalent currents approach.” *IEEE Trans. Antennas Propag.* 62, no. 4 (April): 2041–2051. <https://doi.org/10.1109/tap.2014.2298534>. Cited on p. 28.
- Persson, P., and L. Josefsson. 2001. “Calculating the mutual coupling between apertures on a convex circular cylinder using a hybrid UTD-MoM method.” *IEEE Trans. Antennas Propag.* 49, no. 4 (April): 672–677. <https://doi.org/10.1109/8.923330>. Cited on p. 17.
- Peterson, A. F. 1990. “The ‘interior resonance’ problem associated with surface integral equations of electromagnetics: numerical consequences and a survey of remedies.” *Electromagn.* 10, no. 3 (July): 293–312. <https://doi.org/10.1080/02726349008908245>. Cited on p. 19.

BIBLIOGRAPHY

- Peterson, A. F. 2002. "Solution of the MFIE using curl-conforming basis functions." In *Proc. IEEE Antennas Propag. Soc. Int. Symp. (APSURSI)*, 1:70–73. San Antonio, TX, US, June. <https://doi.org/10.1109/aps.2002.1016253>. Cited on p. 45.
- . 2006. *Mapped Vector Basis Functions for Electromagnetic Integral Equations*. San Rafael, CA, US: Morgan & Claypool. Cited on p. 39.
- . 2008. "Observed baseline convergence rates and superconvergence in the scattering cross section obtained from numerical solutions of the MFIE." *IEEE Trans. Antennas Propag.* 56, no. 11 (November): 3510–3515. <https://doi.org/10.1109/tap.2008.2005461>. Cited on p. 45.
- Peterson, A. F., and R. Mittra. 1987. *Mutual Admittance between Slots in Cylinders of Arbitrary Shape*. Technical report. Urbana, IL, US: Univ. Illinois, Coordinated Sci. Lab., UILU-ENG-87-2247, August. Cited on p. 19.
- Peterson, A. F., S. L. Ray, and R. Mittra. 1997. *Computational Methods for Electromagnetics*. Hoboken, NJ, US: Wiley-IEEE Press. Cited on pp. 2, 31.
- Petre, P., and T. K. Sarkar. 1992. "Planar near-field to far-field transformation using an equivalent magnetic current approach." *IEEE Trans. Antennas Propag.* 40, no. 11 (November): 1348–1356. <https://doi.org/10.1109/8.202712>. Cited on pp. 26, 27.
- . 1994. "Planar near-field to far-field transformation using an array of dipoles." *IEEE Trans. Antennas Propag.* 42, no. 4 (April): 534–537. <https://doi.org/10.1109/8.286223>. Cited on p. 27.
- Pfeiffer, F., T. Weitkamp, O. Bunk, and C. David. 2006. "Phase retrieval and differential phase-contrast imaging with low-brilliance X-ray sources." 2, no. 4 (April): 258–261. <https://doi.org/10.1038/nphys265>. Cited on p. 190.
- Pierri, R., G. D'Elia, and F. Soldovieri. 1999. "A two probes scanning phaseless near-field far-field transformation technique." *IEEE Trans. Antennas Propag.* 47, no. 5 (May): 792–802. <https://doi.org/10.1109/8.774132>. Cited on p. 28.
- Pierri, R., G. Leone, and R. Moretta. 2020. "Phaseless near-field techniques from a random starting point." In *Proc. XXXIIIrd General Assembly Sci. Symp. Int. Union Radio Sci. (URSI GASS)*. Rome, IT, September. <https://doi.org/10.23919/ursigass49373.2020.9232012>. Cited on p. 197.
- Piestun, R., and D. A. B. Miller. 2000. "Electromagnetic degrees of freedom of an optical system." *J. Opt. Soc. Amer. A* 17, no. 5 (May): 892–902. <https://doi.org/10.1364/josaa.17.000892>. Cited on p. 134.
- Poggio, A. J., and E. K. Miller. 1973. *Integral equation solutions of three-dimensional scattering problems*, edited by R. Mittra. Elmsford, NY, US: Pergamon. Cited on pp. 17, 22.
- Pohl, V., H. Boche, and C. Yapar. 2017. "Modulated wideband converter for compressive phase retrieval of bandlimited signals." In *Proc. 11th Int. ITG Conf. Syst. Commun. Coding*. Hamburg, Germany, February. <https://ieeexplore.ieee.org/document/7938086>. Cited on p. 197.
- Pohl, V., F. Yang, and H. Boche. 2014. "Phaseless signal recovery in infinite dimensional spaces using structured modulations." *J. Fourier Anal. Appl.* 20 (6): 1212–1233. <https://doi.org/10.1007/s00041-014-9352-3>. Cited on p. 190.
- Popovidi-Zaridze, R., D. Karkashadze, G. Ahvlediani, and J. Khatiashvili. 1978. "Investigation of possibilities of the method of auxiliary sources in solution of two-dimensional electrodynamics problems." *Radiotech. Electron.* 22 (2). Cited on p. 32.

- Qiu, T., and D. P. Palomar. 2017. "Undersampled sparse phase retrieval via majorization–minimization." *IEEE Trans. Signal Process.* 65, no. 22 (November): 5957–5969. <https://doi.org/10.1109/tsp.2017.2745459>. Cited on p. 190.
- Qureshi, M. A., C. H. Schmidt, and T. F. Eibert. 2013. "Efficient near-field far-field transformation for nonredundant sampling representation on arbitrary surfaces in near-field antenna measurements." *IEEE Trans. Antennas Propag.* 61, no. 4 (April): 2025–2033. <https://doi.org/10.1109/tap.2012.2231932>. Cited on p. 28.
- Ramos, T., B. E. Grønager, M. S. Andersen, and J. W. Andreasen. 2019. "Direct three-dimensional tomographic reconstruction and phase retrieval of far-field coherent diffraction patterns." *Phys. Rev. A* 99, no. 2 (February): 023801. <https://doi.org/10.1103/physreva.99.023801>. Cited on p. 190.
- Rao, S. M., and D. R. Wilton. 1990. "E-field, H-field, and combined field solution for arbitrarily shaped three-dimensional dielectric bodies." *Electromagn.* 10, no. 4 (October): 407–421. <https://doi.org/10.1080/02726349008908254>. Cited on pp. 34, 45, 52.
- Rao, S. M., D. R. Wilton, and A. W. Glisson. 1982. "Electromagnetic scattering by surfaces of arbitrary shape." *IEEE Trans. Antennas Propag.* 30, no. 3 (May): 409–418. <https://doi.org/10.1109/tap.1982.1142818>. Cited on pp. 34, 37, 38, 85.
- Raviart, P. A., and J. M. Thomas. 1977. "A mixed finite element method for 2-nd order elliptic problems." In *Mathematical Aspects of the Finite Element Method*, edited by I. Galligani and E. Magenes, 292–315. Berlin/Heidelberg, DE: Springer. <https://doi.org/10.1007/bfb0064470>. Cited on p. 37.
- RFspin. 2021a. "Model DRH18 – Double-Ridged Waveguide Horn Antenna." <https://www.rfspin.com>. Cited on pp. 162, 165, 192.
- . 2021b. "Model DRH400 – Double-Ridged Waveguide Horn Antenna." <https://www.rfspin.com>. Cited on pp. 155, 165.
- Rius, J. M., E. Ubeda, and J. Parron. 2001. "On the testing of the magnetic field integral equation with RWG basis functions in method of moments." *IEEE Trans. Antennas Propag.* 49, no. 11 (November): 1550–1553. <https://doi.org/10.1109/8.964090>. Cited on pp. 45, 46.
- Rodríguez Varela, F., J. Fernandez Álvarez, B. Galocha Iragüen, M. Sierra Castañer, and O. Breinbjerg. 2021a. "Numerical and experimental investigation of phaseless spherical near-field antenna measurements." *IEEE Trans. Antennas Propag.* 69, no. 12 (December): 8830–8841. <https://doi.org/10.1109/tap.2021.3090846>. Cited on p. 197.
- Rodríguez Varela, F., M. J. López Morales, R. Tena-Sánchez, A. T. Muriel Barrado, E. de la Fuente González, G. Posada Quijano, C. Zarzuelo Torres, M. Sierra Pérez, and M. Sierra Castañer. 2021b. "Multi-probe measurement system based on single-cut transformation for fast testing of linear arrays." *Sensors* 21 (5): 1744. <https://doi.org/10.3390/s21051744>. Cited on pp. 197, 203.
- Rogers, J. 1985. "On combined source solutions for bodies with impedance boundary conditions." *IEEE Trans. Antennas Propag.* 33, no. 4 (April): 462–465. <https://doi.org/10.1109/tap.1985.1143594>. Cited on pp. 12, 23.
- Rohde & Schwarz. 2021. "R&S HF907 Antenna – Double-Ridged Waveguide Horn Antenna." <https://www.rohde-schwarz.com>. Cited on p. 172.
- Rubinowicz, A. 1926. "Über die Eindeutigkeit der Lösung der Maxwellschen Gleichungen." *Physikalische Zeitschrift* 27 (July): 707–710. Cited on p. 11.

BIBLIOGRAPHY

- Rylander, T., P. Ingelström, and A. Bondeson. 2012. *Computational electromagnetics*. 2nd ed. New York, NY, US: Springer-Verlag. <https://doi.org/10.1007/978-1-4614-5351-2>. Cited on p. 2.
- Saad, Y. 1996. *Iterative Methods for Sparse Linear Systems*. 2nd ed. Boston, MA, US: PWS. <https://doi.org/10.1137/1.9780898718003>. Cited on pp. 90, 136, 137.
- Saad, Y., and M. H. Schultz. 1986. "GMRES: A generalized minimal residual algorithm for solving nonsymmetric linear systems." *SIAM J. Sci. Stat. Comput.* 7, no. 3 (July): 856–869. <https://doi.org/10.1137/0907058>. Cited on pp. 56, 136.
- Saccardi, F., F. Mioc, L. Foged, J. Estrada, P. Iversen, M. Edgerton, and J. Graham. 2019. "Comparative investigation of spatial filtering techniques for ground plane removal in PEC-based automotive measurements." In *Proc. Antenna Meas. Techn. Assoc. Symp. (AMTA)*. San Diego, CA, US, October. <https://doi.org/10.23919/amtap.2019.8906476>. Cited on p. 28.
- Saporetti, M. A., F. Saccardi, L. J. Foged, J. Zackrisson, M. Righero, G. Giordanengo, G. Vecchi, and D. Trenta. 2019. "Reduced sampling in NF antenna measurement using numerical defined expansion functions." In *Proc. 13th Eur. Conf. Antennas Propag. (EuCAP)*. Krakow, PL, April. <https://ieeexplore.ieee.org/document/8739300>. Cited on p. 186.
- Sarkar, T. K., and A. Taaghool. 1999. "Near-field to near/far-field transformation for arbitrary near-field geometry utilizing an equivalent electric current and MoM." *IEEE Trans. Antennas Propag.* 47, no. 3 (March): 566–573. <https://doi.org/10.1109/8.768793>. Cited on pp. 26, 27.
- Scattono, F., D. Sekuljica, A. Giacomini, F. Saccardi, A. Scannavini, E. Kaverine, S. Anwar, N. Gross, P. O. Iversen, and L. J. Foged. 2021. "Towards testing of 5G millimeter wave devices using plane wave generators." In *Proc. 15th Eur. Conf. Antennas Propag. (EuCAP)*. Düsseldorf, DE, April. <https://doi.org/10.23919/eucap51087.2021.9411117>. Cited on p. 28.
- Schelkunoff, S. A. 1936. "Some equivalence theorems of electromagnetics and their application to radiation problems." *Bell System Tech. J.* 15 (1): 92–112. <https://doi.org/10.1002/j.1538-7305.1936.tb00720.x>. Cited on pp. 10, 27.
- Schelkunoff, S. A., and H. T. Friis. 1952. *Antennas: Theory and Practice*. New York, NY, US: Wiley. Cited on p. 13.
- Schmidt, C. H., and T. F. Eibert. 2009. "Multilevel plane wave based near-field far-field transformation for electrically large antennas in free-space or above material halfspace." *IEEE Trans. Antennas Propag.* 57, no. 5 (May): 1382–1390. <https://doi.org/10.1109/tap.2009.2016699>. Cited on p. 28.
- Schmidt, C. H., M. M. Leibfritz, and T. F. Eibert. 2008. "Fully probe-corrected near-field far-field transformation employing plane wave expansion and diagonal translation operators." *IEEE Trans. Antennas Propag.* 56, no. 3 (March): 737–746. <https://doi.org/10.1109/tap.2008.916975>. Cited on p. 28.
- Schmidt, C. H., and Y. Rahmat-Samii. 2009. "Phaseless spherical near-field antenna measurements: concept, algorithm and simulation." In *Proc. IEEE Antennas Propag. Soc. Int. Symp. (APSURSI)*. North Charleston, SC, US, June. <https://doi.org/10.1109/aps.2009.5171897>. Cited on pp. 190, 202.
- Schnattinger, G. 2014. "Elektromagnetische Nahfeld- und Fernfeld-Bildgebungsverfahren basierend auf hierarchischen Felddarstellungen." Doctoral diss., Munich, DE: Tech. Univ. Munich. <https://mediatum.ub.tum.de/?id=1230918>. Cited on p. 29.
- Schroeder, W., and I. Wolff. 1994. "The origin of spurious modes in numerical solutions of electromagnetic field eigenvalue problems." *IEEE Trans. Microw. Theory Techn.* 42, no. 4 (April): 644–653. <https://doi.org/10.1109/22.285071>. Cited on p. 34.

- Senior, T. B. A., and J. L. Volakis. 1995. *Approximate Boundary Conditions in Electromagnetics*. IEE Electromagnetic Waves 41. London, UK: Inst. Elect. Eng. Cited on pp. 2, 10.
- Shafieipour, M., J. Aronsson, and V. Okhmatovski. 2017. "On higher order imperative in computational electromagnetics through benchmarking of boundary element methods for canonical scattering problems." In *Proc. IEEE Int. Symp. Antennas Propag. & USNC/URSI Nat. Radio Sci. Meeting (APSURSI)*. San Diego, CA, US, July. Cited on p. 2.
- Shechtman, Y., Y. C. Eldar, O. Cohen, H. N. Chapman, J. Miao, and M. Segev. 2015. "Phase retrieval with application to optical imaging: a contemporary overview." *IEEE Signal Process. Mag.* 32, no. 3 (May): 87–109. <https://doi.org/10.1109/msp.2014.2352673>. Cited on p. 190.
- Shi, Y., and C. Liang. 2015. "An efficient single-source integral equation solution to EM scattering from a coated conductor." *IEEE Antennas Wireless Propag. Lett.* 14:547–550. <https://doi.org/10.1109/lawp.2014.2371460>. Cited on p. 13.
- Silver, S. 1949. *Microwave Antenna Theory and Design*. New York, NY, US: McGraw-Hill. Cited on p. 11.
- Singh, A., M. Andreello, N. Thawdar, and J. M. Jornet. 2020. "Design and operation of a graphene-based plasmonic nano-antenna array for communication in the terahertz band." *IEEE J. Sel. Areas Commun.* 38 (9): 2104–2117. <https://doi.org/10.1109/jsac.2020.3000881>. Cited on p. 1.
- Sissouno, N., F. Boßmann, F. Filbir, M. Iwen, M. Kahnt, R. Saab, C. Schroer, and W. zu Castell. 2019. "A direct solver for the phase retrieval problem in ptychographic imaging." *Math. Comput. Simulation* 176 (October): 292–300. <https://doi.org/10.1016/j.matcom.2019.11.003>. Cited on p. 190.
- Smith, M. H., and A. F. Peterson. 2005. "Numerical solution of the CFIE using vector bases and dual interlocking meshes." *IEEE Trans. Antennas Propag.* 53, no. 10 (October): 3334–3339. <https://doi.org/10.1109/tap.2005.856332>. Cited on p. 47.
- Sommerfeld, A. 1912. "Die Greensche Funktion der Schwingungsgleichung." *Jahresbericht der Deutschen Mathematiker-Vereinigung* 21:309–352. Cited on p. 8.
- . 1949. *Partial Differential Equations in Physics*. New York, NY, US: Academic. Cited on p. 8.
- Steatite Ltd. 2021. "QSR-1200-A-755 & QWF-DL-2-18-S-R – 1.2 m Reflector Antenna." <https://www.steatiteqpar-antennas.co.uk>. Cited on p. 162.
- Steinbach, O., and M. Windisch. 2009. "Modified combined field integral equations for electromagnetic scattering." *SIAM J. Numer. Anal.* 47 (2): 1149–1167. <https://doi.org/10.1137/070698063>. Cited on p. 12.
- Stephanson, M. B., and J.-F. Lee. 2009. "Preconditioned electric field integral equation using Calderón identities and dual loop/star basis functions." *IEEE Trans. Antennas Propag.* 57, no. 4 (April): 1274–1279. <https://doi.org/10.1109/tap.2009.2016173>. Cited on pp. 41, 44.
- Stratton, J. A. 1941. *Electromagnetic Theory*. New York, NY, US: McGraw-Hill. Cited on p. 11.
- Stratton, J. A., and L. J. Chu. 1939. "Diffraction theory of electromagnetic waves." *Phys. Rev.* 56, no. 1 (July): 99. <https://doi.org/10.1103/physrev.56.99>. Cited on p. 18.
- Stupfel, B. 2015. "Implementation of high-order impedance boundary conditions in some integral equation formulations." *IEEE Trans. Antennas Propag.* 63, no. 4 (April): 1658–1668. <https://doi.org/10.1109/tap.2015.2392125>. Cited on p. 54.

BIBLIOGRAPHY

- Stupfel, B., and Y. Morel. 2008. "Singular value decomposition of the radiation operator—application to model-order and far-field reduction." *IEEE Trans. Antennas Propag.* 56, no. 6 (June): 1605–1615. <https://doi.org/10.1109/tap.2008.923311>. Cited on p. 134.
- Stutzman, W. L., and G. A. Thiele. 2013. *Antenna Theory and Design*. 3rd ed. Hoboken, NJ, US: Wiley. Cited on p. 15.
- Sumithra, P., and D. Thiripurasundari. 2017. "Review on computational electromagnetics." *Adv. Electro-magn.* 6 (1): 42–55. <https://doi.org/10.7716/aem.v6i1.407>. Cited on p. 2.
- Sun, D.-K., J.-F. Lee, and Z. Cendes. 2001. "Construction of nearly orthogonal Nédélec bases for rapid convergence with multilevel preconditioned solvers." *SIAM J. Sci. Comput.* 23 (4): 1053–1076. <https://doi.org/10.1137/s1064827500367531>. Cited on pp. 39, 111.
- Tataria, H., M. Shafi, A. F. Molisch, M. Dohler, H. Sjöland, and F. Tufvesson. 2021. "6G wireless systems: vision, requirements, challenges, insights, and opportunities." *Proc. IEEE* 109 (7). <https://doi.org/10.1109/jproc.2021.3061701>. Cited on p. 1.
- Tena-Sánchez, R., F. Rodríguez Varela, L. J. Foged, and M. Sierra Castañer. 2021a. "Reconstruction of relative phase of self-transmitting devices by using multiprobe solutions and non-convex optimization." *Sensors* 21 (7): 2459. <https://doi.org/10.3390/s21072459>. Cited on pp. 197, 203.
- Tena-Sánchez, R., and M. Sierra-Castañer. 2018. "Evaluation of software defined radio receiver for phaseless near-field measurements." In *Proc. 40th Ann. Meeting Symp. Antenna Meas. Techn. Assoc. (AMTA)*. Williamsburg, VA, USA, November. <https://ieeexplore.ieee.org/document/8604160>. Cited on p. 195.
- Tena-Sánchez, R., M. Sierra-Castañer, R. Albarracín-Sánchez, F. R. Varela, A. Scannavini, and L. J. Foged. 2021b. "Feasibility study of near field multiprobe system as EMC measurement set-up." In *Proc. 15th Eur. Conf. Antennas Propag. (EuCAP)*. Dusseldorf, DE, March. <https://doi.org/10.23919/eucap51087.2021.9410953>. Cited on pp. 195, 197, 203.
- Tena-Sánchez, R., M. Sierra-Castañer, and L. J. Foged. 2020. "Relative phase reconstruction based on multiprobe solutions and post-processing techniques." In *Proc. 14th Eur. Conf. Antennas Propag. (EuCAP)*. Copenhagen, DK, March. <https://doi.org/10.23919/eucap48036.2020.9135867>. Cited on pp. 195, 197, 203.
- Thomson, W. 1851. "X. A mathematical theory of magnetism." *Phil. Trans. R. Soc.*, 243–268. <https://doi.org/10.1098/rstl.1851.0012>. Cited on p. 7.
- Tice, T. E., and J. H. Richmond. 1955. "Probes for microwave near-field measurements." *IRE Trans. Microw. Theory Techn.* 3, no. 3 (April): 32–34. <https://doi.org/10.1109/tmtt.1955.1124943>. Cited on p. 26.
- Tiesinga, E., P. J. Mohr, D. B. Newell, and B. N. Taylor. 2020. "The 2018 CODATA Recommended Values of the Fundamental Physical Constants (Web Version 8.1)." Database developed by J. Baker, M. Douma, and S. Kotchigova. <http://physics.nist.gov/constants>. Cited on p. 7.
- Tong, M. S., W. C. Chew, B. J. Rubin, J. D. Morsey, and L. Jiang. 2009. "On the dual basis for solving electromagnetic surface integral equations." *IEEE Trans. Antennas Propag.* 57, no. 10 (October): 3136–3146. <https://doi.org/10.1109/tap.2009.2028622>. Cited on p. 37, 47.
- Trintinalia, L. C., and H. Ling. 2000. "An improved triangular patch basis for the method of moments." In *Proc. IEEE Antennas Propag. Soc. Int. Symp. USNC/URSI Nat. Radio Sci. Meeting (APSURSI)*, 4:2306–2309. Salt Lake City, UT, US, July. <https://doi.org/10.1109/aps.2000.874955>. Cited on p. 46.

- . 2001. “First order triangular patch basis functions for electromagnetic scattering analysis.” *J. Electromagn. Waves Appl.* 15, no. 11 (November): 1521–1537. <https://doi.org/10.1163/156939301X00085>. Cited on p. 111.
- Tsalamengas, J. L. 2016. “A generalized reaction theorem that eliminates internal resonances in the electric and magnetic field integral equations.” *IEEE Trans. Antennas Propag.* 64, no. 11 (November): 4745–4752. <https://doi.org/10.1109/tap.2016.2602400>. Cited on p. 22.
- Tzoulis, A., and T. F. Eibert. 2005. “A hybrid FEBI-MLFMM-UTD method for numerical solutions of electromagnetic problems including arbitrarily shaped and electrically large objects.” *IEEE Trans. Antennas Propag.* 53, no. 10 (October): 3358–3366. <https://doi.org/10.1109/tap.2005.856348>. Cited on p. 17.
- Ubeda, E., and J. M. Rius. 2005a. “Monopolar divergence-conforming and curl-conforming low-order basis functions for the electromagnetic scattering analysis.” *Microw. Opt. Tech. Lett.* 46 (3): 237–241. <https://doi.org/10.1002/mop.20955>. Cited on p. 45.
- . 2005b. “MFIE MoM-formulation with curl-conforming basis functions and accurate kernel integration in the analysis of perfectly conducting sharp-edged objects.” *Microw. Opt. Techn. Lett.* 44 (4): 354–358. <https://doi.org/10.1002/mop.20633>. Cited on p. 45.
- . 2006. “Novel monopolar MFIE MoM-discretization for the scattering analysis of small objects.” *IEEE Trans. Antennas Propag.* 54, no. 1 (January): 50–57. <https://doi.org/10.1109/tap.2005.861529>. Cited on p. 45.
- Varela, F. R., B. G. Iragüen, and M. S. Castañer. 2021. “Practical considerations in phaseless spherical near-field measurements.” In *Proc. Antenna Meas. Techn. Assoc. Symp. (AMTA)*. Daytona Beach, FL, US, October. <https://doi.org/10.23919/amtas2830.2021.9620657>. Cited on p. 197.
- Varela, F. R., B. G. Iragüen, M. S. Castañer, J. F. Álvarez, M. Mattes, and O. Breinbjerg. 2019. “Combination of spherical and planar scanning for phaseless near-field antenna measurements.” In *Proc. Antenna Meas. Techn. Assoc. Symp. (AMTA)*. San Diego, CA, US, October. <https://doi.org/10.23919/amtap.2019.8906466>. Cited on pp. 197, 202.
- Varela, F. R., B. G. Iragüen, and M. Sierra-Castañer. 2020. “Near-field to far-field transformation on arbitrary surfaces via multi-level spherical wave expansion.” *IEEE Trans. Antennas Propag.* 68, no. 1 (January): 500–508. <https://doi.org/10.1109/tap.2019.2935108>. Cited on p. 28.
- Wandzura, S. 1992. “Electric current basis functions for curved surfaces.” *Electromagn.* 12 (1): 77–91. <https://doi.org/10.1080/02726349208908297>. Cited on p. 46.
- Wang, G., L. Zhang, G. B. Giannakis, M. Akcakaya, and J. Chen. 2018. “Sparse phase retrieval via truncated amplitude flow.” *IEEE Trans. Signal Process.* 66, no. 2 (January): 479–491. ISSN: 1053-587X. <https://doi.org/10.1109/tsp.2017.2771733>. Cited on p. 190.
- Wang, K., J. Kornprobst, and T. F. Eibert. 2016. “Microstrip fed broadband mm-wave patch antenna for mobile applications.” In *Proc. IEEE Int. Symp. Antennas Propag. (APSURSI)*, 1637–1638. Fajardo, PR, US, July. <https://doi.org/10.1109/aps.2016.7696525>. TechRxiv: 20151530. Cited on p. 1.
- Wang, M., F. Gao, S. Jin, and H. Lin. 2019. “An overview of enhanced massive MIMO with array signal processing techniques.” *IEEE J. Sel. Topics Signal Process.* 13, no. 5 (September): 886–901. <https://doi.org/10.1109/jstsp.2019.2934931>. Cited on p. 1.
- Wang, Y., T. F. Eibert, and Z. Nie. 2018. “Adaptive cross approximation algorithm accelerated inverse equivalent current method for near-field antenna measurement.” *IEEE Trans. Antennas Propag.* 67, no. 3 (March): 1874–1883. <https://doi.org/10.1109/tap.2018.2889023>. Cited on p. 28.

BIBLIOGRAPHY

- Wang, Y., and W. C. Chew. 1989. "An iterative solution of the two-dimensional electromagnetic inverse scattering problem." *Int. J. Imaging Syst. Technol.* 1 (1): 100–108. <https://doi.org/10.1002/ima.1850010111>. Cited on p. 28.
- Want, R. 2011. "Near field communication." *IEEE Pervasive Comput.* 10 (3): 4–7. <https://doi.org/10.1109/mprv.2011.55>. Cited on p. 1.
- Warnick, K. F., and A. F. Peterson. 2007. "3D MFIE accuracy improvement using regularization." In *IEEE Antennas Propag. Soc. Int. Symp. (APS)*, 4857–4860. Honolulu, HI, US, June. <https://doi.org/10.1109/aps.2007.4396632>. Cited on p. 45.
- Waterman, P. C. 1965. "Matrix formulation of electromagnetic scattering." *Proc. IEEE* 53, no. 8 (August): 805–812. <https://doi.org/10.1109/proc.1965.4058>. Cited on p. 19.
- Weber, W. E. 1846. "Elektrodynamische Maafsbestimmungen über ein allgemeines Grundgesetz der elektrischen Wirkung." *Abhandlungen bei Begründung der Königl. Sächs. Gesellschaft der Wissenschaften am Tage der zweihundertjährigen Geburtstagfeier Leibnizens*, 211–378. Cited on p. 7.
- Wegglar, L. 2011. "High Order Boundary Element Methods." Doctoral diss., Saarbrücken, DE: Saarland University. <https://doi.org/10.22028/d291-26256>. Cited on pp. 77, 79.
- Wiedenmann, O. 2015. "Near-Zone and Domain Decomposition Based Preconditioning Methods for the Solution of Surface Integral Equations." Doctoral diss., Munich, DE: Tech. Univ. Munich. <https://mediatum.ub.tum.de/?id=1228605>. Cited on p. 60.
- Wilton, D. R., and A. W. Glisson. 1981. "On improving the electric field integral equation at low frequencies." *Proc. URSI Radio Sci. Meet. Dig* (Los Angeles, CA, US) (June): 24. Cited on p. 40.
- Woodhouse, I. H. 2017. *Introduction to microwave remote sensing*. Boca Raton, FL, US: CRC Press. <https://doi.org/10.1201/9781315272573>. Cited on p. 1.
- Wu, A. C. T., and C. N. Yang. 2006. "Evolution of the concept of the vector potential in the description of fundamental interactions." *Int. J. Modern Phys. A* 21 (16): 3235–3277. <https://doi.org/10.1142/s0217751x06033143>. Cited on p. 7.
- Wu, T.-K., and L. L. Tsai. 1977. "Scattering from arbitrarily-shaped lossy dielectric bodies of revolution." *Radio Sci.* 12 (5): 709–718. <https://doi.org/10.1029/rs012i005p00709>. Cited on p. 17.
- Wu, B.-Y., and X.-Q. Sheng. 2013. "Application of asymptotic waveform evaluation to hybrid FE-BI-MLFMA for fast RCS computation over a frequency band." *IEEE Trans. Antennas Propag.* 61, no. 5 (May): 2597–2604. <https://doi.org/10.1109/tap.2013.2246532>. Cited on p. 3.
- Wu, J.-Y., and R. Lee. 1997. "The advantages of triangular and tetrahedral edge elements for electromagnetic modeling with the finite-element method." *IEEE Trans. Antennas Propag.* 45, no. 9 (September): 1431–1437. <https://doi.org/10.1109/8.623133>. Cited on p. 2.
- Yaccarino, R. G., and Y. Rahmat-Samii. 1999. "Phaseless bi-polar planar near-field measurements and diagnostics of array antennas." *IEEE Trans. Antennas Propag.* 47, no. 3 (March): 574–583. <https://doi.org/10.1109/8.768794>. Cited on pp. 28, 190, 202.
- Yaghjian, A. D. 1981. "Augmented electric and magnetic-field integral equations." *Radio Sci.* 16 (06): 987–1001. <https://doi.org/10.1029/rs016i006p00987>. Cited on p. 19.
- . 1986. "An overview of near-field antenna measurements." *IEEE Trans. Antennas Propag.* 34, no. 1 (January): 30–45. <https://doi.org/10.1109/tap.1986.1143727>. Cited on p. 26.

- Yan, S., J.-M. Jin, and Z. Nie. 2013. "Accuracy improvement of the second-kind integral equations for generally shaped objects." *IEEE Trans. Antennas Propag.* 61, no. 2 (February): 788–797. <https://doi.org/10.1109/tap.2012.2224835>. Cited on pp. 45, 47.
- Yan, S., and J.-M. Jin. 2013. "Self-dual integral equations for electromagnetic scattering from IBC objects." *IEEE Trans. Antennas Propag.* 61, no. 11 (November): 5533–5546. <https://doi.org/10.1109/tap.2013.2276929>. Cited on pp. 37, 47, 52.
- Yan, S., J.-M. Jin, and Z. Nie. 2009. "EFIE analysis of low-frequency problems with loop-star decomposition and Calderón multiplicative preconditioner." *IEEE Trans. Antennas Propag.* 58, no. 3 (March): 857–867. <https://doi.org/10.1109/tap.2009.2039336>. Cited on p. 41.
- . 2011a. "Improving the accuracy of the second-kind fredholm integral equations by using the buffa-christiansen functions." *IEEE Trans. Antennas Propag.* 59, no. 4 (April): 1299–1310. <https://doi.org/10.1109/tap.2011.2109364>. Cited on pp. 37, 44, 47, 64.
- . 2011b. "On the testing of the identity operator and the accuracy improvement of the second-kind SIEs." In *Proc. IEEE Int. Symp. Antennas Propag. (APSURSI)*, 3185–3188. Spokane, WA, US, July. <https://doi.org/10.1109/aps.2011.5997210>. Cited on pp. 45, 47, 56, 61.
- Yang, X., Y. R. Zheng, M. T. Ghasr, and K. M. Donnell. 2017. "Microwave imaging from sparse measurements for near-field synthetic aperture radar." *IEEE Trans. Instrum. Meas.* 66, no. 10 (October): 2680–2692. <https://doi.org/10.1109/tim.2017.2708379>. Cited on p. 1.
- Yeung, M. S. 1999. "Single integral equation for electromagnetic scattering by three-dimensional homogeneous dielectric objects." *IEEE Trans. Antennas Propag.* 47, no. 10 (October): 1615–1622. <https://doi.org/10.1109/8.805907>. Cited on p. 13.
- Yinusa, K. A., and T. F. Eibert. 2013. "A multi-probe antenna measurement technique with echo suppression capability." *IEEE Trans. Antennas Propag.* 61, no. 10 (October): 5008–5016. <https://doi.org/10.1109/tap.2013.2271495>. Cited on p. 175.
- Yinusa, K. A. 2015. "Echo Suppression Techniques for Near-Field Antenna Measurements." Doctoral diss., Munich, DE: Tech. Univ. Munich. <https://mediatum.ub.tum.de/?id=1252148>. Cited on p. 28.
- Yinusa, K. A., C. H. Schmidt, and T. F. Eibert. 2012a. "Modeling of unknown echoic measurement facilities with equivalent scattering centers." In *Proc. 6th Eur. Conf. Antennas Propag. (EuCAP)*, 2104–2108. Prague, CZ. <https://doi.org/10.1109/eucap.2012.6205875>. Cited on p. 179.
- . 2012b. "Scattering centers modeling of non-anechoic measurement environments." *Adv. Radio Sci.* 10:69–73. <https://doi.org/10.5194/ars-10-69-2012>. Cited on p. 179.
- Ylä-Oijala, P., S. P. Kiminki, K. Cools, F. P. Andriulli, and S. Järvenpää. 2012a. "Stable discretization of combined source integral equation for scattering by dielectric objects." *IEEE Trans. Antennas Propag.* 60, no. 5 (May): 2575–2578. <https://doi.org/10.1109/tap.2012.2189706>. Cited on pp. 47, 50, 52.
- Ylä-Oijala, P., S. P. Kiminki, and S. Järvenpää. 2010. "Solving IBC-CFIE with dual basis functions." *IEEE Trans. Antennas Propag.* 58, no. 12 (December): 3997–4004. <https://doi.org/10.1109/tap.2010.2078473>. Cited on pp. 37, 47, 52.
- . 2013a. "Electric and magnetic combined source integral equations for electromagnetic transmission problems." *Eng. Anal. Boundary Elements* 37, no. 1 (January): 68–73. <https://doi.org/10.1016/jenganabound.2012.08.012>. Cited on pp. 47, 50, 52.

BIBLIOGRAPHY

- Ylä-Oijala, P., M. Taskinen, and S. Järvenpää. 2005. "Surface integral equation formulations for solving electromagnetic scattering problems with iterative methods." *Radio Sci.* 40, no. 06 (December): 1–19. <https://doi.org/10.1029/2004rs003169>. Cited on pp. 46, 111.
- Ylä-Oijala, P., S. P. Kiminki, K. Cools, F. P. Andriulli, and S. Järvenpää. 2012b. "Mixed discretization schemes for electromagnetic surface integral equations." *Int. J. Numer. Model. Electron. Netw. Devices Fields* 25, nos. 5-6 (January): 525–540. <https://doi.org/10.1002/jnm.844>. Cited on p. 37.
- Ylä-Oijala, P., S. P. Kiminki, J. Markkanen, and S. Järvenpää. 2013b. "Error-controllable and well-conditioned MoM solutions in computational electromagnetics: ultimate surface integral-equation formulation." *IEEE Antennas Propag. Mag.* 55, no. 6 (December): 310–331. <https://doi.org/10.1109/map.2013.6781749>. Cited on pp. 37, 45.
- Ylä-Oijala, P., J. Lappalainen, and S. Järvenpää. 2018. "Characteristic mode equations for impedance surfaces." *IEEE Trans. Antennas Propag.* 66, no. 1 (January): 487–492. <https://doi.org/10.1109/tap.2017.2772873>. Cited on p. 54.
- Ylä-Oijala, P., J. Markkanen, S. Järvenpää, and S. P. Kiminki. 2014. "Surface and volume integral equation methods for time-harmonic solutions of Maxwell's equations (invited paper)." *Prog. Electromagn. Res.* 149:15–44. <https://doi.org/10.2528/pier14070105>. Cited on pp. 37, 45.
- Ylä-Oijala, P., M. Taskinen, and S. Järvenpää. 2008. "Analysis of surface integral equations in electromagnetic scattering and radiation problems." *Eng. Anal. with Boundary Elements* 32, no. 3 (March): 196–209. <https://doi.org/10.1016/j.enganabound.2007.08.004>. Cited on p. 46.
- Yuan, X. 1990. "Three-dimensional electromagnetic scattering from inhomogeneous objects by the hybrid moment and finite element method." *IEEE Trans. Microw. Theory Techn.* 38, no. 8 (August): 1053–1058. <https://doi.org/10.1109/22.57330>. Cited on p. 34.
- Zhang, L., A. Deng, M. Wang, and S. Yang. 2010. "Numerical study of a novel MFIE formulation using monopolar RWG basis functions." *Comput. Physics Commun.* 181 (1): 52–60. <https://doi.org/10.1016/j.cpc.2009.08.012>. Cited on p. 45.
- Zhang, Y., T. J. Cui, W. C. Chew, and J.-S. Zhao. 2003. "Magnetic field integral equation at very low frequencies." *IEEE Trans. Antennas Propag.* 51, no. 8 (August): 1864–1871. <https://doi.org/10.1109/tap.2003.814753>. Cited on pp. 44, 84.
- Zhao, J.-S., and W. C. Chew. 2000. "Integral equation solution of Maxwell's equations from zero frequency to microwave frequencies." *IEEE Trans. Antennas Propag.* 48, no. 10 (October): 1635–1645. <https://doi.org/10.1109/8.899680>. Cited on p. 41.
- Zhao, K., M. N. Vouvakis, and J.-F. Lee. 2005. "The adaptive cross approximation algorithm for accelerated method of moments computations of EMC problems." *IEEE Trans. Electromagn. Compat.* 47, no. 4 (November): 763–773. <https://doi.org/10.1109/temc.2005.857898>. Cited on p. 28.
- Zheng, J., T. Yang, H. Liu, T. Su, and L. Wan. 2020. "Accurate detection and localization of unmanned aerial vehicle swarms-enabled mobile edge computing system." *IEEE Trans. Ind. Inform.* 17, no. 7 (July): 5059–5067. <https://doi.org/10.1109/tii.2020.3015730>. Cited on p. 1.
- Zhu, G.-Y., H.-X. Zhou, and W. Hong. 2019. "An overlapping domain decomposition method based on Calderón preconditioned CFIE." *IEEE Antennas Wireless Propag. Lett.* 18 (9): 1731–1735. <https://doi.org/10.1109/lawp.2019.2928521>. Cited on p. 48.
- Zhu, Y., and A. C. Cangellaris. 2006. *Multigrid finite element methods for electromagnetic field modeling*. Hoboken, NJ, US: Wiley. Cited on p. 39.

BIBLIOGRAPHY

- Zink, M., M. Bachmann, B. Brautigam, T. Fritg, I. Hajnsek, A. Moreira, B. Wessel, and G. Krieger. 2014. "TanDEM-X: the new global DEM takes shape." *IEEE Geosci. Remote Sens. Mag.* 2, no. 2 (June): 8–23. <https://doi.org/10.1109/mgrs.2014.2318895>. Cited on p. 1.

Publications of the Author

- Eibert, T. F., D. Ostrzyharczik, J. Kornprobst, and J. Knapp. 2022a. "On the generation of distributed spherical harmonics expansions for inverse source solutions." TechRxiv: 21330690.
- . 2022b. "Solution of inverse source problems with distributed spherical harmonics expansions." In *Proc. 3rd URSI Atlantic/Asia-Pacific Radio Sci. Meeting (AT-AP-RASC)*. Gran Canaria, ES, June. <https://doi.org/10.23919/at-ap-rasc54737.2022.9814176>. TechRxiv: 20146901.
- Faul, F. T., J. Kornprobst, T. Fritzel, H. Steiner, R. Strauss, A. Weiss, R. Geise, and T. F. Eibert. 2018. "A concept study of near-field measurements and corresponding field transformations of the modulated fields of air navigation systems." In *Kleinheubacher Tagung*. Miltenberg, DE, September.
- Faul, F. T., J. Kornprobst, T. Fritzel, H.-J. Steiner, R. Strauß, A. Weiß, R. Geise, and T. F. Eibert. 2019. "Near-field measurement of continuously modulated fields employing the time-harmonic near- to far-field transformation." *Adv. Radio Sci.* 17:83–89. <https://doi.org/10.5194/ars-17-83-2019>.
- Knapp, J., J. Kornprobst, and T. F. Eibert. 2019a. "Equivalent source and pattern reconstruction from oversampled measurements in highly-reflective environments." *IET Microw. Antennas Propag.* 13 (October): 2232–2241. <https://doi.org/10.1049/iet-map.2019.0171>.
- . 2020. "Suppressing undesired echoes by sparsity based time gating of reconstructed sources." In *Proc. 14th Eur. Conf. Antennas Propag. (EuCAP)*. Copenhagen, DK, March. <https://doi.org/10.23919/eucap48036.2020.9135733>. TechRxiv: 20127098.
- Knapp, J., J. Kornprobst, A. Paulus, and T. F. Eibert. 2019b. "Time-gating the sources in inverse equivalent source reconstruction problems to eliminate mutual coupling effects." In *Proc. Int. Conf. Electromagn. Adv. Appl. (ICEAA)*. Granada, ES, September. <https://doi.org/10.1109/iceaa.2019.8878914>.
- Knapp, J., A. Paulus, J. Kornprobst, U. Siart, and T. F. Eibert. 2021. "Multifrequency phase retrieval for antenna measurements." *IEEE Trans. Antennas Propag.* 69, no. 1 (January): 488–501. <https://doi.org/10.1109/tap.2020.3008648>. arXiv: 2105.09928.
- Kornprobst, J., J. Knapp, and T. F. Eibert. 2019a. "Approximate inverse of the Rao-Wilton-Glisson basis functions Gram matrix via monopolar representation." In *Proc. IEEE Int. Symp. Antennas Propag. USNC-URSI Radio Sci. Meeting (APSURSI)*. Atlanta, GA, US, July. <https://doi.org/10.1109/apusncursinrsm.2019.8888979>. TechRxiv: 20151677.
- Kornprobst, J., R. A. M. Mauermayer, O. Neitz, J. Knapp, and T. F. Eibert. 2019b. "On the solution of inverse equivalent surface-source problems." *Prog. Electromagn. Res.* 195:47–65. <https://doi.org/10.2528/pier19050904>.
- Kornprobst, J., and T. F. Eibert. 2017a. "Accurate and stable solutions to electromagnetic scattering problems by means of the electric field integral equation augmented by a weak combined source condition." In *Proc. Int. Conf. Electromagn. Adv. Appl. (ICEAA)*, 1240–1242. Verona, IT, September. <https://doi.org/10.1109/iceaa.2017.8065495>. TechRxiv: 20154170.

- Kornprobst, J., and T. F. Eibert. 2017b. "An accurate combined source integral equation for perfect electrically conducting bodies." In *Proc. IEEE Int. Symp. Antennas Propag. & USNC/URSI Nat. Radio Sci. Meeting (APSURSI)*, 1457–1458. San Diego, CA, US, July. <https://doi.org/10.1109/apusncursinrsm.2017.8072771>. TechRxiv: 20151767.
- . 2017c. "RWG discretized combined source integral equation with improved iterative solver convergence." In *Kleinheubacher Tagung*. Miltenberg, DE, September.
- . 2018a. "A combined source integral equation with weak form combined source condition." *IEEE Trans. Antennas Propag.* 66, no. 4 (April): 2151–2155. <https://doi.org/10.1109/tap.2018.2800734>. arXiv: 2010.08797.
- . 2018b. "A magnetic field integral equation with accurately discretized geometrical singularities." In *Kleinheubacher Tagung*. Miltenberg, DE, September.
- . 2018c. "A weak-form combined source integral equation with explicit inversion of the combined-source condition." *IEEE Antennas Wireless Propag. Lett.* 17, no. 12 (December): 2174–2178. <https://doi.org/10.1109/lawp.2018.2869926>. arXiv: 2010.08757.
- . 2018d. "Accurate identity operator discretization for the combined field integral equation." In *Proc. IEEE Int. Symp. Antennas Propag. & USNC-URSI Radio Sc. Meeting (APSURSI)*, 2437–2438. Boston, MA, US, July. <https://doi.org/10.1109/apusncursinrsm.2018.8608501>. TechRxiv: 20151734.
- . 2018e. "An accurate low-order discretization scheme for the identity operator in the magnetic field and combined field integral equations." *IEEE Trans. Antennas Propag.* 66, no. 11 (November): 6146–6157. <https://doi.org/10.1109/tap.2018.2866578>. arXiv: 2010.08436.
- . 2018f. "Improved accuracy combined source and magnetic field integral equations with low-order discretization." In *Proc. 12th Eur. Conf. Antennas Propag. (EuCAP)*. London, UK, April. <https://doi.org/10.1049/cp.2018.0822>. TechRxiv: 20154167.
- . 2019. "Investigations on the solution of the magnetic field integral equation with Rao-Wilton-Glisson basis functions." In *Proc. Int. Conf. Electromagn. Adv. Appl. (ICEAA)*. Granada, ES, September. <https://doi.org/10.1109/iceaa.2019.8879174>.
- . 2022. "Accuracy analysis of div-conforming hierarchical higher-order discretization schemes for the magnetic field integral equation," TechRxiv: 21153130.
- Kornprobst, J., J. Knapp, R. A. M. Mauermayer, O. Neitz, A. Paulus, and T. F. Eibert. 2021a. "Accuracy and conditioning of surface-source based near-field to far-field transformations." *IEEE Trans. Antennas Propag.* 69, no. 8 (August): 4894–4908. <https://doi.org/10.1109/tap.2020.3048497>. arXiv: 2004.08918.
- Kornprobst, J., J. Knapp, O. Neitz, and T. F. Eibert. 2019c. "Measurement-error controlled iterative least-squares solutions of inverse field transformation problems." In *Proc. 41st Ann. Symp. Antenna Meas. Techn. Assoc. (AMTA)*. San Diego, CA, US, October. <https://doi.org/10.23919/amtap.2019.8906459>. TechRxiv: 20126231.
- Kornprobst, J., R. A. M. Mauermayer, A. Paulus, and T. F. Eibert. 2019d. "Method-of-moments modeling of conducting objects within the fast irregular antenna field transformation algorithm." In *Proc. 41st Ann. Symp. Antenna Meas. Techn. Assoc. (AMTA)*. San Diego, CA, US, October. <https://doi.org/10.23919/amtap.2019.8906355>. TechRxiv: 20126102.
- Kornprobst, J., R. A. M. Mauermayer, and T. F. Eibert. 2020. "Versatile low-cost and light-weight RF equipment for field measurements." In *Proc. 14th Eur. Conf. Antennas Propag. (EuCAP)*. Copenhagen, DK, March. <https://doi.org/10.23919/eucap48036.2020.9135598>. TechRxiv: 20126489.

- Kornprobst, J., R. A. M. Mauermayer, E. Kılıç, and T. F. Eibert. 2019e. "An inverse equivalent surface current solver with zero-field enforcement by left-hand side Calderón projection." In *Proc. 13th Eur. Conf. Antennas Propag. (EuCAP)*. Krakow, PL, April. TechRxiv: 20153630. <https://ieeexplore.ieee.org/document/8739983>.
- Kornprobst, J., R. A. M. Mauermayer, E. Kılıç, B. Möhring, and T. F. Eibert. 2019f. "Improved-accuracy Calderón projector with Rao-Wilton-Glisson discretization for inverse equivalent current methods." In *Proc. Photonics Electromagn. Res. Symp. (PIERS)*. Rome, IT, June.
- Kornprobst, J., T. Mittermaier, P. Schmidbauer, and T. F. Eibert. 2016. "Signal recovery for self-mixing receivers." In *Kleinheubacher Tagung*. Miltenberg, DE, September.
- Kornprobst, J., T. J. Mittermaier, and T. F. Eibert. 2017a. "Orthogonal frequency division multiplexing with amplitude shift keying subcarrier modulation as a reliable and efficient transmission scheme for self-mixing receivers." *Adv. Radio Sci.* 15:99–106. <https://doi.org/10.5194/ars-15-99-2017>.
- . 2018a. "A millimeter-wave self-mixing array with large gain and wide angular receiving range." *IEEE Trans. Antennas Propag.* 66, no. 2 (February): 702–711. <https://doi.org/10.1109/tap.2017.2780897>. arXiv: 2105.08685.
- . 2018b. "A non-reciprocal receive array with large beamwidth and gain." In *Proc. 11th German Microw. Conf. (GeMiC)*, 33–35. Freiburg, DE, March. <https://doi.org/10.23919/gemic.2018.8335021>. TechRxiv: 20153666.
- Kornprobst, J., T. J. Mittermaier, R. A. M. Mauermayer, G. F. Hamberger, M. G. Ehrnsperger, B. Lehmeier, M. T. Ivrlač, U. Imberg, T. F. Eibert, and J. A. Nossek. 2021b. "Compact uniform circular quarter-wavelength monopole antenna arrays with wideband decoupling and matching networks." *IEEE Transactions on Antennas and Propagation* 69, no. 2 (February): 769–783. <https://doi.org/10.1109/tap.2020.3016422>. arXiv: 2105.09333.
- Kornprobst, J., O. Neitz, J. Knapp, R. A. M. Mauermayer, and T. F. Eibert. 2019g. "Solving inverse equivalent surface source problems by the normal error system of normal equations." In *Proc. Int. Conf. Electromagn. Adv. Appl. (ICEAA)*. Granada, ES, September. <https://doi.org/10.1109/iceaa.2019.8879105>.
- Kornprobst, J., A. Paulus, and T. F. Eibert. 2021c. "Improved discretization of the full first-order magnetic field integral equation." In *Proc. 15th Eur. Conf. Antennas Propag. (EuCAP)*. Düsseldorf, DE, March. <https://doi.org/10.23919/eucap51087.2021.9410970>. arXiv: 2010.07351.
- Kornprobst, J., A. Paulus, J. Knapp, and T. F. Eibert. 2021d. "Phase retrieval for partially coherent observations." *IEEE Trans. Signal Process.* 69:1394–1406. <https://doi.org/10.1109/tsp.2021.3057261>. arXiv: 2002.02939.
- . 2022. "Multi-probe array design for partially-coherent phase retrieval in near-field measurements." TechRxiv: 21330702.
- Kornprobst, J., K. Wang, G. Hamberger, and T. F. Eibert. 2017b. "A mm-wave patch antenna with broad bandwidth and a wide angular range." *IEEE Trans. Antennas Propag.* 65, no. 8 (August): 4293–4298. <https://doi.org/10.1109/tap.2017.2710261>. arXiv: 2105.08162.
- Mauermayer, R. A. M., J. Kornprobst, and T. Fritzel. 2019. "A low-cost multicopter based near-field antenna measurement system employing software defined radio and 6-D laser metrology." In *Proc. 41st Ann. Symp. Antenna Meas. Techn. Assoc. (AMTA)*. San Diego, CA, US, October. <https://doi.org/10.23919/amtap.2019.8906481>. TechRxiv: 20126321.

PUBLICATIONS OF THE AUTHOR

- Mauermayer, R. A. M., and J. Kornprobst. 2022. "A cost-effective tethered-UAV-based coherent near-field antenna measurement system." *IEEE Open J. Antennas Propag.* 3:984–1002. <https://doi.org/10.1109/ojap.2022.3198269>. TechRxiv: 20115938.
- Ostrzyharczik, D., J. Knapp, J. Kornprobst, and T. F. Eibert. 2023. "Inverse source solutions with Huygens-surface conforming distributed directive spherical harmonics expansions." *IEEE Trans. Antennas Propag.* 71 (2): 1684–1696. <https://doi.org/10.1109/tap.2022.3228752>. TechRxiv: 21259221.
- Paulus, A., J. Knapp, J. Kornprobst, and T. F. Eibert. 2022a. "Reliable linearized phase retrieval for near-field antenna measurements with truncated measurement surfaces." *IEEE Trans. Antennas Propag.* 70, no. 8 (August): 7362–7367. <https://doi.org/10.1109/tap.2022.3145383>. arXiv: 2109.10864.
- . 2020. "Improved-reliability phase-retrieval with broadband antenna measurements." In *Proc. 14th Eur. Conf. Antennas Propag. (EuCAP)*. Copenhagen, DK, March. <https://doi.org/10.23919/eucap48036.2020.9135084>. TechRxiv: 20126813.
- Paulus, A., J. Kornprobst, and T. F. Eibert. 2022b. "Electromagnetic field transformations of near-field data without global reference for magnitude and phase." In *Proc. 44th Ann. Meeting Symp. Antenna Meas. Techn. Assoc. (AMTA)*. Denver, CO, US, October. TechRxiv: 20352672.
- Paulus, A., J. Kornprobst, J. Knapp, and T. F. Eibert. 2021. "Linear phase retrieval for near-field measurements with locally known phase relations." In *Proc. 15th Eur. Conf. Antennas Propag. (EuCAP)*. Düsseldorf, DE, March. <https://doi.org/10.23919/eucap51087.2021.9411328>. arXiv: 2011.08980.
- Paulus, A., J. Kornprobst, R. A. M. Mauermayer, and T. F. Eibert. 2019. "Comparison of source localization and scatterer modeling in near-field antenna measurements." In *Proc. 13th Eur. Conf. Antennas Propag. (EuCAP)*. Krakow, PL, April. TechRxiv: 20154089. <https://ieeexplore.ieee.org/document/8739513>.
- Wang, K., J. Kornprobst, and T. F. Eibert. 2016. "Microstrip fed broadband mm-wave patch antenna for mobile applications." In *Proc. IEEE Int. Symp. Antennas Propag. (APSURSI)*, 1637–1638. Fajardo, PR, US, July. <https://doi.org/10.1109/aps.2016.7696525>. TechRxiv: 20151530.